Three-dimensional behaviour of brickwork masonry arch bridges

Bowen Liu

Submitted in accordance with the requirements for the degree of Doctor of Philosophy

The candidate confirms that the work submitted is their own, except where work which has formed part of jointly authored publications has been included. The contribution of the candidate and the other authors to this work has been explicitly indicated below. The candidate confirms that appropriate credit has been given within the thesis where reference has been made to the work of others.

The work in Chapter 2 of the thesis has appeared in publication as follows:

Bowen Liu, Anastasios Drougkas, and Vasilis Sarhosis. A material characterisation framework for assessing brickwork masonry arch bridges: From material level to component level testing. Construction and Building Materials, 2023; 397:132347.

I was responsible for Investigation, Methodology, Writing – original draft, Visualization, Formal analysis, Data curation, Formal analysis.

The contribution of the other authors includes: Anastasios Drougkas: Investigation, Methodology, Conceptualization, Writing – review & editing. Vasilis Sarhosis: Supervision, Methodology, Conceptualization, Writing – review & editing.

The work in Chapter 3 of the thesis has appeared in publication as follows:

Bowen Liu, Anastasios Drougkas, Vasilis Sarhosis, Colin Smith, and Matthew Gilbert. Experimental investigation on the shear behaviour of the brickwork-backfill interface in masonry arch bridges. Engineering Structures, 2023; 292:116531.

I was responsible for Writing – review & editing, Data curation, Writing original draft, Visualization, Conceptualization, Methodology, Formal analysis.

The contribution of the other authors includes: Anastasios Drougkas: Writing – review & editing, Conceptualization, Methodology. Vasilis Sarhosis: Supervision, Conceptualization, Methodology, Writing – review & editing. Colin C. Smith: Supervision, Writing – review & editing. Matthew Gilbert: Supervision, Writing review & editing.

The work in Chapter 4 of the thesis has appeared in publication as follows:

Vasilis Sarhosis, Bowen Liu and Matthew Gilbert. The 3D response of a large-scale

masonry arch bridge - Part I: Performance under low and medium loading levels. Engineering Structures, 2024; 316: 118496.

I was responsible for Writing – original draft, Visualization, Validation, Methodology, Formal analysis, Data curation, Conceptualization.

The contribution of the other authors includes: Vasilis Sarhosis: Writing – review & editing, Writing – original draft, Validation, Supervision, Methodology, Funding acquisition, Data curation, Conceptualization. Matthew Gilbert: Writing – review & editing, Funding acquisition, Conceptualization.

The work in Chapter 5 of the thesis has appeared in publication as follows:

Bowen Liu, Vasilis Sarhosis, Adam Booth and Matthew Gilbert. The 3D response of a large-scale masonry arch bridge - Part II: Performance at failure. Engineering Structures, 2024; 313: 118308.

I was responsible for Writing – review & editing, Writing – original draft, Validation, Methodology, Investigation, Data curation, Formal analysis, Conceptualization, Visualization.

The contribution of the other authors includes: Adam Booth: Writing – review & editing, Software, Resources, Methodology, Investigation, Formal analysis, Conceptualization. Vasilis Sarhosis: Writing – review & editing, Writing – original draft, Visualization, Validation, Supervision, Project administration, Methodology, Investigation, Funding acquisition, Formal analysis, Data curation, Conceptualization; Matthew Gilbert: Writing – review & editing, Validation, Supervision, Project administration, Methodology, Investigation, Funding acquisition, Formal analysis, Data curation, Conceptualization.

The work in Chapter 6 of the thesis has appeared in publication as follows:

Bowen Liu, Joshua Collier and Vasilis Sarhosis. Digital image correlation based crack monitoring on masonry arch bridges. Engineering Failure Analysis, 2025; 169: 109185.

I was responsible for Methodology, Software, Data curation, Writing- Original draft preparation, Visualization, Investigation, Writing- Reviewing and Editing.

The contribution of the other authors includes: Joshua Collier: Software, Investigation, Writing- Reviewing and Editing. Vasilis Sarhosis: Conceptualization, Funding acquisition, Formal analysis, Supervision, Writing- Reviewing and Editing.

The work in Chapter 7 of the thesis has appeared in publication as follows:

Liu, B., Kawabe, D., Kim, CW. and Sarhosis, V. Full life-cycle vibration-based monitoring of a full-scale masonry arch bridge with increasing levels of damage. Engineering Structures, 2024; 315: 118466.

I was responsible for Writing – original draft, Data curation, Conceptualization, Investigation, Visualization, Formal analysis.

The contribution of the other authors includes: Chul-woo Kim: Writing – review & editing, Supervision, Project administration, Methodology, Conceptualization. Daigo Kawabe: Writing – review & editing, Data curation, Conceptualization. Vasilis Sarhosis: Writing – review & editing, Validation, Supervision, Project administration, Methodology, Funding acquisition, Conceptualization.

Acknowledgement

Frist and foremost, I would like to express my deepest gratitude to my supervisor, Prof. Vasilis Sarhosis, for giving me the opportunity to work on this project. His invaluable academic guidance, continuous encouragement, and unwavering support over the past four years have been instrumental to my growth and success. The experiences I gained under his guidance have significantly contributed to my professional and personal development. Working with him has been an enjoyable journey.

I would like to thank my colleges, all investigators and researchers in the ERMABI project. They have offered valuable support in designing and performing the full-scale bridge tests and provided many valuable suggestions in my research work. Also, I would like to extend my thanks to the technician team of George Ealy Laboratory, University of Leeds, in particular, Mr. Ian Day, Mr. Robert Clark, and Mr. Marvin Willem. It is only with their support and assistance that experiments can happen.

Furthermore, I would like to express my sincere gratitude to my examiners Dr Enrico Tubaldi and Dr Suhalia Ghazi Mattar for their time, insightful questions, and valuable feedback. Your expertise and constructive comments have not enriched my work but also inspired me to think more deeply about its broader implications. Thank you for making this experience both challenging and rewarding.

Finally, I would like to thank my parents for their love and unconditional support. I also want to express my gratitude to my friends for their encouragement and accompany.

I wrote this as the last part after finishing other chapters, but I found it is the most difficult part to write. There are countless people and memories that have overwhelmed my thoughts. The submission of the thesis marks the end of nearly my eleven years of studies, but also the beginning of my next journey. I just want to say a big thank you to everyone who has been a part of my life.

Leeds, December 2024

Bowen Liu

Abstract

Masonry arch bridges form a pivotal part of the transport networks of the UK and many other countries worldwide. Nonetheless, these historical structures face substantial challenges in terms of their safety and functionality. Factors such as climate change and natural hazards contribute to the continuous deterioration of materials, while growing demands are imposed upon them by modern traffic systems. Despite extensive research conducted on masonry arch bridges over the past two decades, the understanding of their fundamental behaviour remains limited, especially concerning their three-dimensional (3D) response characteristics. This dissertation aims to comprehensively assess 3D behaviour and failure mechanisms of brickwork masonry arch bridges under different loading scenarios, improving the resilience of these critical infrastructure assets.

The dissertation initiates with the characterisation of material and mechanical parameters of masonry arch bridges. Initially, small-scale material level tests are conducted to determine the properties of masonry units and mortar, as well as the internal friction angle and cohesion of the backfill materials. Then, the compressive strength and Young's modulus of masonry prisms, as well as unit-mortar bond properties are experimentally assessed at the component level. Further, large-scale shear box tests are carried out to identify the frictional properties existing between the masonry specimens with different bonds and backfill materials. Additionally, both static and high-cycle fatigue three-point bending tests are conducted on masonry flat arches. The experimental results highlight the inherent variability of masonry properties. Moreover, crack propagation and load-deflection curves obtained from the flat arche tests reveal a rapid degradation in stiffness when load magnitude changes.

Utilizing the materials characterised, a full-scale masonry arch bridge is constructed in the laboratory. The bridge is well instrumented with various sensors to capture its 3D response under loads. Static and cyclic (three loading cycles) patch loads are applied to nine locations on the backfill surface, including both centric and eccentric locations. The magnitudes of the load are increased gradually from 150 kN (approximately 22-25% of the peak load that the bridge is expected to carry) to 250 kN (~50% of the ULS), until the bridge failure. Crack evolution, accumulation of damage, load-deflection responses of the arch barrel, in-plane and out-of-plane deflection of the spandrel walls are analysed.

In addition to the contacting gauges, digital image correlation (DIC) is utilised to monitor the initiation and propagation of full-field strain/cracking in the spandrel wall during these tests. Comparing DIC data with readings from displacement gauges, the results confirm that DIC can measure the deformations of the untreated surface with satisfied accuracy, using the inherent brick bond patterns and natural characteristics of the masonry surface as tracking points. DIC results provide valuable insights into the cracking behaviour of the masonry arch bridge throughout the entire loading-unloading process, offering critical information on the load levels that induced the onset and the activation of hinges. Additionally, the interaction between the arch barrel and spandrel wall, as well as the crack mechanism in the spandrel wall, are analysed.

Moreover, along with the loading tests, hammer-induced vibration response of the bridge are collected, and modal parameters of the bridge with different levels of damage are identified using stochastic subspace identification (SSI) method. Also, numerical analysis is performed to identify the mode shapes of the bridge. Full life-cycle vibration-based assessment is carried out by analysing the correlation between stiffness degradation and variations in the bridge's modal parameters. The results demonstrate that the first-order frequency had the highest sensitivity to the damage accumulation in the masonry arch bridge. The evolution of early-stage damage, the formation of the first hinge, and the fully activation of a four-hinge mechanism are successfully captured.

Table of Contents

List of Figures

List of Tables

List of Abbreviations

NDT	Non-destructive tests
SHM	Structural health monitoring
DIC	Digital image correlation
FEM	Finite element modelling
DEM	Discrete element modelling
ULS	Ultimate limit state
SSI	Stochastic subspace identification
CV	Coefficient of variation
SL	Soldier course brickwork-limestone interface
SC	Soldier course brickwork-clay interface
EL	English bond brickwork-limestone interface
EC	English bond brickwork-clay interface
RC	Reinforced concrete
3D	Three-dimensional
LVDT	Linear variable differential transformer
GPR	Ground penetrate radar
FOV	Field of view
CAN	Controller area network
$f_{c,u}$	Compressive strength of masonry units
$f_{b,u}$	Flexural strength of masonry units
$f_{t,u}$	Tensile strength of masonry units
R_{tf}	Bending tensile strength of masonry units
E_u	Young's modulus of masonry units
ρ_u	Density of masonry units
δ	Shape correction factor
b	Specimen width
h	Specimen hight
L_c	Specimen length
d_c	Diameter of a cylinder
F_{sp}	Splitting load
F	Failure load

l	Distance between supports
ρ_j	Density of mortar joints
$f_{c,j}$	Compressive strength of mortar joints
E_j	Young's modulus of mortar joints
$f_{b,j}$	Flexural strength of mortar joints
$f_{c,m}$	Compressive strength of masonry
E_m	Young's modulus of masonry
v_m	Poisson's ratio of masonry
$f_{f,i}$	Flexural bond strength at unit-to-mortar interface
$f_{t,i}$	Tensile bond strength at unit-to-mortar interface
φ_i	Interface friction angle
C_i	Interface cohesion
A_c, A	Load bearing area
φ	Internal friction angle of backfill material
c	Cohesion of backfill material
S_v	Vertical total stress
γ	Unit weight of the backfill material
P_p	Passive lateral soil pressure
K_p	Passive lateral earth pressure coefficient
R^2	Coefficient of determination
R_{cr}	Relative critical roughness
R_{max}	Absolute vertical distance between the highest peak and lowest valley along the surface profile
D_{50}	Average particle size of a soil
$f_{s,peak}$	Peak shear strength
$f_{s,res}$	Residual shear strength
$F_{s,peak}$	Peak load
$F_{s,res}$	Residual load
A_i	Cross-sectional area of a masonry triplet parallel to the bed joints
τ	Shear strength of triplets
σ_c	Pre-compression
f	Frequency
f_1 to f_5	Five orders of frequency
$f_{1,n}$ to $f_{5,n}$	Five orders of normalised frequency

V	Train velocity
d	Wheelbase distance of a train
L_m	Length of a masonry arch bridge
L_t	Total length of a train
N	Number of loading cycles
δ	Vertical deflection
S	Stiffness
S_n	Normalised stiffness
D_p	Peak radial deflection
D_r	Residual deflection
G	Energy
ε_r	Implied relative dielectric permittivity
L_{open}	Load inducing the crack
$\boldsymbol{x(t)}$	State vector at continuous time
$\boldsymbol{y(t)}$	Displacement vector at continuous time
$\boldsymbol{f(t)}$	External force vector at continuous time
$\boldsymbol{M, D, K}$	Mass, damping and stiffness matrices
$\boldsymbol{C}$	Output matrix
$\boldsymbol{I}$	Unit matrix
$\boldsymbol{A}$	System matrix
$\boldsymbol{S}$	Diagonal matrix with non-negative real elements
$\boldsymbol{U, V}$	Unitary matrices
$\boldsymbol{w_k, v_k}$	Zero-mean white noise vectors
m	Number of measurement points on the structure
ξ	Damping ratio
Δ	Discrepancy
E'	Equivalent elastic modulus

1 Introduction

1.1 Background

Masonry is one of the oldest structural forms around the world not only results from the abundance of raw materials such as stone and clay, but also for its good durability, simplicity of construction, cost-effectiveness, and excellent in bearing gravitational loads [1]. Typical masonry includes churches, monuments, towers, arch bridges, etc. They are widely distributed, and a large number of them, which have been in use for centuries, are still in service today.

Masonry arch bridges are a vital part of the transportation infrastructure system around the world. The most representative masonry arch bridges include the Göltzsch Viaduct bridge in Germany, Knaresborough Viaduct and Ouse Valley Viaduct in the UK, (see Figure 1.1). It is estimated that there are approximately 200,000 masonry arch bridges and culverts in Europe and 40,000 masonry arch bridges in the UK. On the railways, approaching half the bridge spans in the UK network are of masonry arch construction, amounting to >25,000 spans.

Figure 1.1 Masonry arch bridges. (a) Knaresborough Viaduct; (b) Göltzsch Viaduct [2]; and (c) Ouse Valley Viaduct [3].

The majority of masonry arch bridges were built between the 17th and 19th centuries [4,5]. Keeping these old bridges safe and functional is of great significance, not only for their contribution to the landscape but more importantly, because the cost of replacing them may be too high to be acceptable. It is estimated that the average reconstruction cost of each bridge is £800k, and the cost of replacing all these bridges conservatively exceeds £20bn at 2011/21 prices (ERMABI, 2019).

However, the health status of the ageing masonry arch bridges is of great concern. For example, after serving for years, these bridges inevitably suffered several damages due

to:

a) **Environmental effects**: several environmental factors such as the temperature, moisture (in the forms of rain, ice and snow), soil conditions, vegetation, solar radiation (in particular short-wave radiation), chemicals in the air, and pollution-derived parameters can cause long-term erosion of masonry and thus results in the severe structural deterioration of masonry arch bridges [6,7];

b) **Natural disasters and effects of climate change**: masonry structures are extremely vulnerable to earthquakes due to their low shear and tensile strength. On the other hand, climate change results in an increased risk of flooding and rainstorms, and effects such as scour can result in the bridge collapse (e.g., an arch bridge in Tadcaster, North Yorkshire, was destroyed by the 2015 Boxing Day floods) [8,9]; and

c) **Man-made or anthropogenic effects**: the long-term man-made or anthropogenic vibrations, as well as the increasing traffic loads, may cause fatigue failure and accidental damage to masonry arch bridges.

In addition to the material deterioration over time, most masonry arch bridges are being subjected to increasing demands in terms of vehicle and train numbers, speeds, and axle loads, which also post considerable risk to their structural safety. For instance, with the introduction of long-wheelbase freight wagons, railway arch bridges in northwestern England have been subjected to higher loads than expected and suffered severe unforeseen and costly damage. In Europe, it is proposed for passenger traffic that the maximum speed should be allowed up to 350 km/h, which will significantly amplify the vibration of the bridges [10]. Moreover, fatigue damage has been observed on some masonry arch bridges, and the repeated application of heavy loads would rapidly accelerate the deterioration of the arch bridges, as suggested by maintenance engineers [11].

In recent years, the fatigue behaviour of masonry is gaining increasing attention from the scientific community and engineers. Fatigue is defined as the failure of a material under cyclic stresses (or strains) below the strength limit. Since there is always no obvious macroscopic plastic deformation in structures, and the upper bound of the cyclic load that causes fatigue failure is generally far less than the 'safe' load estimated by static analysis, fatigue failure usually occurs very suddenly and may lead to catastrophic accidents.

Several experimental studies have been carried out on the compressive fatigue behaviour of brickwork masonry, including masonry prisms and columns [12–15]. Regarding the fatigue behaviour of the masonry arch bridge, [16] have carried out the first high-cycle fatigue test on the masonry arch bridge under plane-strain conditions. Through testing four bridges with different backfill materials subjected to a range of loading scenarios; they found that repeated cyclic loading at safe working load levels did not significantly affect the ultimate load-carrying capacity of the virgin masonry arch bridge. As the upper bound of the cyclic load increased, more severe damage was observed, such as loss of bricks from the arch barrel, which resulted in a considerable reduction in the ultimate capacity of the bridge.

So far, the study on characteristics of the three-dimensional response of the bridge, fatigue behaviour, and damage accumulation of brickwork masonry arch bridge under static/cyclic/fatigue loading is still at the initial stage. The serviceability and permissible limit states of masonry arch bridges under static/fatigue loads considering the interaction between different components are not fully understood by the scientific community and engineers. Moreover, experimental data is not sufficient regarding the 3D response of the bridge and structural behaviour under high-cycle fatigue loads, which bring considerable difficulties for the development of numerical models on masonry arch bridge.

1.2 Aim, Objectives, and Thesis Outline

The overall aim of this PhD project is to gain an improved understanding of the 3D behaviour of masonry arch bridges under static and quasi-static loads, primarily utilizing laboratory experiments.

The objectives of this PhD project include:

1. Gain an up-to-date understanding of the behaviour of brick masonry through the literature review.

2. Comprehensively characterise material and mechanical parameters of masonry arch bridges.

3. Gain a better understanding on the 3D response characteristics of masonry arch bridges subjected to different loads.

4. Using advanced non-contact sensing technics to monitor the damage accumulation and assess the conditions of masonry arch bridge.

This doctoral thesis is publication-based and includes 6 peer-reviewed journal publications. Chapter 2 to Chapter 7 consist of previously published papers that cope the objectives of this research project. Chapter 8 summaries the main findings of the research, limitations, and recommendations for the future works. The main contributions of this doctoral project included:

1.2.1   Chapter 2: Publication #1 (Liu et al., 2023a)

A material characterization framework was developed and a comprehensive dataset of properties representing historic masonry structures was provided through a series of laboratory tests from the material level to the component level.

1.2.2   Chapter 3: Publication #2 (Liu et al., 2023b)

Frictional parameters between masonry arch bridge and backfill materials were characterized, considering two masonry bond configurations (i.e., English bond and stretcher bond) and two types of backfill materials (i.e. crushed limestone and clay).

1.2.3   Chapter 4: Publication #3 (Sarhosis, Liu and Gilbert, 2024a)

A full-scale masonry arch bridge was designed and constructed in the laboratory using the materials characterized in chapter 2 and 3. Patch loads with increasing magnitudes were applied at different locations on the top of the backfill in order to investigate the 3D response and damage accumulation in the bridge. Details of the experimental setup, material characterisation, and results obtained from static and repeated load tests at low- and medium load levels are presented in Chapter 4, focusing on the elastic behaviour and early-stage damage initiation and accumulation in the masonry arch bridge.

1.2.4   Chapter 5: Publication #4 (Liu et al., 2024b)

Results obtained from the high-level loading test and two failure-level tests were analysed in Chapter 5. In particular, the three-dimensional behaviour, load-carrying capacity, failure mechanism, and residual capacity of the masonry arch bridge were discussed.

1.2.5   Chapter 6: Publication #5 (Liu et al., 2025)

Apart from the results from obtained from physical attaching gauges, digital image

correlation (DIC) was used for full-field displacement/strain analysis. This chapter presented the results obtained from DIC. Specifically, the accuracy of DIC was verified by comparing the results obtained from DIC and LVDTs. Then, critical loading values that induced hinges were discussed. Furthermore, the interaction mechanism between the arch barrel and spandrel wall was analysed.

1.2.6 Chapter 7: Publication #6 (Liu et al., 2024c)

Along with the loading tests on the masonry arch bridge, full lifecycle vibration-based monitoring on the bridge was conducted. The modal parameters (i.e., frequency and damping ratio,) of the bridge were identified using stochastic subspace identification (SSI) method. The correlation analysis between the damage accumulation and variations in modal parameters of the bridge were investigated.

2 Multi-scale Material Characterisation

This chapter represents the slightly modified post-print version of the article: **B. Liu**, A. Drougkas, V. Sarhosis, "A material characterisation framework for assessing brickwork masonry arch bridges: From material level to component level testing", Construction and Building Materials, 397 (2023) p. 132347. The formatting and numbering of equations, tables and figures have been adapted to this document.

2.1 Abstract

This chapter aims to present a systematic framework for material characterisation to assess brickwork masonry arch bridges. An extensive laboratory campaign was carried out to characterise brickwork and backfill material in masonry arch bridges. Initially, the strength and Young's modulus of bricks and mortar, as well as the internal friction angle and cohesion of the backfill materials (e.g., crushed limestone and puddling clay), were characterised by undertaking small-scale material level tests. Then, the compressive strength and Young's modulus of masonry prisms, as well as unit-to-mortar bond properties (e.g., tensile strength, angle of friction and cohesion) were assessed at the component level. Further, large-scale shear box tests were carried out to identify the frictional properties, including the interface friction angle and cohesion, between the brickwork and backfill material. Moreover, both static and high-cycle fatigue three-point bending tests were performed on masonry flat arches to obtain fatigue crack growth and stiffness degradation parameters. Outputs from this experimental campaign can be used for parameter identification and model calibration of complex/high-fidelity numerical models developed to assess masonry arch bridges.

2.2 Introduction

Assessing the structural performance of ageing masonry infrastructure (see Figure 2.1) is a complex task. Masonry is a brittle composite material with great inherent variability at the material level. The mechanical behaviour of masonry largely depends on the material properties of masonry units (i.e., bricks) and bonding materials (i.e., mortar), as well as the bond properties between units and mortar. Moreover, masonry arch bridges are vulnerable to material degradation induced by various factors, including weathering, chemical and biological factors. Existing and ageing masonry arch bridges

characterised by (a) low bond strength of mortar joints, and (b) cracking along mortar joints [17].
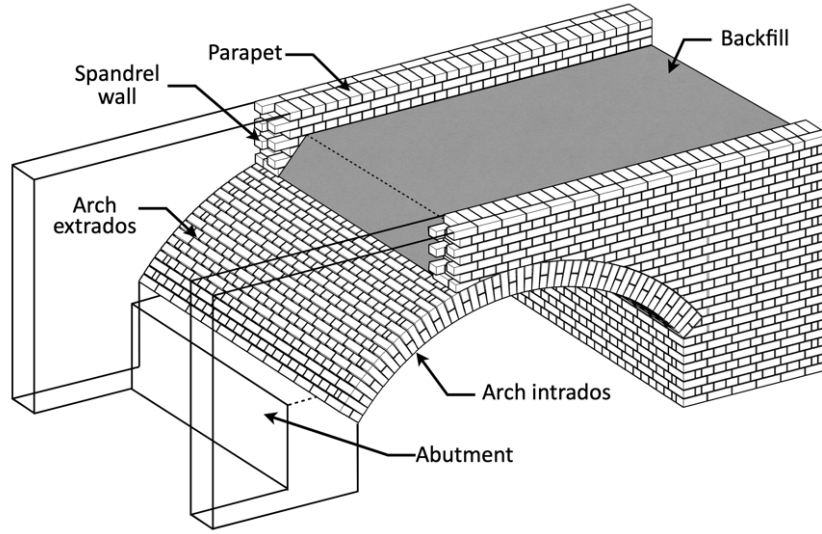
Figure 2.1 Primary elements of a masonry arch bridge.

To assess the strength properties of historical masonry arch bridges, destructive testing that takes samples from real bridges can be the most straightforward and accurate method. For example, utilizing Brazilian testing on masonry core specimens containing inclined mortar layers to determine the shear strength of masonry was investigated by [18]. First, 22 masonry cores were tested, with the core samples placed with different mortar layer inclinations (α) (i.e., α ranging from 0 degree to 50 degrees), and the axial stress at failure σ_c and the shear capacity f_v have been calculated according to the formulas:

$$\sigma_c = (F/A) \times \cos \alpha \tag{2.1}$$

$$f_v = (F/A) \times \sin \alpha \tag{2.2}$$

Then, direct shear tests were performed on 9 masonry panels under three levels of compressive stress. The linear regression analysis on the correlation between shear and compression stresses obtained from Brazilian testing and shear testing on masonry panels were compared, and a good agreement was obtained regarding the initial shear strength and friction angle of the mortar joint. On the other hand, 45 core samples with different joint configurations were drilled from an old masonry arch bridge. By performing Brazilian testing and compression testing with loading caps on cylindrical masonry core samples, the compressive strength, Young's modulus, tensile and shear capacities of aged masonry were determined [19]. The testing results provide an accurate assessment of the mechanical properties of the aged masonry arch bridge. However, such

destructive testing can result to irreversible damage to the structure due to the removal of material. In addition, invasive sampling can cause physical alterations to the bridge, which can be problematic, if the masonry arch bridge is listed and contains historical significance.

For in-service bridges, visual inspection, non-destructive tests (NDT) and structural health monitoring (SHM) may be preferable, as they enable real-time and continuous assessment of masonry arch bridges without causing any damage to bridges. Visual inspection can be used to capture any potential surface-level defects (i.e., cracks). More recently visual inspection can be done with the use of drones which are able to take a series of photos of the bridge and develop three-dimensional reconstruction models. Additionally, non-destruction vision-based technics can also be used as digital image correlation (DIC) to obtain localised stain maps [20–22]. Vibration-based structural monitoring can also be used to obtain the dynamic response of the masonry arch bridges (i.e., natural frequencies and mode shapes) [23–25]. Analysing changes in these dynamic characteristics of the bridge over time can indicate the presence of damage and signs of deterioration in masonry arch bridges. Moreover, in-situ flat jack testing can be adopted to evaluate acting normal stress and compressive behaviour of masonry [26–28]. Other techniques, such as ultrasound, ground penetrating radar, and acoustic emission, can provide internal hidden details and help to identify the non-visible by human eye damage in masonry arch bridges [29–31].

Over the years, a series of full-scale experimental tests on masonry arch bridges have been done to understand their mechanical response [32–34]. Such tests have been used later for the development and validation of high-fidelity models. Even though such newly built specimens are not specifically representative of a particular masonry arch bridge, their mechanical properties (i.e., relatively strong units with low bond strength) can broadly reflect the mechanical performance of masonry and reproduce the failure mechanism of a real masonry arch bridge. For example, twenty-four tests on small scale masonry arch bridges carried out by Royles and Hendry [35] clearly demonstrated the enhancement effects of backfill, spandrels and wingwalls on the load-carrying capacity of masonry arch bridges. According to their experimental observations, the typical failure mode for single-ring masonry arch bridges under static loads is a four-hinge mechanism, with higher compressive stresses concentrated at the springings, quarter, and three-quarters of the arch barrel. For multi-ring masonry arch bridges, the occurrence of shear cracks between adjacent rings results in ring separation, which significantly reduces the

structural integrity of masonry arch bridges [36,37]. When subject to fatigue loads below the safe working load, the stiffness of the bridge was reduced. However, the residual capacity of cracked bridges did not decrease significantly unless any considerable damage occurred, such as the loss of bricks [16]. More recently, the fatigue behaviour of masonry arch bridges is receiving increasing attention from engineers and scientific communities [11]. Ronca et al. [38] performed the first high-cycle fatigue tests on masonry prisms and proposed stress life relationships for masonry under centric compression cyclic loads. Followed by Ronca's study, other compression fatigue tests on masonry have been carried out considering the effects of centric/eccentric loading, degree of water saturation of specimens, loading rates and stress gradients [12,14,15]. Alexakis et al. [39] performed fatigue tests on masonry beams to investigate the damage accumulation of brick masonry under bending cyclic loads. Although some insights into the fatigue behaviour of masonry have been discussed, the main focus was on the reduction in the load-carrying capacity of specimens with the increase in loading cycles. Nevertheless, the crack propagation and damage accumulation in masonry subjected to high-cycle fatigue load have not been thoroughly discussed, which is, however, of great help in understanding the stiffness degradation and fatigue life of masonry.

While the experimental testing of structures is effective in capturing the structural response under mechanical loading, the high cost of performing tests, complex construction process, various restrictions of testing facilities, and potentially extremely long test periods make it challenging to conduct laboratory experiments on large-scale masonry arch bridges. Hence, several numerical methods ranging from simple to complex/high fidelity (i.e., FEM and DEM) have been developed and increasingly used to predict the in-service behaviour of masonry arch bridges [40–43]. To precisely reproduce the mechanical behaviour of a masonry arch bridge, a large number of input parameters are required, including the primary material properties of masonry units, mortar and backfill materials for plugging into constitutive models, interface parameters determining the interaction between the contact elements, and damage accumulation parameters, when fatigue phenomena in the structure are of interest.

From previous studies [44,45], it was shown that these input parameters can significantly influence the computational accuracy of the model, and therefore they should be carefully and reasonably selected. Most of these parameters can be characterized by experiments at the material level and the component level. For example, Table 2.1 summarises some material and mechanical properties (mean values) of

masonry obtained from experimental studies in recent years. From Table 2.1, the variability in the mechanical behaviour of masonry is evident. Also, it is suggested that the type of units, mix proportion of mortar and their bond performance can significantly affect the mechanical properties of masonry.

To the best of the authors' knowledge, there is no framework that indicates what types of experiments can be conducted in the laboratory to characterise critical parameters for assessing the static and fatigue behaviour of masonry arch bridges. To this end, this study performed an extensive experimental campaign to characterize material properties of brickwork masonry arch bridges. A series of newly built specimens were tested under different stress conditions. The selection of materials to construct those specimens was based on representative materials that found in real masonry arch bridges (i.e., relative strong units and low strength mortar). The primary aim of this chapter is to develop a systematic framework that links experimental approaches to the parameters that can be identified. Also, from the material level to the component level testing, a high-quality dataset is provided regarding the material properties of masonry units, mortar joints, and backfill materials, bond strength properties at the unit-to-mortar interface, shear behaviour at the masonry-to-backfill interface, as well as the stiffness degradation parameters of masonry flat arches under high-cycle fatigue loading, which allows researchers to develop and validate numerical models of masonry arch bridges.

Table 2.1 Mechanical and material properties of brickwork masonry obtained from experiments in recent years (mean values).

Study	Type	Masonry units — Compressive strength $f_{c,u}$ (MPa)	Masonry units — Young's modulus E_u (GPa)	Mortar — Mix ratio (C:L:S)	Mortar — Compressive strength $f_{c,j}$ (MPa)	Mortar — Young's modulus E_j (GPa)	Masonry — Compressive strength $f_{c,m}$ (MPa)	Masonry — Young's modulus E_m (GPa)	f_{cm}/E_m (%)	Flexural bond strength $f_{f,i}$ (MPa)	Tensile bond strength $f_{t,i}$ (MPa)	Interface friction angle φ_i (°)	Cohesion C_i (MPa)
S. B. Singh et al. [53]	Burnt clay brick	12.2-14.4	1.2-2.0	1:0:3/1:1:4/1:0:5	12.66-20.85	1.02-1.81	2.07-5.41	1.70-6.12	0.12-0.16	0.095-0.215	-	-	-
	Concrete brick	16.7	6.0	1:0:3/1:1:4/1:0:5	12.66-20.85	1.02-1.81	9.05-11.59	3.35-6.12	0.19-0.4	0.002-0.082	-	-	-
S. Jafari et al. [52]	Clay-solid brick	-	-	General mortar	-	-	8.0-20.7	2.58-9.35	0.14-0.31	0.33-0.43	-	38.7-41.7	-
J. R. et al. [51]	Solid wire-cut brick	61	22.0	-	12.7-14.5	8.1-11.1	30.1	-	-		0.523	31	-
G. S. et al. [50]	Burnt clay brick	3.17-10.67	0.49-0.51	1:0:4/1:0:6	7.32-10.57	5.8-9.0	2.15-5.24	-	0.09-0.39	-	-	-	-
S. Phajiu et al. [49]	Brick	11.12	3.36	1:0:4	3.8	2.56	2.5	2.7	0.09	-	-	-	-
H. Varum [48]	Ceramic brick	15.36	-	1:9:45	1.33	-	1.1-1.11	0.99-1.87	0.06-0.11	0.12-0.55	0.233	-	-
F. Khalaf [47]	Clay brick	24.0-92.0	-	1:1:6/2:1:10/4:1:12	7.8-22.2	-	-	-	-	0.228-0.585	0.067-0.264	-	-
M. Maheri et al. [46]	Lime-sand brick	11.0	7.50	1:0:3	34	12.0	4.69-5.97	-	-	0.033-0.487	0.116-0.157	-	-
	Clay brick	13.8	-	Cement-agg.	6.6	7.0	5.31-9.13	-	-	-	-	-	-
S. Kallioras et al. [8]	Solid clay brick	46.8	-	-	4.12	-	9.23	8.12	0.11	0.23	-	29	0.15

2.3 Material characterisation framework

Figure 2.2 shows a framework for the laboratory experimental programme and the corresponding parameters which can be identified. According to the framework, there are two levels of testing that can be conducted under laboratory conditions. These are: a) material level testing and b) component level testing. At the material level testing, the properties of materials (e.g., masonry units, mortar joints, and backfill materials) in a masonry arch bridge can be characterised. The component level testing can be utilized to characterise the mechanism parameters of interfaces and the interactions between different elements in a masonry arch bridge (e.g., unit-to-mortar interface and interaction between masonry and backfill), as well as to assess the static and fatigue performance of masonry components under different stress conditions.
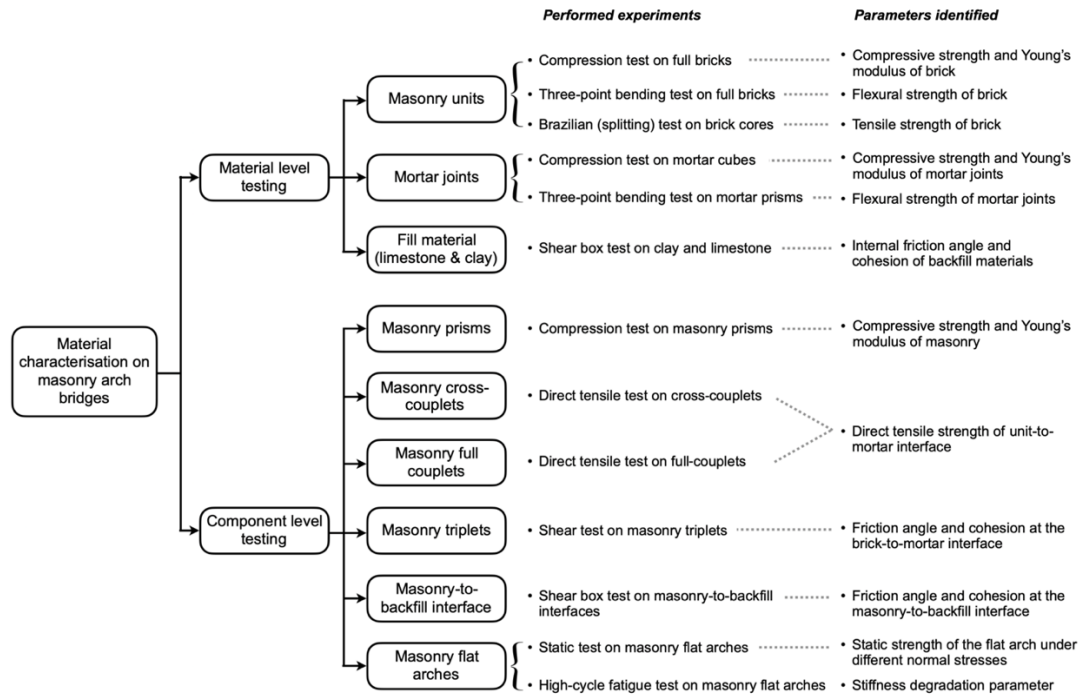
Figure 2.2 Material characterisation framework: experiments and parameters identified.

Following the proposed framework, in the present study, an extensive experimental campaign was designed and carried out from material level to component level to systematically assess the static and fatigue behaviour of masonry arch bridges. The experimental specimens constructed by using new materials were designed to have the similar mechanical behaviour of real masonry arch bridges (i.e., strong masonry units bonding with low strength mortar). Through experimental tests, a comprehensive set of parameters representing the low strength masonry arch bridge was identified.

Specifically, as the first step, the material properties of masonry units, mortar joints and backfill were characterised. Also, the compressive behaviour of masonry prisms and unit-to-mortar bond properties were determined through component level tests. In addition, large-scale shear box tests were carried out to identify the interface frictional parameters between masonry and backfill materials and assess the influence of masonry bond types and backfill properties on the masonry-to-backfill shear behaviour. Finally, both static and high-cycle fatigue loading tests were performed on masonry flat arch specimens to investigate the static and fatigue bending behaviour of masonry.

2.4 Characterization of masonry units, mortar joints and backfill materials

2.4.1 Material properties of masonry units and mortar joints

For the masonry units, high compressive strength/low water absorption fired clay bricks (referred to as the type A brick) were selected. The type A brick measured 215 mm in length × 102.5 mm in width × 63 mm in height, and the density of the brick was determined to be 2,470 kg/m³. Mechanical properties of the type A brick, including compressive strength $f_{c,u}$, flexural strength $f_{b,u}$, and tensile strength $f_{t,u}$, were characterised by standard compression tests, three-point bending tests, and Brazilian (splitting) tests, respectively, following the procedure required by the British standard BS EN 772 [54]. For the mortar, a low strength mix with cement:lime:sand proportions (by volume) equal to 1:2:9, corresponding to type O mortar, was adopted to represent the low bond strength material that may be encountered in old masonry arch bridges [55–58].

2.4.1.1 Compression tests on bricks

For the compression tests, a compression load was applied to the bed face of the type A brick with a bearing area equal to 215 mm × 102.5 mm. Two load distribution plates consisting of a timber plate (for better load distribution by avoiding hard contacting between steel plate and brick) and a steel plate were positioned on the top and bottom of the brick, with the timber side attached to the brick (see Figure 2.3 (a)). After the specimen was centrally positioned in the test rig, a compression load was applied continuously under load control at a constant stress rate of 0.4 MPa/s. The value of $f_{c,u}$ was determined by dividing the ultimate compression load by the bearing area (A_c), and a shape correction factor δ was applied as suggested by the British standard BS EN 772-

1 [59]. The compressive strain was measured using four strain gauges attached to the stretcher faces of the bricks. Nine bricks were tested in total to ensure the consistency of the results. Moreover, Young's modulus of type A brick was obtained by calculating the slope of the stress-strain curve in the interval of 5% to 33% peak stress.
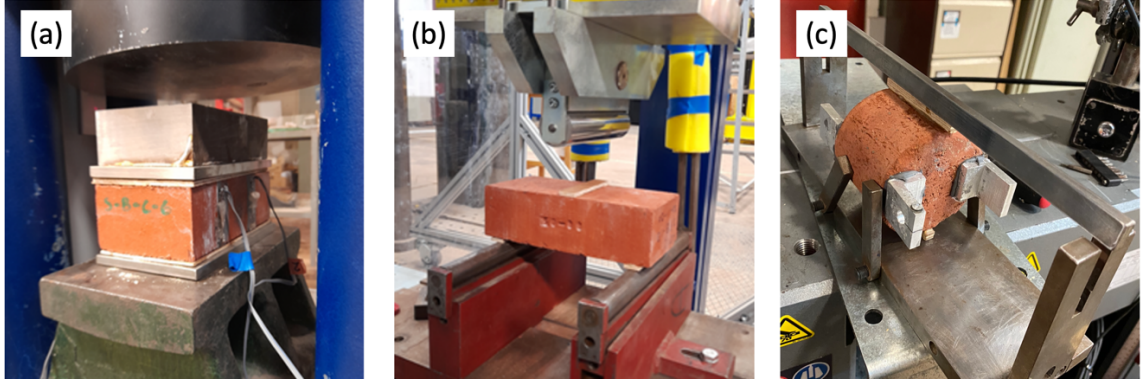
Figure 2.3 Characterisation on material properties of the type A bricks. (a) compression tests; (b) three-point bending tests; and (c) Brazilian (splitting) tests.

2.4.1.2 Three-point bending tests on bricks

The flexural strength of the type A brick was determined by three-point bending tests according to Eq. 2.3 (see Figure 2.3 (b)). Eight bricks were tested in total to ensure the repeatability of the results. The brick was placed on two supports with a span of 175 mm, and a bending load was applied to the middle of the brick. The test was executed in displacement control at a constant rate of 1 mm/min until brick failure. The bending tensile strength (R_{tf}) of the unit can be determined by the following equation according to the British standard BS EN 1052-2 [60]:

$$f_{b,u} = 3Fl/2bh^2 \tag{2.3}$$

$$R_{tf} = Fl/bh^2 \tag{2.4}$$

where F is the failure load (N); l is the distance between supports (mm); b and h are the specimen width and height, respectively (mm).

2.4.1.3 Brazilian (splitting) tests on bricks

The tensile strength of the type A brick was determined by Brazilian (splitting) tests, following the procedure outlined in the British standard BS EN 12390-6 [61]. Regarding the sampling procedure, nine cylindrical specimens having a diameter of 75±0.7 mm and a height of 63 mm were first drilled from five full bricks. For each specimen, two plywood strips were mounted in diametrically opposed locations on the cylindrical face of the specimens for the application of the splitting force (see Figure 2.3 (c)). The width of plywood was approximately 5 mm, which was 6.7% of the diameter of cylindrical

specimens, allowing the size effect present during splitting tests to be disregarded [62]. Two LVDTs were mounted on the two flat faces of the cylindrical specimen, perpendicular to the expectant splitting crack, to capture the growing of the width of the splitting crack. The tests were performed by using a 600 kN Instron Universal Testing Machine under displacement control at a constant rate of 0.07 mm/min. $f_{t,u}$ of the brick was derived from the splitting load (F_{sp}) and dimensions of the brick cylinder according to:

$$f_{t,u} = \frac{2F_{sp}}{\pi L_c d_c}$$
(2.5)

where L_c is the specimen length, and d_c stands for the diameter of a cylinder.

2.4.1.4   Bending and compression tests on mortar

The flexural strength ($f_{b,j}$) and compressive strength ($f_{c,j}$) of type O mortar were characterised at different curing ages, ranging from 13 to over 200 days, to identify the variation of mortar properties over time. It is worth noting that all the mortar specimens were cured under laboratory conditions. Three-point bending tests were carried out on mortar prisms with dimensions equal to 160 x 40 x 40 mm in accordance with the British standard BS EN 1015-11 [63].
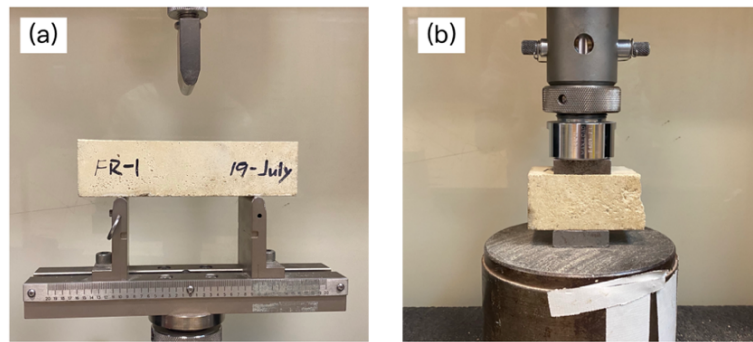
Figure 2.4 Characterisation on material properties of the type O mortar. (a) Three-point bending tests; and (b) compression tests.

As shown in Figure 2.4 (a), the mortar prism was placed on two supports with a span of 100 mm, and a vertical load was applied at the middle of the specimen under displacement control at a constant rate of 0.5 mm/min. After the prism failed under the bending load, the two parts obtained from the previous flexural test were used to evaluate the compressive strength of mortar (see Figure 2.4 (b)). Two steel plates were placed underneath and above the specimen, respectively, to control the load-bearing area as 40 mm x 40 mm. The compression load was applied at a displacement control of 0.5 mm/min. It is noteworthy that, for the testing at each curing age, at least three prisms

were tested under bending loads, and accordingly, six specimens were compressed to determine the average compressive strength of type O mortar.

2.4.1.5 Results from testing bricks and mortar

Table 2.2 lists mean values and the coefficient of variation (CV) of material properties for bricks and mortar obtained from the experiments. The mortar properties listed in Table 2.2 were 28-day strength parameters as indicative.

Table 2.2 Material properties of bricks and mortar.

Material	Type A brick		Type O mortar (28-day)	
	No. of specimens	Mean values (CV)	No. of specimens	Mean values (CV)
Density (kg/m³)	9	2470 (1.3%)	6	1738 (2.4%)
Compressive strength (MPa)	9	111.3 (6.2%)	6	2.4 (6.0%)
Flexural strength (MPa)	8	19.76 (9.6%)	6	0.85 (13.7%)
Bending tensile strength (MPa)	8	13.17(9.6%)	-	-
Tensile strength (MPa)	9	6.73 (13.5%)	-	-
Modulus of elasticity (MPa)	9	31762.6 (15.7%)	6	112.6 (36.9%)

Typical response graphs obtained from the splitting tests on bricks, three-point bending tests and compression tests on mortar are shown in Figure 2.5 (a), (b), & (c), respectively. A good agreement was observed, suggesting a high consistency between different tests on bricks and mortar specimens. Also, the peak splitting load for the brick was equal to 50.77 kN on average, and the critical splitting crack width was 0.012 mm with a CV of 21%. According to Eq. (2.5), $f_{t,u}$ of the brick was determined to be equal to 6.73 MPa with a CV equal to 13.5%. Figure 2.5 (d) & (e) show the evolution of $f_{b,j}$, $f_{c,j}$, and density (ρ_j) of mortar for different curing periods. The curing of mortar is related to the process of the hydration of cement, during which the strength of mortar increases with the gradual loss of moisture, followed by carbonation. The strength of mortar increased significantly from 13 days to 28 days, with ρ_j dropping from 1,822 kg/m³ to 1,738 kg/m³. Very similar average strength and density of mortar were observed after 28 days of curing. Moreover, the flexural strength of type O mortar was observed to be approximately 35% of its compressive strength.
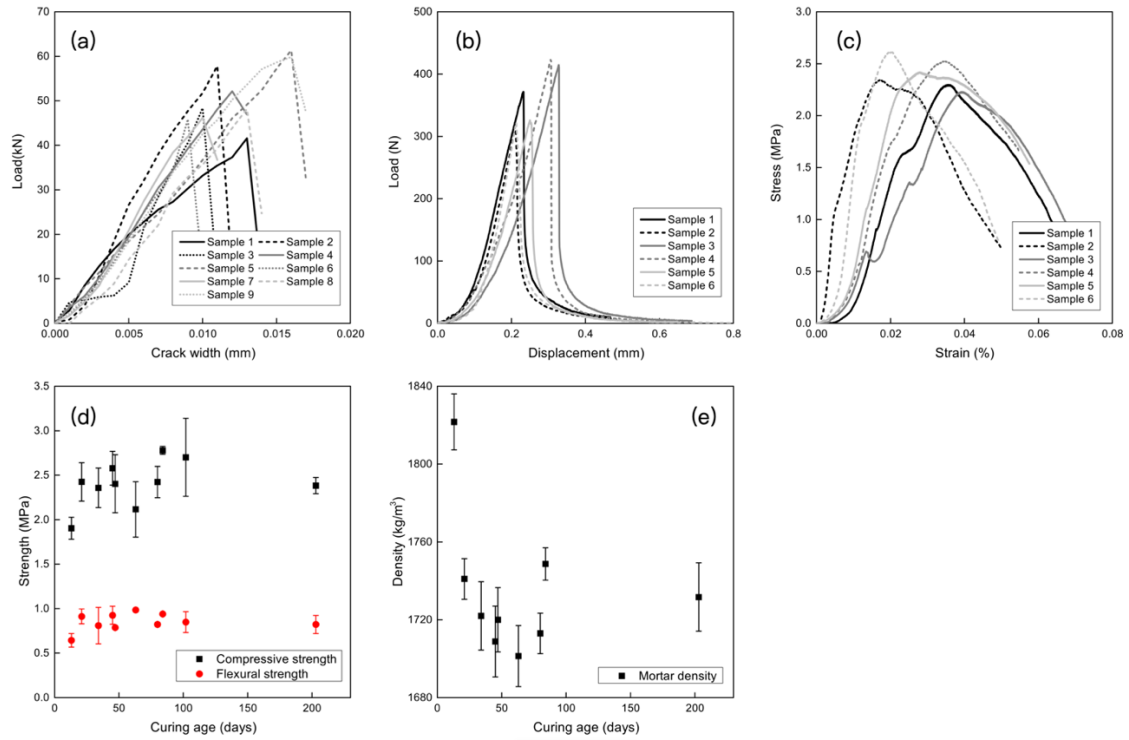
Figure 2.5 Testing results from bricks and mortar: (a) brick splitting test results; three-point bending test results (b) and compression test results (c) on mortar after curing for 28 days; variation in strength (d) and density (e) of mortar at different curing periods.

2.4.2 Material properties of limestone and puddling clay

The influence of the presence of backfill on the load-carrying capacity of a masonry arch bridge can be considerable. The backfill is responsible for transmitting and distributing live loads from the road or rail surface to the arch barrel and for laterally stabilising the arch barrel as it sways under load [34,64]. To date, several analysis models and high-fidelity numerical tools able to quantify the effects of backfill on the mechanical behaviour of masonry arch bridges have been developed. In such models, several properties are required to define the constitutive law of the backfill material, such as the density, internal friction angle (φ), cohesion (c) etc.

According to a statistic performed by Callaway on the available literature that explicitly states the type of backfill material, the cohesive materials (i.e., clay) and granular materials (i.e., sand, gravel, and Carstone) were the most adopted ones for masonry arch bridges. For instance, there were 10 out of 43 masonry arch bridges used clay, and 20 out of 43 masonry arch bridges used granular materials for backfill [34]. Thus, in the present study, direct shear box tests were carried out to characterise the material properties of the two most representative and widely used backfill materials, including crushed limestone and puddling clay. The limestone adopted in the study belonged to the MOT

type 1 graded crushed limestone according to the requirements of the UK Ministry of Transport's specification for highway works [65], which was a cohesionless coarse-grained angular fill material. The bulk density of limestone was determined to be 1,919 kg/m³. Table 2.3 lists the index properties for the cohesive puddling clay containing some mudstones and rock particles. Figure 2.6 shows the grain-size distribution of the limestone and puddling clay used.

Table 2.3 Summary of main characteristics of the puddling clay.

Property	Value/classification
Classification	CL
Natural moisture content	11%
Liquid limit	32%
Plastic limit	17%
Plasticity index	15%
Maximum dry density	1,840 kg/m³
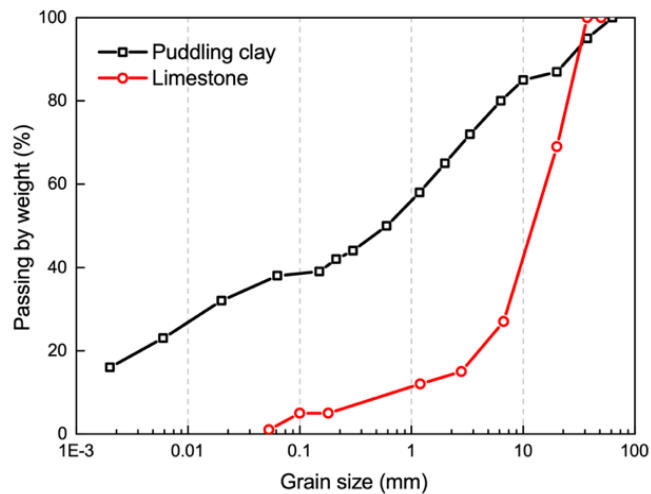
Figure 2.6 Grain-size distribution of the limestone and puddling clay.

2.4.2.1 Direct shear box tests on backfill materials

Direct shear box tests were carried out to characterise the frictional properties of the two backfill materials selected. For the limestone, a 300 mm large square shear box with a height of 200 mm was used (see Figure 2.7 (a)), which meets the requirements outlined in the standard ASTM-2011 [66], including that (a) the length of the shear box should be at least ten times larger than the maximum particle diameter of the soil, and (b) the

minimum specimen thickness shall be no less than six times the maximum grain diameter. Given the fact that the size of the shear box has little influence on the accuracy of results as long as the above requirements are met [67], a small-scale 100 mm square shear box was used for clay (see Figure 2.7 (b)).
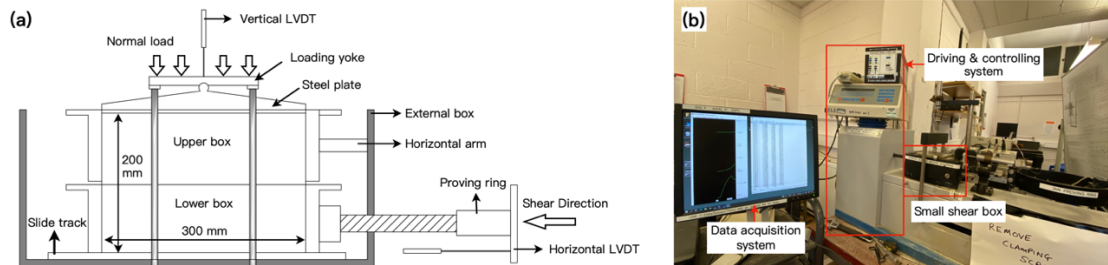
Figure 2.7 Direct shear box test apparatus. (a) large-scale direct shear box for testing limestone; and (b) small-scale direct shear box for testing puddling clay.

To assess the internal friction angle of the backfill materials, the peak shear strength was determined under three levels of normal compression, with two repetitions under each normal stress to ensure the consistency of the results. A similar instrumentation plan was adopted for the small and large direct shear box tests, namely, two LVDTs were mounded to capture the vertical deformation of the soil specimen and the horizontal displacement of the lower box, respectively, and a load cell for monitoring the shear force.

For the clay, the shear resistance was characterised under consolidated drained conditions. It is worth noting that the clay sample was put in a sealed bag to prevent evaporation of water. Regarding the sampling and testing process, a clay sample with a mass equal to 380 g was placed into the small shear box in three layers. Following the placement of each layer, the clay was compacted manually, and the total thickness of the clay was controlled to be approximately 25 mm. Two sets of the porous plate and perforated grid plate were positioned underneath and above the clay sample, allowing water drainage during consolidation and shearing. The target normal stress (i.e., 50 kPa, 111 kPa, and 164 kPa) was applied immediately after the clay was placed and was kept constant for three days for clay consolidation. Subsequently, the vertical settlement of the clay was measured. Accordingly, the density of consolidated clay was calculated to be equal to 1,716 kg/m³ on average with a CV equal to 6.7%. Prior to shearing, the upper and lower box was unlocked by removing two clamping screws and separated slightly by turning two gap screws. A low shear rate of 0.300 mm/min was selected to minimise the influence of excess pore pressure during shearing. The maximum shear displacement was set to be 15 mm, corresponding to 15% of the specimen size. After shearing, the

moisture content of clay was measured, which was observed to decrease slightly from 10.44% to 9.09% over the 26 days of testing.

For the direct shear box test on limestone, firstly, a 28 kg sample of limestone was placed in four layers into the large shear box. Following the placement of each layer, the limestone was manually compacted by striking a 300 mm long 50 mm wide timber beam with a hammer. The timber beam was moved along the surface to ensure even compaction and a flat surface. After all the limestone was placed into the shear box, the target normal stress (i.e., 115 kPa, 170 kPa, and 226 kPa) was applied via a steel plate placed on top of the limestone for pre-compression. After approximately 5 minutes, no significant volume change was observed due to the incompressibility of the limestone. The average density of the limestone was measured to be 1919 kg/m³ with a CV equal to 2%. Finally, the lower box moved horizontally along slide tracks at a constant rate of 1 mm/min.

2.4.2.2   Results from the direct shear box tests

Figure 2.8 shows the direct shear box test results for limestone and clay. Figure 2.8 (a) shows the peak shear strength under different levels of normal stress and the linear regression analysis results. Given the cohesionless nature of limestone, the intercept of the linear fit to the peak strength obtained from limestone was set to zero. The internal friction angle for limestone was found to be equal to 47.8°, whereas the internal friction angle and cohesion for the puddling clay were determined to be 37.2° and 30 kPa, respectively. The shear stress versus shear displacement under different levels of normal stress for clay and limestone are shown in Figure 2.8 (b) & (c), respectively. Overall, the graphs indicated good consistency of the results. For the puddling clay, the shear resistance curve showed a peak behaviour under the normal stress of 50 kPa and 164 kPa, where the shear stress increased to its peak value with the residual strength decreasing significantly, suggesting that a strain-softening behaviour occurred at the sliding plane. However, the shear failure of clay under 111 kPa normal compression and the failure of limestone was of a ductile type without an obvious peak point observed. In addition, the shear strength of limestone was significantly greater than that of clay under the same normal stress. This could be attributed to the considerable interlocking effect between limestone particles during shearing.
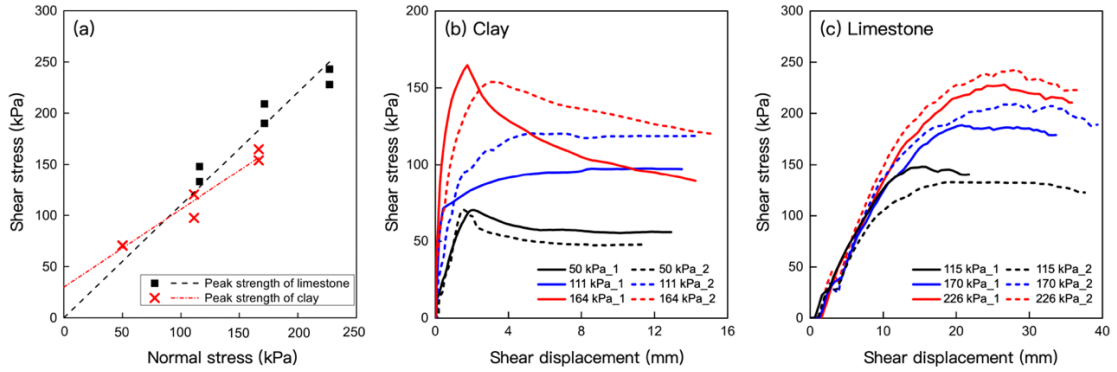
Figure 2.8 Results from direct shear box tests on backfill materials: (a) shear strength envelope for clay and limestone; shear strength versus shear displacement for clay (b) and limestone (c).

2.5 Characterization of brickwork masonry at component level

It is well established that masonry has high compressive strength but relatively low tensile and flexural strengths, which results from the low bond strength between bricks and mortar joints and makes vertical masonry structural components vulnerable to in- and out-of-plane horizontal forces. Indeed, the interaction between bricks and mortar joints can considerably affect the load transfer and cracking process of masonry, and unit-to-mortar bond properties play a vital role in the mechanical behaviour of masonry arch bridges [17].

Different parameters are required to characterise the interaction between bricks and mortar joints for different numerical strategies. For the micro-modelling strategy, masonry units are represented by continuum linear/nonlinear elements, and discontinuities at the unit-to-mortar bonds are represented by nonlinear interfaces [68]. This strategy requires parameters such as the interface friction angle φ_i, cohesion c_i, and tensile bond strength $f_{t,i}$ as inputs to define the force and displacement transfer between the bricks. In addition, a macro-modelling strategy is also widely used for modelling masonry structures, which represents the heterogeneous masonry by a homogenised continuum model, and the discontinuities and nonlinearity behaviour of bonds are reflected by appropriately formulated constitutive laws [69]. For the macro model, the compressive strength ($f_{c,m}$), elastic modulus (E_m), and Poisson's ratio (v_m) of masonry are required as input parameters. Therefore, the study characterized the parameters required for the micro-modelling and macro-modelling strategies through (a) compression tests on masonry prisms, (b) masonry triplet shear tests, and (c) direct tensile tests on masonry cross-couplets and full-couplets. It is noteworthy that the bricks were not wetted before the construction of the specimens, as this is not usually done in

43

actual large-scale practice. The experimental setups and results obtained are reported in this section.

2.5.1 Compressive properties of masonry

2.5.1.1 Compression tests on masonry prisms

The material properties of masonry units and mortar affect the compressive properties of masonry. A strong unit-to-mortar bond could result in high compressive strength masonry. In the present study, the compressive properties (i.e., compressive strength and elastic modulus) of masonry prisms were determined following the guidelines outlined in the British standard BS EN 1052-1 [70]. Eleven masonry stack bond prisms were constructed and cured under laboratory conditions. Each prism specimen was constructed from four type A dry bricks bonded together with 10 mm thick type O mortar joints. The dimensions of the masonry prism were 102 mm in width, 201 mm in length, and 282 mm in height. During the test, two timber and steel plates with an appropriate thickness were positioned on the top and bottom of the prism to ensure that the compressive stress can be evenly distributed over the bearing area. The compression load was applied at a rate of 0.3 MPa/s under load control. In order to obtain the stress-strain relationship of the masonry prism, the compressive stress applied to the specimen was monitored by a load cell built into the actuator, and the compressive strain was monitored by two LVDTs attached to each of the stretcher faces of the prisms (see Figure 2.9).

Figure 2.9 Compression tests on masonry prisms.

2.5.1.2 Results from compression tests on masonry prisms

The compressive strength of masonry prisms varied from 27.72 MPa to 41.53 MPa, with a mean value of 34.11 MPa and a CV of 13.9%. E_m was calculated according to the

stress-strain relationship obtained from the masonry prisms under compression, which was determined to be equal to 4.626 GPa with a CV equal to 28.2%. The highly scattered results could be attributed to several factors, including the specimen size effect, variation in specimen geometry, friction at the ends of specimens, and possible eccentricity in the loading applied due to geometric imperfections [71].

2.5.2 Tensile bond strength of unit-mortar interfaces

It has been generally determined that masonry has little resistance to horizontal loads acting parallel to the bed joint, and most masonry walls develop cracks at the unit-to-mortar interfaces due to the lower tensile strength of discontinuities. The tensile strength and shear behaviour of unit-to-mortar interfaces are influenced by a variety of factors, including the surface texture and water absorption of units, the mortar composition, temperature, and humidity conditions [17]. For numerical analysis, bond properties between bricks and mortar can significantly affect the out-of-plane behaviour of masonry. To this end, direct tensile tests and triplet shear tests were performed in the study to comprehensively assess the bond properties of unit-to-mortar interfaces.

2.5.2.1 Direct tensile tests on unit-mortar interfaces

The determination of the tensile strength at the unit-to-mortar interface is difficult as the tensile strength is quite low and suffers from a high degree of variability [72]. Current experimental methods fall into two categories, including flexural tensile strength tests (i.e., bond wrench tests, diagonal compression tests, and Z-shape bending tests) and direct tensile strength tests (i.e., cross-couplet tensile tests and full-couplet tensile tests) [47,73]. In the present study, both full-couplet and cross-couplet tests were performed to fully evaluate the direct tensile strength of the unit-to-mortar interface.

Figure 2.10 (a) & (b) show the experimental setup for the cross-couplet and full-couplet tensile tests, respectively. For the cross-couplet tests, the sampling and testing procedure followed the requirements outlined in the standard ASTM C952-12 [74]. In total, thirteen cross-couplet specimens made of type A dry bricks bonded with 10 mm thick type O mortar joints were constructed and cured under laboratory conditions for 21 days. During testing, the upper brick was supported at three locations, and a vertical compression load was applied to the lower brick at a constant rate of 0.2 mm/min. A load cell was placed between the actuator and the loading platen to monitor the applied compression load. It is worth noting that due to the low bond strength of the type O mortar joint, three of the thirteen specimens broke under the self-weight of the lower

brick before any load was applied.
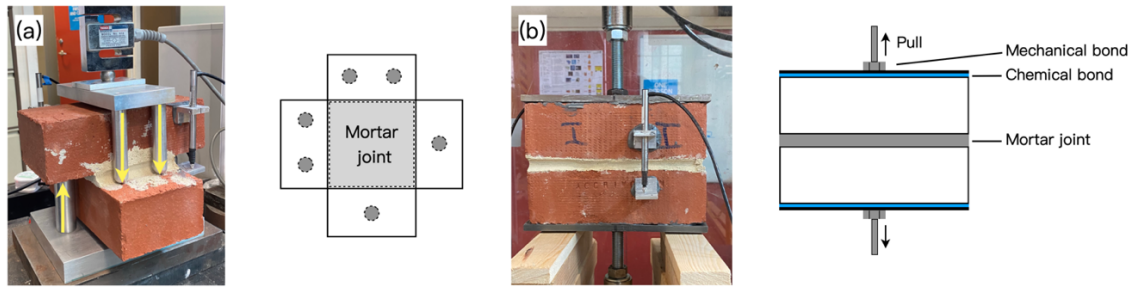
Figure 2.10 Characterisation on the direct tensile bond strength of the unit-to-mortar interface. (a) Cross-couplet tensile test; and (b) full-couplet tensile test.

To improve the issue of brick cross-couplets failure under the self-weight of the lower brick, six full-couplet specimens with a larger bonding area were constructed and tested (see Figure 2.10 (b)). The full-couplet specimens were also made of type A dry bricks bonded with 10 mm thick mortar joints, but the bonding area increased to 210 x 102 mm. The tensile load was applied to the full-couplet specimens through a plate-rod system. More specifically, two steel plates with dimensions of 210 x 102 x 5 mm were fabricated, and a hexagon nut was welded to the centre of one surface of each plate. Then, the flat sides (without nut) of the steel plates were glued to the top and bottom surfaces of the specimen using a chemical adhesive (Teroson UP 130). Two threaded rods were then screwed into the hexagonal nuts. During the test, the lower rod was clamped to keep it stationary, while the tensile force was applied by pulling the upper rod at a constant rate of 0.2 mm/min. It was observed that two specimens failed at the steel plate-to-brick interfaces under tension due to the poor quality of the chemical bond. Thus, four valid results were obtained.

2.5.2.2 Results from cross-couplet and full-couplet tensile tests

Figure 2.11 shows the failure types of cross-couplet and full-couplet specimens. According to the experimental observations, failure modes of cross-couplets included: (1) pure bond failure occurred at the unit-to-mortar interface, leading to the lower brick falling off; (2) shear crack occurred at the mortar joint due to the relatively low shear strength of mortar compared to the tensile bond strength at the unit-to-mortar interface; and (c) the combination of above two modes. However, all the full-couplet specimens had the same failure type, which was that specimens failed along the unit-to-mortar interfaces (Figure 2.11 (e) to (h)). Moreover, it could be seen from Figure 2.11 (a) that the C_1 specimen had a poor bond quality and a relatively small bond area compared to the other specimens, resulting in the lowest tensile strength measured from the C_1

specimen.
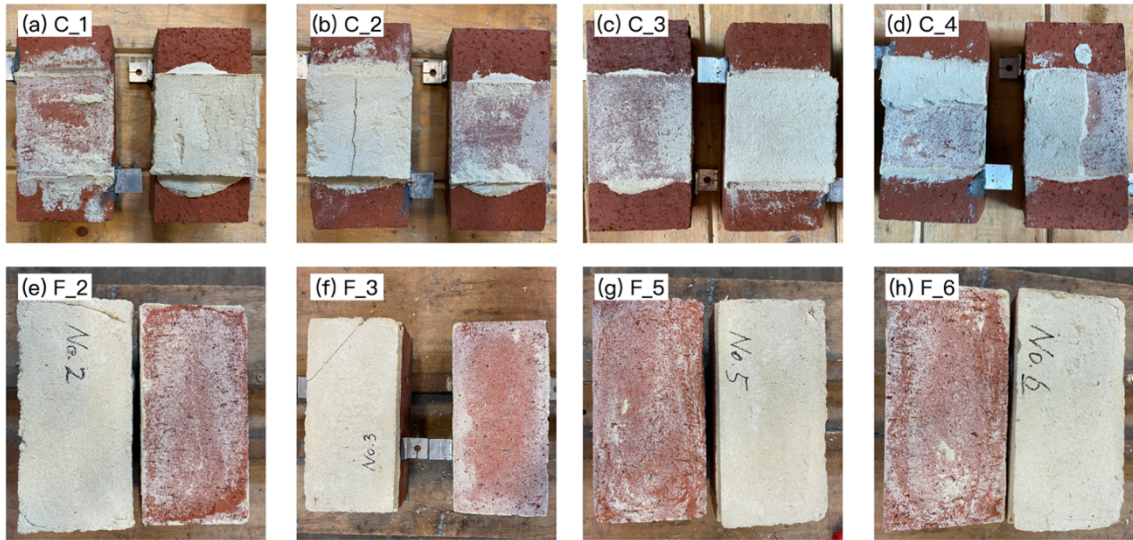
Figure 2.11 Failure modes of brick cross-couplets and full-couplet specimens under tension.

The difference in failure modes between cross-couplet and full-couplet specimens may help to explain that the average tensile strength measured from cross-couplet specimens was larger than that from full-couplet specimens. Figure 2.12 shows the individual tensile strength values obtained from the cross-couplet and full-couplet specimens. The value of $f_{t,i}$ was determined by dividing the ultimate load by the bonding area. The results showed a high variation across the tests, ranging from 0.043 MPa to 0.342 MPa, with an average value of 0.166 MPa and a CV of 54.3%. The significant scatter in the data was due to various factors, including the inherent variations in material properties, inconsistent quality of the workmanship of the bricklayer, differences in surface texture and the suction behaviour of bricks etc. The dispersed results obtained under laboratory conditions also emphasised the heterogeneity of real masonry arch bridges.
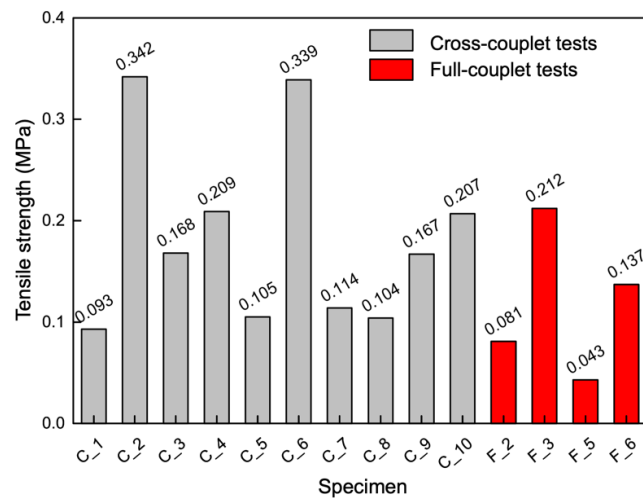
Figure 2.12 Tensile bond strength values.

2.5.3   Frictional properties of unit-to-mortar interface

2.5.3.1   Experimental setup for masonry triplet shear tests

Masonry triplet shear tests were carried out on thirteen specimens under different levels of pre-compression (i.e., 0.1, 0.2, 0.6, and 1.0 MPa), following the requirements outlined in the British standard BS EN 1052-3 [75]. All masonry triplets were constructed with type A dry bricks bonded with 10 mm thick mortar joints. Figure 2.13 shows the test rig used. During the test, a vertical (shear) load was applied via two 15 mm diameter steel rollers positioned 14 mm from the centre lines of the mortar beds, and a steel plate was used to distribute the load over the top of the middle brick. The outer two bricks were supported on two steel plates, with each plate supported on a 15 mm diameter steel roller placed 14 mm from the centre line of the mortar joint. Pre-compression was applied by an independent steel frame system consisting of two square steel tubes, two thread rods, and bolts, allowing the compression load to be adjusted through loosening or fastening the bolts. Two pads were attached to two ends of bricks to distribute the compression load clamped by the steel frame. In addition, a load cell was placed between the steel frame and a load distribution pad to monitor the compression load applied. A monotonic shear load was applied under displacement control at a rate of 1 mm/min. The shear slip of mortar joints was monitored by two LVDTs, as shown in Figure 2.13 (a).
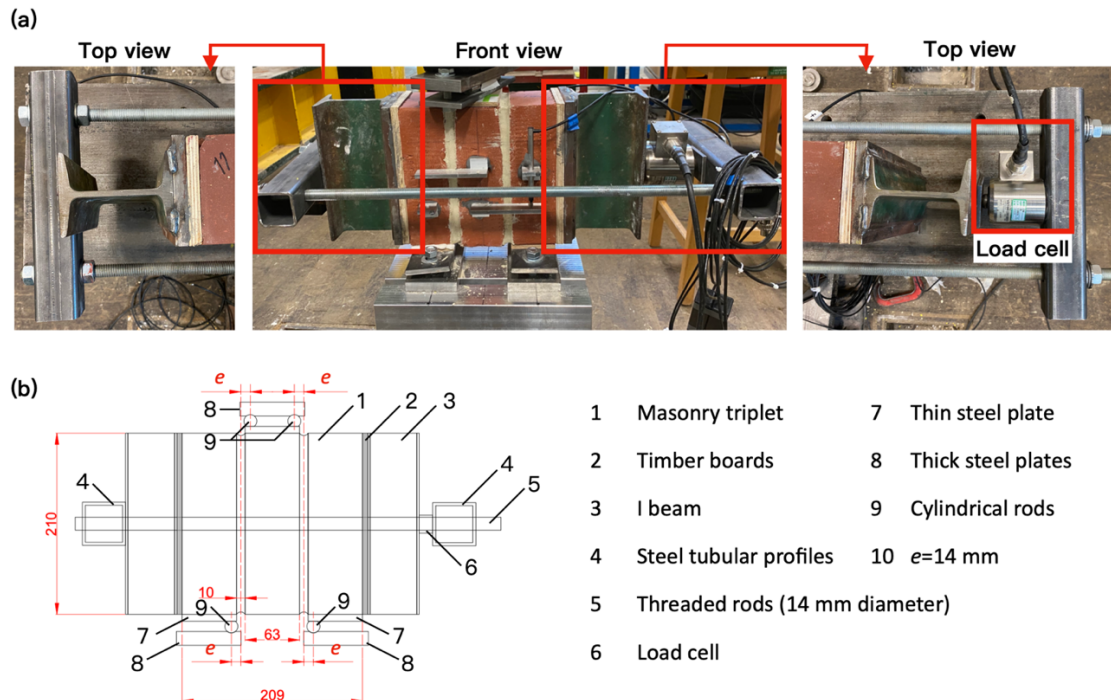
Figure 2.13 Triplet shear test. (a) Test set-up; and (b) schematic representation of the test.

2.5.3.2   Results from masonry triplet shear tests

Figure 2.14 shows the two failure modes of masonry triplets observed in the tests, including the pure interface failure that the mortar joint detached from the brick (Figure 2.14 (a)) and the combined interface failure and mortar tensile/shear failure (Figure 2.14 (b)). Table 2.4 summarises the peak ($f_{s,peak}$) and residual shear strength ($f_{s,res}$) obtained from the masonry triplet shear tests under different levels of pre-compression, which can be derived from the peak load ($F_{s,peak}$) and residual load ($F_{s,res}$) according to the following equations:

$$f_{s,peak} = \frac{F_{s,peak}}{2A_i} \tag{2.6}$$

$$f_{s,res} = \frac{F_{s,res}}{2A_i} \tag{2.7}$$

where A_i stands for the cross-sectional area of a masonry triplet parallel to the bed joints.

It could be seen that both the peak and residual strength exhibited by masonry triplets were dependent upon the level of horizontal compression, that the strength increased as the compression level went up. A Mohr-coulomb failure criterion could be used to describe the sliding failure of masonry triplets, which indicates that the shear failure occurs as soon as the following equation is not satisfied:

$$\tau \leq c_i + \sigma_c \times \tan \varphi_i \tag{2.8}$$

where τ is the shear strength of triplets; c_i and φ_i represent the cohesion and friction angle at the unit-to-mortar interface, respectively; and σ_c stands for the pre-compression.

Figure 2.14 (c), the peak shear strength and the linear regression analysis results, suggested that the friction angle and cohesion of the unit-to-mortar interface were equal to 36.3° and 0.29 MPa, respectively. While the values of residual friction angle and residual cohesion were equal to 31.0° and 0.12 MPa, respectively. The detailed shear stress-displacement curves are plotted in Figure 2.14 (d). Moreover, by comparing the cohesion and tensile bond strength at the brick-mortar interface, it is found that the ratio between c_i and $f_{t,i}$ was around 1.75, slightly larger than the value of 1.4 suggested by Milani and Lourenço [76]. However, this might be resulted from the high variability of the $f_{t,i}$ characterised in the study.

Table 2.4 Peak and residual shear strength obtained from masonry triplet shear tests. CV is in parentheses.

σ_c (MPa)	$f_{s,peak}$ (MPa)	$f_{s,res}$ (MPa)
0.1	0.292 (19.4%)	0.192 (11.8%)
0.2	0.437 (14.5%)	0.240 (22.0%)
0.6	0.833 (11.8%)	0.467 (10.9%)
1.0	0.936 (8.0%)	0.735 (1.8%)
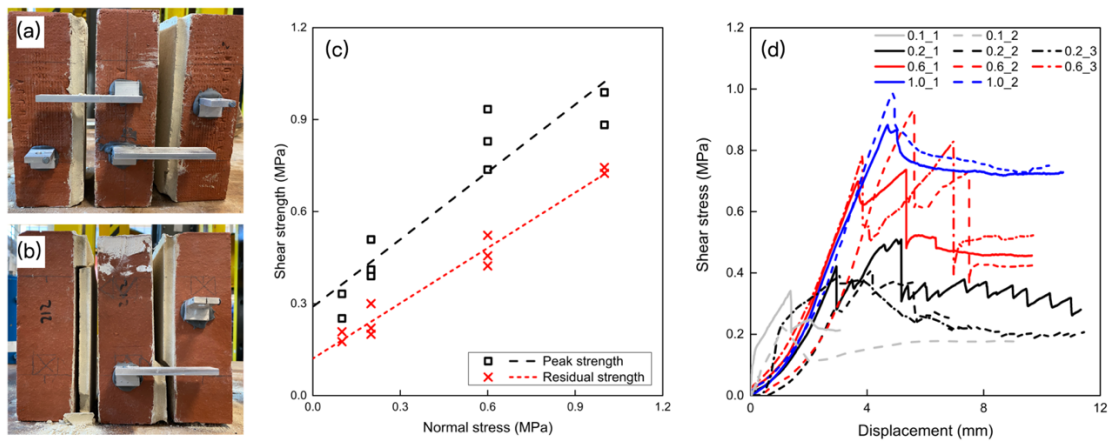
Figure 2.14 Results from masonry triplet shear tests. (a) Failure type 1; (b) failure type 2; (c) relationship between shear strength and pre-compression stress; and (d) shear stress versus vertical displacement curves.

2.6 Static & fatigue behaviour of masonry flat arches under bending loads

After serving for hundreds of years and under increasing traffic loads, old masonry arch bridges have inevitably suffered significant structural deterioration and damage. Fatigue damage to masonry arch bridges caused by long-term traffic loads has been observed and is attracting the attention of engineers and researchers. For example, several bending and longitudinal cracks were detected to propagate in the arch barrel of the Marsh Lane Viaduct (Leeds, UK) and the Osobowicki Bridge (Wroclaw, Poland) [39,77]. In order to assess the damage accumulation and fatigue failure mechanism of masonry under bending loads, both static and cyclic loading tests were performed on masonry flat arch specimens.

2.6.1 Experimental setup for the masonry flat arch tests

Masonry flat arches were constructed by bonding nine type A dry bricks with eight 10 mm thick mortar joints in between. The dimensions of the specimens were 647 mm in length, 210 mm in height, and 102 mm in width (see Figure 2.15 (a)). Static and cyclic loading tests were carried out after the specimens were cured for three months under laboratory conditions, at which point the full strength of the type O mortar was considered to be reached (see Figure 2.5 (d)). In accordance with the real stress conditions that masonry arch barrels experience during the passage of trains, the combined axial compression and vertical bending loads were applied to the masonry flat arches. The axial compression was provided by an independent steel frame similar to that used for triple shear tests but with longer rods to accommodate the larger specimens. A load cell with 100 kN capacity was placed between the flat arch and steel frame to monitor the axial load applied (see Figure 2.15 (b)). The flat arches were placed on two supports with a span of 584 mm, and the static/cyclic load was applied to the middle brick via a loading plate. A servo-hydraulically driven actuator was used for the static/cyclic loading application. Figure 2.15 (c) indicates the instrumentation plan, which was the same for both static and fatigue tests. More specifically, five LVDTs were used to monitor the mid-span vertical deflection (LVDT 1), the horizontal crack opening (LVDT 2 & 3) and shear displacement (LVDT 4 & 5) of the two central joints.

Figure 2.15 Static and fatigue testing on masonry flat arches under bending loads. (a) Masonry flat arch specimen; (b) schematic representation of the test setup (unit: mm); and (c) instrumentation plan.

Regarding the loading protocol, for the static tests, three levels of σ_c (i.e., 0.1, 0.2, and 0.4 MPa) were adopted in the study to investigate the correlation between the flexural strength of masonry flat arches with the axial pre-compression stresses. Under each pre-

compression level, three specimens were tested. During the test, a monotonic load was applied vertically to the middle brick at a constant rate of 1 mm/min.

Figure 2.16 Incremental cyclic loads applied to the masonry flat arch specimen.

For the fatigue test, a pre-compression of 0.2 MPa was adopted to simulate the axial constraint provided by the surrounding bricks in a real arch barrel. Incremental cyclic loads were applied, with the loading range remaining at 4 kN, while the peak load increased by 4 kN every approximately 350,000 cycles (see Figure 2.16). The frequency of the fatigue load was 1 Hz, corresponding to a typical passenger train with an axle distance of 10 m passing over a bridge at a velocity of 36 km/h. The cyclic loading started from 4 kN to 8 kN, which was approximately 6.5% to 12.9% of the ultimate capacity in accordance with the results obtained from the static tests. Five incremental loading stages were carried out in total, and the last of which had a loading range of 20 kN to 24 kN. To accurately capture the response of the specimens, the data logging rate was set at 5 Hz (5 points were recorded per second), namely five times higher than the loading frequency.

2.6.2 Results from the static tests on masonry flat arches

The peak loads and average flexural strength obtained from static tests on nine masonry flat arches are presented in Table 2.1. Figure 2.17 shows the failure mechanisms observed in the specimens. It is worth noting that the hydraulic system lost control during the experiment for the ninth specimen (σ_c = 0.4 MPa), which led to an unexpected load being suddenly imposed on the flat arch, resulting in the collapse of the specimen.

It is worth noting that the existence of the steel frame significantly affected the behaviour and failure mechanisms of masonry flat arches. The steel frame limited the lateral

deformation of the masonry flat arch at its geometric central axis and considerably increased the stiffness of the specimen. With the increase in the vertical load, the deflection of the specimens increased, the compression load applied by the steel frame was also increased significantly. During the tests, the primary damage in the flat arch specimens was observed to be occurred within the central area, including three central bricks and two mortar joints in between. Three types of failure could be summarized as following: (1) brick cracking along the thrust line due to the high compression stress (Figure 2.17 (a)), (2) shear failure of the specimen along the mortar joints (Figure 2.17 (b)), and (3) collapse of the specimen (Figure 2.17 (c)). Among the six specimens under 0.1 and 0.2 MPa pre-compression, five had the same failure mode of brick cracking, except the second specimen under 0.2 MPa of σ_c collapsed. The two specimens under 0.4 MPa of σ_c failed due to mortar crushing and shear failure.

Table 2.5 Summary of the static test results on nine masonry flat arch specimens.

σ_c (MPa)	Number	Failure mechanism	Peak load (kN)	Average peak load (kN)
0.1	1	Cracking of bricks	57.04	
	2	Cracking of bricks	55.64	59.46
	3	Cracking of bricks	65.71	
0.2	4	Cracking of bricks	60.60	
	5	Specimen collapse	58.08	61.80
	6	Cracking of bricks	66.71	
0.4	7	Mortar crushing and shear failure	33.62	
	8	Mortar crushing and shear failure	49.10	41.32
	9	-	-	

Figure 2.18 shows responses of flat arch specimens under three levels of pre-compression, including the vertical deflection at the middle span obtained from LVDT 1 (Figure 2.18 (a)), the horizontal crack opening for the left and right-side central joints obtained from LVDT 2 and 3, respectively (Figure 2.18 (b)), and the shear slip for the left and right-side central joints obtained from LVDT 4 and 5, respectively (Figure 2.18 (c)). Under the same pre-compression level, the ultimate strength of the three tested specimens varied within an acceptable range considering the variability of masonry mechanical properties. However, other features of the response showed a certain degree

of variation. It could be seen that the shear slip and crack opening primarily occurred at one central joint rather than two joints at the beginning of the test. As the bending moment increased, the crack propagated upwards. As the load approached the peak value, another central joint crushed. For example, for the third specimen under the pre-compression of 0.2 MPa, it could be seen that the right-side joint cracked first when the vertical load increased to approximately 5 kN. As the bending moment increased, the crack width of the right-side joint continued to increase. However, at that location almost no shear slip was observed (see Figure 2.18 (c)), indicating that the flat arch was rotating round the top hinge point at this stage. When the vertical load increased to 45 kN, 68% of the ultimate load carrying capacity, a crack appeared in the left-side central joint, and the shear slip also occurred, indicating downward sliding of the middle brick.
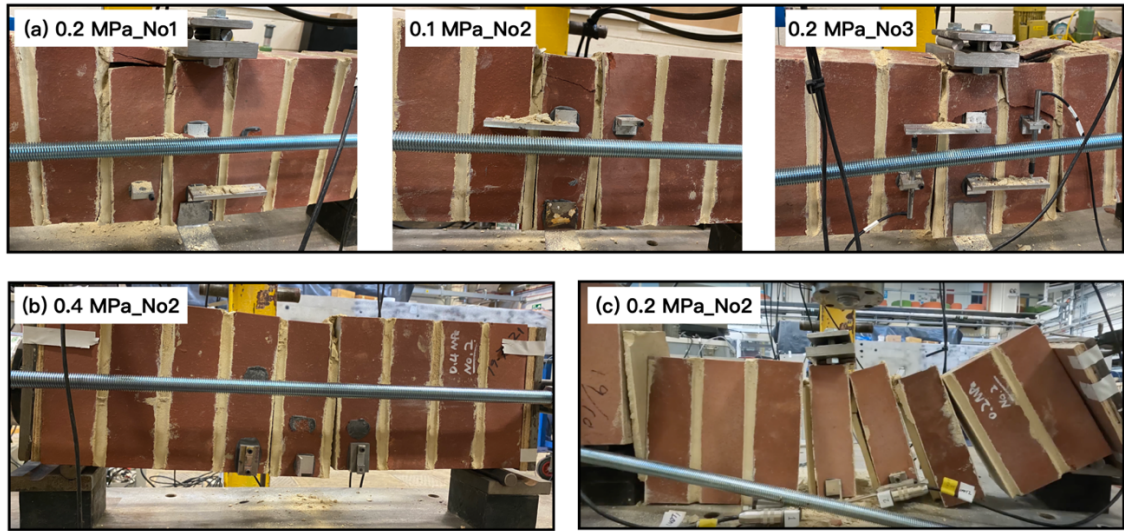
Figure 2.17 Failure modes of masonry flat arches under static loads. (a) Cracking of brick; (b) mortar crushing and shear failure of the specimen; and (c) collapse of the specimen.

The results shown in Table 2.5 and Figure 2.18 suggest that the flat arch specimens under 0.1 MPa and 0.2 MPa of σ_c had similar ultimate strength, whereas the specimens under 0.4 MPa of σ_c had the lowest ultimate capacity. This phenomenon was closely related to the failure mechanisms of the specimens. By comparing the responses of the specimens under 0.1 MPa and 0.2 MPa pre-compression levels, it could be seen that as σ_c increased, the ultimate capacity of specimens increased slightly. However, the slope of the load-deflection curves suggested that the stiffness of the specimen was enhanced significantly with a higher pre-compression level. Given that the flat arches under 0.1 and 0.2 MPa pre-compression had the same failure mode (bricks cracked under compression), the ultimate capacity of the specimen was directly related to the compressive strength of masonry. Thus, increasing the pre-compression level from 0.1

MPa to 0.2 MPa did not significantly contribute to the load-carrying capacity of the flat arch. However, when σ_c was increased to 0.4 MPa, the ultimate capacity of the specimens decreased, which could be attributed to the fact that the highest pre-compression level led to the mortar being crushed more quickly. The drop of the crushed mortar pieces resulted in a significant reduction in friction between bricks, which further caused the shear failure of the specimens.
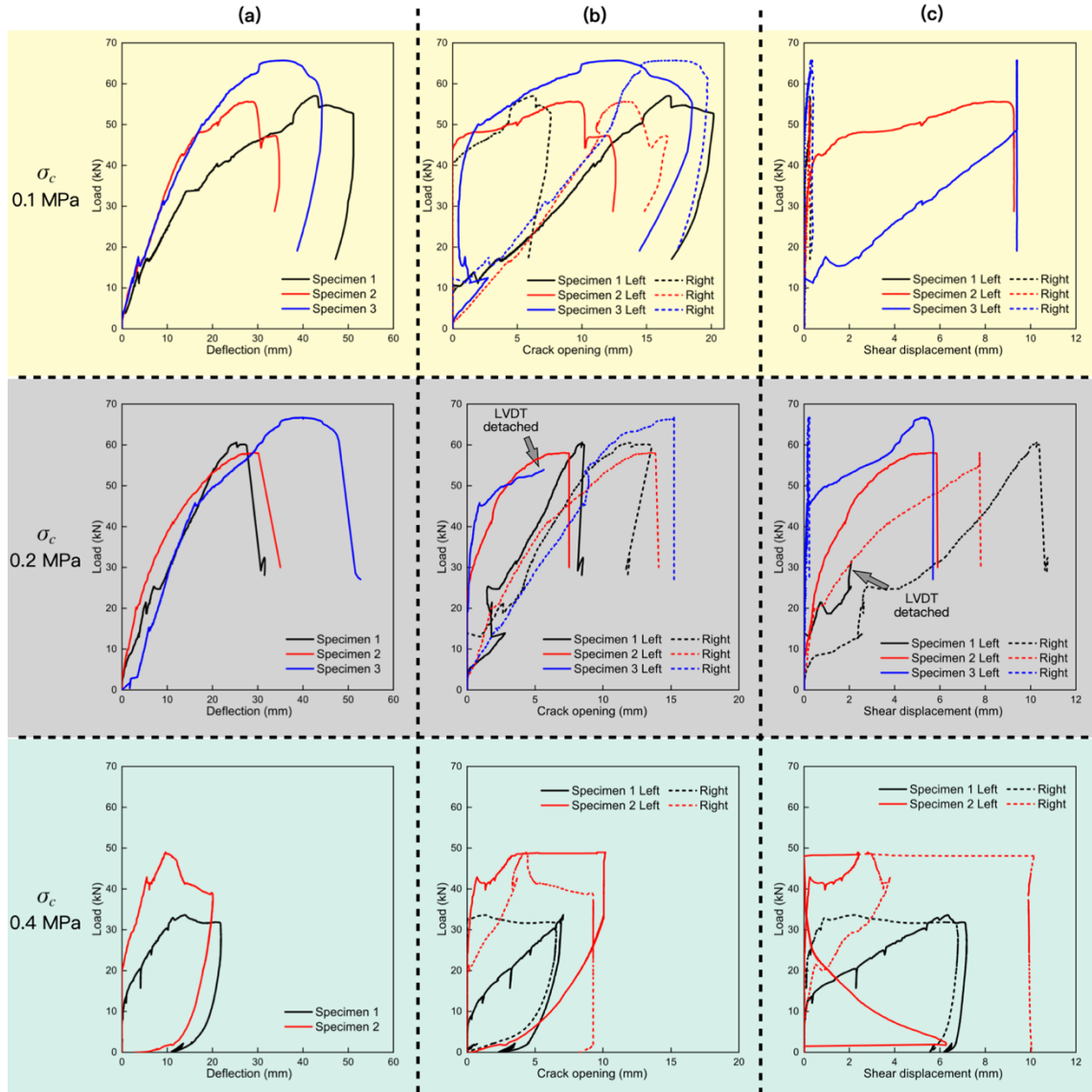
Figure 2.18 Responses of the masonry flat arches under three levels of pre-compression. Column (a) Load versus mid-span deflection; column (b) horizontal crack opening of the two central joints; and column (c) shear displacement of two central joints.

2.6.3 Results from the high-cycle fatigue test on a masonry flat arch specimen

Following the static tests, a high-cycle fatigue test was performed on a masonry flat arch to investigate the damage accumulation and crack propagation in masonry under long-

term cyclic bending loads. Over 1,750,000 loading cycles were performed over twenty days. Ultimately, the specimen did not fail due to fatigue before the end of the test protocol. Nevertheless, the large number of loading cycles applied can still provide valuable insight into the fatigue behaviour and long-term damage accumulation of masonry arch bridges subjected to cyclic vehicle loads over a range of time periods. More specifically, the vibration frequency (f, unit: Hz) induced by a passing train can be estimated by the following Eq. (2.9) [78]:

$$f = \frac{V}{d} \tag{2.9}$$

where V represents the velocity of a train (unit: m/s), and d stands for the wheelbase distance of a train (unit: m).

A train with a total length of L_t m passing through a masonry arch bridge with a length of L_m m requires approximately $(L_m + L_t)/V$ seconds. Then the number of loading cycles (N) induced by a passing train to the bridge can be simplified estimated by the following equation:

$$N = f \cdot \frac{L_m + L_t}{V} \tag{2.10}$$

Assuming the following parameters as an example: $V = 10$ m/s; $d = 10$ m; $L_t = 100$ m; $L_m = 200$ m; and 5 to 20 trains passing over the bridge per day, 1,750,000 loading cycles applied in this study can represent the number of cyclic loads the bridge is subjected to over a period of 8 to 32 years.

Figure 2.19 shows the crack propagation of the specimen during the fatigue test. In principle, the accumulation of damage occurred according to the following process: (1) a bond failure crack appeared along the unit-to-mortar interface at the beginning of the test at the right central joint. (2) As the number of loading cycles and the peak load increased, the crack propagated upwards gradually along the unit-to-mortar interface, and a horizontal crack occurred approximately one-third of the way down the right joint (see the stage of 12 to 16 kN in Figure 2.19). (3) The flat arch behaved as a three-hinge mechanism. Mortar crushed at the top of the right joint under compression. Until this stage, no visible damage had been observed from the left-side central joint (see the stage of 16 to 20 kN in Figure 2.19). (4) The right-side central joint was crushed under high compressive stress as the bending moment gradually increased, and the left-side joint also started to crush. At the end of the test, a monotonic load was applied to the specimen

until failure. The ultimate load was registered as 46.27 kN, which was approximately 74.8% of the static load-carrying capacity.
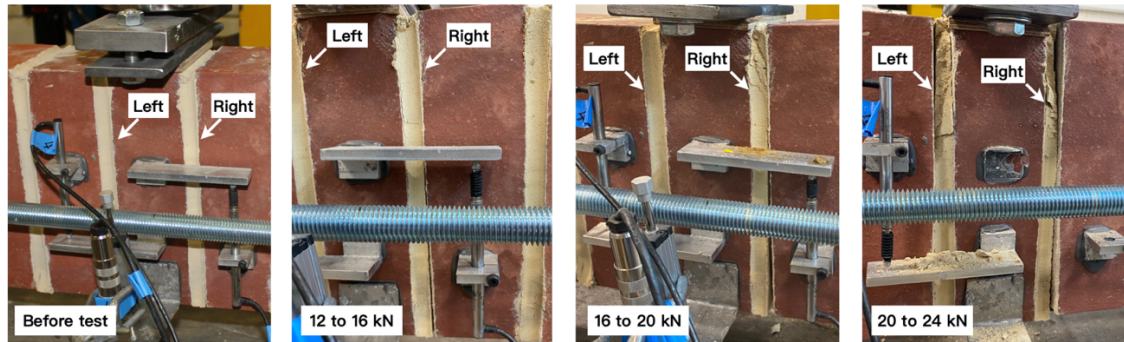
Figure 2.19 Crack propagation in the specimen during the fatigue test.

For assisting in the processing and visualisation of the large dataset collected, an algorithm was developed to extract the maximum and minimum values of every five adjacent sampling points. This allows the upper and lower envelope of the response to be obtained. Figure 2.20 shows the upper and lower envelope for monitored responses of the specimen under high-cycle fatigue loads, including the mid-span deflection monitored by LVDT 1 (Figure 2.20 (a)), shear slip obtained from LVDT 4 and 5, respectively (Figure 2.20 (b) & (c)), and horizontal crack opening obtained from LVDT 2 and 3 (Figure 2.20 (d) & (e)) of the two central joints. Figure 2.20 (a) suggested that as the vertical load increased, the deflection increased significantly. On the other hand, at each loading stage, it was observed that the deflection of the specimen increased faster during the first approximately 10,000 cycles, and then the increasing rate of deflection dropped for higher loading cycles (see Figure 2.20 (a1) to (a5)). Some jumps and fluctuations observed suggested either that the shear slip occurred in the middle brick or that the crack propagated, resulting in a reduction in the stiffness of the specimen. Regarding the shear slip and crack opening of two central joints, Figure 2.20 (b) to (e) illustrated that the damage mainly concentrated on one of the two central joints (the right-side joint in this case), which was similar to the observation from the static tests. The reason might be that after the initiation of a bond crack, the flat arch behaved as a 3-hinge mechanism, and the high compression stress concentrated at the top point of the cracked joint, resulting in the damage concentrated in one joint.
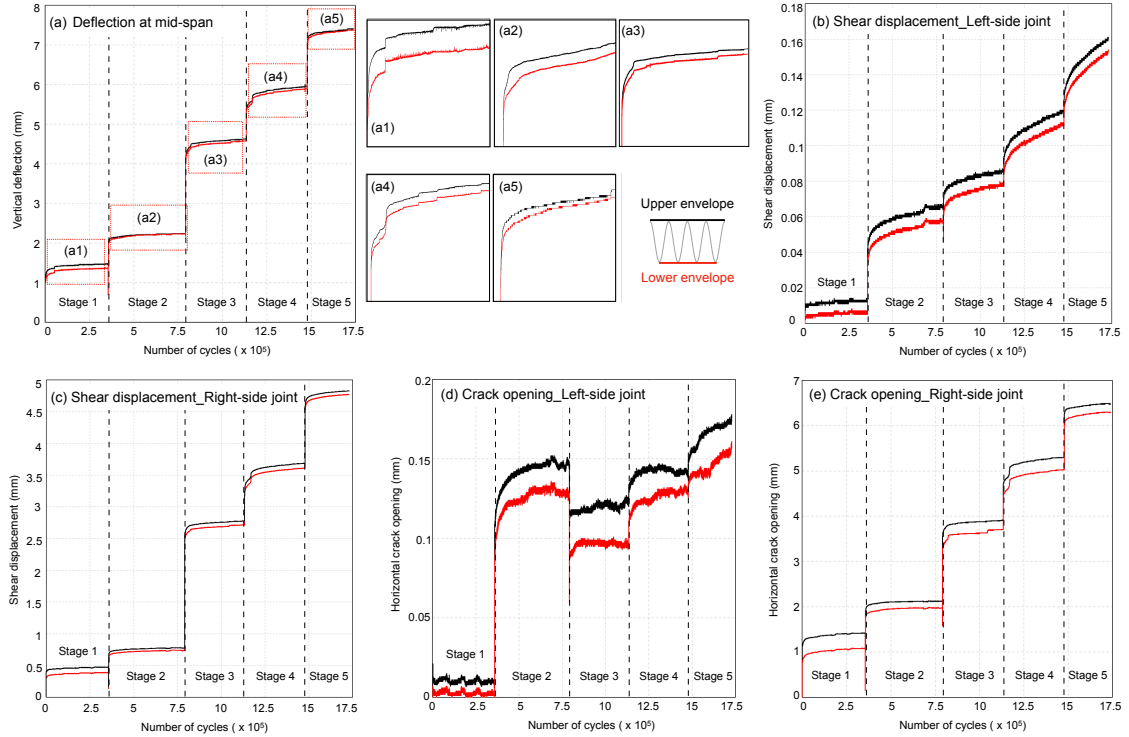
Figure 2.20 Response of the specimen under fatigue loads. (a) Mid-span deflection; shear displacement of the left (b) and right joint (c); and horizontal crack opening of the left (d) and right central joint (e).

Damage accumulation in the masonry flat arch under long-term fatigue loading can be presented as the stiffness degradation of the specimen. Additionally, stiffness parameters are crucial for calibrating high-fidelity numerical models. Figure 2.21 shows the stiffness (S) of the masonry flat arch during the fatigue loading, which was calculated every 20,000 loading cycles according to the following equation.

$$S = F/\delta \tag{2.11}$$

where F stands for the load applied to the specimen, and δ is the corresponding vertical deflection of the specimen at the mid-span.

Figure 2.21 (a) reveals that most of the degradation in the stiffness of the masonry flat arch occurred at the beginning of the test. The stiffness of the specimen dropped approximately 70% from 20.04 to 6.03 kN/mm. After that, the degradation trend became relatively stable with the increase in loading cycles. From Figure 2.21 (b1) to (b5), it can be seen that after each time of increase in the peak loads, the stiffness degradation was more rapid for the first approximately 40,000 cycles and then gradually stabilized. This indicates that any changes in peak loads could accelerate the stiffness degradation of the specimen and might lead to a more rapid progression of damage in masonry. Notably,

the continuous cyclic loading protocol adopted in the test is different with realistic loading scenarios of a real bridge under vehicle/train loads, which are usually composed of several separated vibrations with varied frequencies and magnitudes. The application of such continuous cyclic loading aims to trigger the fatigue damage within a short period of testing time under laboratory conditions. Through this way, the fatigue life of the specimen can be assessed based on the total number of loading cycles a specimen can carry before failure. However, according to the observation in this study, the pauses and variations in realistic cyclic loading, may accelerate the stiffness degradation of the specimen and lead to a more rapid progression of damage in masonry, which requires further investigation.

It is also noteworthy that the stiffness of the specimen 'jumped' each time the peak of the cyclic load changed. These jumps, in addition to a drop from 5.36 kN/mm to 3.71 kN/mm from stage 2 to stage 3, showed a slight increase at the beginning of each stage compared to the residual stiffness of the previous loading stage. For example, S increased from 5.42 kN/mm at the end of stage 1 to 5.69 kN/mm at the beginning of stage 2 (Figure 2.21 (b1) & (b2)). This phenomenon could be attributed to the fact that an independent steel frame clamped the specimen during the test, and therefore, the calculated stiffness represented the stiffness of the steel frame-masonry flat arch composite system. As the bending moment of the specimen increased with the peak load, the horizontal force of the steel frame on the flat arch increased as the lateral deformation of the masonry flat arch was restricted. This interaction between the steel frame and masonry specimen might result in fluctuations in the stiffness of the specimen when the peak cyclic load was changed.
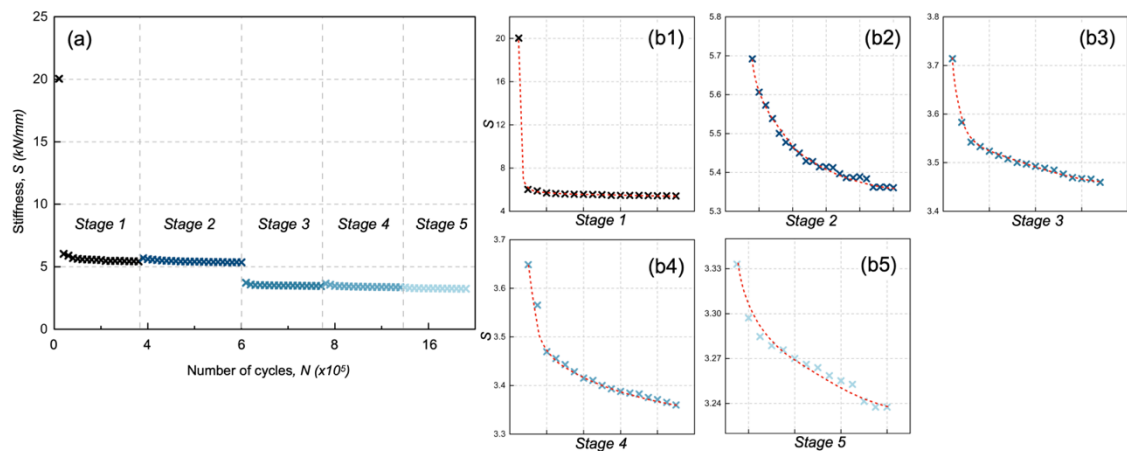
Figure 2.21 (a) Stiffness of the masonry flat arch during fatigue loading. Stiffness degradation of the specimen in stage 1 (b1) to stage 5 (b5).

2.7 Conclusions

Based on the characteristics of masonry and the requirements of existing complex/high fidelity numerical methods for input mechanical parameters, this study presents a systematic material characterisation framework to assess the static and fatigue behaviour of brickwork masonry arch bridges. An extensive experimental campaign from the material level to the component level was conducted to comprehensively characterise the material and mechanical parameters of brickwork masonry arch bridges. This study first characterised the material properties of bricks, mortar joints, and two types of backfill materials, including crushed limestone and puddling clay. Then, the compressive properties of masonry prisms, the bond strength properties of the unit-to-mortar interface, and the frictional parameters of the masonry-to-backfill interface were determined. In addition, the static and fatigue behaviour of masonry flat arch specimens were characterised. More specifically, from the analysis results, the following can be concluded:

1. The properties of backfill had a significant effect on the frictional properties between masonry and backfill, whereas the influence of masonry bond types could be negligible for the bond types investigated. The average interface friction angle and cohesion of the masonry-to-clay interface were determined to be equal to 13.7° and 18.8 kPa, respectively, and the masonry-to-limestone interface had an average friction angle of 34.5° with zero interface cohesion.

2. The pre-compression stress affected the static performance of masonry flat arches subjected to bending loads. Using 0.1 MPa and 0.2 MPa pre-compression levels, the flat arch behaved as a three-hinge mechanism and failed due to the cracking of bricks under high compression. However, when applied 0.4 MPa pre-compression, mortar crushed faster than in other cases, leading to reduced friction between bricks and mortar joints and triggering the shear failure of the flat arch specimen.

3. Over 1,750,000 incremental loading cycles were performed in the study to investigate the damage accumulation of masonry flat arch subjected to high-cycle fatigue loads. Similar to its static behaviour, the flat arch behaved as a three-hinge mechanism under fatigue loads, with damage concentrated on one central joint. As the bending moment increased, the mortar joint was crushed under high compression stress. The residual strength of the masonry flat arch after the fatigue loading test was reduced to approximately 75% of its static load-carrying capacity.

4. With the increase in loading cycles and peak loads, damage accumulation captured in the flat arch included the growth in the width of the bond failure crack, an increase in vertical deflection of the specimen, and degradation of the stiffness of the specimen.

The results presented in the chapter could provide valuable insight into the static and fatigue behaviour of masonry arch bridges. The systematic framework and comprehensive material and mechanical properties of masonry characterised in the study could be used to calibrate and develop high-fidelity numerical models for masonry arch bridges and other structures in masonry construction.

Acknowledgement

3 Frictional Behaviour Between Masonry and Backfill Materials

This chapter represents the slightly modified post-print version of the article: **B. Liu**, A. Drougkas, V. Sarhosis, C. Smith, M. Gilbert, "Experimental investigation on the shear behaviour of the brickwork-backfill interface in masonry arch bridges", Engineering Structures, 292 (2023) p. 116531. The formatting and numbering of equations, tables and figures have been adapted to this document.

3.1 Abstract

This chapter presents the results from an experimental campaign to characterise the shear behaviour of the brickwork-backfill interaction in masonry arch bridges. Two representative backfill materials found in real masonry arch bridges (compacted crushed limestone and clay) were sheared against brickwork masonry specimens with two different bond patterns (a soldier course bond and an English bond). The results demonstrated that the interface shear behaviour between masonry and backfill was different from the internal shear behaviour of backfill materials. When compacted crushed limestone was adopted as the backfill material, the ratio between the masonry-limestone interface friction angle (φ_i) and the internal friction angle (φ) of limestone was determined to lie within the range from 0.70 to 0.75. However, when clay was used as backfill material, the φ_i/φ ratio was much lower, and of the order of 0.51 to 0.52 under the assumption of zero-cohesion at the interface, or 0.35 to 0.39 if interface cohesion was considered. Moreover, the properties of the backfill material had a significant influence on the interface shear behaviour, whereas the effects of brickwork bonding pattern were marginal. This study provides valuable insight into the identification of brickwork-backfill interface parameters for the numerical analysis of masonry arch bridges.

3.2 Introduction

Masonry arch bridges form a vital part of the transportation infrastructure systems of many countries. For example, it is estimated that there are approximately 40,000 masonry arch bridges in the UK [40]. To assess load-bearing capacity and to predict the in-service behaviour of masonry arch bridges, reliable numerical or analytical methods

are needed. A number of input parameters are generally required for these methods to characterize the behaviour of bridges, including the material properties of the masonry units, mortar joints and backfill, as well as the interface parameters between masonry and backfill. The selection of these parameters plays a determining role in whether the numerical or analytical methods employed can accurately model structural performance, and varying these parameters can significantly impact the calculation results [44,45]. The masonry material properties can be determined by standard small-scale laboratory experiments [62,79]. Also, the properties of the backfill materials, including internal friction angle φ and cohesion c, can be characterised via direct shear box tests [80]. However, although masonry and backfill interface parameters (i.e., interface friction angle φ_i (or friction coefficient μ_i), interface cohesion c_i and stiffness) have been recognised as having a strong influence on the load-carrying capacity of masonry arch bridges [81], there is no commonly used experimental procedure for obtaining them.

Table 3.1 lists soil properties and interface parameters for masonry arch bridges adopted by researchers in recent studies. A noticeable discrepancy can be observed in the selection of these parameters across studies. For instance, most researchers adopted a ratio of the friction angle of the interface between the masonry-backfill and of the backfill itself (φ_i/φ) at approximately 0.70, with a minimum of 0.46 and a maximum of 0.82. One of the reasons for these discrepancies may be the different backfill materials investigated. However, even the studies that adopted the same backfill material (e.g., both [82] and [83] used crushed limestone backfill), they assigned different ratios of φ_i/φ in their numerical models. This inconsistency in parameter settings can be primarily attributed to the limited understanding of the interface interaction between masonry and backfill materials. Moreover, to the best of the authors' knowledge, no study has considered the influence of backfill properties or masonry bond patterns when selecting interface parameters, despite the fact that masonry of different bond patterns has different surface roughness and texture, which may lead to variations in interface frictional parameters, as previously reported [84].

In the past, direct shear box tests were widely used to evaluate the shear behaviour of a variety of soils and interfaces between soil and construction materials (i.e., wood, steel and concrete) [85–87]. For instance, for a cohesionless sand material, as the sand particles become more angular, the 'interlocking' between particles becomes more pronounced, leading to higher shear strength and internal friction angle [88]. Also, the

roughness and texture of the surface, soil properties, particle size, and moisture content have been identified to be the most critical factors affecting the shear behaviour between soil and construction materials [89–93]. Moreover, previous research has pointed out that the peak shear stress at soil-structure interfaces is most likely to be different from the shear strength of the soil itself, depending on the relative surface roughness. As the surface roughness increases, the shear strength of the interface tends to increase and gradually approaches that of e.g., sand when the surface roughness is close to the particle size [94]. However, for clay-structure interfaces, except in the case of very smooth surfaces, the interface shear strength is often assumed to be approximately equal to, or slightly smaller than, the shear strength of the clay itself [92,95]. These studies emphasize that the shear behaviour of the soil-structure interface largely depends on the soil properties and structure surface characteristics.

Table 3.1 Frictional properties of backfill materials and masonry-backfill interface adopted in the previous numerical studies.

Studies	Types of backfill	Backfill properties		Masonry-backfill interface parameters		φ_i/φ
		Internal friction angle φ (°)	Cohesion c (kPa)	Interface friction angle φ_i (°)	Cohesion c_i (kPa)	
Sarhosis et al. 2019 [96]	Reddish-brown sand with a little clay	37	7	25	0	0.68
Gilbert et al. 2010 [82]	Crushed limestone	54.5	3.3	24.8	1.1	0.46
Grosman et al. 2021 [83]	50 mm graded crushed limestone	43.8	1	28	19	0.64
Forgács et al. 2021 [97]	Typical limestone	37	5	20	-	0.54
Scozzese et al. 2019 [9]	A granular mixture fill	38	-	31	-	0.82
Oliveira et al. 2010 [98]	Not specified	30	-	20	-	0.67
Pulatsu et al. 2019 [81]	Not specified	30	20	20	0	0.67
Bayraktar et al. 2021a [99]	Not specified	35	50	17	-	0.49
Bayraktar et al. 2021b [100]	Not specified	30	80	17	-	0.57
Pantò et al. 2022 [101]	Not specified	43.5	1	31	2.9	0.71

In the case of masonry arch bridges, the backfill is responsible for transmitting and distributing live loads from the road or rail surface to the arch barrel and for laterally stabilising the arch barrel as it sways under loading. Therefore, understanding the shear behaviour between masonry and backfill materials is essential in assessing the mechanical behaviour of masonry arch bridges. Moreover, experimental evidence is necessary to establish reasonable friction parameters at the masonry-backfill interface when developing numerical models of masonry arch bridges.

To this end, this chapter aims to present an experimental procedure to characterise the shear behaviour of the backfill-arch ring and backfill-spandrel wall interaction in masonry arch bridges. A total of 36 experimental tests have therefore been carried out to characterise the frictional properties of limestone and clay, as well as the interface frictional parameters of the four types of brickwork-backfill interfaces typically found in masonry arch bridges in the field. Based on the test results and post-shear failure characterisations, the influence of masonry bond patterns and backfill properties on the interface shear behaviour was analysed. Finally, the ratios of friction angle between the backfill and brickwork-backfill interfaces were summarised according to the types of backfill and the cohesion characteristics of brickwork-backfill interfaces.

3.3 Experimental programme

3.3.1 Units, mortar, and masonry specimens

High compressive strength/low water absorption fired clay bricks (hereafter referred to as Type A bricks) were used in the study as masonry units. The bricks had nominal dimensions of 215 mm length × 102 mm width × 63 mm height and a density of 2,470 kg/m³. The compressive strength, Young's modulus, flexural strength, and also the tensile strength of the Type A bricks were characterised via standard compression tests, three-point bending tests, and Brazilian (splitting) tests, following the procedure and requirements outlined in [54,102]. Table 3.2 lists the number of test samples, the determined strength properties, and also the coefficient of variation (CV) of the test results for the Type A bricks used. Cement mortar with a mix ratio of 1:2 (cement/sand by volume) and a water/binder ratio of 0.4 (by weight) was selected as the bonding material to ensure good joint durability and rapid hardening time.

Previous studies have pointed out that the hardness of construction materials can affect the shear strength parameters at soil-construction material interfaces, particularly for

soft construction materials such as wood, geomembranes, and soft polymer [103–105]. When relatively high normal stresses are applied, the motion of soil particles along the soil-solid contact interface is characterised by both sliding and ploughing, resulting in an increase in interface friction [106,107]. However, this effect is observed to be less significant as the hardness of the construction material increases. For hard construction materials such as concrete and steel, the roughness and texture of the solid surface and soil characteristics, such as soil density, water content, particle size and morphology, are the dominating factors affecting interface behaviour [91,108], rather than the strength of the construction materials. The critical factor that determines whether a construction material is classified as 'soft' or 'hard' in shear box testing is whether the material's surface is disturbed by soil particles during shearing. In the study, the high strength bricks and cement mortar were used to achieve high durability of the brickwork specimens, avoiding damage to mortar joints by backfill particles during the tests, and maintaining the same surface roughness and texture over the twelve tests performed on each brickwork specimen. Moreover, according to the findings from the steel-soil interface and the concrete-soil interface tests, the strength properties of the bricks and mortar joints are not expected to affect the friction behaviour of the brickwork-backfill interface, as long as the brickwork surface is not disturbed.

Table 3.2 Material properties of bricks.

Material properties	Number of samples	Mean values (MPa)	CV
Compressive strength	9	111.3	6.2%
Flexural strength	8	19.8	9.6%
Tensile strength	9	6.7	13.5%
Young's modulus	9	31762.6	15.7%

3.3.2 Brickwork specimens

Given the fact that the roughness and texture of a solid surface can significantly affect the shear behaviour at soil-structure interfaces, two types of joint layouts were considered in the study to investigate the influence of bond patterns and joint arrangements on the shear behaviour at the masonry-backfill interface. In designing the brickwork specimens, a primary consideration was to employ bond patterns representative of those found in real brickwork masonry arch bridges. Figure 3.1 shows

a schematic drawing of a typical brickwork masonry arch bridge found in the UK. As shown in Figure 3.1, the backfill material fills the void between the spandrel walls and arch barrel, and forms a level surface for vehicles and trains to pass over. Consequently, there are two types of masonry-backfill interfaces, namely spandrel wall-backfill interfaces and arch ring-backfill interfaces; see Figure 3.1.
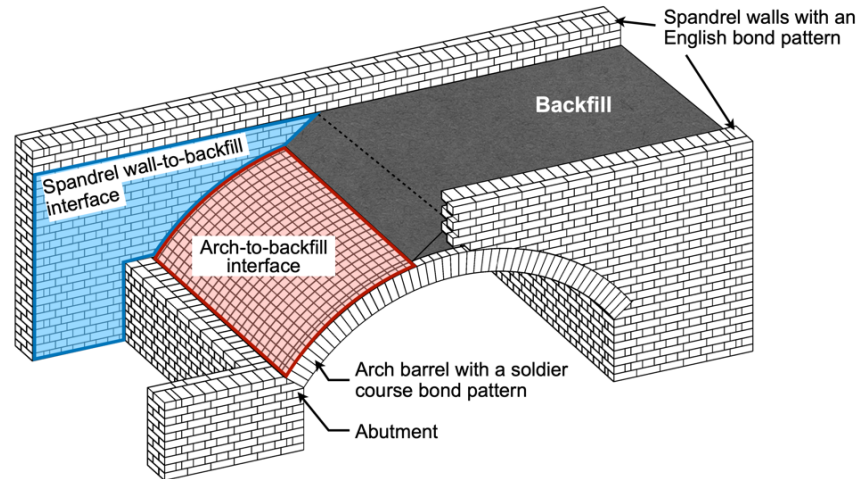
Figure 3.1 Typical brickwork masonry arch bridge showing the spandrel wall-backfill interface and arch-backfill interfaces.

The primary function of spandrel walls in a masonry arch bridge is to resist the horizontal soil pressure from the backfill. Spandrel walls can be built in multi-wythe arrangements to provide better resistance to lateral soil pressures. For masonry arch bridges found in the UK, English bond and Flemish bond are the most widely used [109,110]. Compared to masonry constructed using Flemish bond, English bond has a lower mortar volume and higher strength, and is therefore more widely used in the construction of load-bearing components, including spandrel walls in brick-masonry bridges [111]. In this study, one of the two brickwork specimens was therefore designed to have the same layout of joints as English bond, to simulate the interaction between backfill and spandrel walls (Figure 3.2 (a)). Brickwork with English bond is constructed by laying alternate courses of stretchers and headers. Joints between the stretchers were centred on the headers in the course below.

The main load-carrying element in a masonry arch bridge is the arch barrel, which may consist of a single ring or multiple concentric rings (multi-ring). Geometric parameters of an arch barrel (i.e., span-rise ratio, ring thickness) can significantly affect its load-carrying capacity. In addition, the spatial arrangement of bricks with mortar joints influences crack propagation and the mode of failure of the arch [83]. To simulate the

joint arrangement on the extrados of an arch barrel, an aligned joint layout was adopted in this study as a second bond pattern [112]. More specifically, for a single-ring voussoir arch, bricks were laid directly at the side of one another along the arch line, with the narrow edge facing out. All joints were aligned when observed from the top of the arch (Figure 3.1), which can be referred to as a soldier course bond type (Figure 3.2 (b)).
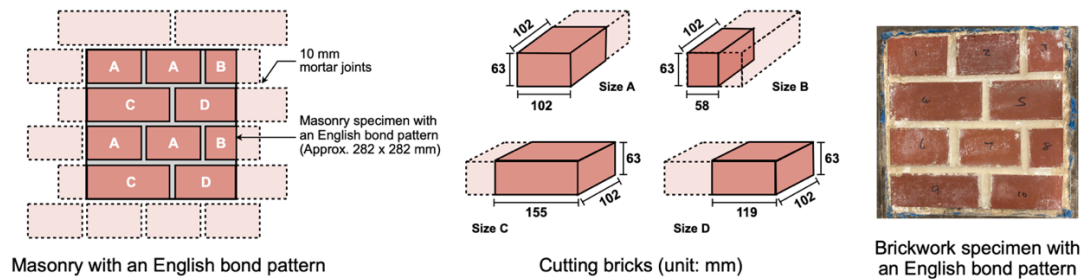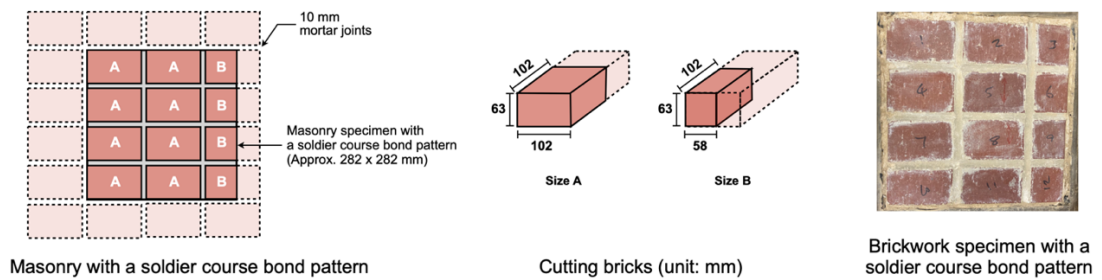
Figure 3.2 Brickwork specimens (unit: mm). (a) Brickwork specimen with an English bond pattern to simulate the spandrel wall-backfill interface; (b) Brickwork specimen with a soldier course bond pattern to simulate the arch-backfill interface.

Figure 3.2 shows the method of constructing experimental specimens from brickwork with an English and a soldier course bond pattern. Both brickwork specimens had similar dimensions, measuring approximately 282 mm in length, 282 mm in width, and 102 mm in depth (single Wythe), allowing them to be accommodated by the shear box. To achieve the designed bond patterns within the confined space, Type A bricks were cut into four different sizes. More specifically, the brickwork specimen with an English bond pattern consisted of four bricks in size A, two each of bricks in sizes B, C, and D, while the specimen with a soldier course bond pattern contained six bricks in size A and four bricks in size B. The bricks were bonded with cement mortar joints measuring 10 mm in thickness. A 10 mm thickness was selected based on its common application in practice and its widespread adoption in experimental and numerical studies [19,113–115]. The brickwork joints were concave (see Figure 3.3), which is representative of joint profiles found in real masonry arch bridges [116]. This concave shape had an approximate radius

of 5 mm and a maximum depth of 4 mm, which was created by pressing a curved steel jointer against the joints before the mortar hardened. Moreover, the smeared mortar was removed from the surface of the brickwork specimens using a Nylon brush. The two specimens used in this study were constructed on the same day by the same experienced mason to minimize any variability in specimens.
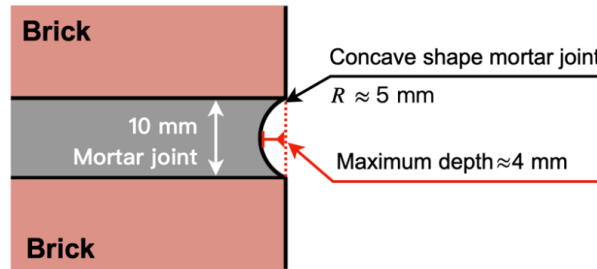
Figure 3.3 Concave shape mortar joints.

3.3.3   Direct shear tests on backfill materials

The selection of soil is crucial, as its properties can considerably affect soil-structure interface behaviour. Typically, material that was easily accessible at the worksite was employed as backfill in the construction of masonry arch bridges, which means there is significant variation in backfill properties across bridges [64]. Although there is no comprehensive report on the materials most commonly used, available literature suggests that over 65% of masonry arch bridges have used clay, sand, and limestone gravel as the backfill material [34]. In addition, most previous experimental studies on masonry arch bridges have used clay and compacted crushed limestone as backfill materials [16,36]. Therefore, this study adopted these two widely used materials, i.e., compacted crushed limestone and cohesive puddling clay (also often called 'puddle clay'), to assess the effects of soil properties on the shear behaviour of masonry-backfill interfaces.

Limestone is a cohesionless course-grained angular fill material. The grain-size distribution of the limestone used in this study is shown in Figure 3.4. The puddling clay used in the study contained some mudstones and rock particles. Its index properties and grading curve are shown in Table 3.3 and Figure 3.4, respectively [117–119].

To determine the shear properties (i.e., internal friction angle and cohesion) of the limestone and clay, a series of direct shear box tests were carried out. More specifically, a large shear box (Figure 3.5 (a)) was used for the direct shear tests on limestone to meet the requirements outlined [66], such as that the length of the shear box should be at least

ten times larger than the maximum particle diameter of the soil. The large shear box employed was 300 mm square with a thickness of 200 mm. A steel plate with grids at the inner surface was placed on top of the sample for the application of normal stress. Shear displacement was controlled by a belt-driven motor that pushes or pulls the lower shear box horizontally along slide tracks. Movement of the upper shear box was prevented by a horizontal arm fixed to the external box. During the pre-testing compression and shearing, a proving ring mounted between the arm and the lower shear box was used to measure the shear force applied, and two LVDTs were used for measuring the vertical deformation of the sample and the horizontal displacement of the lower shear box, respectively.
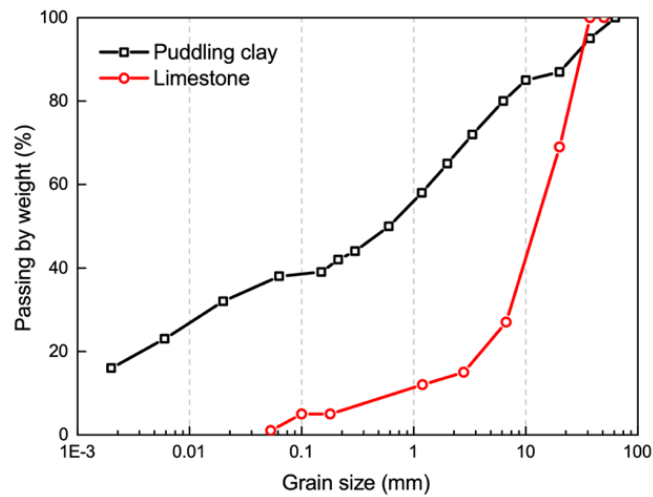
Figure 3.4 Particle-size distribution of the limestone and puddling clay used in the study.

Table 3.3 Summary of main characteristics of the puddling clay used.

Property	Value/classification
Classification	Lean Clay (CL)
Natural moisture content	11%
Liquid limit	32%
Plastic limit	17%
Plasticity index	15%
Maximum dry density	1,840 kg/m^3

Six direct shear box tests on limestone were performed under three levels of normal stress (115 kPa, 170 kPa, and 226 kPa), with two repetitions at each normal stress level to check the repeatability of the results. The same normal stress levels were adopted in the direct shear box tests on limestone as in the interface shear tests between brickwork specimens and backfill materials; the rationale for adopting these normal stress levels will be discussed in section 3.1. Given that the maximum particle diameter of limestone is approximately 25 mm, the thickness of the limestone sample was set to be 200 mm, the full capacity of the large shear box, to meet the requirement that the minimum specimen thickness shall be no less than six times the maximum grain diameter [120]. For the sampling and testing procedure, a total of 28 kg of limestone was placed into the shear box in four separate layers for each test. Each sample was manually compacted evenly by striking a 300 mm long, 50 mm width timber plate with a hammer to approximately reproduce the dense state of the backfill found in real masonry arch bridges. After all limestone was placed into the shear box, the target normal stress was applied via a steel plate placed on top of the sample for pre-compression. No significant volume change in the limestone observed after approximately 5 mins of compression due to its incompressible behaviour. The bulk density of limestone after compression was determined to be equal to 1,919 kg/m³ with a CV equal to 2.0%. Before shearing, the upper shear box was raised around 5 mm against the lower box by turning four gap screws fitted in the four corners of the upper box. During shearing, the lower shear box was moved horizontally at a rate of 1 mm/min until a total displacement of at least 20 mm was achieved. It is worth noting that the constant normal stress was kept applied to the sample during the whole process of pre-compression, uplifting of the upper box, and shearing.

Considering that: a) the size of the shear box does not affect the accuracy of the characterisation of soil shear properties as long as the requirements outlined in [120] are satisfised; and b) with a smaller size shear box and lower volume of clay, the quality of compaction can be more easily controlled, a small shear box was used for testing the clay under consolidated drained conditions (see Figure 3.5 (b)). It is worth noting that the clay sample during testing was in its natural state, which means that it had a natural moisture content and was not fully saturated (i.e., the clay is unlikely to be fully saturated unless the bridge has been flooded for a long period). This was to ensure the experimental results were representative of the behaviour of the clay in the field. Nevertheless, any large particles of mudstone or rock were removed from the clay sample before testing to

minimize inconsistencies due the size of the shear box used.
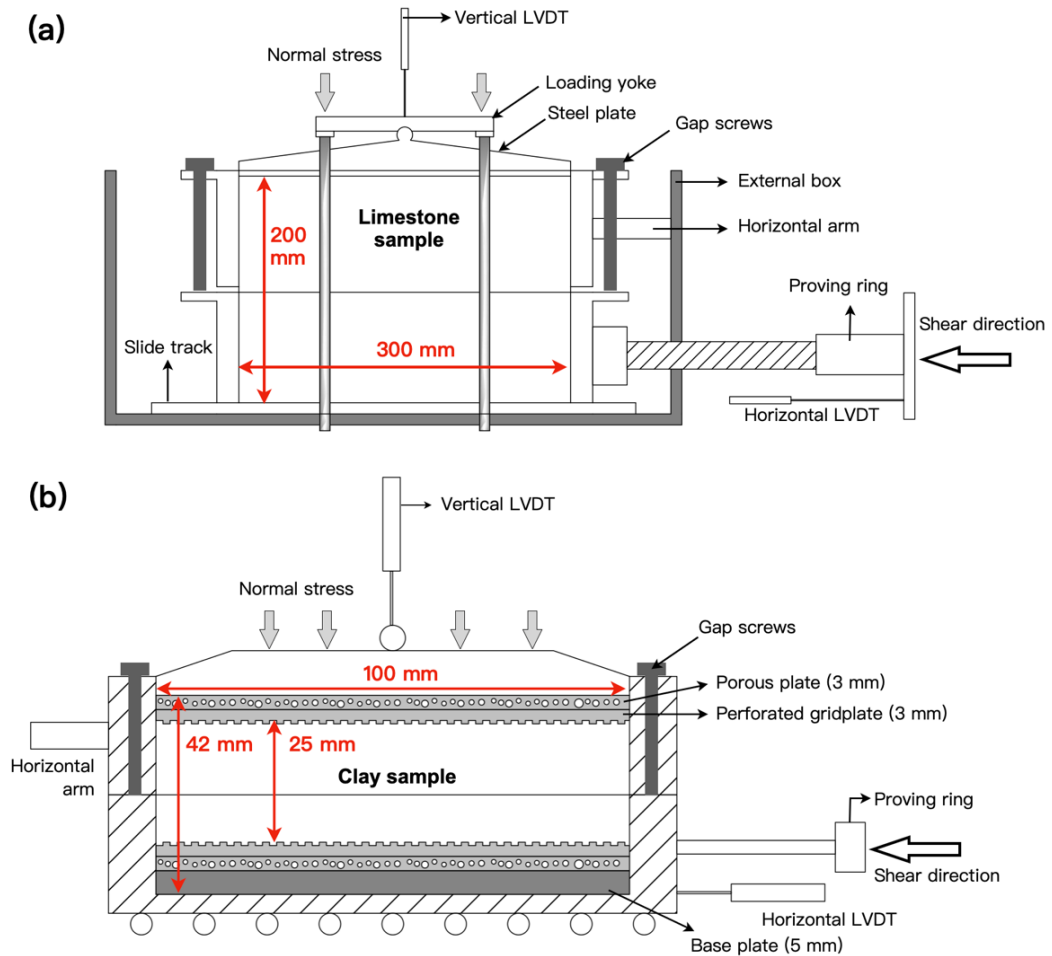
Figure 3.5 (a) Large shear box apparatus for testing limestone; and (b) small shear box apparatus for testing clay.

A total of six tests were performed on clay samples at three levels of normal stresses (50 kPa, 111 kPa, and 167 kPa) with two repetitions under each normal stress to ensure consistency. The sample preparation and testing procedure were as follows: firstly, approximately 380 g of clay was weighed from a sealed plastic bag. The sample was then placed into a clean shear box over a set of porous and perforated grid plates. After that, the sample was manually compacted until its thickness reached approximately 25 mm. Another set of porous and perforated grid plates were placed on top of the sample following the manual compaction. Then, the shear box was installed in the apparatus, with the loading yoke hooking onto the lower shear box. Immediately after assembly of the shear box, the target constant normal load was applied for 3 days (the clay consolidation time was set to be the same as that for brickwork-clay interface shear tests), and the vertical deformation was monitored. After three days of consolidation, the

volume change of the sample was recorded, and the average density of clay was determined to be 1,716 kg/m³ with a CV equal to 6.7%. Before shearing, the upper and lower boxes were unlocked by removing two clamping screws and separated slightly by turning two gap screws. Finally, the sample was sheared at a low rate of 0.300 mm/min. The maximum horizontal displacement was 15 mm. LVDTs were used to measure the vertical deformation and horizontal displacement. The shear force was recorded by a load cell with a capacity of 2 kN placed between the lower shear box and the horizontal arm. The moisture content of the clay was measured after each test. Over the 26-day test, the moisture content of clay decreased slightly, ranging from 10.44% to 9.09%.

3.4 Brickwork-backfill interface shear strength tests

To accommodate the brickwork specimens, the large-scale shear box was used for the brickwork-backfill interface shear strength tests, and the configuration of the modified apparatus is shown in Figure 3.6. The shear response of the brickwork-backfill interfaces, including the soldier course brickwork-limestone (SL) interface, soldier course brickwork-clay (SC) interface, English bond brickwork-limestone (EL) interface, and English bond brickwork-clay (EC) interface, were investigated. For each brickwork-backfill combination, three levels of normal stress were applied, and two repetitions of each test were carried out to check the repeatability of the results. In total, 24 interface shear tests were performed.
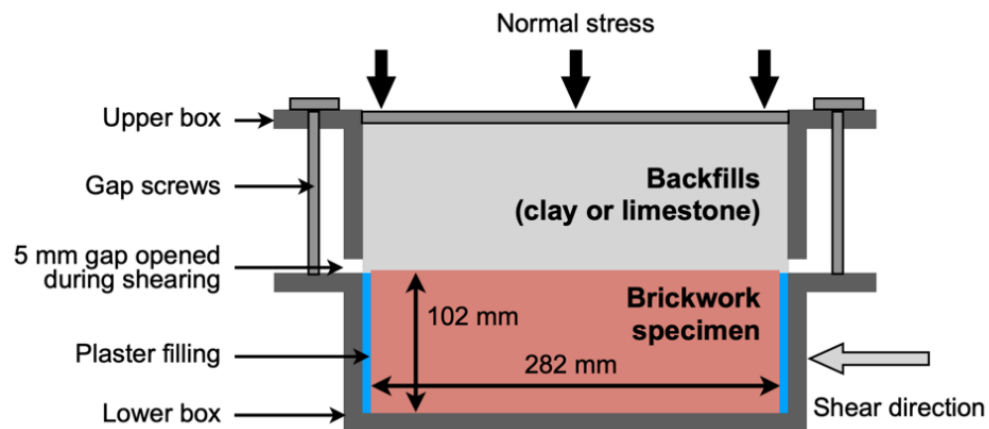
Figure 3.6 Large shear box for brickwork-backfill interface shear tests.

3.4.1 Determination of normal stress levels

The levels of normal stress applied in interface shear box tests were determined to represent real stress conditions found on masonry arch bridges. Assuming zero pore

water pressures (neglecting any soil suction), effective stresses are assumed to be equal to total stresses. Given the depth of backfill at the arch vault is H, the vertical total stress, S_v, at the arch barrel can be calculated as:

$$S_v = \gamma \cdot H \tag{3.1}$$

where γ is the unit weight of the backfill material.

A smooth interface between spandrel wall-backfill has been assumed to obtain approximate estimates of operational stresses. Now, based on the Rankine's theory [121], the passive lateral soil pressure P_p acting on the spandrel wall at the depth of H can be expressed as:

$$P_p = \gamma H K_p + 2c\sqrt{K_p} \tag{3.2}$$

where K_p, the passive lateral earth pressure coefficient, is related to the internal friction angle of soil (φ) and can be obtained by:

$$K_p = tan^2\left(45 - \frac{\varphi}{2}\right) \tag{3.3}$$

Assuming that a masonry arch bridge has a backfill depth over the crown of the arch barrel equal to 1 m [122], and assigning typical values of 20 kN/m³ and 40° for γ and φ of the backfill (cohesionless) respectively, the passive vertical soil pressure on the arch barrel was calculated to be equal to 20 kPa, as per Eq.(3.1). The full passive condition could give 92 kPa lateral pressure on spandrel walls (Eq.(3.2)). If an active action of passing vehicles was taken into consideration, additional active pressures would be applied to the arch barrel vertically and spandrel wall horizontally, depending on the weight and speed of the vehicle, and could reach a peak of 500 kPa at the spandrel wall and diminishes with distance from the load (for an analytical solution of the lateral stress acting on a retaining wall caused by a horizontal line load on a backfill see [123]). Considering the real stress state of a masonry arch bridge analysed above and the capacity of the large-scale shear box, the three levels of normal stresses for the interface shear tests were determined to be 115 kPa, 170 kPa, and 226 kPa, respectively.

3.4.2 Interface shear test procedures

After 30 days of curing, the brickwork specimen was placed in the lower half of the large shear box. The dimensions of the brickwork specimens were approximately 282 mm long

× 282 mm wide × 102 mm high, allowing them to be perfectly accommodated by the lower shear box. There was a gap of approximately 9 mm between the specimen and the walls of the shear box, which was filled with plaster so that the specimen was fixed in position after the plaster had become solid (Figure 3.6). Following installation of the brickwork specimen, a certain amount of backfill material (15.9 kg of limestone or 16.6 kg of puddling clay) was placed in the upper shear box in three separate layers. Each placement was followed by manual compaction to achieve a dense state of backfill, in line with the soil conditions found in real masonry arch bridges. It should be noted that the same masonry specimen was used for the 12 interface shear tests (6 tests with limestone and 6 tests with clay) to maintain similar surface roughness and texture. Then, the tested masonry specimen was removed, and another specimen with a different bond type was installed.

After placing the backfill material into the upper box, the testing procedures were different for the limestone and clay cases. For the brickwork-limestone interface tests, the procedures for pre-compression and shear were the same as those for the direct shear box tests on limestone. On the other hand, the brickwork-clay interface tests were performed under consolidated drained conditions. The states of the clay samples in the interface shear tests were the same as those in the direct shear box tests on clay, both being the natural states of the puddling clay.

Figure 3.7 shows a typical consolidation curve for clay under constant normal stress. Clay was compressed sharply as a normal load was applied due to the air extrusion and the grid plate bedding into the sample. The second phase represents the clay consolidation with the dissipation of excess pore pressure. Clay was assumed to be fully consolidated when no significant volume change was observed. The time to 100% consolidation largely depends on the availability of drainage paths around the sample. In this study, the clay was surrounded by the masonry underneath and steel plates around and above. Limited drainage paths could result in the clay taking considerable time to reach 100% consolidation. To determine the clay consolidation time, the first test was started after 7-days of consolidation under the normal stress of 115 kPa. Then, the test was repeated in the same loading conditions but with the consolidation time reduced from 7-days to 3-days. Since no significant difference was observed in peak interface shear stress and shear stress versus horizontal displacement, the consolidation time for brickwork-clay interface shear tests was set to be 3 days for the rest of the tests considering the feasibility

of the tests under laboratory conditions. A low shear rate of 0.300 mm/min was adopted to minimize the influence of excess pore pressure during shearing. The minimum horizontal displacement was 20 mm, which was 6.7% of the sample size.
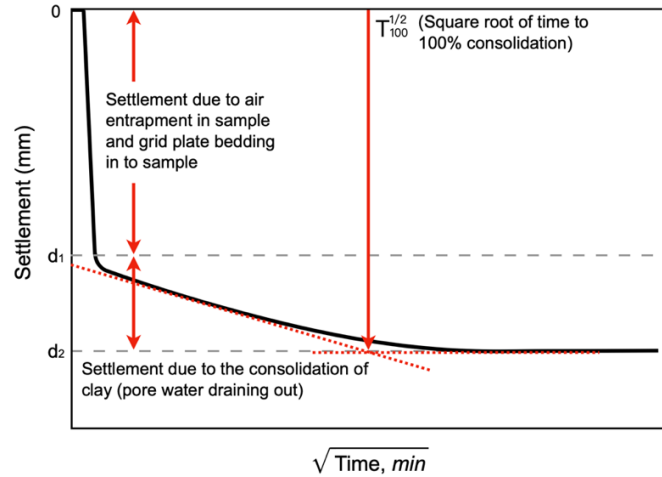
Figure 3.7 Clay consolidation curve under a constant normal stress.

The average density of the consolidated clay was determined to be equal to 2,035 kg/m³ with a CV of 1.8%. Also, the moisture content of the clay samples tested in the large shear box decreased from 11.90% (day 0) to 10.31% (day 96), see Figure 3.8. Values of clay density and moisture content obtained from twelve interface shear tests between brickwork specimens and the clay backfill were similar, suggesting that similar clay conditions were achieved.
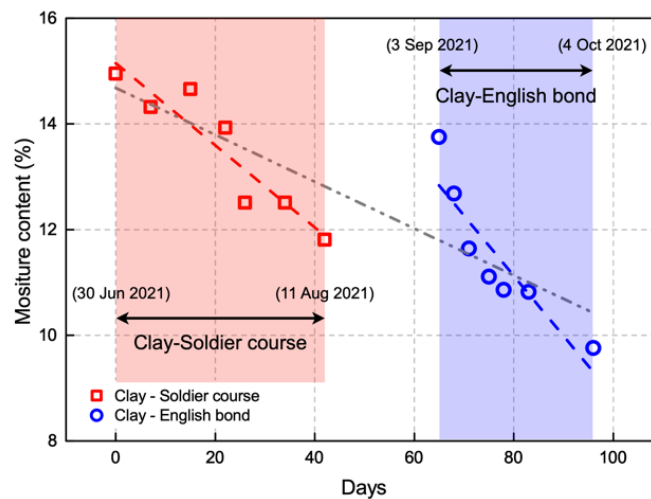
Figure 3.8 Moisture content of clay during the shear tests on masonry-clay interfaces.

3.5 Experimental results

3.5.1 Direct shear test results on clay and limestone

A total of twelve direct shear tests were carried out on two backfill materials under three different levels of normal stress, with two repetitions under the same conditions. Results from the small-scale direct shear tests on clay are shown in Figure 3.9. Figure 3.9 (a) shows the shear strength and linear regression analysis results, together with the coefficient of determination (R^2). φ of clay was determined to be 37.2° and c was 30 kPa. The friction angle of the clay obtained is higher than expected for normal clay, which was attributed to the fact that the natural clay sample used in this study contained some larger particles. The failure of the clay was a ductile type under the normal stress of 111 kPa, whereas a peak stress followed by the strain-softening behaviour was observed under the normal stress of 50 kPa and 167 kPa, as shown in Figure 3.9 (b). Figure 3.9 (c) shows the vertical displacement versus the horizontal displacement during shearing. At low normal stress, the clay sustained a slight volume contraction under shear, followed by a dilation phase, while under the normal stress of 111 kPa, the contraction of the sliding surface was more pronounced. From Figure 3.9 (c), it can be seen that the volumetric response of clay under a normal stress of 167 kPa was less repeatable compared to that under the other two levels of normal stress. For one test, the sample tended to dilate from the beginning, whereas the other sample initially contracted and then slightly dilated. This type of variability in volumetric response has also been reported in previous studies [86]. The volumetric response of the soil under shear is closely related to the particle movements at the shear zone [124]. The difference in dilative/contractive behaviour may be attributed to the difference in shear zone thickness in different tests. Also, the greater randomness of the granular properties of the natural clay adopted in the study compared to the reconstituted clay could also make this difference more pronounced.

Figure 3.10 shows the large-scale direct shear test results on limestone. In Figure 3.10 (a) the shear strength envelope suggests that the φ value of limestone was equal to 47.8° with the zero-cohesion assumption. Figure 3.10 (b) demonstrates that the shear failure of limestone was ductile, with no obvious peak point observed. The shear stress gradually increased during shearing and reached a critical state at a shear strain of approximately 6% to 10%. Both the vertical displacement and the peak shear stress of limestone showed very good agreement between the two tests under the same normal stress. Moreover,

Figure 3.10 (c) suggests that the limestone tended to contract slightly at the beginning and then underwent considerable dilation until the end of the tests. The maximum vertical dilation was measured to be 8 mm. This significant volume dilation can be explained by the particle movement mechanism of limestone during shearing. The manual compaction and pre-compression make the limestone denser, with a great degree of interlock between particles. At the same time, the limestone contained several large particles with an angular shape, leading to great particle-particle friction. These factors result in the limestone grains at the slip plane being not only able to slide during shearing but also to tumble and lift. The rearrangement of particles at the slip plane requires much energy and could result in an increase in the volume of limestone during shearing [125].
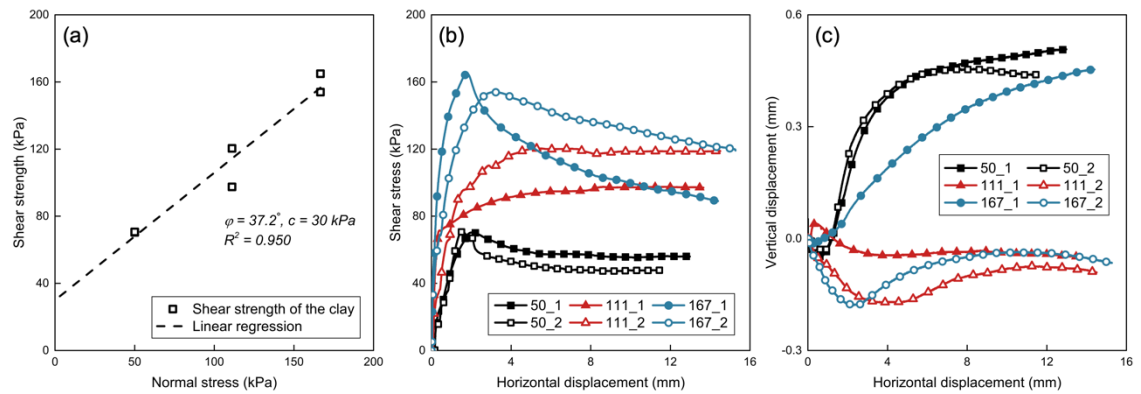
Figure 3.9 Experimental results of small-scale direct shear tests on clay. (a) Shear strength envelope; (b) shear stress versus horizontal displacement; and (c) vertical displacement versus horizontal displacement.
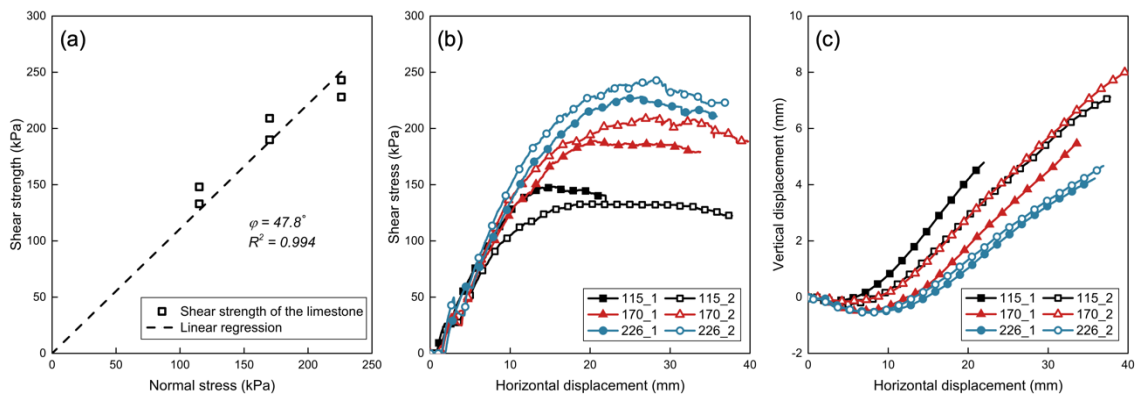
Figure 3.10 Experimental results of the large-scale shear box tests on limestone. (a) Shear strength envelope; (b) shear stress versus horizontal displacement; and (c) vertical displacement versus horizontal displacement.

3.5.2 Experimental results on brickwork-backfill interfaces

A total of twenty-four interface shear tests were carried out on four types of brickwork-

backfill interfaces under three different levels of normal stress, with two repetitions under the same conditions. After the tests, no damage was observed in the brickwork specimens, indicating that the surface roughness and texture of brickwork specimens remained consistent over multiple tests. Previous studies have demonstrated that soil density can significantly impact the interface shear behaviour [126,127]. Table 3.4 summarises the values of soil density achieved after pre-test compaction for the limestone and after 3-days of consolidation for the clay. It can be seen that the variation of density is very small, with a maximum CV of less than 2%, indicating that similar soil conditions were achieved, and the effect of backfill density variation on the interface behaviour between brickwork and backfill can be assumed to be negligible.

Table 3.4 Density of the backfill materials after consolidation (before shearing).

Interface	Brickwork bond pattern	Type of backfill	Number of tests	Density of the backfill after consolidation, before shearing	
				Mean value (kg/m³)	CV
EC	English bond	Clay	6	2,021	1.4%
SC	Soldier course	Clay	6	2,048	2%
EL	English bond	Limestone	6	1,865	1.2%
SL	Soldier course	Limestone	6	1,876	Less than 1%

Experimental results obtained from the four types of brickwork-backfill interfaces are summarized in Table 3.5, including mean values and corresponding CVs of shear strength under three levels of normal stress. Overall, very similar shear strengths were obtained from two repetitions of the test under the same conditions, indicating a high degree of repeatability of the experimental results.

Results from the interface shear tests between clay and brickwork constructed with an English bond pattern are illustrated in Figure 3.11. From the shear strength envelope and the linear regression analysis (Figure 3.11 (a)), the EC interface had a friction angle of 14.5° with a cohesion intercept of 16.7 kPa. Under the zero-cohesion assumption, φ_i increased to 19.2°. The shear stress increased with the horizontal displacement increase and reached a peak after 4 mm to 5 mm displacement (1.3% to 1.7% shear strain), followed by a slight decrease in residual shear strength for the further displacement (See Figure 3.11 (b)). The vertical displacement versus horizontal displacement curves

(Figure 3.11 (c)) are less repeatable than the peak shear stress and shear stress development. The upper half of clay samples underwent a slight contraction within 0.2 mm during shearing, except for the one test under 226 kPa normal stress where the contraction of the clay sample reached up to 0.68 mm.

Table 3.5 Summary of the interface shear test results.

| Interface | Brickwork bond pattern | Type of backfill | Mean value and (CV) of the shear strength (kPa) | | | φ_i (°) | c_i (kPa) |
			σ_n=115 kPa	σ_n=170 kPa	σ_n=226 kPa		
EC	English bond	Clay	47.2 (3.0%)	58.9 (4.2%)	76.0 (7.5%)	14.5	16.7
						19.2	0
SC	Soldier course	Clay	48.2 (1.4%)	57.6 (2.5%)	73.6 (3.3%)	12.9	20.9
						18.9	0
EL	English bond	Limestone	87.4 (2.6%)	106.2 (9.7%)	146.2 (4.0%)	33.3	0
SL	Soldier course	Limestone	84.6 (7.0%)	120.5 (3.4%)	162.8 (1.0%)	35.7	0
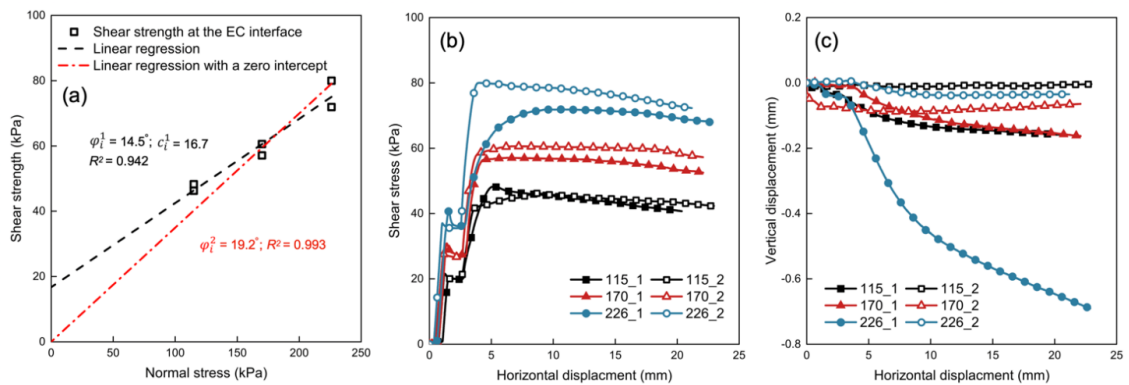
Figure 3.11 Experimental results on EC interface. (a) Shear strength envelope; (c) shear stress versus horizontal displacement; and (d) vertical displacement versus horizontal displacement.
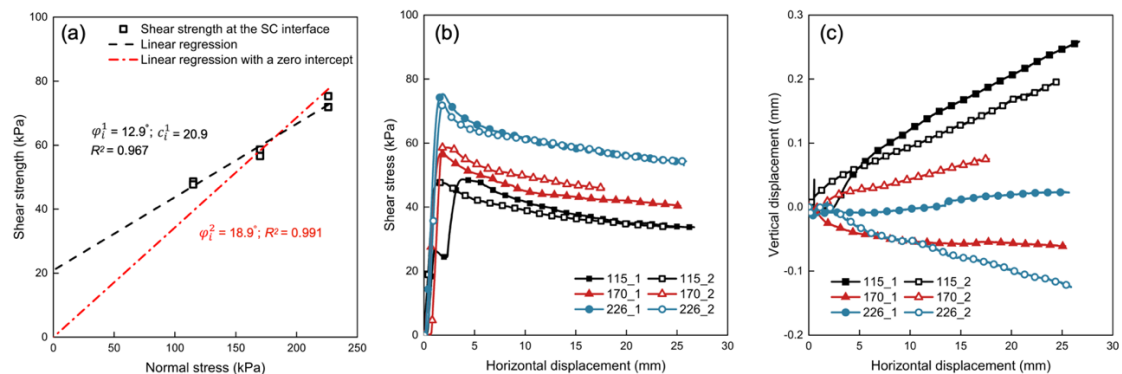
Figure 3.12 Experimental results on SC interface. (a) Shear strength envelope; (b) shear stress versus horizontal displacement; and (c) vertical displacement versus horizontal displacement.

Experimental results on the SC interface are shown in Figure 3.12. Figure 3.12 (a) illustrates φ_i of 12.9° and c_i of 20.9 kPa at the SC interface. The assumption of zero-cohesion at the interface could result in an increase in φ_i to 18.9°. Shear stress curves (Figure 3.12 (b)) showed a peak behaviour that the interface shear stress increased and reached a peak after a horizontal displacement of 2 to 3 mm (less than 1% of the shear strain). After the peak, a reduction in residual shear strength was observed, indicating strain-softening behaviour at the sliding plane. Moreover, the vertical deformation of clay samples exhibited a certain degree of variability across the tests (Figure 3.12 (c)). The clay dilated under lower normal stresses, and the dilation of the samples decreased as the normal stress increased. However, for the two tests at 170 kPa and 226 kPa normal stress, respectively, the clay samples contracted from the beginning of shearing.
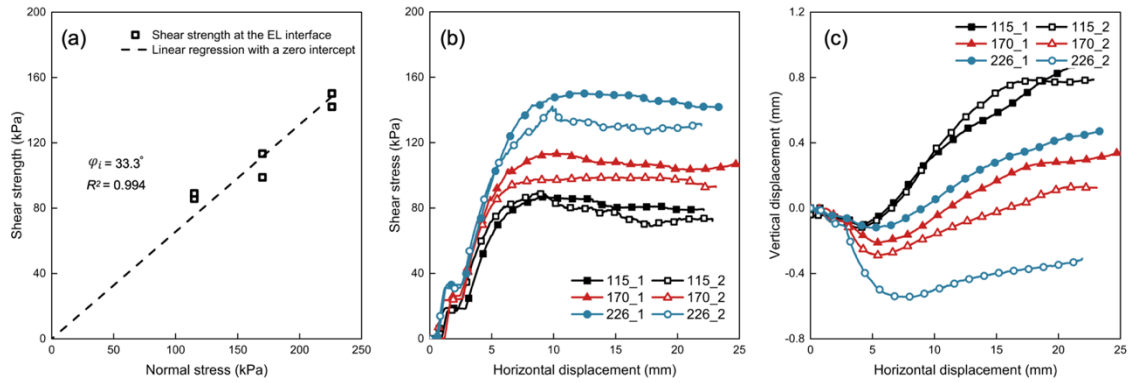
Figure 3.13 Experimental results on EL interface. (a)Shear strength envelope; (b) shear stress versus horizontal displacement; and (c) vertical displacement versus horizontal displacement.
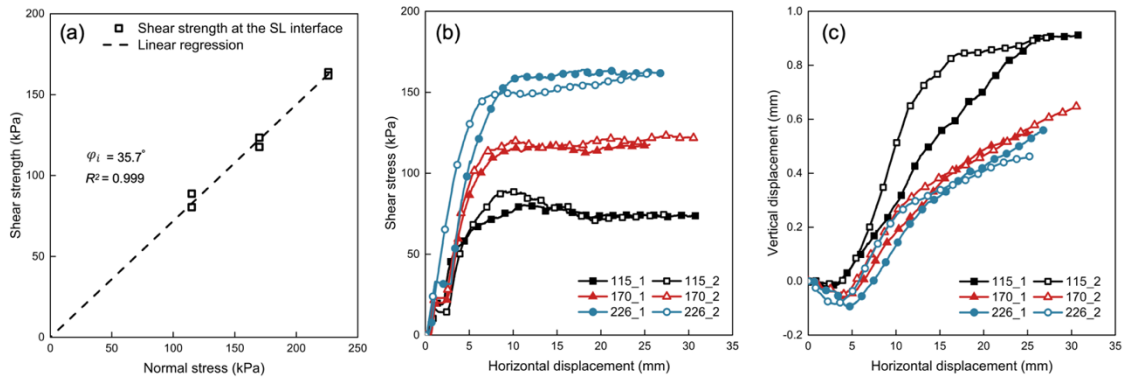
Figure 3.14 Experimental results on SL interface. (a) Shear strength envelope; (b) shear stress versus horizontal displacement; and (c) vertical displacement versus horizontal displacement.

Shear testing results on the EL and SL interfaces are shown in Figure 3.13 and Figure 3.14, respectively. The value of φ_i at the EL interface was determined to be 33.3° with a zero-cohesion assumption from the shear strength envelope shown in Figure 3.13 (a). For the SL interface, φ_i increased slightly to 35.7° (Figure 3.14 (a)). The shear strength

and shear stress development show a very good agreement for the two tests under the same conditions. The EL and SL interfaces have a similar ductile failure type. Specifically, interface shear stress increased with the increment in the horizontal displacement and reached a peak after shearing approximately 9 to 11 mm (3.0% to 3.7% of the sample size). No noticeable reduction in residual shear strength was observed, indicating the post-peak strain-softening behaviour was marginal (See Figure 3.13 (b) and Figure 3.14 (b)). Regarding the volumetric response of the limestone, Figure 3.13 (c) and Figure 3.14 (c) suggested that the limestone underwent a slight contraction and then dilation after the shear failure occurred.

3.6 Discussion

3.6.1 Influence of bond patterns on the shear behaviour of brickwork-backfill interface

For a continuous surface, it has been identified that surface roughness can significantly affect the interface resistance between soil and construction materials [9,64]. For example, by shearing Kawasaki clay against steel with different roughness, Tsubakihara et al. [128] found that, for smoother surfaces, the interface sliding occurred at the peak stress, followed by a reduction in residual strength. Conversely, when the surface roughness of steel was increased, shear failure occurred within the sand rather than at sand-steel interfaces, which means that the residual strength stays as the peak value. Subsequently, Hu and Pu [129] observed that the critical roughness of a surface is not only related to R_{max}, the absolute vertical distance between the highest peak and lowest valley along the surface profile, but can also be affected by the particle size of the soil. Therefore, a relative critical roughness, R_{cr}, can be used to describe how the surface roughness and particle size affect the shear behaviour of the soil-structure interface. R_{cr} can be expressed by the following equation:

$$R_{cr} = R_{max}/D_{50} \tag{3.4}$$

where D_{50} represents the average particle size of a soil.

For brickwork, the surface roughness of bricks, the profile of mortar joints, and the joint arrangement can affect its surface roughness and texture. The former two factors could be deemed identical for the two masonry specimens used in this study due to the usage of the same materials and construction methods. However, the different layouts of joints

in the two masonry specimens result in different textures, which may further affect their shear behaviour at the brickwork-backfill interface. Based on the experimental results obtained from EL, SL, EC, and SC interfaces, there were no statistically significant differences found to indicate that the joint layout of the brickwork had a significant effect on the frictional properties of the four interfaces investigated in this study.

For the brickwork and clay combinations (EC and SC interfaces), their shear stress-displacement relationships (Figure 3.11 (b) and Figure 3.12 (b)) suggest that the shear behaviour of the brickwork-clay interface was in line with the typical shear behaviour of soil against a relatively smooth surface (i.e., the shear stress had a peak behaviour, the residual strength decreased, and shear failure occurred at the brickwork-clay contact interface) [128]. On the other hand, Figure 3.11 (a) and Figure 3.12 (a) demonstrate that the shear strength obtained at the EC interface was approximately 2.2% and 3.2% greater than that at the SC interface under normal stresses of 170 kPa and 226 kPa, respectively. Also, φ_i at the EC interface was always greater than that at the SC interface, irrespective of whether zero-cohesion at the interface was assumed. For instance, φ_i at the EC interface was 12.4% and 1.6% greater than that at the SC interface when cohesion or zero cohesion was considered, respectively.

The larger shear strength and φ_i obtained from the EC interface compared to those obtained from the SC interface may, to some extent, reflect how the joint layout affects the shear behaviour of the brickwork-clay interface by influencing particle movement at the sliding plane. Specifically, clay particles fill in the concave joints under normal compression. During shearing, the clay over the bricks shears against the surface of the brick, forming the clay-brick interface. For clay particles filling the bed joints (perpendicular to the shear direction), the shear causes their movement to be obstructed by the bed joints, so that the shear failure occurs within the clay, creating clay-clay interfaces (see Figure 3.15 (c1)), which can be evidenced by the post-shear image of the masonry specimen shown in Figure 3.15 (b). Regarding the effect of head joints (parallel to the shear direction) on the clay movement, the head joints of the brickwork constructed with the soldier bond type are aligned, allowing clay particles embedded into the head joints to move along the joint under shearing (Figure 3.15 (a)). However, for the brickwork constructed with the English bond pattern, head joints are interrupted by several equally spaced bed joints. Thus, the movement of clay particles may be restricted, which could trigger lifting and squeezing of the particles during their rearrangement (see

Figure 3.15 (c2)). The more complex movement and rearrangement of clay particles at the EC interface would then require more energy, resulting in the EC interface having a larger shear strength and interface friction angle compared to those of the SC interface [130].

However, for the brickwork and limestone combinations (EL and SL interfaces), the experimental results were inconsistent with the results obtained from brickwork-clay interfaces. Specifically, the values of shear strength obtained from the EL interface were smaller than those from SL interface under normal stresses of 170 kPa and 226 kPa, and the value of φ_i for the EL interface was also slightly smaller than that for the SL interface (see Figure 3.13 (a) and Figure 3.14 (a)). The main reason for the inconsistency between the results from brickwork-clay interfaces and brickwork-limestone interfaces was the fact that the particle size of limestone was significantly larger than that of the clay used (Figure 3.2). The larger limestone particle sizes resulted in the R_{cr} between brickwork and limestone to become smaller than that between brickwork and clay. As a result, shear failure occurred within the limestone rather than at the brickwork-limestone interface. This was confirmed by the shear stress development curves obtained from the EL and SL interfaces (see Figure 3.13 (b) and Figure 3.14 (b)), which showed a ductile failure, without any significant decrease in residual shear strength [128].
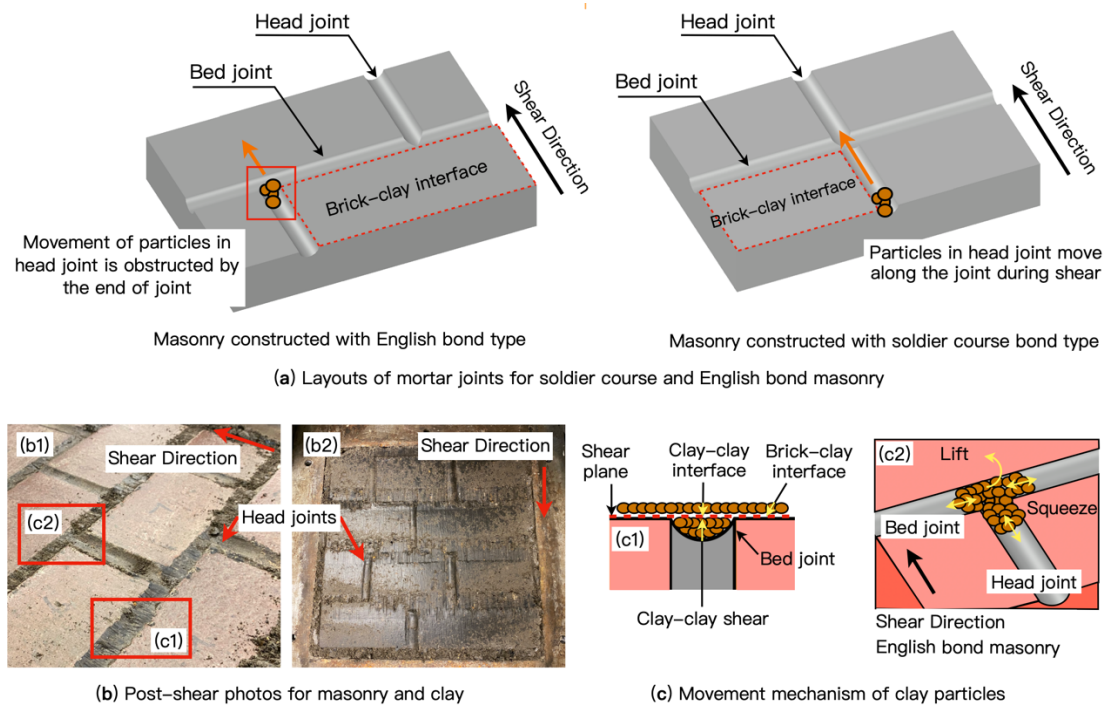
Figure 3.15 (a) Layouts of mortar joints for the soldier course and English bond masonry; (b) post-shear photos for brickwork with an English bond pattern and clay; and (c) movement mechanism of clay particles during shear.

3.6.2 Influence of backfill properties on the shear behaviour between brickwork-backfill interfaces

The force transfer mechanisms for cohesive soils and non-cohesive soils are different. The force transfer mechanism in clay is primarily through the inter-particle bonding, which is due to the cohesive forces between clay particles. Conversely, the transfer of forces in limestone is primarily through friction between the particles [131]. These different force transfer mechanisms result in the shear behaviour between the brickwork-limestone interface and brickwork-clay interface to differ. The results of the current study are overall in agreement with previously published findings on interface shear tests between sand-clay mixtures and structural surfaces [91,132]. Specifically, brickwork-clay interfaces had a lower φ_i than brickwork-limestone interfaces. For example, assuming zero-cohesion at masonry-backfill interfaces, φ_i between clay and brickwork was approximately 55% smaller than that between limestone and brickwork. From the interface shear stress perspective, the peak shear stress at a brickwork-limestone interface was significantly larger than that at a brickwork-clay interface due to the interlock behaviour involving limestone particles and the brickwork-limestone interface. Moreover, the tangential deformation at failure for the brickwork- limestone interface was also significantly larger than that for the brickwork-clay interface. For instance, it was observed that the critical tangential strains were 3.0% to 3.7% and 1.3% to 1.7% for the brickwork-limestone interface and brickwork-clay interface, respectively.

3.6.3 Comparison of the internal shear behaviour of backfills and interface shear behaviour between brickwork and backfill

Generally, as the surface roughness increases, shear failure at the soil-structure interface occurs from fully sliding along the contact interface (for very smooth interfaces) to the interior of the soil, which results in an interface shear behaviour close to the soil-soil shear behaviour [133]. The results of the present study indicate several differences in shear behaviour between the backfill and brickwork-backfill interfaces. Firstly, the shear strength of brickwork-backfill interfaces was significantly lower than that of the backfill materials under the same normal stress. For example, the average shear strength of limestone was 63.4%, 76.0%, and 52.4% higher than that of the brickwork-limestone interfaces at normal stress of 115 kPa, 170 kPa, and 226 kPa, respectively. Similar results were observed for the clay and brickwork-clay interfaces. As for the shear strain, the critical shear strain obtained from the direct shear tests on limestone (6% to 10%) was

almost twice as high as that from the brickwork-limestone interface shear tests (3% to 3.7%).

Table 3.6 summarises the ratio between φ_i of brickwork-backfill interfaces and φ of backfills. These ratios can be used as a guide by researchers and engineers when selecting friction parameters between brickwork and backfill materials when modelling masonry arch bridges. It can be seen from Table 3.6 that the values of φ_i are significantly smaller than φ of the corresponding backfill materials. Different bond types of masonry could result in different interface friction angles, but the difference in φ_i/φ due to the variation of masonry bond patterns was not pronounced. Therefore, the effects of masonry bond types may be negligible when assigning frictional parameters to the brickwork-backfill interfaces. However, Table 3.6 suggests that φ_i/φ is closely related to the types of backfill and the cohesion characteristics at brickwork-backfill interfaces, which has not been adequately considered in previous masonry arch bridge modelling studies (see Table 3.1). For example, taking limestone as the backfill material resulted in φ_i/φ ranging from 0.70 to 0.75 (most previous numerical studies adopted φ_i/φ within or close to this range, as suggested in Table 3.1). But when the clay was adopted as the backfill material, φ_i/φ was determined to be 0.35 to 0.39, when the interface cohesion was taken into consideration. The zero-cohesion assumption at the brickwork-clay interface led to an increase in φ_i/φ to approximately 0.5.

Table 3.6 Summary of shear parameters for backfills and brickwork-backfill interfaces.

Samples/interfaces		Friction angle (°)	Cohesion (kPa)	R^2	φ_i/φ
Clay		37.2	30.0	0.950	-
Limestone		47.8	0	0.994	-
EC interface	With cohesion	14.5	16.7	0.942	0.39
	Zero-cohesion	19.2	0	0.993	0.52
SC interface	With cohesion	12.9	20.9	0.967	0.35
	Zero-cohesion	18.9	0	0.991	0.51
EL interface		33.3	0	0.994	0.70
SL interface		35.7	0	0.999	0.75

3.7 Conclusions

The present study presents an experimental procedure to assess the interface shear behaviour between brickwork masonry and backfill materials. Thirty-six experimental tests were performed to investigate the internal shear behaviour of backfill materials and the interface shear behaviour between brickwork and backfill materials in masonry arch bridges. The brickwork specimens were constructed using Type A bricks with cement mortar to achieve good durability and to keep the surface texture of the specimen effectively unchanged for all 12 experiments carried out on each brickwork specimen. The friction angle and cohesion intercept of limestone, puddling clay, and four types of brickwork-backfill interfaces were characterised. Moreover, the effects of masonry bond patterns and backfill properties on the shear behaviour at brickwork-backfill interfaces were assessed. From the analysis of the results, the following conclusions can be drawn:

1. For the brickwork and clay combinations, shear failure occurred at the brickwork-clay interfaces. In these cases, the bond pattern of brickwork was found to affect the movement of clay particles. The values of φ_i and shear strength obtained from the SC interface were smaller than those obtained from the EC interface due to the aligned joint arrangement of the brickwork specimens with a soldier course bond pattern. However, for the limestone, which had much larger particle sizes, shear failure occurred within the limestone and was of a ductile type. Nevertheless, in the cases investigated in the study, the influence of brickwork bond patterns on the shear behaviour at brickwork-backfill interfaces was not significant and may be considered negligible when assessing masonry arch bridges.

2. The properties of the backfill materials had a marked impact on brickwork-backfill interface shear behaviour. The critical shear strain, peak shear stress and interface friction angle of brickwork-limestone interfaces were significantly larger than those of brickwork-clay interfaces.

3. The internal angle of friction of the backfill materials was higher than the interface angle of friction between brickwork and backfill. On the other hand, backfill type was found to significantly affect the shear behaviour at the brickwork-backfill interface. In the case of limestone backfill, φ_i/φ ranged from 0.70 to 0.75. In the case of clay backfill, φ_i/φ was determined to be 0.51 to 0.52 under the assumption of zero-cohesion at the masonry-clay interface, or 0.35 to 0.39 if interface cohesion was taken into account. These ratios provide experimentally-derived parameters that

researchers and practicing engineers can refer to when modelling masonry arch bridges numerically.

However, the results presented herein relate to the specific brickwork and backfill employed and different material combinations may furnish different outcomes. The results are strongly influenced by the relative roughness of the brickwork surface and the backfill, as well as the arrangement and profile of the mortar joints.

The results obtained from this study may provide researchers and engineers with a firm basis of the procedure to be undertaken to obtain the interface parameters between masonry and backfill.

Acknowledgement

4 The 3D Response of a Masonry Arch Bridge Under Low and Medium Loading Levels

This chapter represents the slightly modified post-print version of the article: V. Sarhosis, **B. Liu**, M. Gilbert, "The 3D response of a large-scale masonry arch bridge - Part I: performance under low and medium loading levels", Engineering Structures, 316 (2024), p. 118496. The formatting and numbering of equations, tables and figures have been adapted to this document.

4.1 Abstract

Masonry arch bridges are characterised by three-dimensional (3D) behaviour when subjected to external eccentric loading (e.g., vehicle loads). The arch ring, abutments, backfill and spandrel walls may interact with each other in a complex manner, leading to a 3D mode of response that can have a significant impact on the initiation and propagation of damage. However, there is a dearth of experimental data from tests designed to investigate the 3D behaviour of masonry arch bridges, particularly under loading levels below those required to cause failure. This chapter presents results from tests on a large-scale brickwork masonry arch bridge subjected to low- and mid-level static loads under laboratory conditions. Point loads of increasing magnitude were applied at different locations on the top of the backfill in order to investigate 3D response and damage accumulation. Details of the experimental setup, material characterisation, and the results obtained from static and repeated load tests at low- and mid-level load magnitudes are presented herein. Results demonstrate that the bridge exhibited a 3D mode of response under eccentric point loads. Loading at the mid-span resulted in greater deformation of the arch barrel compared to loading at the quarter- and three-quarter-span points, due to the shallower backfill depth over the crown. Under the mid-level loading, stiffness degradation was observed during the testing regime, suggesting an accumulation of damage in the bridge. Moreover, when loading was applied close to a spandrel wall, measurable out-of-plane deformation of the spandrel wall was observed, with this deformation increasing significantly as the load was increased from 150 kN to 250 kN. This results from a combination of increased lateral soil pressure and decreased shear resistance at the arch-spandrel wall interface.

4.2 Introduction

Masonry arch bridges are of significant historical and structural importance, both in the UK and worldwide. In Europe, most masonry arch bridges were constructed over a century ago and are still in active service today, forming pivotal parts of railway and highway transport networks, as well as being cultural landmarks [40]. However, these structures are ageing and often exhibit various signs of deterioration, leading to concerns over their long-term reliability. Observed deterioration can be because traffic loads and speeds have increased significantly compared to those present when the bridges were designed and constructed, with the higher demands imposed by modern traffic potentially presenting a threat to their safety [10]. Additionally, masonry material properties naturally deteriorate over time, due to environmental factors and the effects of climate change, which may lead to loss of material and to a further reduction in the stiffness and load-carrying capacity of a masonry arch bridge [6]. Therefore, developing an understanding of the circumstances in which cracks propagate and damage accumulates in a masonry arch bridge is likely to be of considerable interest to asset owners and engineers, since it can potentially help them make more informed decisions in respect of maintenance and rehabilitation strategies.

Over the years, a series of experimental tests have been carried out to assess the structural behaviour of masonry arch bridges. Most of these tests have focused on structural behaviour of the arch barrel, since this is the main load-carrying element in a masonry arch bridge [134,135]. Melbourne et al. [37,136] performed a series of large-scale laboratory tests on brickwork arches with different bond configurations. In these tests, single-ring arches were observed to fail in four-hinge failure mechanisms, whereas multi-ring arches were often observed to experience separation of adjacent rings due to the low shear resistance of the bonding material between rings. In addition, the effects of backfill material on the overall behaviour of masonry arch bridges, including underlying soil-structure interaction mechanisms, have been extensively investigated [36,137]. As reported in [64], the backfill distributes the live load from the traffic surface to the arch barrel, effectively prestresses the barrel through self-weight of the backfill, and also restrains lateral sway of the barrel, all significantly increasing bridge load-carrying capacity. However, the type of backfill employed can affect the capacity of the bridge. For example, according to an experimental study performed by Gilbert et al. [138], a bridge backfilled with crushed limestone is likely to have significantly higher

strength than a comparable bridge backfilled with clay. Also, according to the results obtained from 24 arch specimens, the load-carrying capacity of a bridge can be enhanced by 150% and 320% via inclusion of unreinforced and reinforced spandrel walls respectively [35]. In addition, the presence of spandrel walls can also affect the failure mechanism of a masonry arch bridge (e.g., sliding and overturning of spandrel walls may occur under loading [139]).

To explore the 3D behaviour of masonry arch bridges, several computational strategies have been developed which model material non-linearity, actual arch shape, and fill-arch interaction, though which make a range of different assumptions and simplifications [68,112]. For example, for the large-scale bridge with complex geometric characteristics, continuum models considering the masonry material as a homogeneous deformable element can be developed, and damages developed under loads are represented by plastic deformation [140,141]. However, these continuum models with isotropic material properties are not able to reflect the effects of brick arrangements and masonry textures. To overcome these issues, a micro-modelling strategy is proposed, which model the bricks and mortar joints separately and can reproduce the detailed cracking patterns developed in masonry. The high computational demands make it infeasible for adopting the detailed micro-model to large-scale structures. As an alternative, macro-modelling strategies have been proposed, which simulate the masonry units as rigid or deformable blocks and mortar joints as zero-thickness interface elements [81,83,112,115,141–144]. Although these high-fidelity models have been used to model structural behaviour and load-carrying capacity, there is currently relatively little experimental data available from physical tests to validate these numerical models [36]. In addition, understanding 3D behaviour and the interaction between the various different elements of a masonry arch bridge is still limited.

In this study, a large-scale brickwork masonry arch bridge was constructed and tested under controlled laboratory conditions, to develop an improved fundamental understanding of the 3D mode of response of masonry arch bridges when subjected to a range of loading regimes. The experimental campaign was divided into two parts: Part I (the present chapter) focused on application of low- and mid-level magnitude loads, while Part II covers results from load tests to failure [145].

Thus, this chapter presents details of the response of a brickwork arch bridge subjected to point loads at low- and mid-level loading magnitudes. The experimental campaign

started with a comprehensive characterisation of material properties; Subsequently, experimental testing was carried out on a large-scale masonry arch bridge. To respectively accommodate the bridge and facilitate the planned testing, a reinforced concrete (RC) U-frame and steel reaction frame were specifically designed and fabricated, with the latter used to mount a hydraulic actuator for load application. A large-scale masonry arch bridge containing an arch barrel, compacted backfill, abutments and spandrel walls was constructed using high compressive strength bricks bonded with weak mortar joints to reproduce the low bond strength characteristics often found in real masonry arch bridges. During the testing, nine loading locations were selected, at quarter-span, mid-span, and three-quarter–span points both eccentric to and on the bridge centreline. The eccentric loading is representative of the loading a bridge is often subjected to in practice and allows 3D bridge behaviour to be assessed. On the other hand, the application of loading increasing in magnitude from low-level loading up to mid-level loading enabled elastic behaviour and damage accumulation to be investigated. Finally, experimental results are presented and discussed, considering aspects such as crack evolution, stiffness variation, arch barrel deformation, and out-of-plane spandrel wall deformation.

4.3 Experimental programme

4.3.1 Base slab and reinforced concrete end walls

In order to accommodate a large-scale masonry arch bridge and to provide longitudinal restraint, a base slab with two reinforced concrete (RC) end walls was constructed, forming a U-frame (Figure 4.1). The base slab and RC end retaining walls designed to provide sufficient support to the bridge, and the testing rig to be stiff enough to keep deformations under external loading to a minimum. Therefore, a dense reinforcement arrangement was adopted for the base slab and RC end walls (Figure 4.1 (a) to (c)). Moreover, a nominally C30-grade concrete was utilized for the base slab and RC walls (Figure 4.1 (d)). The compressive strength of concrete cube specimens was tested to be equal to 22.5 MPa at 35 days of curing with a coefficient of variation (CV) equal to 9%, and increased to 28.5 MPa (CV = 3%) after curing for 445 days (the time for ultimate tests on the bridge).
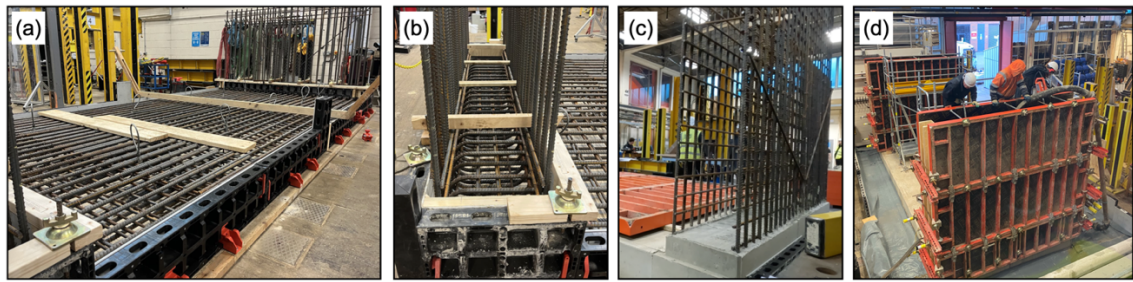
Figure 4.1 Base slab and RC end walls: (a) reinforcement layout for the base slab; (b) reinforcement layout for slab-vertical wall connection; (c) reinforcement layout for end walls; and (d) pouring concrete for RC end walls.

4.3.2 Steel reaction frame

A steel reaction frame was specifically designed for mounting the hydraulic actuator and applying vertical loads. The beams and columns of the reaction frame were manufactured using steel I-sections, as indicated in Figure 4.2. Overall, the reaction frame was 6,200 mm in length, 3,520 mm in width, and 4,000 mm in height, covering the whole testing area. The frame consisted of ten columns, two longitudinal beams, and five transverse beams, which were all connected by high-strength bolts. Additionally, six short movable beams were incorporated into the frame to facilitate different loading scenarios.

Elements	No.	Length	Mass per meter	Dimension				
				B	D	T	t	r
		mm	kg/m	mm	mm	mm	mm	mm
Vertical column	10	3543	46	203.6	203.2	11.0	7.2	12.7
Longitudinal beam	2	6390	67	189.9	453.6	12.7	8.5	10.2
Transverse beam	5	3330	74	190.5	457.2	14.5	9.1	10.2
Short movable beam	6	1550	60	178.8	409.4	14.3	8.8	10.2
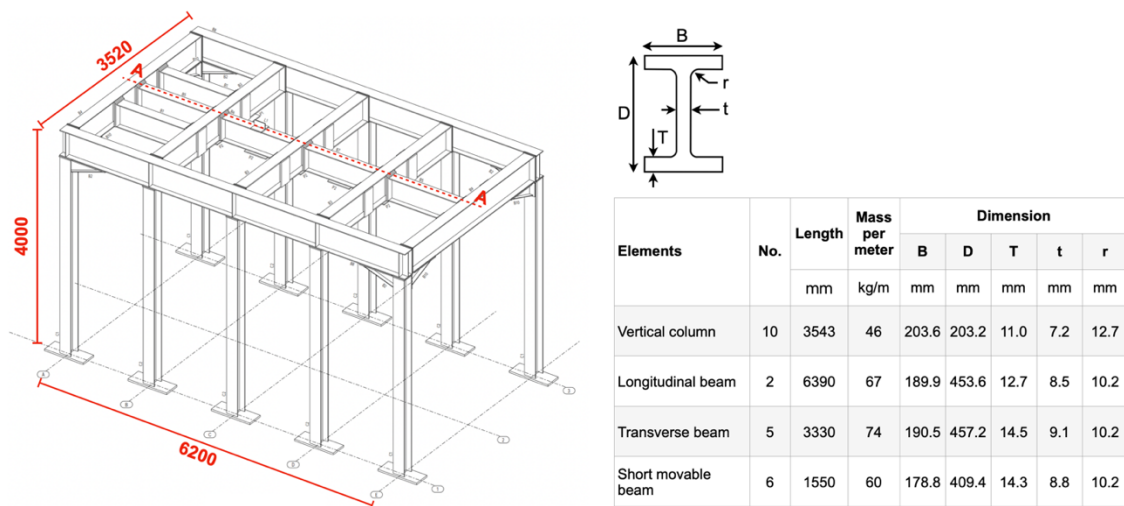
Figure 4.2 Details of steel reaction frame (all units in mm).

The reaction frame should be as stiff as possible in order to minimize deformation of the reaction frame during the application of vertical loading. To achieve this, ten columns were directly connected to the strong floor via twenty bolts, each of which had a resistance of approximately 115 kN. The maximum loading that can be applied through the reaction frame depends on the loading locations and the layout of the short movable

beams. Including a safety factor of 1.5, this allowed a load of up to 750 kN to be applied at any point along the central longitudinal line (A-A in Figure 4.2). However, for eccentric loading locations, a lower load, of up to 500 kN can be applied. For any load case, the maximum deformation of the steel reaction frame was to be less than 6 mm.

4.3.3 Large-scale masonry arch bridge

A large-scale single-span brickwork masonry arch bridge was designed and constructed to investigate its three-dimensional (3D) response under point (patch) loading and to assess arch-backfill-spandrel interaction mechanisms. The masonry arch bridge consisted of an arch barrel, abutments, spandrel walls, and compacted crushed limestone backfill. A schematic drawing that includes detailed dimensions of the bridge is shown in Figure 4.3. It should be noted that the geometry of the bridge and the materials employed in its construction were chosen to where possible match those employed in previous experimental tests on masonry arches/arch bridges carried out at Bolton Institute and University of Salford [36,146,147] thereby providing a degree of comparability between tests.

Specifically, the masonry arch bridge was constructed using type A engineering bricks bonded with 10 mm thick type O mortar joints. Also, MOT type I graded crushed limestone was selected as the backfill material. The material properties of the bricks, mortar joints, and crushed limestone used in the study are characterised and reported in section 4.4. Overall, the masonry arch bridge was 5,885 mm in length, 2,915 mm in width, and 2,015 mm in height. The whole bridge was constructed by the same experienced bricklayer to minimize variability due to workmanship effects.

Figure 4.4 shows a 3D photogrammetry model and detailed bond configurations for different components of the masonry arch bridge. Figure 4.5 shows stages in the actual process of construction. Specifically, before the brickwork was constructed, four polystyrene slabs were placed at the four interior corners of the RC walls. The purpose of this was to avoid hard contact between the spandrel walls and the RC end walls. Construction of the masonry arch bridge commenced with the building of the two abutments and the lower part of spandrel walls (Figure 4.5 (a)). The height and width of the abutments were equal to 600 mm (containing eight courses) and 440 mm (two-brick thick), respectively. Bricks were arranged alternatively using two types of stack bond patterns, as indicated in Figure 4.4 (b). Notably, at the springings of the arch, bricks were precisely cut to form inclined faces of approximately 36 degrees relative to the horizontal.

The spandrel wall was one and a half bricks thick and was constructed using an English bond pattern to provide resistance to lateral soil pressures [111] (Figure 4.4 (d)). An arch-shaped timber centring supported by scaffolding was then placed between the abutments for the construction of the arch barrel (Figure 4.5 (b)). The arch barrel was constructed using a header bond configuration (Figure 4.4 (b)), with a thickness of 215 mm, an intrados span of 3,000 mm, and a span:rise ratio of 4:1.

The voids between the walls forming the abutments, and later the volume above and behind the arch barrel, were filled in layers with crushed limestone fill material. The purpose of this was to elevate the working surface inside the bridge, thereby facilitating subsequent construction. The limestone was placed in layers of 110 mm thickness and compacted using a 12 kN electric plate compactor (ALTRAD PCLX 12/40) to achieve a density representation of backfill found in the field. At the locations close to the masonry, a 16 kN trench rammer (Wacker Neuson AS50) with a small plate measuring 340 x 280 mm was used to achieve as homogeneous compaction as possible (see Figure 4.5 (c)). Note that the abutments and lower parts of the spandrel walls had cured for more than 30 days prior to placement and compaction of the limestone fill. Therefore, no damage to the masonry was expected or observed during the compaction process.
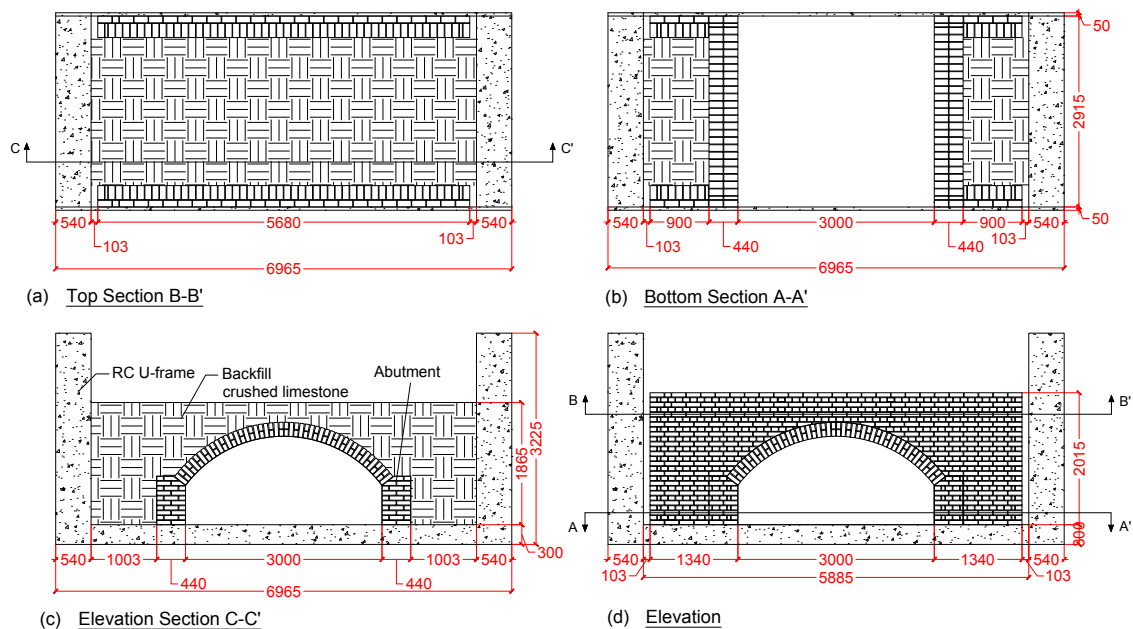
Figure 4.3 Details of the large-scale masonry arch bridge: (a) top view; (b) bottom section A-A'; (c) elevation section C-C'; and (d) elevation (side view) (all dimensions in mm).
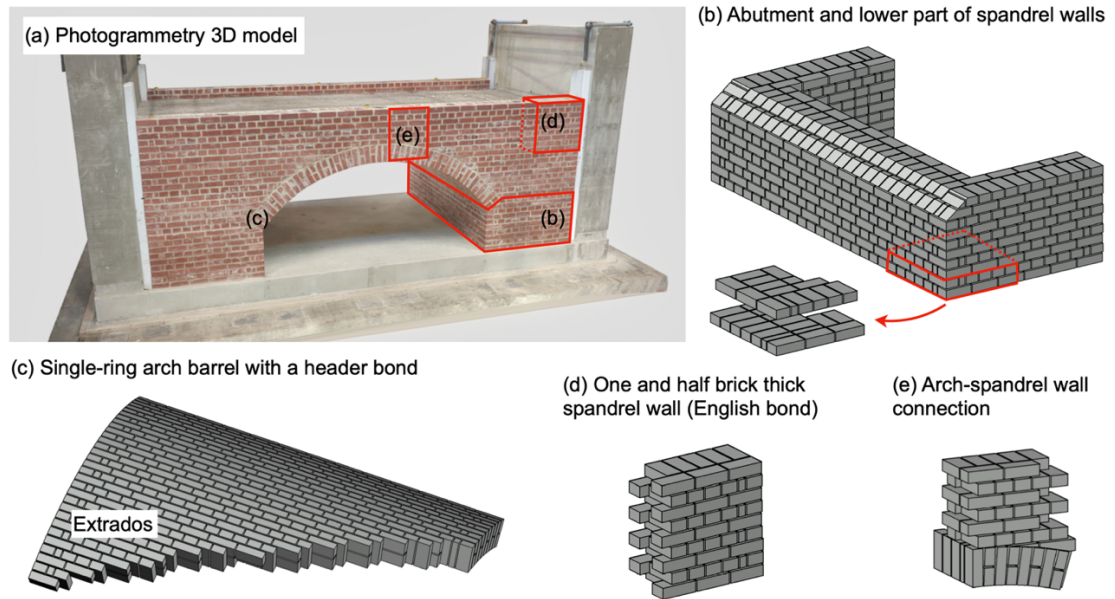
Figure 4.4 Masonry configuration (a) 3D photogrammetry model; (b) to (e) bond configurations for different elements.
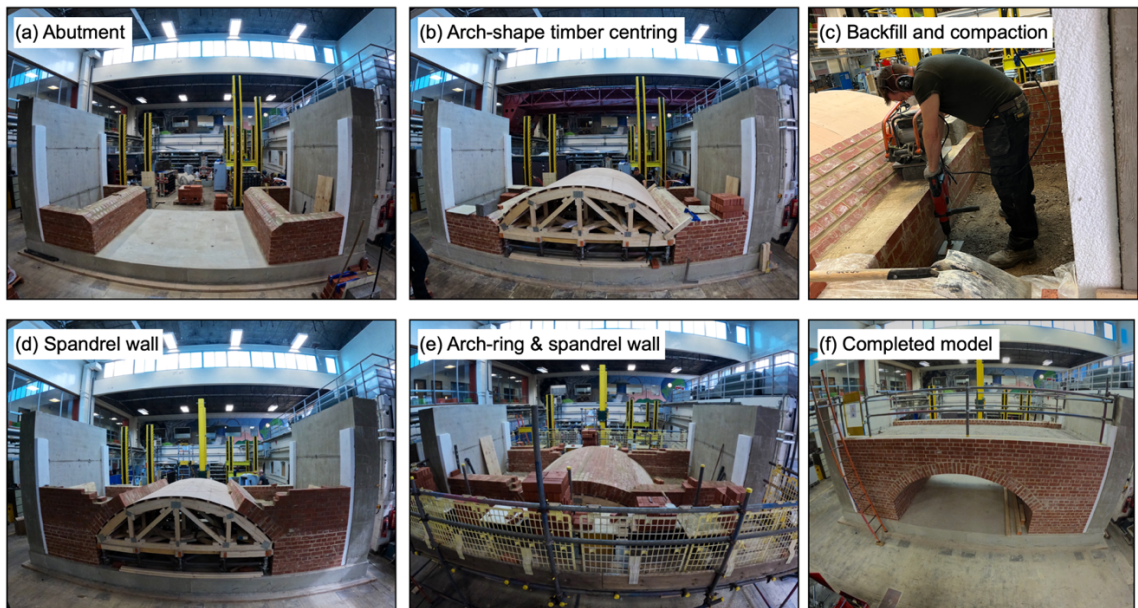
Figure 4.5 Construction process: (a) to (e) different construction stages; (f) completed masonry arch bridge.

After the crushed limestone was placed to the height of the abutment (600 mm above the base slab), the construction activities proceeded with the construction of the remaining arch barrel and spandrel walls. To achieve proper alignment and minimise variations in the thickness of mortar joints, the bricks at the junction between the arch barrel and spandrel walls were cut into specific shapes that closely matched the curvature of the arch (Figure 4.4 (e)). This approach can avoid, to the greatest extent possible, the

formation of weak planes caused by excessive mortar thickness, thereby ensuring structural integrity and consistency throughout the construction. Following the completion of the brickwork construction, the limestone was placed and compacted in layers in the same way as described before until it reached the target height of 1,865 mm (300 mm over the crown of the arch). The completed masonry arch bridge is shown in Figure 4.5 (f).

4.3.4 Instrumentation

The masonry arch bridge was instrumented using a variety of methods to capture its 3D response under centreline and eccentric patch loads. Prior to installation of the instrumentation, the north-side face and the arch intrados were painted white to facilitate identification of crack initiation and propagation. Figure 4.6 and Figure 4.7 show the instrumentation plan adopted in the study. Specifically, to capture the radial deflection and 3D deformed shape of the arch barrel, fifteen linear variable differential transformers (LVDTs) were positioned on the arch intrados, along the quarter-span, crown and three-quarter-span points perpendicular to the contact faces (L22 to L36 in Figure 4.6 (a) and (c), as well as Figure 4.7 (c))). In the transverse direction, five LVDTs were evenly distributed across the width of the bridge. These LVDTs had ranges of at least 50 mm and an accuracy of 0.001 mm to provide highly precise readings.
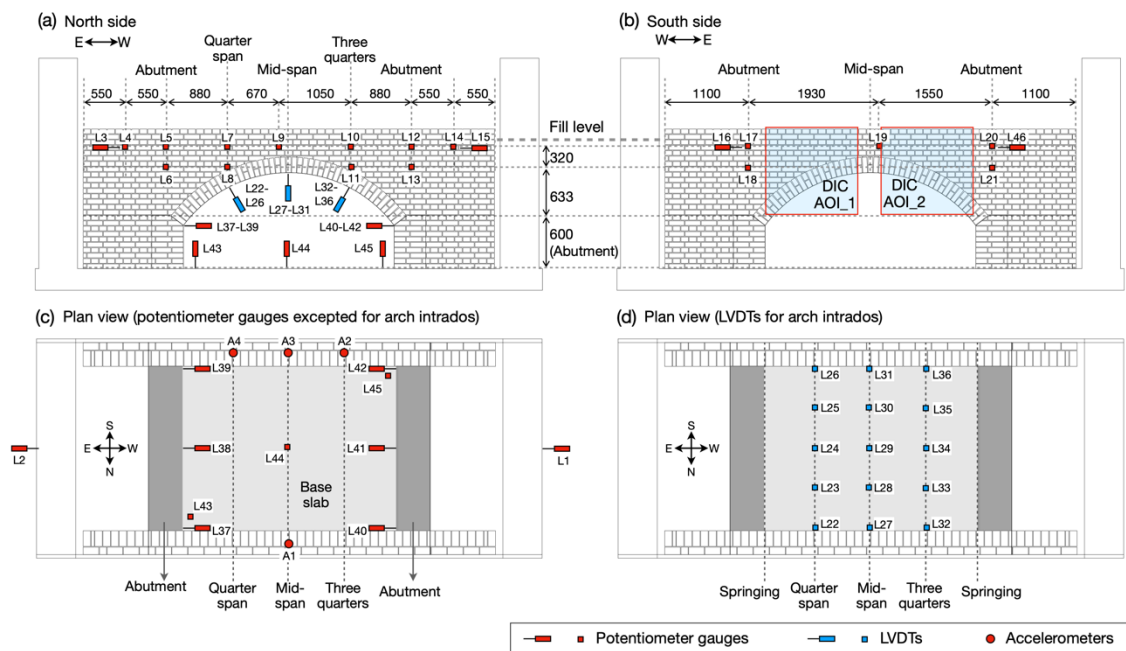
Figure 4.6 Instrumentation layout (unit: mm).
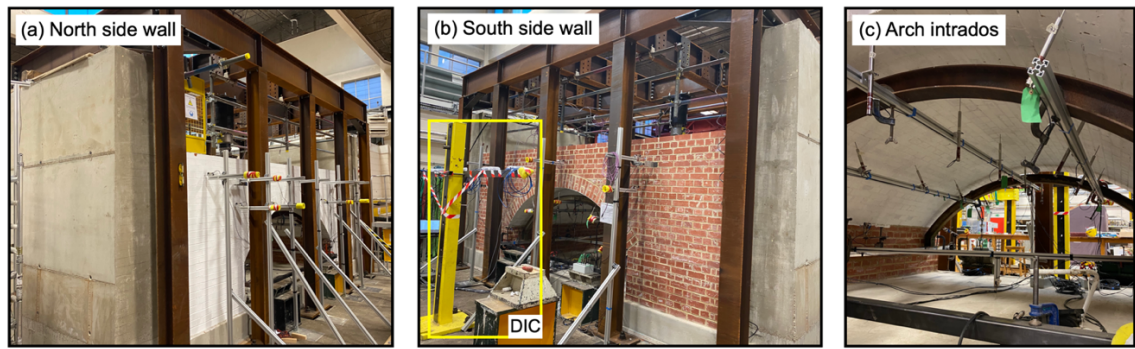
Figure 4.7 Instrumentation for (a) the north side wall; (b) the south side wall; and (c) arch intrados.

The out-of-plane deformation of the spandrel walls was monitored using potentiometer-based displacement transducers. Specifically, the north-side spandrel wall was instrumented using eleven potentiometers (L4 to L14 in Figure 6 (a), as well as Figure 4.7 (a)) that had ranges of 50 mm and an accuracy of 0.01 mm. The placement of these potentiometers was informed by preliminary numerical simulations, which indicated that the area between the abutments and above the arch barrel would experience more significant out-of-plane deformations under loading. Conversely, the south-side spandrel wall was equipped with two pairs of low-distortion lens monochrome digital cameras to capture the strain/deformation response. Each pair of cameras had a coverage area of approximately 1,500 by 1,500 mm. To enable comparison of the deformation results between the two spandrel walls, five additional potentiometer gauges were placed on the south-side wall (L17 to L21 in Figure 4.6 (b), as well as Figure 4.7 (b)). In addition, two potentiometer gauges were placed at each side of the spandrel walls (L3, L15, L16, and L46) to monitor in-plane deformations.

Moreover, six potentiometer gauges (L37 to L42 in Figure 4.6 (c)) were placed at the inner surface of the abutments to monitor sliding of the abutments. Finally, out-of-plane deformation of RC end walls, as well as uplift of the base slab were monitored in real-time to detect any movements that might occur during the tests. It is noteworthy that all instrumentation was supported directly on the strong floor, independent from the bridge and testing rig. A fifty-channel data logger was employed, collecting data at a rate of 2 Hz.

4.3.5   Loading protocol

A hydraulic actuator with a capacity of 750 kN was used to apply the applied loads, used in conjunction with a steel section of base area of 300 by 300 mm to spread the load onto

the surface of the backfill. The actuator was connected to either the short movable beams or the joint between the short beam and transverse beam of the reaction frame, enabling the load to be applied at different locations, such as at quarter-span, mid-span and three-quarter-span points along the centre line, as well as at eccentric, off-centre lines. In total, nine loading locations were selected, Point A to Point I, as shown in Figure 4.8. The application of both centreline and eccentric loading was designed to enable the three-dimensional response of the bridge to be investigated.
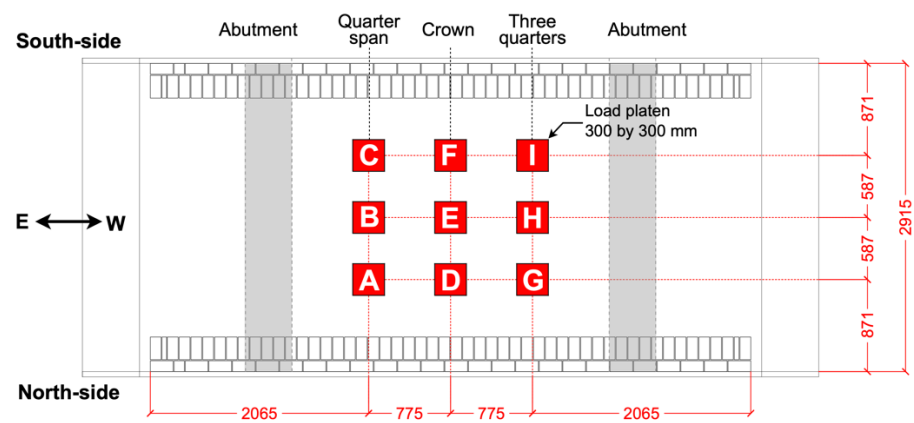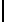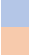
Figure 4.8 Loading locations (all units in mm).

Table 4.1 Loading protocol adopted in the experimental campaign.

	T1	T2	T3	T4	T5	T6	T7	T8	T9	T10	T11	T12	T13	T14	T15	T16	T17	T18	T19	T20
A	LS						LS	LC					MS	MC						
B		LS						LS	LC										MS	MC
C			LS	LC													MS	MC		
D				LS	LC									MS	MC					
E					LS	LC												MS	MC	
F						LS	LC									MS	MC			
G									LS	LC		MS	MC							
H											LS	LC							MS	MC
I												LS	LC			MS	MC			

Testing sequence →

Legend:
- Low-level static (150 kN)
- Low-level cyclic (150 kN)
- Mid-level static (250 kN)
- Mid-level cyclic (250 kN)

Loads with increasing magnitudes were applied to investigate the behaviour of the bridge when subject to increasing levels of damage, with results when low- and mid-level loads were applied reported in the present chapter. The loading protocol is shown in Table 4.1.

Prior to conducting tests, a preliminary numerical simulation suggested that the load-carrying capacity of the masonry arch bridge was between 620 and 680 kN (ultimate limit state, ULS). Thus, a low-level loading magnitude of 150 kN was adopted, approximately 22-25% of the peak load that the bridge was expected to carry, to assess the elastic behaviour and the initial stiffness of the bridge. A mid-level load magnitude of 250 kN was adopted (approaching 50% of the expected ULS load), which is generally considered to be a 'safe' working load according to the National Highways' design code [148].

The first two tests (T1 and T2) served as a trial to check the proper functioning of the loading and instrumentation systems, with a static load applied at points A and B. From Test 3 onwards, a static load with the target magnitude was first applied, followed by three loading cycles of the same magnitude and loading rate, herein termed 'cyclic loading'. The latter loading was applied to more fully investigate the inelastic performance of the bridge. Notably, a minimum interval of half an hour was implemented between the static and cyclic loading tests to enable the system to reach an equilibrium point. The tests under the low loading level were carried out from Point A to Point I, in alphabetical order. Only a single short reaction beam and mounted actuator needed to be moved to change the loading location. However, for the mid-level tests, it was necessary to move all the short reaction frame beams transversely to provide increased reaction frame stiffness. Therefore, the loading sequence was adjusted accordingly to reduce the time spent moving the short beams. Thus, loads were firstly applied at points A, G, and D near the north side wall. Subsequently, all short beams and the actuator were moved to the south side, with the loads applied at points F, C, and I. Finally, the short beams and the actuator were moved to the centreline, with the loads applied at points E, H, and B. Note that for both the static and cyclic load tests conducted at low and mid-levels, load control was employed, with the loading and unloading rate set at a constant value of 10 kN/min.

4.4 Material characterisation

A high compressive strength/low water absorption fired clay brick (referred to as a Class A engineering brick) was selected as the masonry unit. The Class A brick, nominally 215 mm in length × 102.5 mm in width × 63 mm in height, had a measured density of 2,470 kg/m³. A low-strength type O mortar, with a mix proportion of 1:2:9 (cement:lime:sand by volume), was selected as the bonding material [58]. The adoption of these materials

was designed to reproduce the low-bond strength characteristics found in many bridges in the field [149,150]. Note that the same materials have been used in previous large-scale laboratory experiments performed on masonry arches/arch bridges (e.g., see [34,36], therefore providing a degree of comparability between tests.
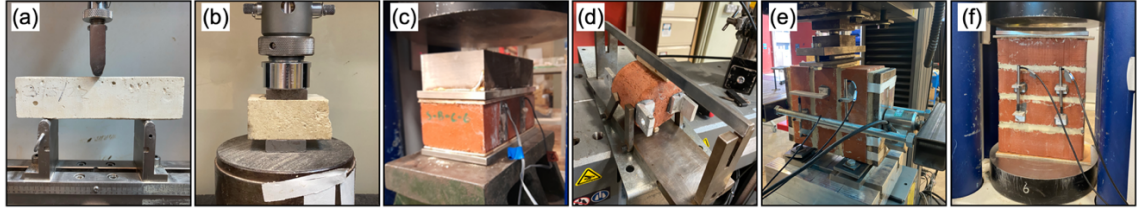
Figure 4.9 Material characterisation: (a) three-point bending tests on mortar prisms; (b) compression tests on mortar cubes; (c) compression tests on bricks; (d) Brazilian tests on cylindrical brick specimens; (e) triplet shear tests; (f) compression tests on masonry prisms.

Figure 4.9 shows a series of small-scale laboratory tests that were performed to characterise the material and mechanical properties of the bricks, mortar, and resulting masonry. It should be noted that all the masonry specimens (i.e., triplets, full couplets, and prisms) were constructed at the same time as the construction of the masonry arch bridge, and testing of these small-scale specimens was carried at around the same time as the bridge was tested to failure. In other words, the curing time for the bridge and the small specimens were similar, at approximately 360 days, ensuring a better indication of the strength characteristics of the material used.

Specifically, three-point bending and compression tests (Figure 4.9 (a) and (b)) were carried out on mortar specimens to characterise its flexural strength ($f_{b,j}$), compressive strength ($f_{c,j}$), and Young's modulus (E_j) [63]. Compression tests on full bricks (Figure 4.9 (c)) and Brazilian tests on brick cylinders (Figure 4.9 (d)) were conducted to determine the compressive strength ($f_{c,u}$), Young's modulus (E_u), and tensile strength ($f_{t,u}$) of the Class A engineering brick [54]. Shear tests were performed on masonry triplet specimens (Figure 4.9 (e)) with different levels of axial compression, i.e., 0.1, 0.2, and 0.6 MPa, to determine the friction angle (φ_i) and cohesion (C_i) at the unit-mortar interface [75]. Compression tests (Figure 4.9 (f)) were conducted on stack-bonded masonry prisms to characterise the compressive strength ($f_{c,m}$) and Young's modulus of masonry, respectively. The experimental results in terms of mean values, CVs, and the number of tests performed are shown in Table 4.2.

Moreover, MOT type I graded crushed limestone was used as the backfill material. For the masonry arch bridge, approximately 30,057 kg of limestone was filled into a space of

13.98 m³. Therefore, the bulk density of the limestone was around 2,150 kg/m³. In addition, by performing a series of large-scale shear box tests, the friction angle of the limestone used was determined to be equal to 47.8 degrees, assuming a zero-cohesion. Further details of the experimental design, along with interpretation of the shear box test results, are provided in [151].

Table 4.2 Material and mechanical properties of bricks, mortar, masonry, and the backfill material.

Properties	Units	No. of tests	Mean values	CV
Compressive strength of brick, $f_{c,u}$	MPa	9	111.3	6.2%
Young's modulus of brick, E_u	MPa	9	31762	15.7%
Tensile strength of brick, $f_{t,u}$	MPa	9	6.730	13.5%
Brick density, ρ_u	kg/m³	9	2470	1.3%
Flexural strength of mortar, $f_{b,j}$	MPa	20	0.627	20.9%
Compressive strength of mortar, $f_{c,j}$	MPa	40	1.736	25.7%
Young's modulus of mortar, E_j	MPa	40	128.6	35.3%
Mortar density, ρ_j	kg/m³	20	1680	2.3%
Friction angle at brick-to-mortar interface, φ_i	Degree	3	44.9	-
Cohesion at brick-to-mortar interface, C_i	MPa	3	0.40	-
Compressive strength of masonry, $f_{c,m}$	MPa	3	30.84	24.2%
Young's modulus of masonry, E_m	MPa	3	10128	48.4%
Internal friction angle of limestone, φ	Degree	6	47.8	-
Limestone density (bulk), ρ_b	kg/m³	-	2150	-

4.5 Test results

4.5.1 Damage evolution

After each load test on the bridge, cracks were visually inspected and accurately mapped. Figure 4.10 shows the mapped crack evolution on three exposed surfaces of the masonry arch bridge, namely the arch intrados, the north-side, and the south-side spandrel walls.

In Figure 4.10, the low- and mid-level testing was divided into four stages. Cracks that formed in previous tests are presented in grey, whereas newly formed cracks occurring in different tests are mapped and distinguished using different colours. Figure 4.11 shows a selection of observed cracks.

No cracks were observed during the first three load tests conducted at points A, B, and C (located above the quarter span). This could be resulted from: a) at the quarter-span location, the backfill was deeper than at the arch crown, allowing for better load distribution over the arch; and b) The quarter-span locations were closer to the arch supports, providing greater bending resistance compared to mid-span locations. However, when a static load was applied at point D (T4), at the mid-span of the arch and close to the north-side spandrel wall, the first crack was observed (Figure 4.11 (a)). This crack extended approximately 1760 mm, spanning from courses 15 to 36, between the spandrel and the arch ring. At the peak load, the width of this crack was measured to be 1.0 mm, reducing to 0.5 mm once the load was removed. Figure 4.12 presents the load-deflection curves obtained from two rows of LVDTs positioned near the north-side face. From the data obtained at location L27, at the mid-span edge of the arch, an inflexion point appeared when the load increased to approximately 60 kN, suggesting the crack initiated then. Similar behaviour was observed when the load was applied at point F, i.e., separation between the south-side spandrel wall and the arch ring was developed. After the initiation of the two cracks, any subsequent off-centre loading resulted in the propagation of these cracks, as shown in Figure 4.10 (a) and Figure 4.11 (b). Moreover, after the low-level testing, it was observed that the arch ring and spandrel wall became separated from courses 7 to 42 on the north-side, while the crack length on the south-side was shorter, extending from courses 13 to 35.

The first stage of mid-level load testing started from Point G (T12), including three loading locations near the north-side spandrel wall (i.e. G, A, and D). After the static test at Point G, tensile cracks were observed at the arch intrados, at the location underneath the load platen (Figure 4.10 (b) and Figure 4.11 (c)). This tensile crack did not extend to the south-side but stopped at approximately three-quarters of the arch width. In addition to the opening at the arch intrados, the separation between the spandrel wall and the arch barrel propagated approximately 130 mm further on the right side of the arch. Subsequently, the three loading cycles applied at Point G led to the initiation of a diagonal crack on the spandrel wall, which originated from the three-quarter span and extended

upwards (Figure 4.11 (d)). Applying the load at Point A (T13, quarter-span) resulted in: (a) opening of a crack in the arch intrados under the load platen (initiated at a load level of approximately 160 kN); (b) propagation of separation between the arch and spandrel wall; and (c) occurrence of a diagonal crack in the spandrel wall. Following these two tests, the application of loads at the mid-span (T14, point D) did not trigger any visible damage to the bridge. Moreover, loading eccentrically at the north-side did not initiate any damage/cracking to the south-side spandrel wall.
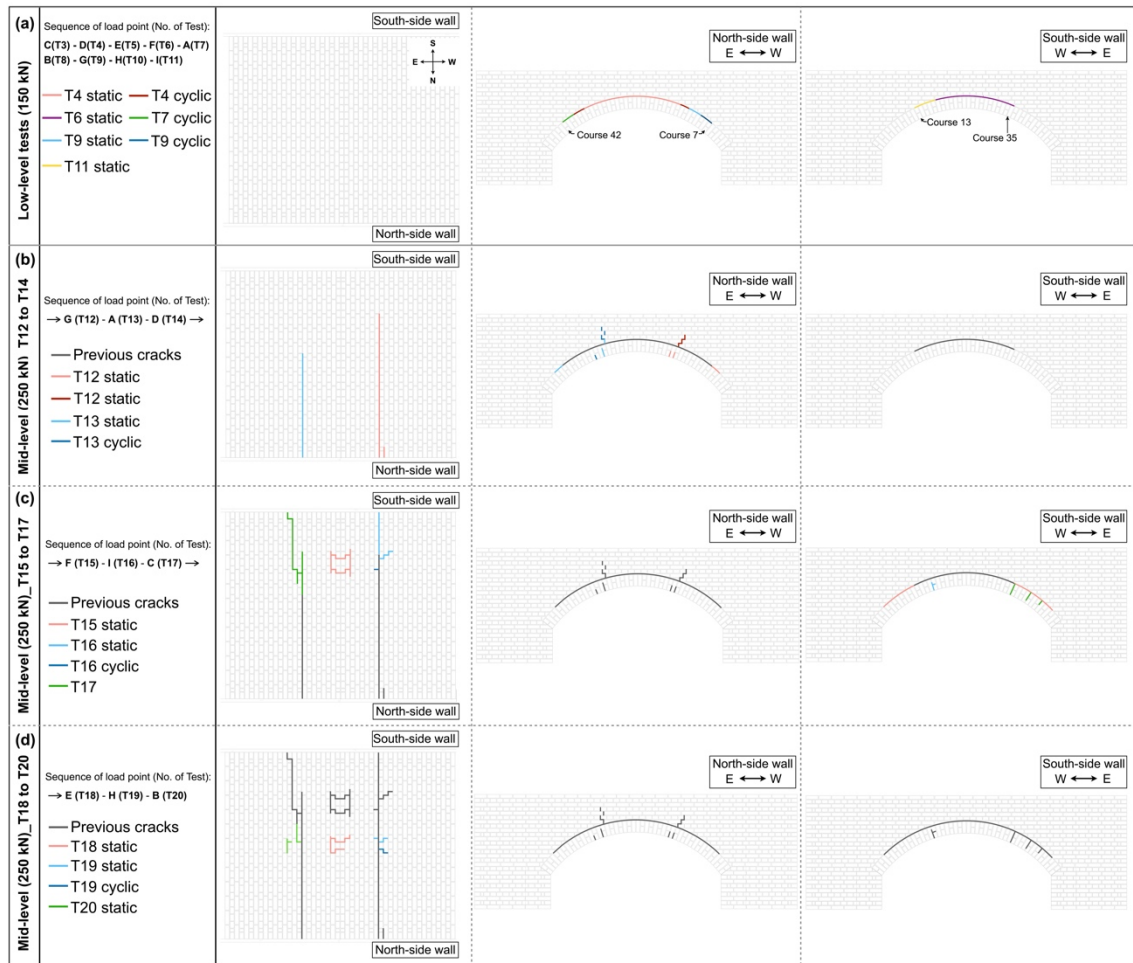
Figure 4.10 Crack evolution under low- and mid-level testing. (a) Low-level testing; (b) T12 to T14 at mid-level; (c) T15 to T17 at mid-level; and (d) T18 to T20 at mid-level.

During the second stage of the mid-level testing, the static/cyclic loads were sequentially applied at Point F, I, and C, the three locations near the south-side spandrel wall. In this case, when static loading was applied at the mid-span, cracks forming a square-shape were observed at the arch intrados along the mortar joints, directly beneath the loading location (Figure 4.11 (e)). This square-shaped crack had similar dimensions to the cross-sectional area of the load platen, measuring approximately 300 by 300 mm (Figure 4.10 (c)). The presence of this localized damage indicates the occurrence of shear failure at

the mortar joints under loading. Also, separation between the arch and south-side spandrel wall propagated extensively on both the right and left sides, and the length of the extended crack was similar to that of the crack observed on the north-side. Subsequently, when loading was applied at the quarter- and three-quarter span points, the previous tensile cracks at the arch intrados extended towards the south-side along the bed joints (Figure 4.11 (f)), and also diagonal cracks developed at the arch intrados under the loading position (Figure 4.10 (c)). Notably, no cracking was observed at the south-side spandrel wall, which may be due to the fact that the more extensive cracks developing in the arch intrados absorbed more energy.

In the final stage of mid-level load tests, loading was applied along the longitudinal centre line of the bridge, starting from Point E, followed by point H and point B, as illustrated in Figure 4.10 (d). Applying loads at mid-span (T18) again resulted in shear cracks developing at the arch intrados beneath the load platen (Figure 4.11 (g)). Subsequently, when loads were applied at the quarter- and three-quarter span points, new cracks developed in the arch intrados under the applied loading. In T19, application of the cyclic loading led to the cracks propagating (Figure 4.11 (h)). Moreover, loading along the longitudinal centreline of the bridge did not cause any observable damage to the spandrel walls, suggesting only localized damage to the bridge occurred under the applied patch loads.
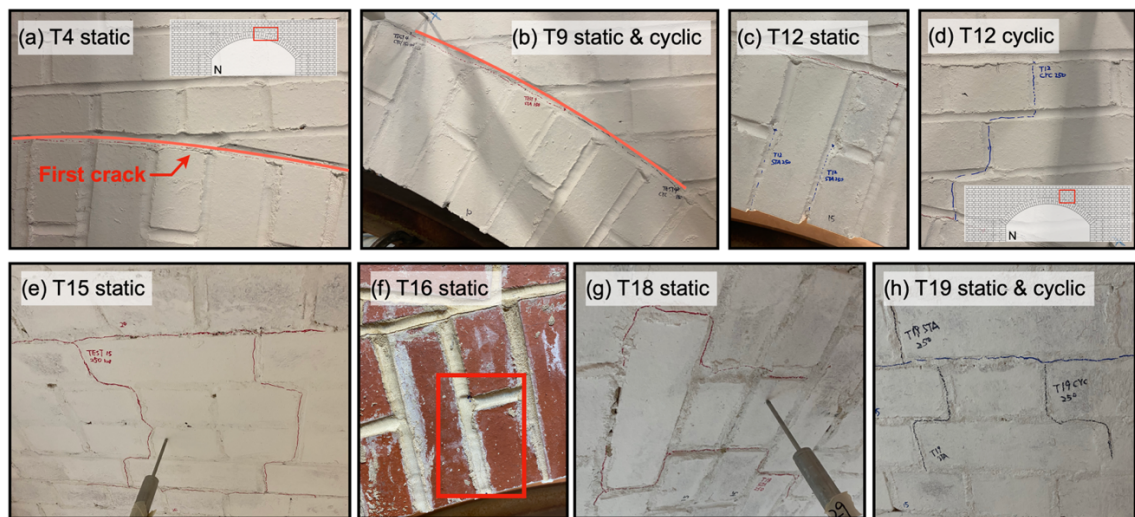
Figure 4.11 Observed cracks after the tests.
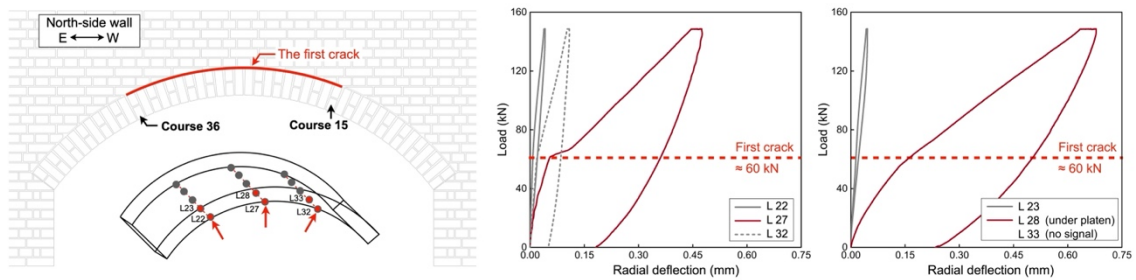
Figure 4.12 The occurrence of the first crack and the corresponding load-deflection curves (T4 at point D).

4.5.2   Stiffness characteristics of the bridge

Figure 4.13 shows plots of load vs radial deflection of the arch intrados, together with the measured stiffness obtained from static loading tests; these were obtained from the LVDT positioned directly under the loading location. The value of stiffness (S) was determined by calculating the slope of the load-radial deflection curve within the 10% to 40% peak load interval. Under the low-level testing, cracks primarily developed at the interfaces between the arch ring and spandrel walls. Figure 4.13 (a) indicates that, apart from the test at Point D, no significant change in stiffness was found from the other eight tests during the loading process. In other words, the bridge behaved in an essentially elastic manner under low-level loading. The maximum value of peak radial deflection (D_p) recorded was equal to 0.679 mm from test 4 (loading at point D). Also, when the load was applied at the mid-span, the value of D_p was approximately twice as high as that when the load was applied at the quarter- and three-quarter span points. On the other hand, in all nine tests undertaken using low level loads, some residual deflection (D_r) was detected, albeit this was small in magnitude. More specifically, when a static load was applied over the quarter- and three-quarter span points, the maximum value of D_r was 0.10 mm, and the average ratio between D_r and D_p was 19.7%. Loading at the mid-span resulted in the average ratio between D_r and D_p increasing to 30%, with the maximum value of D_r increasing to 0.23 mm. The presence of residual deformation does not necessarily indicate that the bridge moved into the plastic behaviour phase, involving activation of the backfill; instead, it can be attributed to localized plastic deformation occurring in the arch barrel in the region of the load and also the potential plastic deformations developing in the backfill. In fact, the bridge overall appeared to remain in the elastic phase. For instance, taking T4 with loading at point D as an example, which had the largest D_r, after the static load was removed, only the four points surrounding the loading area recorded residual deformations of the arch barrel greater than 0.05 mm (Figure 4.14).

106

In Figure 4.13 (b) the variation in stiffness over the course of the low-level loading test sequence is presented. When the loads were located at mid-span, the stiffness was observed to be lower than when the loads were located at the quarter- and three-quarter-span points. This can be attributed to the shallower backfill depth above the crown of the arch, leading to more concentrated loading being applied to the arch barrel. This in turn led to greater elastic deformation of the arch barrel. Of the six tests conducted with loading at the quarter- and three-quarter span points, the value of S was observed to be slightly lower in later tests (note: the linear fit of the stiffness values did not consider the mid-span tests), likely resulting from progressive propagation of the cracks between the arch ring and spandrel walls.

Figure 4.13 (c) and (d) show the load-radial deflection curves and stiffness variations under the mid-level loads. As observed in the low-level tests, loading at the mid-span resulted in larger values of D_p compared to loading at the quarter- and three-quarter span points. The maximum value of D_p measured was equal to 1.377 mm. Regarding the stiffness characteristics, as the load increased from 150 kN to 250 kN, the value of S decreased significantly at all nine locations. This reduction in stiffness was less pronounced at the mid-span loading cases compared to loading at the quarter- and three-quarter span points, as the later cases led to tensile cracks developing in the arch intrados across the arch barrel as well as diagonal cracks in the spandrel walls (Figure 4.10 (b) to (d)). This global damage resulted in significant stiffness degradation. However, loading at the mid-span caused primarily local rather than global damage, which had less impact on bridge stiffness. Moreover, throughout the testing sequence under the mid-level loading, the degradation in stiffness became more significant, suggesting that damage accumulated during the loading sequence (note that the linear fit of the stiffness values in Figure 4.13 (d) did not account for the mid-span tests).
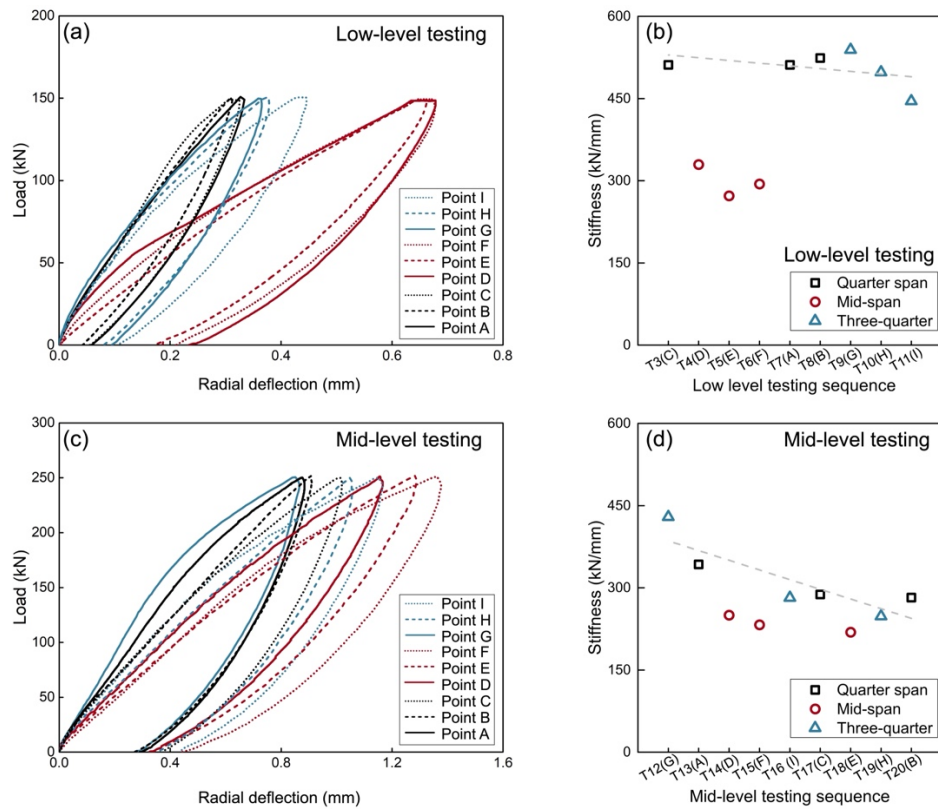
Figure 4.13 Load-peak deflection curve of the arch intrados under (a) low level and (c) mid-level static testing; Stiffness variation with the static testing sequence under (b) low level and (d) mid-level testing.
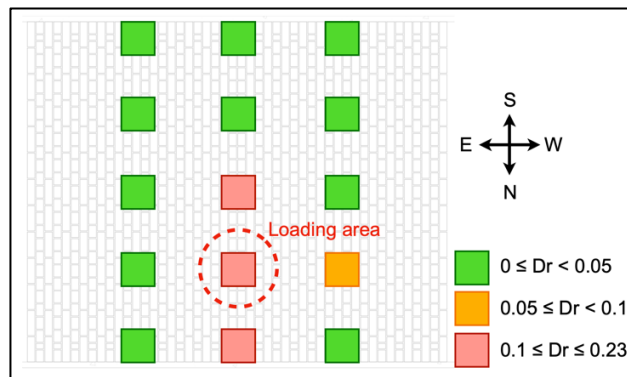
Figure 4.14 Residual deformation of the arch barrel for the low-level loading test at point D (unit: mm).

4.5.3 Deformation characteristics of the arch barrel

Figure 4.15 compares the radial deflection of the arch barrel under low- and mid-level loading magnitudes. The data was obtained from the LVDT placed underneath the loading platen, as well as the two LVDTs placed at the same transverse cross-section of the arch. When the patch load was applied at quarter- and three-quarter-span points, the bridge exhibited similar behaviour, i.e., the arch underneath the loading platen moved downwards, the opposite location moved upwards, and the crown of the arch moved

slightly downwards. On the other hand, when the patch load was applied at the mid-span, the arch crown moved downwards, while the deformation at the quarter- and three-quarter span points was minimal.
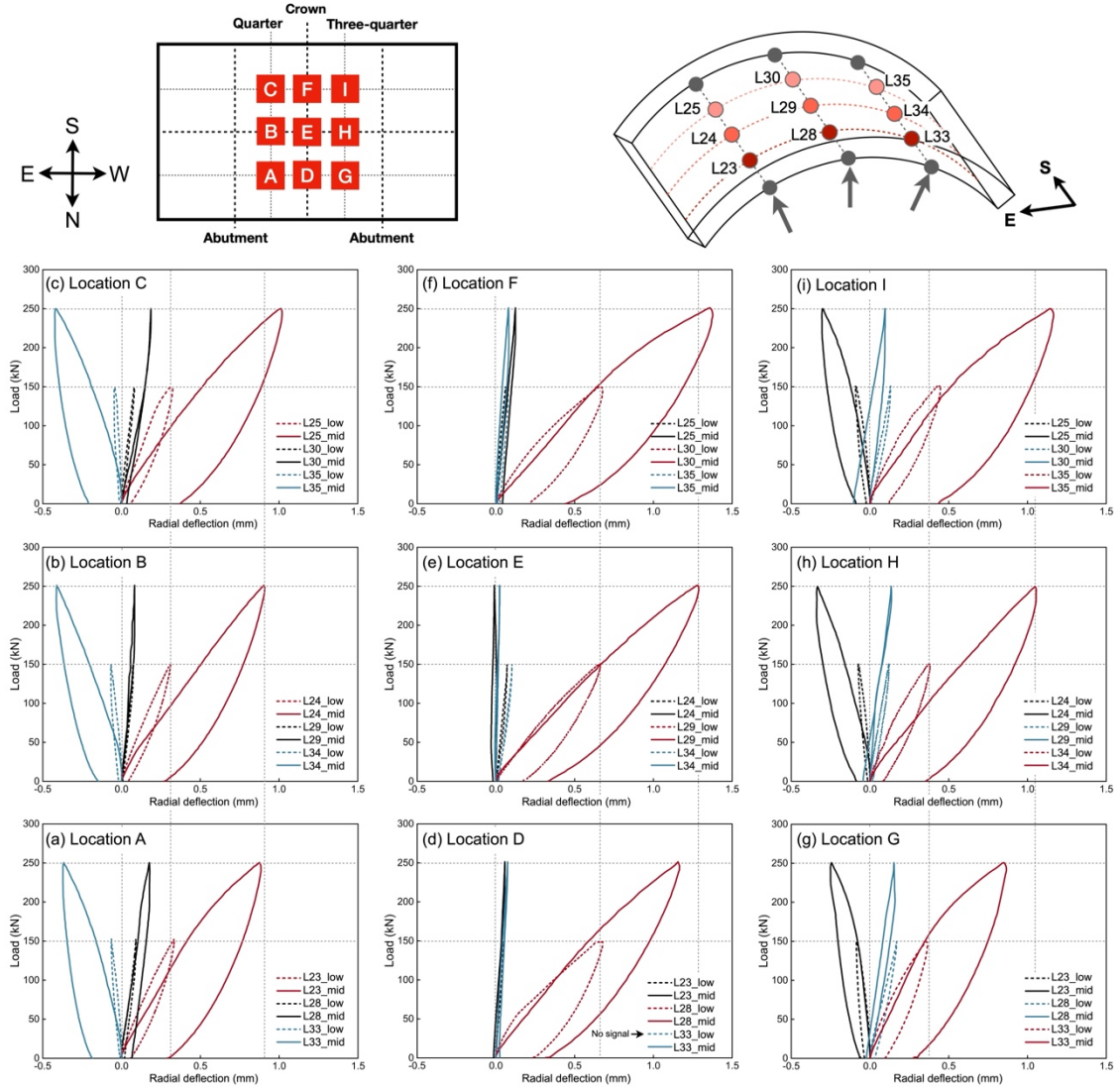
Figure 4.15 Load-radial deflection curves of the arch barrel from three LVDTs from the same cross sections under low and mid-level loading.

Another observation is that loading at the quarter- and three-quarter span points resulted in a near symmetrical response along the transverse centreline in terms of both the peak deformation values and arch barrel deformed shapes (Figure 4.15 (a), (b), (c) and (g), (h), (i)). In particular, under the low-level static loads, D_p of the arch ranged from 0.309 mm to 0.43 mm, which increased to 0.851 mm to 1.148 mm when the load increased to 250 kN. On the other hand, when the patch loading was applied symmetrically along the longitudinal centreline, the response of the bridge was not strictly symmetrical. This was demonstrated by the fact that the south-side eccentric

patch loading always induced larger deformations of the arch barrel compared to cases involving loading at the north-side (Figure 4.15 (c), (f), (i) and (a), (d), (g)). The reason for this unsymmetrical behaviour may be attributed to various factors, such as the inherent variability of masonry properties, slight asymmetry of the structural geometry, and the influence of loading sequence, which in this particular case appears most significant.

In terms of the peak radial deflection, loading at the mid-span resulted in a greater peak deflection of the arch compared to loading at the quarter- and three-quarter span points. For instance, when a load of 150 kN was applied at the mid-span, D_p of the arch was found to be 1.87 times larger than that when loading was applied at the quarter- and three-quarter span points. When the loading magnitude was increased to 250 kN, deflection of the arch significantly marked. Nevertheless, it is noteworthy that the increase in D_p was more pronounced in the cases with loading at the quarter- and three-quarter span points compared to cases involving mid-span loading. This phenomenon can be attributed to the cracking behaviour and structural mechanism of the arch barrel. Specifically, at the mid-span, an increase in the load from 150 kN to 250 kN did not cause significant global damage to the bridge. However, when loading applied at the quarter- and three-quarter span points was increased from 150 kN to 250 kN, tensile cracks initiated at the arch intrados, forming the first hinge. Conversely, although the shallower depth of backfill over the crown resulted in more concentrated loading being applied to the arch barrel when the load was applied at this location, this could be more effectively distributed through the arch barrel. This contributed to the lesser increase in deformation of the arch when the load was applied at the mid-span.

Figure 4.16 and Figure 4.17 show the deformed shape of the arch barrel at the peak load of 150 kN and 250 kN (static testing), respectively. A 3D response can be observed from the two groups of figures, in which an eccentric applied loading always caused positions close to the loading point to have a larger deformation. The deformation of the arch decreased as the monitoring position became further away from the loading point.
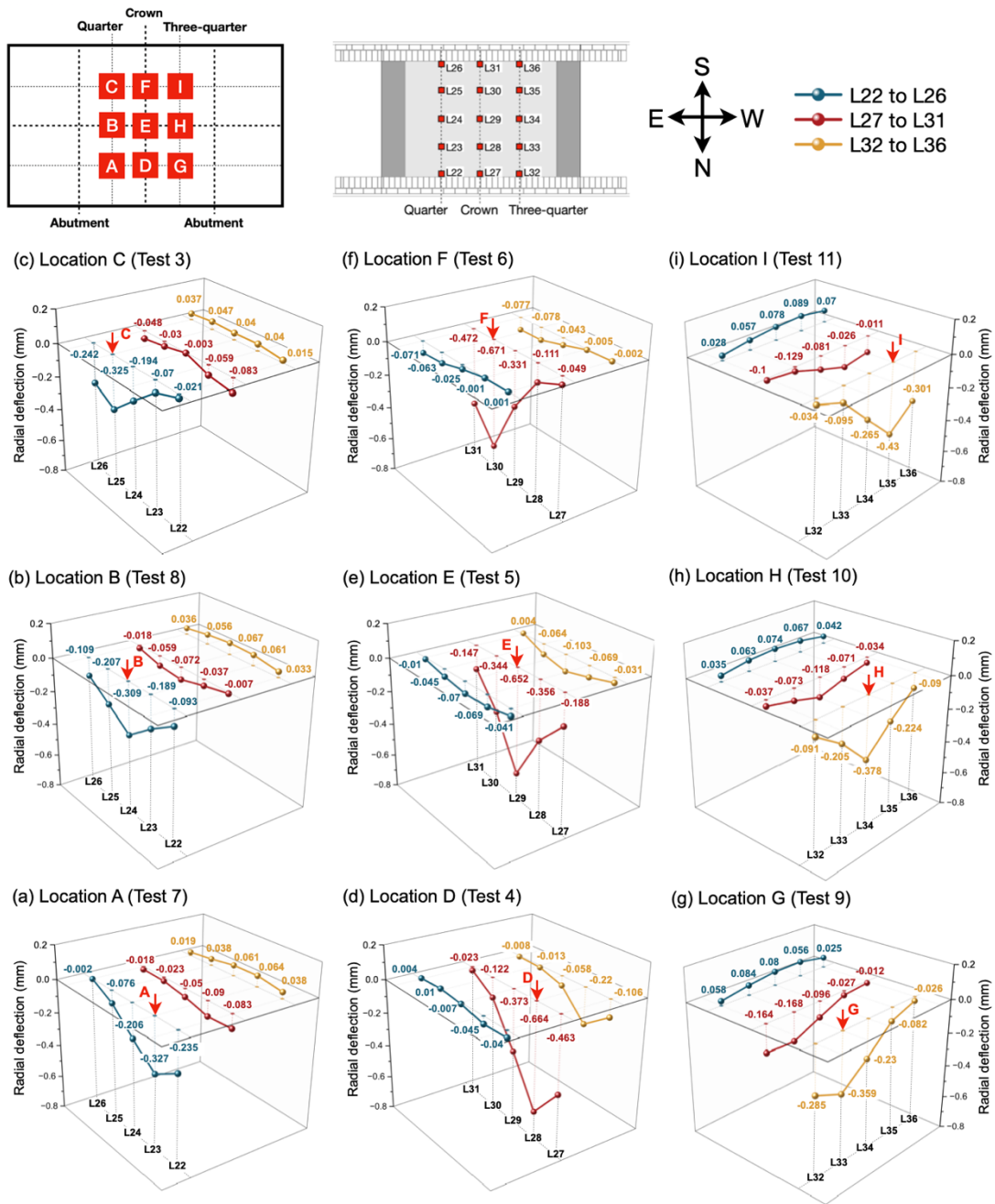
Figure 4.16 The peak values of radial deflection of the arch under the low-level static tests (150kN): (a) to (i) at nine loading locations.
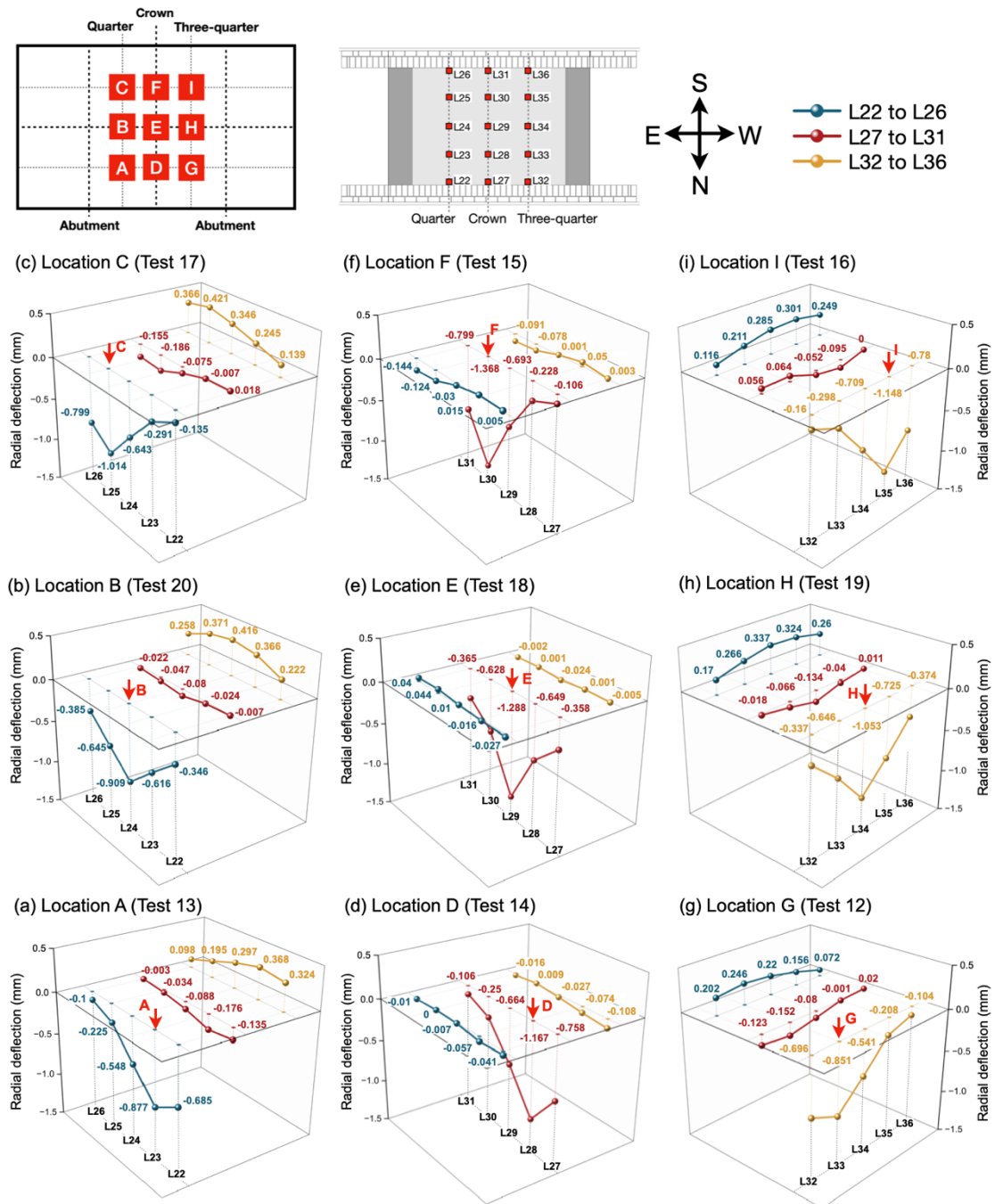
Figure 4.17 The peak values of radial deflection of the arch under the mid-level static tests (250kN): (a) to (i) at nine loading locations.

Figure 4.18 (a) shows a plot of load vs radial deflection of the arch intrados when subjected to the mid-level static and cyclic loading at point A. Similar response characteristics were observed in the other cases. Notably, the cyclic loading tests were not conducted immediately after the static loading test. There was at least a 30-min gap between them to bring the system to an equilibrium point under gravity. For the curves plotted in Figure 4.18 (a), both the static load-deflection curve and the first cyclic load-deflection curve started from 0. However, it doesn't mean that the residual deflection

under the static load was recovered. Instead, the data of static and cyclic loading tests were processed independently. The area enclosed by the loading-unloading curve provides an indicator of the energy (G) absorbed by the structural system during the testing process [152] (it should be noted that G here is not the fracture energy dissipated). This energy absorption corresponds to various phenomena, such as the development of plastic deformations, damage (i.e. initiation and propagation of cracks), as well as compaction / rearrangement of the backfill material. A value of zero G indicates that behaviour is perfectly elastic, with no energy dissipated. The variation in G for the static and cyclic tests, under low- and mid-level loading magnitudes, is presented in Figure 4.18 (b) and (c), respectively.
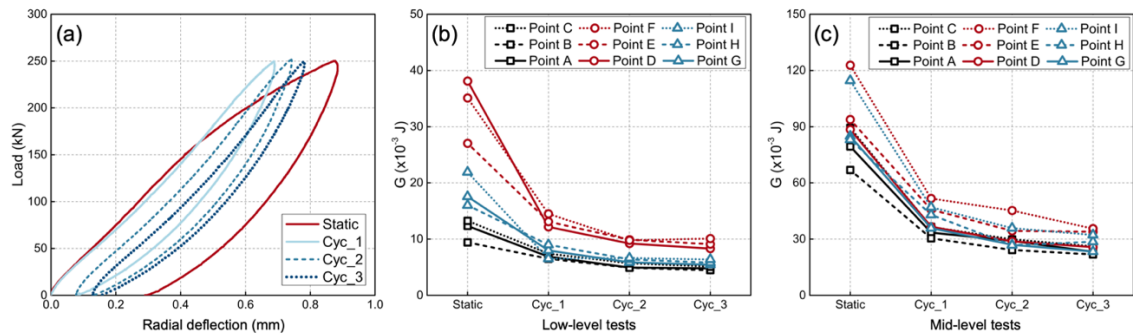
Figure 4.18 (a) Load-radial deflection curves of the arch intrados under static loads and three loading cycles: Point A at mid-level; energy absorbed for the static test and three loading cycles under the (b) low-level testing and (c) mid-level testing.

For the static tests, it was observed that when the load was increased from 150 kN to 250 kN, an increase of 66.7%, the dissipated energy increased significantly, by an average of 492% for cases where loading applied at the quarter- and three-quarter span points, and 210% for cases involving loading at the mid-span (Figure 4.18 (b) and (c)). This significant increase in G is indicative of the progression of damage in the bridge under the mid-level loading. The increment in G was observed to be larger when the load was applied at the quarter- and three-quarter span points, compared to when this was applied at the mid-span. This can be attributed both to the larger volume of backfill present above the arch at the quarter-and three-quarter span points, prone to deform inelastically under load, and the more global nature of the damage observed in the masonry when the load was applied at these locations (e.g. involving formation of tensile cracks in the arch barrel). Moreover, Figure 4.18 (b) and (c) indicate that G progressively decreases in magnitude between the static test and the subsequent three loading cycles. Specifically, at the low-level of load, the value of G derived from Cyc_1 was approximately half that obtained in the corresponding static test. As the number of cycles increased from one to

three, G further decreased by approximately 28% (Figure 4.18 (b)). This decrease was even more pronounced in the mid-level testing (Figure 4.18 (c)). For instance, the value of G dropped by more than 56% between the static test and Cyc_1, followed by a 30% decrease between Cyc_1 to Cyc_3.

The peak and residual values of the arch deflection under cyclic loads can provide insights into the backfill conditions. Figure 4.19 presents the variation of normalized peak and residual deflections of the arch barrel at the location directly under the loading points. The data was normalized by dividing the maximum deflection (at peak load) and residual deflection (after the load removal) from the three loading cycles by the respective values obtained in the corresponding static test. The residual deflection from the three loading cycles gradually decreased over time. It was also significantly smaller than the deflection observed in the corresponding static test. Also, the value of normalised residual deflection approached to zero at the final loading cycle. The higher energy associated with the static test was partly absorbed by the backfill, resulting in increasing density of the crushed limestone fill material. With the application of the following three loading cycles, the limestone became progressively more highly compacted. Together Figure 4.18 (a), (b) and Figure 4.19 indicate that as the number of loading cycles increased, the bridge behaved in a manner that the existing cracks repeatedly opened and closed during the loading-unloading process after the cracks were fully activated.
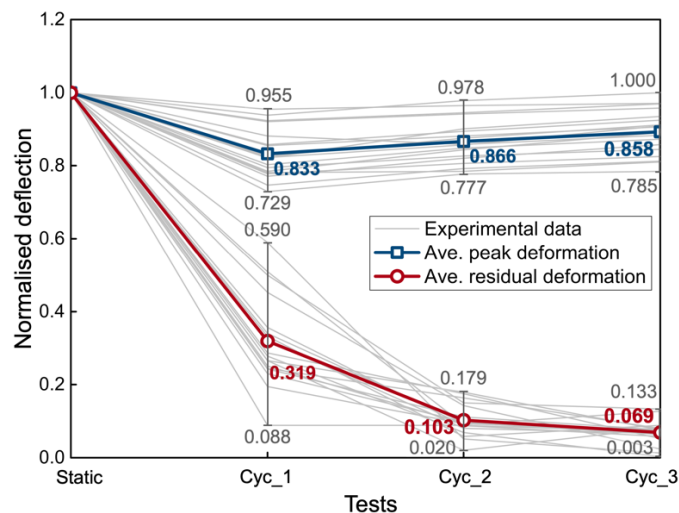
Figure 4.19 Normalized peak and residual deflections of the arch barrel at the location directly under the loading points obtained from the static test and the subsequent three loading cycles.

4.5.4 Out-of-plane deformation of spandrel walls

From field studies [153], it has been observed that the mechanical response of spandrel walls can affect the overall mode of response and the load carrying capacity of a masonry arch bridge. In particular, under the action of active lateral soil pressures, spandrel walls may translate in an out-of-plane direction, relative to the arch barrel. Note that in the present tests, the ends of the spandrel walls were not physically attached to the RC walls; instead, soft polystyrene plates were placed between the RC walls and the spandrel walls, such that the ends of spandrel walls were effectively unrestrained, apart from the effects of backfill. During the low and mid-level tests, no significant in-plane movement of the spandrel wall was observed, though small out-of-plane deformations were observed.
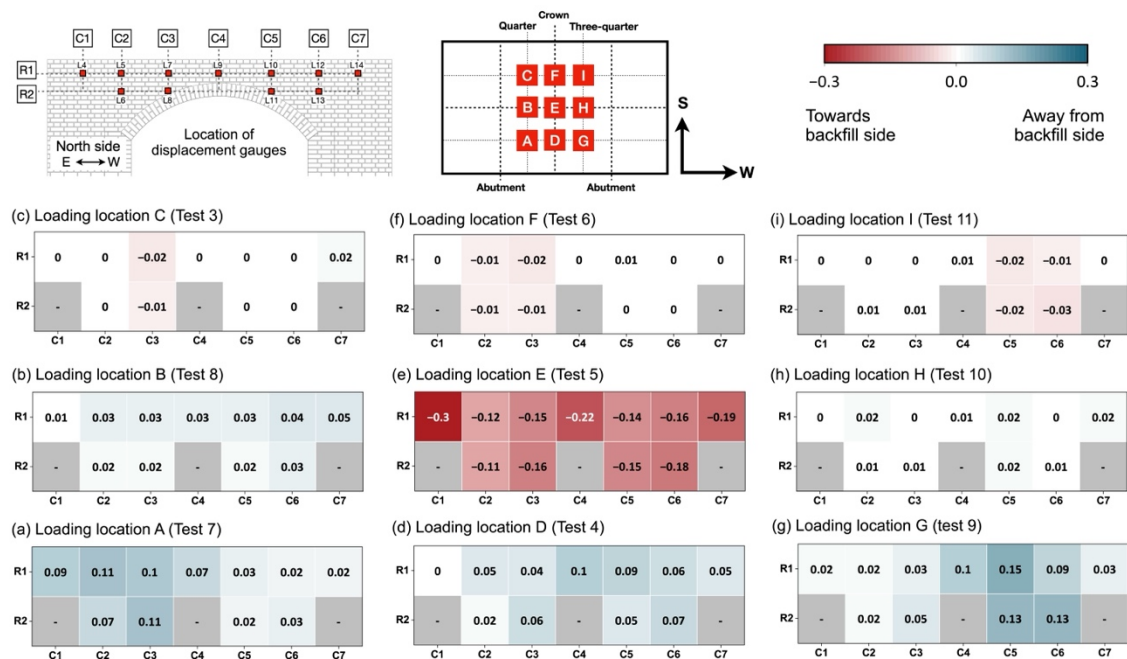
Figure 4.20 Peak values for the out-of-plane deformation of the north-side spandrel wall under the low-level testing.
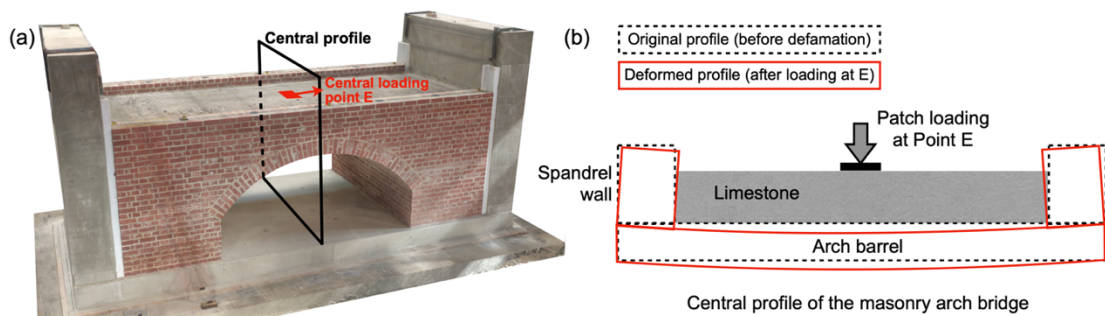
Figure 4.21 Deformation mechanism of the masonry arch bridge at Test 5.

Figure 4.20 and Figure 4.22 show the peak values of the out-of-plane deformation

115

obtained from the displacement gauges placed perpendicular to the north-side spandrel wall under the low and mid-level loads, respectively. Negative values represent inward movement, towards the fill. During the low-level tests, when the loads were applied eccentrically, and close to the south-side spandrel wall, the out-of-plane deformation observed from the north-side wall was minimal, and the maximum value detected was just 0.03 mm (Figure 4.20 (c), (f), and (i)). Similarly, applying the load on the longitudinal centreline, over the quarter- and three-quarter span points, did not cause any significant out-of-plane deformation of the north spandrel wall (Figure 4.20 (b) and (h)). Nevertheless, when the load was applied on the bridge centreline at mid-span, at point E (Test 5), some inward deformation of the spandrel walls was detected, with a maximum value of -0.3 mm (negative means inward movement, towards the backfill) near the end of the wall at the east-side (Figure 4.20 (e)). Figure 4.21 shows the deformation characteristics of the arch barrel and spandrel walls at Test 5. Specifically, under the low-level loading magnitude, the bridge was observed to deform essentially elastically. Downward movement of the centre of the arch under the patch loading led to a slight upward deflection of the two sides of the arch, which further induced inward movement of the spandrel walls as indicated in Figure 4.21 (b). Furthermore, when the load was applied eccentrically near the north-side wall, lateral soil pressures led to some out-of-plane deformation of the north-side wall, with the monitoring point closest to the load location always having the highest reading (Figure 4.20 (a), (d), and (g)). The maximum deformation detected was however relatively small, at 0.15 mm (Figure 4.20 (g)).

The observed out-of-plane deformation characteristics of the north-side spandrel wall from the low-level and mid-level loading tests were similar (Figure 4.22), with e.g. eccentric loading near the south-side not resulting in significant deformation of the north-side spandrel wall. Conversely, when the load was applied near the north-side wall, the maximum out-of-plane deformation of the wall was always observed at the position closest to the loading point. It is notable that the out-of-plane deformation increased nearly threefold when the eccentric load was increased from 150 kN to 250 kN, not only because of the increase in lateral soil pressure, but also a result of the more complete separation of the arch ring and spandrel wall that occurred during the low-level testing. The detachment will have led to a significant reduction in the shear resistance at the arch-spandrel wall interface as the arch moved downwards, contributing to a significant increase in out-of-plane deformation of the north wall as the loading magnitude was

increased. The maximum out-of-plane deformation, of 0.43 mm, was detected in Test 12, with the loading applied at point G (Figure 4.22 (g)).
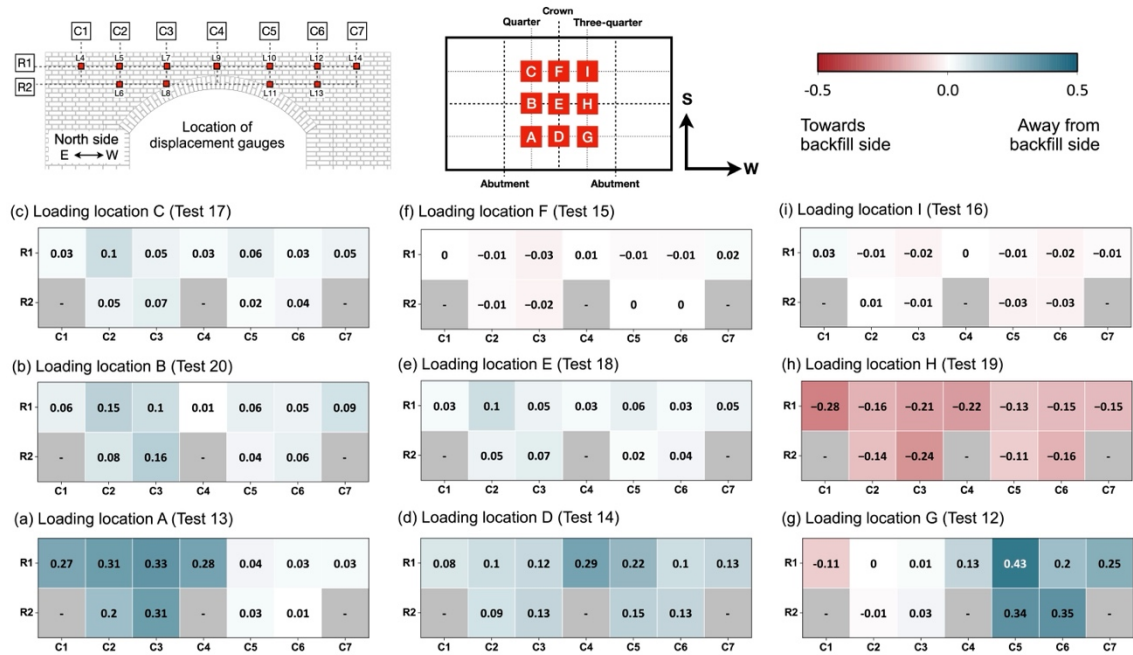
Figure 4.22 Peak values for the out-of-plane deformation of the north-side spandrel wall under the mid-level testing.

4.6 Conclusions

This chapter presents results from load tests performed on a large-scale brickwork masonry arch bridge, tested under laboratory conditions. The primary focus of the study was to assess the three-dimensional response of the bridge under low- and mid-level loads. The bridge had a span of 3m and was constructed from brickwork with weak (Type O) mortar, comprising a single-ring arch barrel, abutments and spandrel walls. Following erection of the brickwork, the bridge was filled in layers with compacted crushed limestone fill material. Patch loads were applied at nine specific locations on the backfill surface over a 300 by 300 mm. Two levels of loading were applied, namely low-level loading with a magnitude of 150 kN, designed to evaluate the elastic response of the bridge, and mid-level loading with a magnitude of 250 kN, designed to assess any stiffness degradation due to crack propagation of the bridge. The application of a load in sequence allowed damage accumulation in the bridge to be investigated. A total of 18 static tests and 18 cyclic loading tests were performed, giving rise to the following conclusions:

1. The first crack occurred between the arch barrel and a spandrel wall when a low-level

eccentric load (of 60 kN) was applied at mid-span near one of the spandrel walls. This crack propagated further when loading was applied close to the spandrel wall at the quarter- and three-quarter span points. In the mid-level load tests, the application of load near a spandrel wall at the quarter- and three-quarter span points not only caused formation of tensile cracks in the arch barrel (the first tensile crack was visible on the arch intrados at a load of approx. 160 kN), but also led to diagonal cracking of the spandrel wall. Moreover, applying mid-level loads at mid-span resulted in the occurrence of local failure, with square-shaped shear cracks observed in the arch intrados directly under the load.

2. With the same loading magnitude, the mid-span loading condition led to greater measured deformation of the arch barrel than when load was applied at the quarter- or three-quarter span points. This was partially due to the shallower depth of backfill over the crown, which allowed a highly concentrated load to be applied to the arch barrel. Additionally, the mid-span locations were farther from the supports (springings) than the quarter- and three-quarter span locations, which may have also contributed to the higher deflection of the arch. Furthermore, eccentrically placed patch loads were observed to induce 3D modes of response in the arch barrel.

3. The stiffness of the bridge decreased slightly following application of the low-level loads, applied at various positions. However, a much greater stiffness degradation was observed following application of the mid-level loads, indicating the occurrence of damage accumulation and some plastic deformation.

4. Analysis of load vs deflection plots indicated that the energy dissipated in an initial static test was almost twice as great as that dissipated in the first loading cycle of a subsequent cyclic load test, for any given loading position under mid-level loads. As the number of loading cycles increased, the energy dissipated progressively decreased. Also, the increase of residual deformation of the arch intrados gradually reduced and approached zero in the third and final loading cycle. This behaviour is related to a) the crushed limestone backfill material progressively becoming more incompressible; and b) cracks that formed under the initial static load later simply opening and closing repeatedly in the later load cycles, without new damage.

5. During the low- and mid-level testing, no noticeable in-plane deformation of the spandrel walls was observed. On the other hand, applying loads near the south-side wall did not induce any significant out-of-plane deformation to the north-side wall.

However, as the loading location moved closer to the north-side wall, out-of-plane deformation of this wall became more pronounced, with the maximum deformation occurring at the position closest to the loading point. Furthermore, increasing the load from 150 kN to 250 kN caused a significant increase in the out-of-plane deformation of the spandrel wall, resulting from a reduction in shear resistance at the arch-spandrel wall interface and the increase in lateral soil pressure acting on the wall.

In summary, the experimental results demonstrated not only the development of early-stage damage in the bridge under loads lower than 'safe' working loads, but also the significant interactions that occur between different components of a masonry arch bridge. Therefore, when seeking to understand the detailed response of a masonry arch bridge it is important to take into account the interactions between the backfill, spandrel walls and arch barrel. Moreover, the detailed response of the bridge (i.e. load-deflection curve and crack pattern) can support the development of both low- and high-fidelity numerical models. A future contribution will focus on the ultimate behaviour of the bridge described, considering load-carrying capacity and the associated mode of failure.

Acknowledgement

5 The 3D Behaviour of a Masonry Arch Bridge at Failure

This chapter represents the slightly modified post-print version of the article: **B. Liu**, V. Sarhosis, A. Booth, M. Gilbert, "The 3D response of a large-scale masonry arch bridge - Part II: performance at failure", Engineering Structures, 313 (2024) p. 118308. The formatting and numbering of equations, tables and figures have been adapted to this document.

5.1 Abstract

Masonry arch bridges continue to form a pivotal part of the transport networks of the UK and many other countries worldwide. However, their three-dimensional response (3D) under loading has to date been relatively little investigated. Here, details of a large-scale masonry arch bridge load tested to failure under laboratory conditions are presented. The bridge consisted of a brickwork arch barrel, abutments, spandrel walls, and compacted limestone as backfill material. Patch loading was applied to the surface of the backfill at the quarter and three-quarter span points to assess the failure mechanism, load-carrying capacity, and residual strength of the bridge. A range of sensors were employed to capture the 3D bridge response and ground-penetrating radar surveys were performed on both the virgin and load-tested bridge to compare its internal structure. The observed evolution of cracks and post-test deformed geometry demonstrated the presence of both a localised 3D mode of response in the arch barrel in the vicinity of the applied load and a global four-hinge mechanism. Failure-level load tests carried out first at the quarter span and then at the three-quarter span points showed that the load-carrying capacity of the bridge had reduced by only 10% in the second test, though the stiffness of the bridge had decreased by around 35%. During the failure-level load tests, significant in-plane and out-of-plane deformations of the spandrel walls were also observed, adding to the much smaller residual deformations recorded in low- and mid-level load tests.

5.2 Introduction

Masonry arch bridges are generally long-lived structures that continue to form a pivotal part of the transport networks of the UK and many other countries worldwide. However,

increasing demands of the modern traffic systems, coupled with gradual degradation of material properties due to environmental effects and extreme events brought about by climate change, there is a pressing need to assess the structural integrity of these masonry arch bridges to ensure their continued safe operation [10,154].

Over the past few decades, research has focused on determining the mode of response and ultimate load carrying capacity of masonry arches, with various experimental, numerical and analytical methods applied, together with in-situ monitoring methods. For example, model-scale tests have been carried out to identify the likely mode of response of large-scale masonry arches and arch bridges. Specifically, it has been shown that a single ring arch is likely to fail in a four-hinge mechanism when subjected to a point load, with hinge locations dependent upon bridge geometry, loading and boundary conditions [32,155]. In the case of multi-ring brickwork arches, the low shear resistance at the interface between adjacent rings can result in the occurrence of ring separation, reducing load-carrying capacity [37,101]. Most previous studies have been conducted assuming plane-strain conditions. However, to consider the three-dimensional (3D) response of a two-ring brickwork arch barrel, Wang and Melbourne conducted large-scale tests on two large-scale (5m span, 4:1 span-to-rise) arches [156,157]. These arches were subjected to static patch loading, resulting in four-hinge failure mechanisms. Notably, the tests revealed certain 3D modes of response, such as the development of 'fan' type cracks in the arch intrados. Following the experimental tests, Zhang et al. [158] simulated these tests using a mesoscale strategy where a pronounced 3D behaviour was also observed. Further, bridges with skew arches usually show a more complex 3D response [159]. The twisting behaviour resulted from the complex geometry characteristics causes the skew arches showing a lower capacity than the square arches with the same span length and span-to-rise ratio [160]. In addition to laboratory testing, non-invasive tests on in-service bridges have been performed to assess their structural behaviour. Methods include exterior damage assessment by photogrammetry [161−163], internal structure inspection via ground-penetrating radar (GPR) surveys [164−166], and dynamic characteristic identification using forced or ambient vibration measurements [167,168].

A masonry arch bridge comprises various structural components, including the arch barrel, spandrel walls, abutments, and backfill material. These components interact with each other when a load is applied to the surface of a bridge, influencing the failure mechanism and bridge load-carrying capacity [112,169]. An early experimental study of

the interaction between different components of a masonry arch bridge was carried out by Royles and Hendry [35]. It was demonstrated that the inclusion of spandrel walls could significantly improve bridge load-carrying capacity (e.g., by approximately 150% for unreinforced spandrel walls and 320% for reinforced ones). Also, when the spandrel void area lying above an arch barrel is backfilled, bridge load-carrying capacity increases significantly. Arch-backfill interaction was further investigated by Gilbert et al. through large-scale experiments and numerical simulations [64,147]. From their studies, it was demonstrated that backfill effectively prestresses the arch barrel via its self-weight, increasing its resistance, and also disperses applied surface loads and restrains sway of the barrel. Furthermore, the performance of masonry arch bridges subjected to long-term fatigue loads may show different characteristics compared to those under static loads. For example, a large-scale experimental campaign performed by Augusthus-Nelson and Swift [16] found that high-cycle fatigue load with a magnitude of 56% of the load-carrying capacity can lead to localised failure occurred in the arch ring, namely bricks at hinge locations of arch intrados fell, leading to the significant reduction in the stiffness of the bridge. In addition to the bridge failure triggered by traffic loads applied on the backfill surface, scouring effects for masonry arch bridges supported by piers sitting cross waterways, fluid-structure interactions can potentially affect the failure modes of bridges. One of the typical modes is the arch collapse due to the pier/abutment settlements, which is caused by scouring effects resulted from water flow [115,170]. Also, flood-induced loads acting on piers in the out-of-plane direction can potentially lead to the collapse of the piers, particularly for those bridges with significantly material deterioration and pre-existing cracks [171,172].

Visual observations by engineers in the field have indicated that masonry arch bridges can display 3D modes of response due to the asymmetric nature of the structure and/or the loading applied to them [83,112,142]. This can for example lead to forward rotation, sliding, and out-of-plane deflection of the spandrel walls [81,173]. Spandrel walls may in extreme circumstances become completely detached from the bridge, with complete overturning or sliding failure potentially also leading to the failure of the bridge. Various numerical studies have been carried out to investigate the 3D response of the masonry arch bridge. For example, Milani and Lourenço [112] developed a detailed 3D numerical model to help understand the behaviour of skew arches. They observed that brick units forming a skew arch were pushed out at the loading location at the peak load, leading to collapse of the bridge. Also, Grosman et al. [83] utilized the ADAPTIC code developed at

Imperial College London to develop a masonry arch bridge model comprising an arch barrel, spandrels and backfill. A patch load was applied at different locations to induce a 3D bridge response. Sensitivity studies have suggested that the behaviour of a masonry arch bridge can be considerably influenced by the material properties and the interaction between different components [140,174–176], highlighting the need for model calibration. However, the is a scarcity of experimental data on the 3D response of masonry arch bridges, with current understanding of the complex interactions that occur between the various components of a bridge remaining quite limited. Especially given that the numerical strategies used by previous researchers have necessarily involved a range of simplifying assumptions, this presents a problem for engineers and researchers wishing to validate both high-fidelity and more simplified numerical models.

In the present chapter, the load-carrying capacity and failure mechanism of the masonry arch bridge has been assessed through an experimental campaign on a large-scale masonry arch bridge constructed in the laboratory. The bridge was comprehensively instrumented with sensors to monitor its 3D response under patch loading, with its internal structure assessed before and after damage using a high-frequency GPR system. Increasing levels of loading were applied to the backfill surface at different locations to investigate damage accumulation and crack propagation. The responses of the bridge under low- and mid-level magnitude static and cyclic loading regimes were summarized in the last chapter [177]. In this chapter, results obtained from high-level and failure-level load tests are presented. The contribution focuses on crack evolution, load-carrying capacity, failure mechanism evolution, with peak and residual deformations of the arch barrel and spandrel walls also discussed.

5.3 Experimental programme

5.3.1 Large-scale masonry arch bridge model

The detailed information regarding the geometry, bond configurations, and construction process of the masonry arch bridge can be found in chapter 4.2.

5.3.2 Instrumentation

In addition to the sensors shown in Figure 4.6, GPR profiles were acquired to image and compare the internal structure of the bridge, prior to testing and after failure [161]. A Sensors & Software pulseEKKO PRO GPR system, equipped with antennas of 1000 MHz centre frequency, was used to record profiles along the longitudinal centre profile of the

bridge (A-A' shown in Figure 5.1). A GPR trace was recorded every 0.02 m, with distances measured using a calibrated odometer wheel. Assuming a velocity of 0.1 m/ns for the crushed limestone backfill (an implied relative dielectric permittivity, ε_r, = 9), a recording time of 80 ns is sufficient to capture reflections throughout the full thickness of the structure.
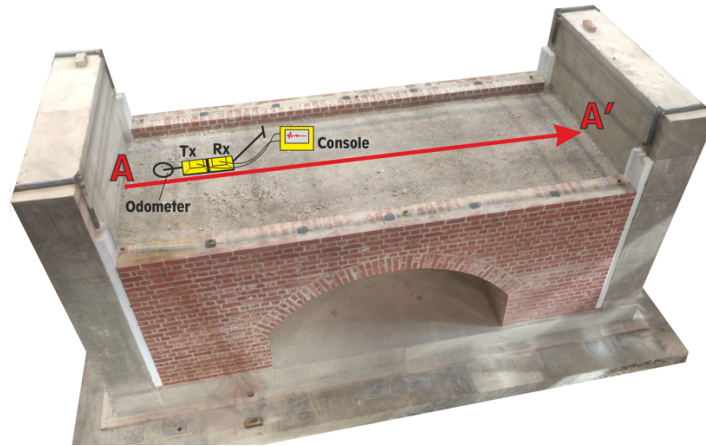
Figure 5.1 Schematic representation of GPR test profile. Sensors&Software equipment is moved along profiles A-A', with 1000 MHz transmitter (Tx) and receiver (Rx) maintained at constant offset in a tow-sled. Data are recorded at a PulseEKKO console, with distances tracked with a calibrated odometer wheel attached to the sled.

5.3.3 Loading protocol

The experimental campaign involved progressive application of patch loads with increasing magnitudes to the masonry arch bridge, with the aim of investigating damage accumulation and crack propagation mechanisms. Low-level and mid-level testing was carried out by applying static/cyclic patch loading to nine specific locations on the backfill surface. This was accomplished using a load spreader beam with a cross-section area of 300 x 300 mm. The selection of loading magnitudes was based on anticipated working load limits and also the ultimate limit state (ULS) load of the bridge obtained from preliminary numerical analysis. Specifically, a low-level load of 150 kN (approximately 20% to 25% of the ULS) was applied to characterise the elastic response of the bridge. Subsequently, the loading magnitude was increased to 250 kN, which was around 50% of the ULS, to evaluate any accumulation of plastic damage in the bridge. The results obtained from the low- and mid-level static/cyclic loading tests are reported in [177].
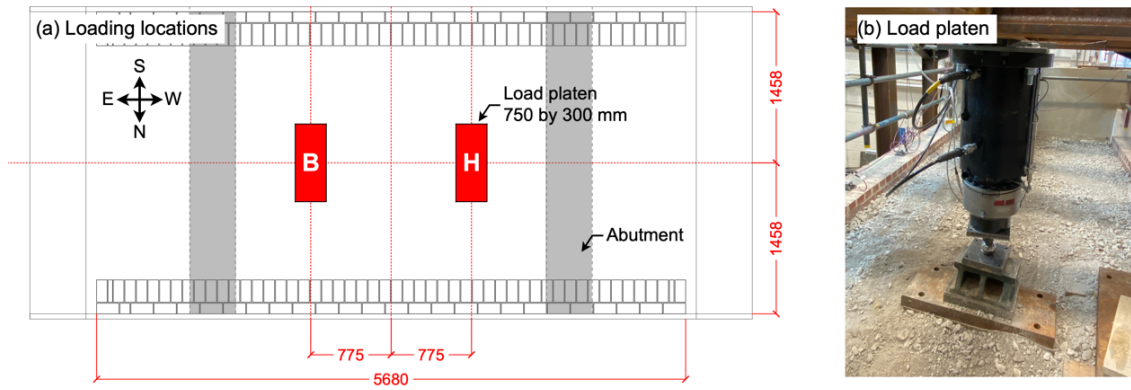
Figure 5.2 Bridge: (a) loading locations; (b) larger load platen used for high- and failure-level load tests (all units in mm).

Following completion of the low and mid-level testing, high-level and failure-level tests were performed to assess the bridge load-carrying capacity, post-failure residual capacity and also the associated modes of response. At these stages of testing, a static patch load with the target magnitude was applied either at Point B or Point H, corresponding to the quarter-span or three-quarter span points along the longitudinal centre line of the bridge (Figure 5.2 (a)). Moreover, based on observations from previous mid-level tests, it was suspected that a 300 x 300 mm load patch may initiate localized failure of the fill, rather than global failure of the bridge. Thus, a larger loading platen, measuring 300 x 750 mm, was utilized when applying higher levels of loading (Figure 5.2 (b)).

Table 5.1 lists the loading protocol adopted in the study. Following the low- and mid-level testing, which were comprehensively detailed in [23], the high-level test was conducted at point B using the larger spreader beam (T21). Then, at the same location, the first failure-level test was carried out (T22). Afterwards, the small platen was used to examine the impact of loading area on the response of the bridge (T23). However, it was observed that, due to local deformations of the backfill, the small platen rotated excessively under the high level of loading, leading to termination of the test. The same behaviour was also encountered during T24, conducted at Point H. Finally, the larger platen was again utilized, with a second failure-level test (T25) conducted at Point H, the three-quarter span point, to assess the residual load-carrying capacity of the bridge. The static loads were applied using a hydraulic actuator with a capacity of 750 kN. All high-level and failure-level tests were carried out under displacement control to better control the post failure response of the bridge. The rate of loading and unloading was set at 0.05 mm/s. The loading times for T21, T22, and T25 were recorded to be approximately 528s, 840s, and 963s, respectively.

Table 5.1 Loading protocol testing on the first bridge.

No. of test	Type of test	Loading location	Loading level	Loading area (mm)	Loading rate
T1 & T2	Trials (Static)	Point A and B	Low-level (150 kN)	300 x 300	10 kN/min
T3 to T11	Static & cyclic	9 locations	Low-level (150 kN)	300 x 300	10 kN/min
T12 to T20	Static & cyclic	9 locations	Mid-level (250 kN)	300 x 300	10 kN/min
T21	Static	Point B	High-level (560 kN)	750 x 300	0.05 mm/s
T22	Static	Point B	Failure-level	750 x 300	0.05 mm/s
T23	Static	Point B	Failure-level	300 x 300	0.05 mm/s
T24	Static	Point H	Failure-level	300 x 300	0.05 mm/s
T25	Static	Point H	Failure-level	750 x 300	0.05 mm/s

5.4 Experimental test results

5.4.1 Inspection of the bridge after failure

After failure of the bridge, an extensive inspection was carried out. Figure 5.3 presents the residual width of the main cracks observed in the north and south-side spandrel walls, as well as residual out-of-plane deformations at the west ends of the two walls. Crack width measurements were taken from the surface of the walls using a vernier calliper with an accuracy of 0.01 mm. Meanwhile, out-of-plane deformations were measured relative to the bases of the spandrel walls. A laser level was used to project a vertical laser line on the side of spandrel walls, and values of out-of-plane deformation were estimated by measuring the horizontal distance between the laser line and the edge of the wall at various elevations. The widest cracks were observed to form in the north-side spandrel wall, measuring 5.65 mm. Overall, the widths of cracks in the north-side wall were greater than those forming in the south-side wall. Also, much larger out-of-plane deformations were observed in the case of the north-side wall, with the maximum recorded deformation of 20.48 mm occurring at the top of the wall. In contrast, no significant out-of-plane deformation of the south-side spandrel wall was recorded. These observations suggested that the response of the bridge was asymmetrical, with varying levels of damage observed in the two spandrel walls, and with the north-side wall suffering more severe damage compared to the south-side wall.

Figure 5.3 Post failure test inspection: (a) width of residual cracks on north-side wall; (b) width of residual cracks on south-side wall; (c) out-of-plane residual deformation of spandrel wall (viewed from the west side) (all units in mm).

Figure 5.4 (a) and (b) show the GPR profiles for the longitudinal centre profile of the virgin and failed bridge, respectively. GPR profiles were identically processed using a standard set of processing routines, including:

1. static corrections to align time-zero in each trace,
2. Kirchhoff migration, using a velocity of 0.12 m/ns and an aperture of 100 traces,
3. Ormsby bandpass filter, with corner frequencies at 100-200-2500-5000 MHz, and
4. removal of the profile-average trace to suppress horizontal striping in the images.

The curved feature with its apex at ~10 ns travel-time is interpreted as the arch intrados, preceded by ~4 ns by reflections from the extrados. These are surrounding by sub-horizontal horizons interpreted as layers within the crushed limestone backfill. The reflections at ~20 ns travel-time are the first-order reverberation of the reflections from the arch and thus provide no additional insight to the structure of the bridge. Figure 5.4 (a) and (b) suggest that layers of backfilled crushed limestone were disturbed after the loading tests, particularly within the region between the quarter- and three-quarter span points, situated over the arch barrel. This disturbance can be attributed to non-uniform compaction of the backfill material resulting from point loading during the testing procedure. Another noteworthy phenomenon is the deflection of arch barrel. It can be seen in Figure 5.4 (b) that deflection of the arch was prominently manifest at three locations, including the quarter-, mid-, and three-quarter span points of the arch, where

loads were applied and hinges formed. Furthermore, no discrete responses (i.e., diffraction hyperbolae) to cracks were evident in the data; the GPR mostly samples unconsolidated material and hence settlement rather than cracking is more likely the dominant deformation mechanism. Furthermore, the ~2 mm aperture of cracks in the masonry is likely beyond the resolution of the GPR wavelet with ~12 mm wavelength; hence the GPR tends to sample bulk layer properties rather than discrete fractures.
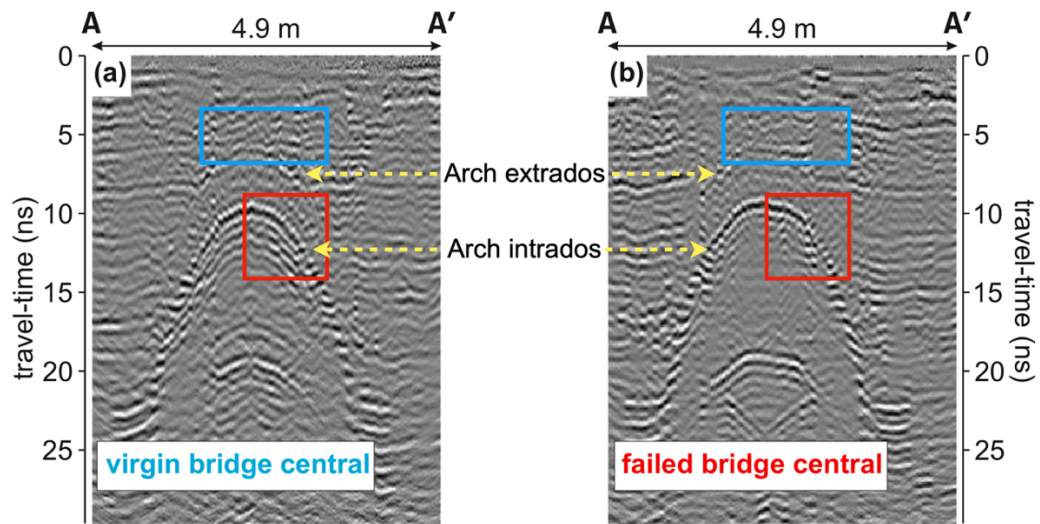
Figure 5.4 Results obtained from GPR testing: (a) longitudinal central profile of the virgin bridge; (b) longitudinal central profile of the bridge after failure.

5.4.2 Damage evolution and bridge failure mechanism

Initially, low- and mid-level load tests were carried out to evaluate the elastic response and the evolution of damage in the bridge under 'safe' working loads (less than 50% of the expected ULS load). After the low- and mid-level tests, cracks on the bridge were all occurred at the mortar joints and were principally comprised of: (a) cracks between the arch ring and spandrel walls at both the north and south side; (b) tensile cracks at the quarter- and three-quarter span points in the arch intrados; (c) short diagonal cracks in the north side spandrel wall; (d) plate-shaped localized cracks visible in the arch intrados at mid-span (see the cracks marked in grey in Figure 5.5 (a)). The application of point loading induced 3D effects in the bridge, though culminated in a four-hinge mechanism. Figure 5.5 shows the progression of cracks in the bridge during the high-level and failure-level tests. Moreover, Figure 5.7 and Figure 5.7 present the failure mechanism of the bridge, as well as photos showing damage to the bridge, observed at T22 and T25, respectively.

Figure 5.5 (a) shows the cracks that developed after T21, which involved a high-level loading of up to 560 kN applied at the quarter-span. During T21, three hinges formed

initially, the first forming at the quarter-span point, with tensile cracks developing transversely in the arch intrados underneath the loading location. Secondly, a tensile crack was observed in the arch extrados between courses 42 and 43, near the east side of the springing, representing the formation of a second hinge. The third hinge was identified in the mid-span region, where compression-induced crushing of mortar joints was observed at the arch intrados. However, at this stage, no cracks were observed in the arch extrados in the mid-span region. Also, deformation of the arch barrel resulted in the initiation and propagation of cracks in both spandrel walls. Specifically, at the quarter-span point where the load was applied, diagonal cracks initiated at the arch-spandrel wall interfaces and propagated upwards towards the east side due to the downward movement of the arch. Conversely, between the mid-span and three-quarter span points, cracks originated from the top of the spandrel walls and extended downwards to the mid-span (location of the 3rd hinge). A comparison of the crack patterns on the two sides of the spandrel walls indicated the presence of more severe cracking in the north-side wall, indicative of a higher degree of damage in this wall. Moreover, apart from global damage characterised by the formation of three hinges, the presence of diagonally aligned tensile cracks in the arch intrados that originated from the region directly underneath the loading platen indicates that the arch barrel was behaving in a 3D manner under the action of the applied patch loading.

Figure 5.5 (b) shows the cracks observed during T22, which involved further load being applied at Point B until the bridge failure mechanism was fully activated (Figure 5.6 (a)). The test was stopped after a plateau was observed in the real-time load-deflection curve, with the peak load at this stage being 639 kN. As the load increased, the width of cracks increased noticeably at the hinge locations (Figure 5.6 (b) and (f)), and fragments of crushed mortar lying in high compression regions fell to the floor (Figure 5.6 (g) and (h)). In addition to the three hinges that had formed during the previous high-level test, the increase in loading led to formation of the last hinge at the west springing (labelled h_4 in Figure 5.6 (a)). Also, further cracks propagated in the spandrel walls due to the significant deformation of the arch barrel, with the overall form of the cracks in the two spandrel walls being similar. For instance, the crack originating from the quarter-span location extended upwards to the top of the wall (Figure 5.6 (b)). Another crack, which initiated in the previous test, propagated downwards until it reached the interface between the arch and spandrel wall at the mid-span region (Figure 5.6 (c) and (e)). Furthermore, due to upward movement of the arch barrel between hinges 3 and 4, the

west side spandrel walls rotated, with tensile cracks originating from the springing (h_4)
propagating diagonally downwards towards the bottom corner of the bridge (Figure 5.6
(d)). The cracks thus separated the spandrel walls into four distinct parts. Moreover, the
extent of the diagonal tensile cracks that formed in the arch intrados increased markedly,
emphasising the 3D nature of the response of the barrel in the region directly underneath
the applied load.
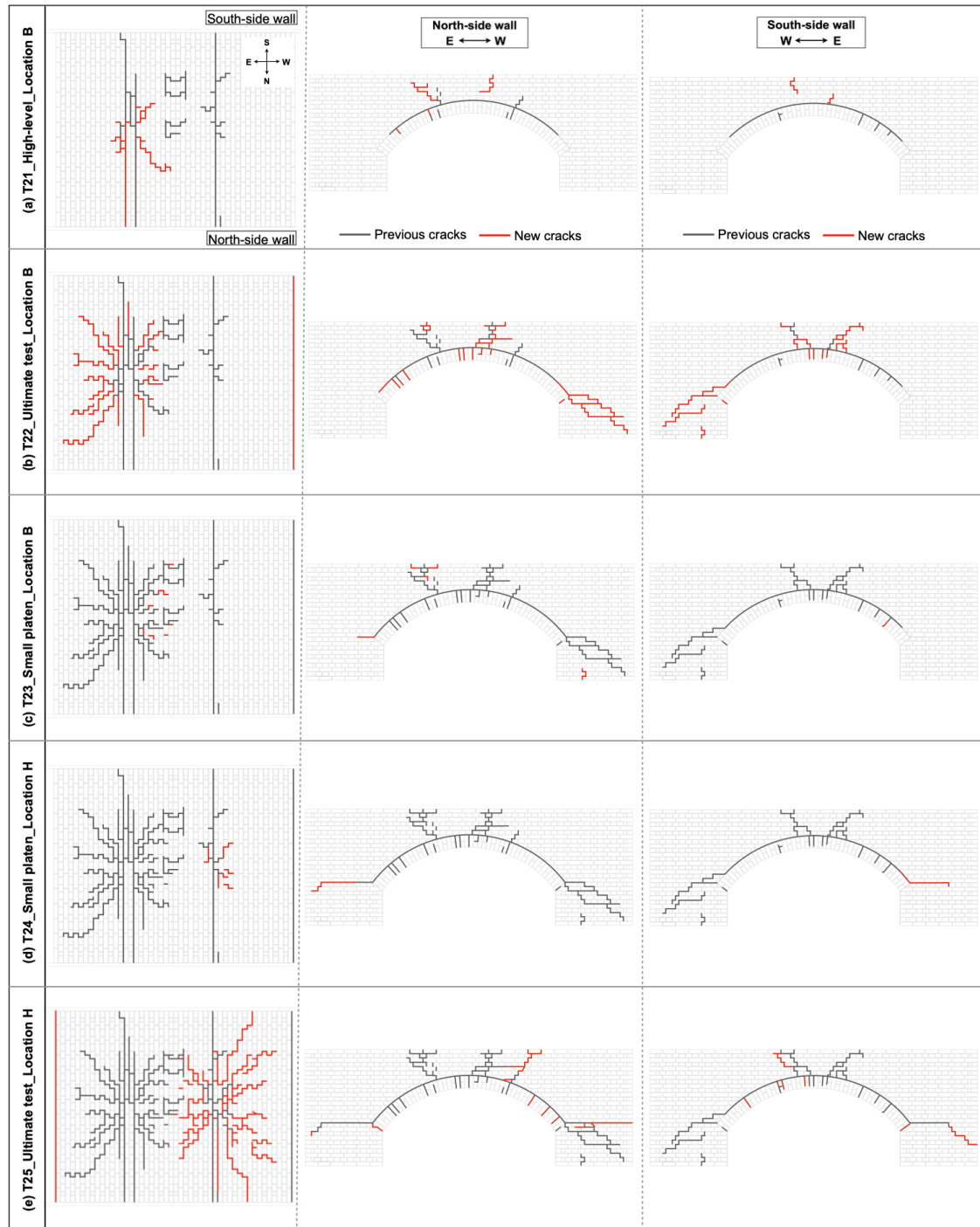
Figure 5.5 Crack evolution under high- and failure-level load tests (new cracks forming in a
given test indicated in red).

Following the first failure-level test, T22, the load platen was replaced with a smaller one having a base area of 300 x 300 mm, and the test was conducted again (i.e., T23) with the other conditions remaining the same to assess the influence of loading area on the response of the bridge. However, when the load exceeded 400 kN, the small loading plate was observed to rotate, with one side of the plate becoming embedded in the backfill. Therefore, the test was terminated for safety issues. Nevertheless, the application of a 400 kN load through the small platen induced an approximately 4.5 MPa compression pressure on the backfill surface, which was 1.56 times greater than the peak compression pressure applied during the previous test, T22. However, after T23, minimal additional crack propagation was observed, as shown in Figure 5.5 (c).

After the failure of the bridge, the actuator was moved to the opposite location, at the three-quarter span point on the bridge centreline (point H in Figure 5.2 (a)), to assess the residual load-carrying capacity of the bridge. The test started using the small platen (T24), but once again the loading platen rotate, with one side becoming embedded in the backfill. In this case the peak load applied during T24 was 299 kN, with the test stopped due to significant bending being observed in the actuator. After the test, some tensile cracks were initiated in the arch barrel under the loading location, as shown in Figure 5.5 (d). Additionally, separation between the lower and upper parts of the spandrel walls was observed, with a crack emerging from the east side springing level (Figure 5.5 (d)).

The final test, T25, was carried out utilizing the larger platen at Point H to assess the residual load-carrying capacity of the bridge. During this test, both global damage and a 3D response were again observed, with the load-carrying capacity reaching 575 kN, only slightly lower than the 639 kN reached in test T22, with the maximum arch deformation increasing to 18.1 mm (further discussed in section 4.2). Figure 5.5 (e) shows the cracks that propagated in the test; the failure mechanism and photos showing damage to the bridge are shown in Figure 5.7. Overall, the cracks observed following T25 were similar in form to those observed following T22, including: (a) a fourth hinge was formed, triggering opening of the mortar joint at the east side springing (Figure 5.7 (a) and (b)); (b) tensile cracks under the location of the load were fully opened, indicating the presence of hinge 1 (Figure 5.7 (c) and (d)); (c) crushing of mortar joints in the high compression mid-span region was observed, with cracks opening in the arch extrados, indicating the presence of hinge 3 (Figure 5.7 (c) and (e)). In addition to mortar crushing in the mid-span region, cracks were also observed in several bricks in this region (Figure 5.7 (e)), indicative of the high compressive stresses; and (d) the spandrel wall was

separated into four parts by three major cracks (Figure 5.7 (c)). Affected by the existing cracks, the crack over h_3 was the one that formed previously in test T22. Moreover, a diagonal crack was observed in the backfill at the peak load (Figure 5.7 (f)). The crack started from the loading platen and propagated diagonally towards the northwest corner of the bridge.
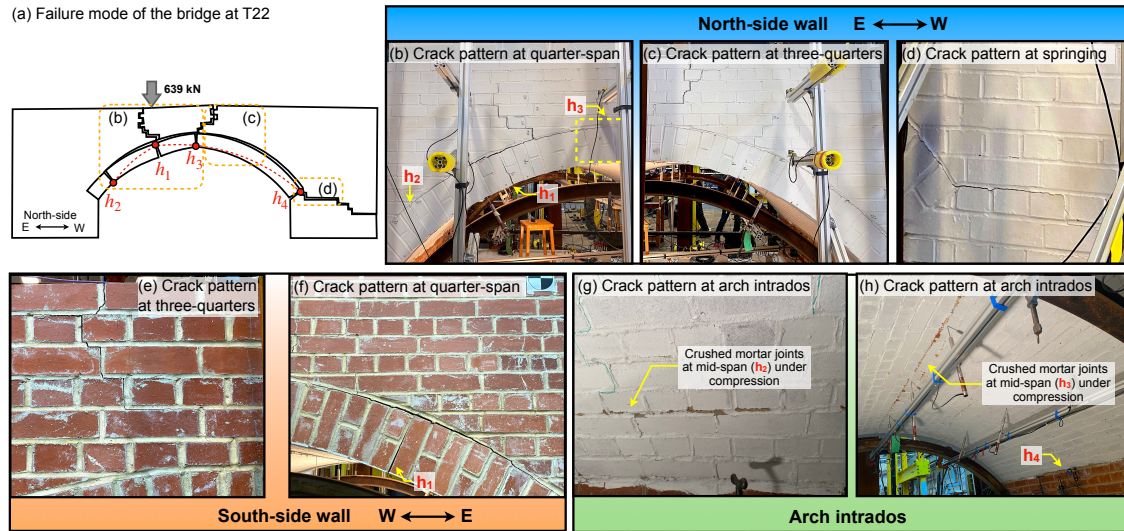
Figure 5.6 (a) Failure mechanism of bridge at T22; (b) to (h) are photos showing observed damage.
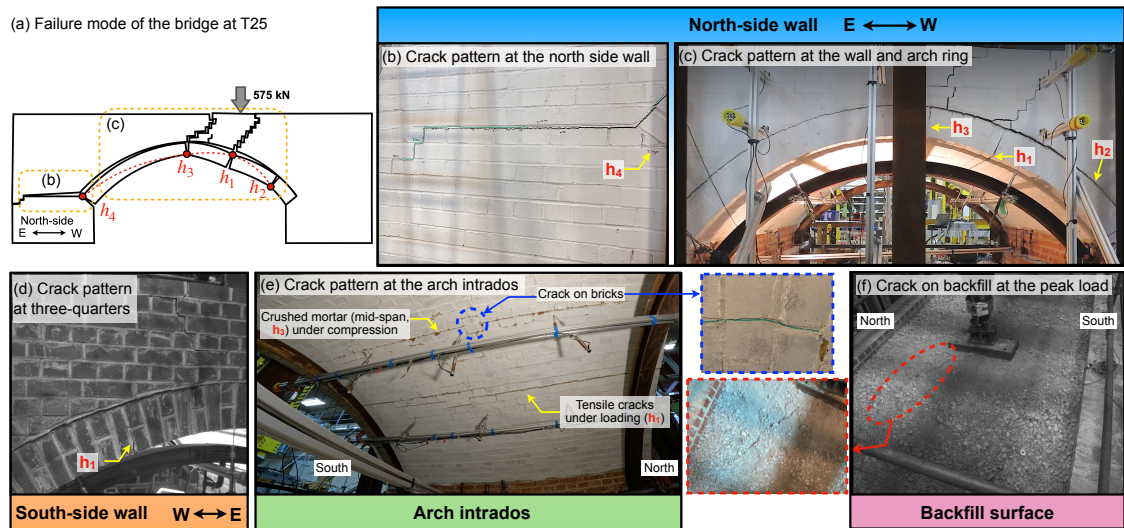
Figure 5.7 (a) Failure mechanism of bridge at T25; (b) to (f) are photos showing observed damage.

5.4.3 Horizontal movement of abutments

Figure 5.8 (a) shows the locations of six displacement gauges positioned to monitor horizontal movements of the abutment, and Figure 5.8 (b) shows horizontal deformations of the abutments recorded at the peak load in tests T21, T22, and T25. The

load-deformation curves of the abutment deformations from T21, T22, and T25 are shown in Figure 5.8 (c), (d), and (e), respectively. Positive values in Figure 5.8 (b) to (e) indicate deformation towards the inward (centre) of the arch barrel. During T21 and T22, when loads were applied near the east-side abutment, significant inward deformation was observed from L39, positioned at the south end of the east abutment. This deformation occurred suddenly as the load approached to its peak (see Figure 5.8 (c)). Also, the peak deformation values increased from 1.55 mm to 2.42 mm as the load increased from 566 kN to 622 kN (see Figure 5.8 (d)). The inward deformation of the abutment at the northeast corner was unexpected, and the underlying mechanism remained unclear. At the other two monitored locations at the east side, minimal deformations were recorded, highlighting an asymmetric response of the east abutment. The west-side abutment experienced a slight outward movement. During T25, when the load was applied at Point H, both sides of the abutments deformed outwards slightly, with the east abutment exhibiting slightly larger deformation compared to the west-side abutment (Figure 5.8 (e)). Notably, the recorded horizontal deformation of the abutment did not indicate that the abutment sliding was the main cause of the bridge failure. The primary global failure mechanism observed was the four-hinge mechanism of the arch barrel. Nevertheless, the response of the abutments suggested their involvement in the bridge behaviour. Therefore, neglecting or oversimplifying the abutments as rigid immovable bodies may not be appropriate when conducting numerical simulations.
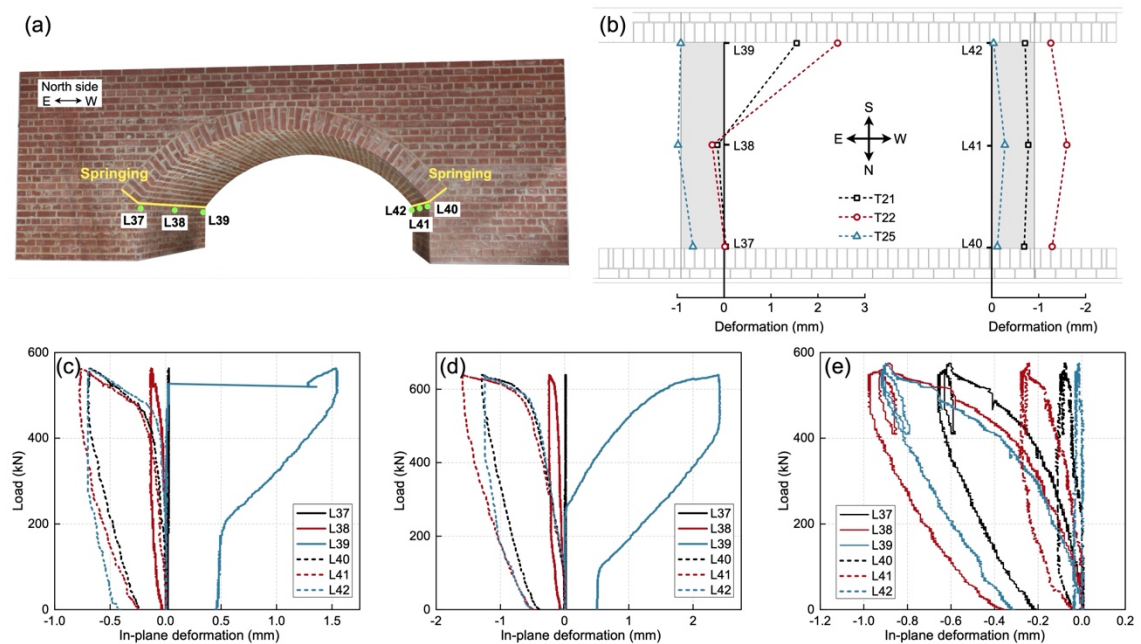
Figure 5.8 Horizontal movement of abutments: (a) locations of displacement gauges; (b) horizontal displacement of abutments at peak loads in tests T21, T22, and T25; load-deformation curves of abutment deformations during (c) T21, (d) T22, and (e) T25.

5.4.4   Load-carrying capacity and stiffness characteristics of the bridge

Figure 5.9 (a) shows the load-deflection curve measured at the arch intrados for tests T21, T22, and T25. The values of displacement were obtained from the LVDT orientated radially directly underneath the loading location. During the high-level test (T21), the peak load and peak deformation of the arch intrados was 566 kN and 3.824 mm, respectively. From the load-deflection curve, a noticeable change in stiffness is evident as the load increased from 375 kN to 480 kN, indicating a transition from near-elastic to plastic behaviour. After the load had reached 566 kN, it was then fully removed, with residual deformation of the arch barrel being approximately 1.6 mm.

Subsequently, in test T22, the load was re-applied at the same location. This time, the arch exhibited a near-elastic response until a load of approx. 525 kN, indicating the presence of an expanded near-elastic range compared to test T21. However, when the load was increased further (e.g. to approx. 620 kN), the load-deflection curve was clearly starting to plateau, with large increases in arch deformation for small increases in load. This suggests that the failure mechanism of the bridge was now being mobilised. Finally, the test was stopped when the load reached 639 kN, with the deformation of the arch intrados at this point being 10.195 mm. (Although at this point the load-deflection curve was very flat, strictly speaking, the peak load-carrying capacity of the bridge was not established in T22, as no decline in load was observed.)

The final test (T25) was performed at Point H using the larger platen to evaluate the residual load-carrying capacity of the bridge. Comparing the results obtained in tests T22 and T25, a decrease in bridge strength of approximately 10% was observed, with the load-carrying capacity dropping from 639 kN to 575 kN. Although damaged after test T22, the bridge was still able to effectively distribute the applied load through the arch barrel and onto the abutments. With the load moved to the three-quarter span point for test T25, the extensive cracks observable on the arch intrados near the quarter-span point would have been unlikely to have affected global bridge behaviour. After the peak load of 575 kN had been reached, the load gradually decreased whilst arch barrel deformations grew markedly. Finally, the test was stopped when the peak deformation of the arch intrados reached over 18 mm, with residual deformation of the arch barrel being 9.7 mm after the load was removed.

Figure 5.9 (b) shows how the elastic stiffness of the bridge drops as the tests proceeded. The stiffness values were determined by calculating the slope of the load-deflection curve

between 10% and 40% of the peak load [178]. The first low-level test (up to 150 kN) conducted at Point B suggested that the elastic stiffness of the virgin bridge was equal to approximately 524 kN/mm. It is important to note that this value might not be directly comparable to the high-level and failure-level tests due to differences in the testing conditions (i.e., load platen and the loading rate). Nevertheless, it is indicative of the ongoing reduction in stiffness that occurs as cracks in the bridge progressively develop.
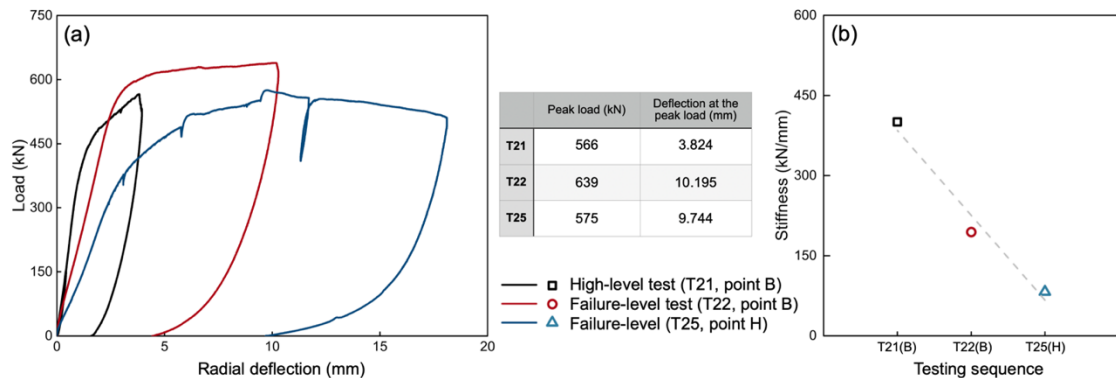
Figure 5.9 Results: (a) load-deflection curve of arch intrados under high- and failure- level tests; (b) stiffness reduction.

5.4.5   Deformation of the arch barrel

Figure 5.10 shows the load versus deflection curves of the arch intrados as measured by three LVDTs positioned on the longitudinal centreline of the bridge. Figure 5.11 presents the radial deflection values and deformed shapes of the arch intrados at the peak load during tests T21, T22 and T25. From Figure 5.10 and Figure 5.11, it is clear that the arch barrel exhibited both a local 3D response and a more global four-hinge mechanism when subject to the applied patch loading.
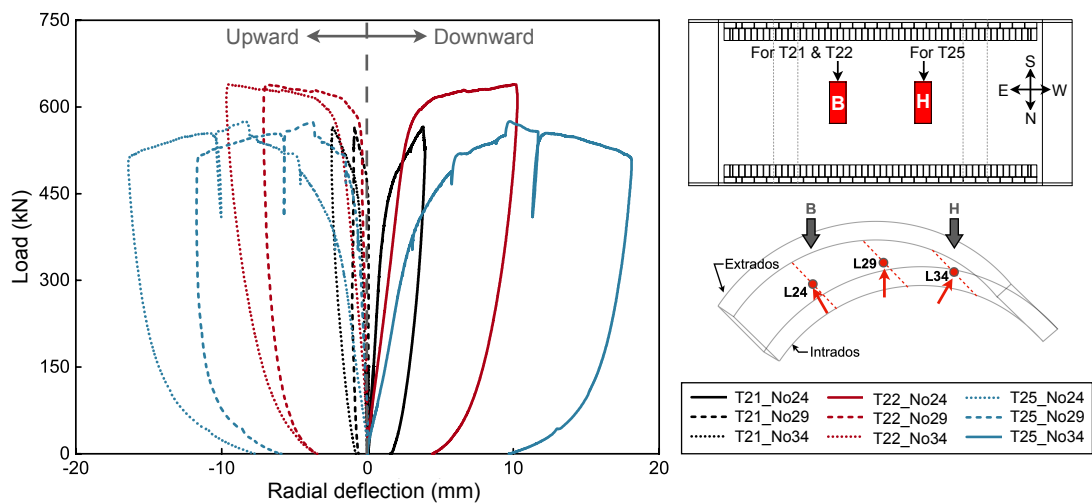
Figure 5.10 Load-radial deflection curves of the arch barrel monitored by three LVDTs positioned on the bridge centreline under high- and failure-level load tests.

The 3D response was most prominent in the vicinity of the applied load, with peak arch barrel deflections recorded on the bridge centreline. Moving transversely away from the bridge centreline, deflections of the arch barrel gradually decreased (Figure 5.11). However, the global response of the arch barrel was characterised by a classical four-hinge mechanism, as evidenced by: (a) on the bridge centreline underneath the loading, the barrel moved downwards, with upward movements observed at the two other monitored locations (Figure 5.10); (b) distribution of the load in the arch barrel led to 3D deformations diminishing at monitoring locations further away from the loading location (Figure 5.11). For instance, in test T25 when the load was applied at point H (Figure 5.11 (c)), the magnitude of the deformation of the barrel on the bridge centreline at the loaded location was almost three times that observed at the edges of the barrel. However, at midspan, differences in deformation on the bridge centreline and at the edges of the arch barrel became much less pronounced. At the quarter-span point (in this case the non-loaded side of the bridge), any 3D response of the arch barrel was difficult to discern, indicating that remote from the load the arch barrel was reverting to a classical four-hinge mode of response.
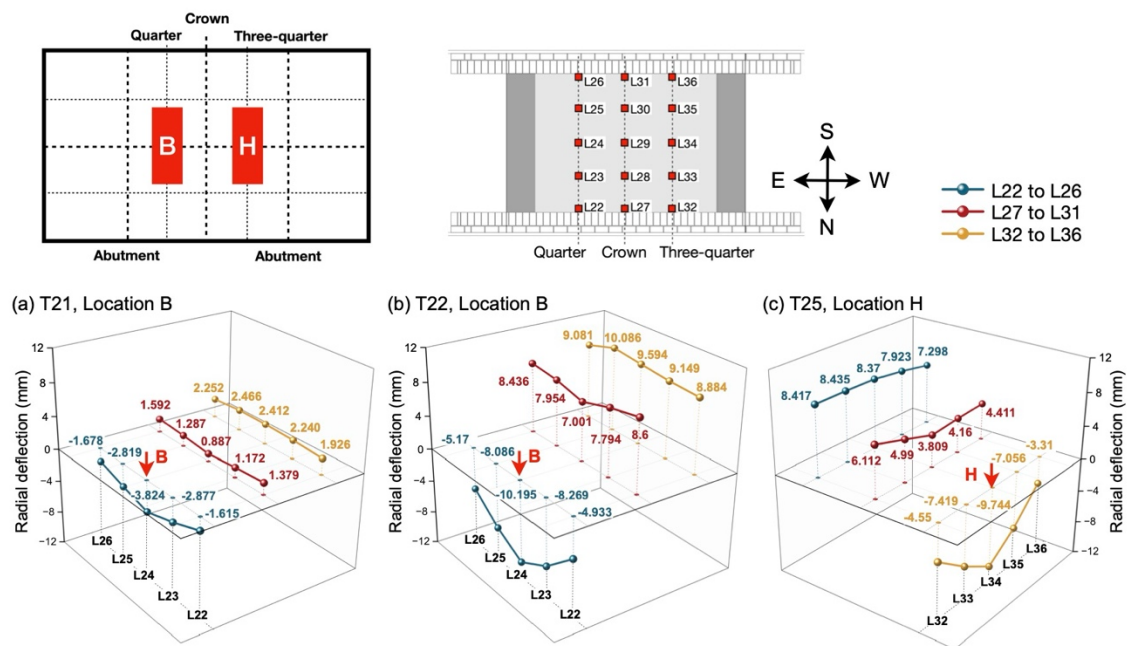
Figure 5.11 Peak radial deflection values and deformed arch barrel shapes at the peak load: (a) T21; (b) T22; (c) T25.

5.4.6 In-plane deformation of spandrel walls

During the test, four potentiometer displacement gauges were employed to monitor in-plane deformation of the two spandrel walls (i.e., L3 and L15 for the south-side wall and L46 and L16 for the north-side wall). Figure 5.12 shows values of the in-plane

deformation at the peak load for all tests, from low level loads to failure level loads. Negative values in Figure 5.12 indicate westward movement. During the low- and mid-level tests, no major cracks developed in the spandrel walls, and in-plane deformations of the spandrel walls were minimal. However, significant in-plane deformations of the spandrel walls were observed in the high-level test (T21) and in subsequent tests up to test T25. The maximum in-plane deformation was recorded at L16 during test T22, which is the first failure-level test conducted at Point B. Moreover, the peak in-plane deformation at the north-side wall was always greater than that at the south-side wall, indicating more severe damage in the north-side wall, which is in keeping with the general post-test observations (Figure 5.3).
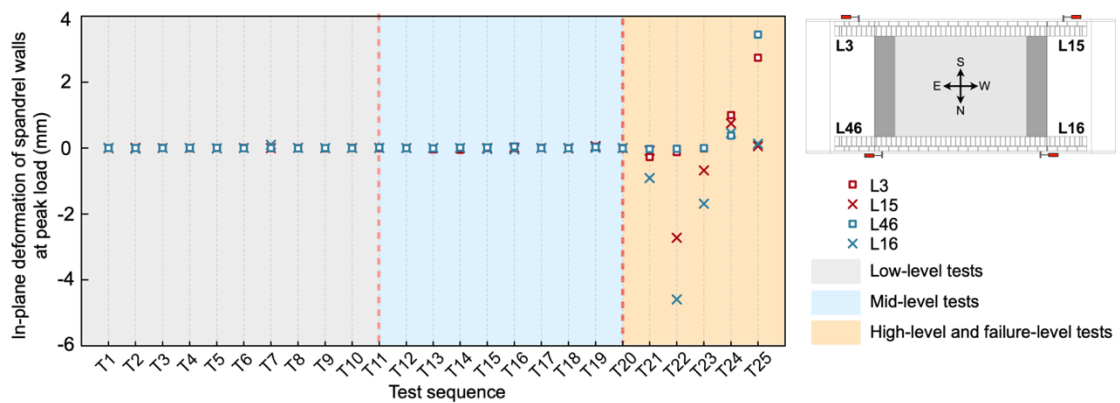
Figure 5.12 Values of in-plane deformation of spandrel walls at the peak load during testing (data obtained from low-level, mid-level, high & failure level tests was respectively highlighted by grey, blue, and yellow windows).
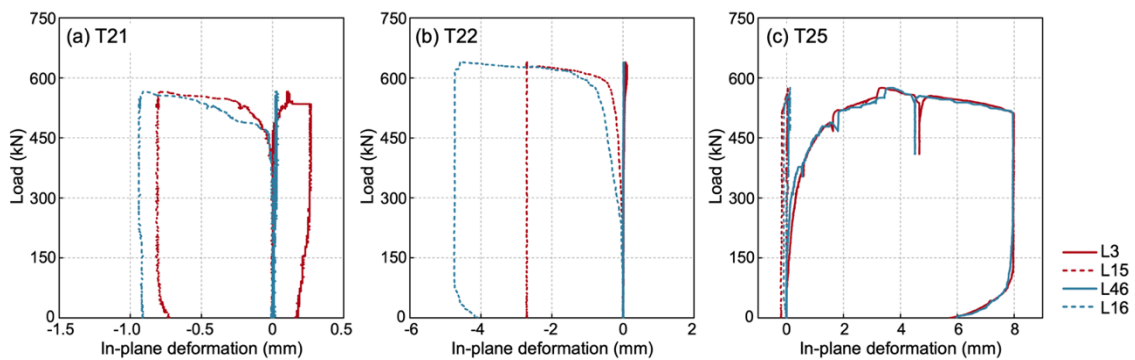
Figure 5.13 Load versus in-plane deformation of the spandrel walls during: (a) T21; (b) T22; (c) T25.

The load versus in-plane deformation curves in tests T21, T22, and T25 are plotted in Figure 5.13 (a), (b), and (c), respectively; negative values indicate movement in the westerly direction. The observed in-plane spandrel wall deformations were closely related to the form of the overall failure mechanism. More specifically, when the bridge was subjected to the high- and failure-level loads, extensive crack propagation occurred in the spandrel walls, eventually causing the walls to separate into several parts. The part

137

of the spandrel wall situated above the non-loaded side of the bridge rotated upwards due to upward deformation of the arch barrel, resulting in significant in-plane deformation. Conversely, the spandrel walls on the loaded side of the bridge experienced only relatively small deformations (less than 0.2 mm). Moreover, during test T21, the peak in-plane deformation of the spandrel wall was less than 1 mm at the peak load of 566 kN. However, in T22 and T25, in-plane deformations of the spandrel walls increased significantly, a consequence of full activation of the bridge failure mechanism.

5.4.7   Out-of-plane deformation of spandrel walls

Figure 5.14 shows the out-of-plane deformations of the spandrel walls recorded at the peak load during tests T21, T22, and T25. As the level of loading increased, the extent of cracking in the spandrel walls increased. Specifically, the monitoring point nearest to the loading location always recorded the highest deformation, since it was subjected to the greatest lateral soil pressures. Also, higher applied loads led to increased downward deformation of the arch barrel, increasing the gap between the arch barrel and the spandrel wall at the location of the applied load. Additionally, the propagation of cracks in a given spandrel wall decreased its resistance to lateral loads. These factors contributed to a pronounced increase in the peak out-of-plane deformations of the spandrel walls in tests T21 to T25. However, it is worth noting that the ends of the spandrel walls in the bridge were "free", which is likely to have allowed greater out-of-plane deformations than if they had e.g., been restrained by wing walls.

(a) T21, Location B

	C1	C2	C3	C4	C5	C6	C7
R1	0.86	0.92	0.63	0.41	0.16	0.21	0.28
R2	-	0.63	0.87	-	0.22	0.2	-

(b) T22, Location B

	C1	C2	C3	C4	C5	C6	C7
R1	2.59	2.34	1.9	1.87	0.54	0.3	0.7
R2	-	1.792	2.63	-	0.43	0.72	-

(c) T25, Location H

	C1	C2	C3	C4	C5	C6	C7
R1	0.31	0.9	0.8	2.82	5.27	3.95	4.68
R2	-	0.589	1.01	-	4.73	4.81	-
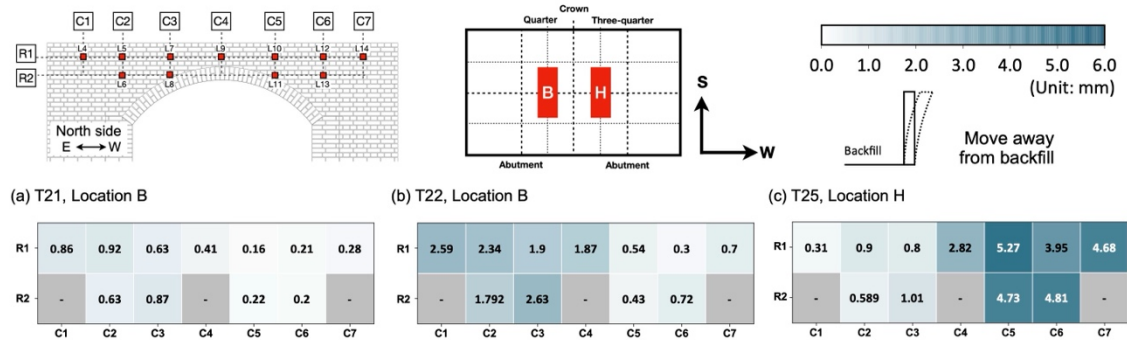
Figure 5.14 Peak values of the out-of-plane deformation of the north-side spandrel wall during: (a) T21; (b) T22; (c) T25.

Over time out-of-plane deformations of a spandrel wall can accumulate and eventually lead to overturning failure. Figure 5.15 shows residual and accumulated out-of-plane spandrel wall deformations measured during the bridge tests in the case of both spandrel walls, starting with the low-level tests, up to the final failure-level test. In the low- and mid-level load tests, the data points highlighted by the dotted lines correspond to results

obtained from static tests, while the subsequent data points between the two dotted lines represent the values obtained from cyclic tests. The residual values are represented by bars, while the accumulated deformations are depicted by blue lines. Note that the accumulated deformations shown in Figure 5.15 were calculated by summing up the residual values recorded after each test, rather than being obtained via continuous monitoring. Thus, any small movements of the spandrel wall that took place at other times, e.g., due to thermal effects, are not included.
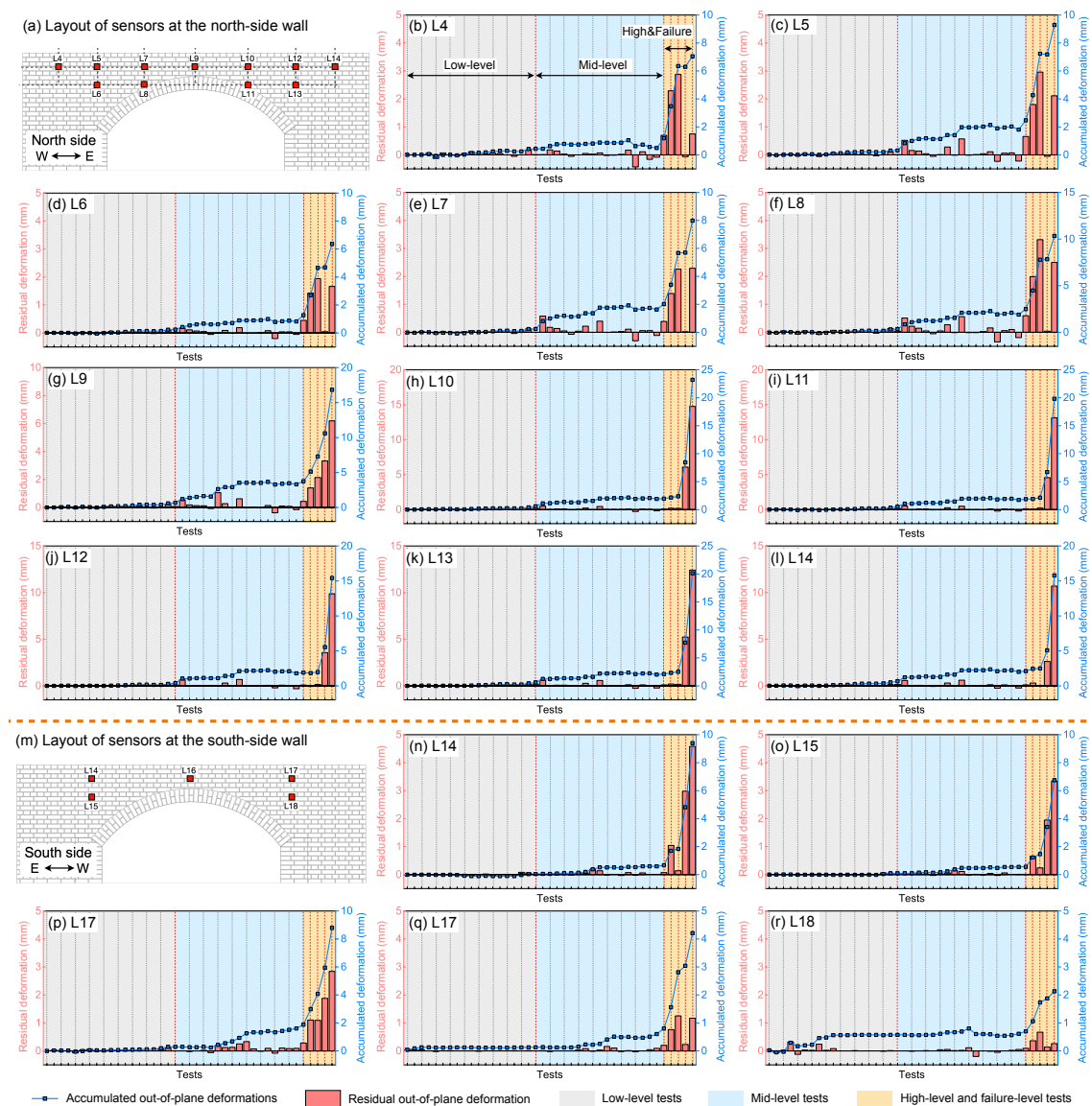
Figure 5.15 Residual and accumulated out-of-plane deformations of the north side, (a)-(l), and south side, (m)-(r), spandrel walls, indicated respectively by red bars and blue lines (data obtained from low-level, mid-level, high & failure level tests was respectively highlighted by grey, blue, and yellow windows).
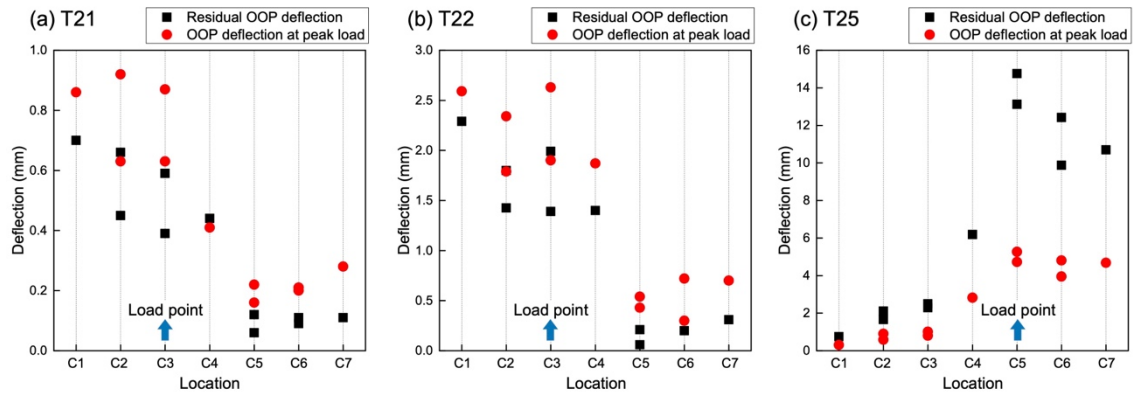
Figure 5.16 Out of plane deflection of north-side spandrel wall: residual values and values at the peak load.

In the low-level tests a load of 150 kN was applied. Despite the initiation and propagation of cracks between the arch barrel and spandrel walls on both sides of the bridge, the bridge did not sustain any significant damage under these loads. Additionally, the lateral soil pressure exerted on the spandrel walls was relatively low. Consequently, the residual and accumulated out-of-plane deformations of both spandrel walls were in these cases negligible. In the mid-level tests a higher load of 250 kN was applied, leading to a marked increase in accumulated deformation when loads were applied close to a given wall. Specifically, in the case of the north-side wall, a gradual increase in accumulated deformation was observed in the first three tests (T12 to T14), where static/cyclic loads were applied eccentrically at three different locations near the north-side wall (at the three-quarter, quarter, and midspan points). Subsequently, the loading position was moved near the south-side wall, and three additional tests (T15, T16, and T17) were conducted. During this phase, out-of-plane deformations of the south-side wall began to accumulate. Finally, the last three mid-level tests were carried out on the bridge centreline, with the accumulated deformations of both walls then remaining relatively stable.

During the high-level and failure-level load tests, significant increases in residual and accumulated deformations were observed, at nearly all monitoring points. Residual deformations of the spandrel walls were found to be greater at monitoring locations lying closest to the position of the applied loading. After all tests had been completed, gauge L10, measuring deformations of the north-side wall recorded the highest accumulated deformation, at approx. 23.2 mm. Most residual deformation was in this case induced in the final load test, with the load applied at Point H. Furthermore, at seven north-side wall monitoring locations (specifically, L8 to L14), out-of-plane deformations larger than 10 mm were recorded; at three of these locations deformations larger than 20 mm were

recorded, indicating bulging of the spandrel wall. Additionally, out-of-plane deformations of the north-side wall were more significant than those of the south-side wall, indicating a highly asymmetric bridge response.

The out-of-plane deflection of the spandrel walls can be resulted from the bending or the sliding of the wall under loads. Figure 5.16 shows the out-of-plane deflection of the north-side wall, showing both the peak load values and the residual values after load removal. The data was collected from seven columns of potentiometer gauges (C1 to C7, as shown in Figure 5.14). The sliding effect can be observed in the movement of the non-loading side wall, specifically at C5, C6, and C7 during T21 and T22, as well as at C1, C2, and C3 during T25. The values recorded by these potentiometers suggest some sliding behaviour of the wall; however, the effect is not significant. For instance, the out-of-plane deflection due to sliding accounted for less than 20% of the maximum out-of-plane deflection. In contrast, bending is more pronounced in these cases. This is evident from the significant increase in out-of-plane deflection at the loading location, indicating that bending plays a dominant role in the wall's response at the out-of-plane direction.

5.4.8 Comparison between the results obtained from previous testing and this study

The full-scale bridge specimen tested in this study shared similar characteristics with a previous experimental study conducted at the University of Salford (UoS), including the use of similar materials and the same geometry of the arch barrel [36].Notably, four 3m span bridges were constructed and load tested at UoS. For comparison, results from the bridge with the highest similarity to the one in this study (referred to as 3-1 in [36]) is analysed. Table 5.2 summaries the key features and results of these two studies.

Table 5.2 Comparison between the key features and results between tests of this study and the previous one performed at the University of Salford.

Features / Results	UoS (bridge 3-1)	This study
Bridge geometry		
Length x width x height of the bridge	7,920 x 3,540 x 1,805 mm	5,886 x 2,915 x 2,015 mm
Span of the arch	3,000 mm	3,000 mm
Span-rise ratio of the arch	4:1	4:1
Arch bond pattern	Two-ring stack bonded	Single ring header bonded

Arch thickness	215 mm (two rings)	215 mm (single ring)
Bridge components	Arch, spandrel walls, abutments, and backfill	Arch, spandrel walls, abutments, and backfill
Backfill depth over the crown	300 mm	300 mm
Spandrel width	330 mm	328 mm
Material		
Brick	Type A engineering brick	Type A engineering brick
Brick compressive strength	115 kN	111.3 kN
Bonding material	1:2:9 lime mortar for radial joints; 1:1:6 strong mortar between rings	1:2:9 lime mortar
Backfill	50 mm graded crushed limestone	MOT type I graded crushed limestone
Test conditions		
Load types (at failure level)	Static full width line load	Static load (300 x 750 mm patch load)
Load location (at failure level)	Over quarter-span of the arch	Over quarter-span of the arch
Boundaries	3D	3D
Results		
Bridge conditions before the failure level load test	Spandrel separation	Spandrel separation; cracks in arch intrados; Formation of three hinges
Failure mechanisms	Four-hinge	Four-hinge
Ultimate load-carrying capacity	540 kN	639 kN

It can be seen from Table 5.2 that the materials adopted by both studies were quite similar, including the same bricks with comparable compressive strength and similar proportioned lime mortar. However, in the UoS 3-1 bridge, a stronger mortar was used to improve bonding between rings, thereby preventing ring separation.

Both bridges failed due to the formation of a four-hinge mechanism. However, the Salford bridge had a lower load-carrying capacity than the Leeds bridge, with a reduction of approximately 18%. This difference could be attributed to several reasons, including

a) Pre-loading condition and existing defects: neither bridge was in a virgin state prior

to the failure test. While the detailed loading sequence and crack patterns of Salford bridge were not fully documented in the literature, it was described as 'spandrels detached'. In contrast, the bridge tested in this study may have sustained more severe damage, as three hinges had already formed during the high-level load test; However, this factor would likely result in an underestimation of the ULS of Leeds bridge rather than making it higher than the Salford bridge.

b) The variability of masonry properties: Masonry is a composite material with inherent variabilities in its material and mechanical properties (i.e., strength of mortar, and defects of construction, etc.). These variabilities can potentially result in the variation of ULS of bridges.

c) Effect of loading area: Among the two factors discussed, the loading area seems to be a more significant factor that affect the ULS loads of the bridges. In the Salford test, a full-width line load was applied over the quarter of the arch, inducing a predominantly 2D structural behaviour. In contrast, a patch load was applied in Leeds test, which not only triggered the global failure mechanism of the bridge but also introduced significantly 3D response characteristics of the arch barrel (i.e., extensive web-pattern cracks observed on the arch intrados, as described in section 5.4.2 and Figure 5.5). The engagement of 3D response likely allowed the bridge to absorb more energy before failure, contributing to its higher ULS value compared to the Salford bridge.

In addition to the 3-1 bridge, the Salford testing also included a 3-2 bridge, which had the same materials and geometry as 3-1 bridge. However, in the 3-2 bridge, the two rings were bonded using a release agent to minimise the tensile bond strength, intentionally promoting ring separation. As a results, this 3-2 bridge exhibited a lower ULS value of 360 was, which was primarily due to a different failure mechanism – the ring separation rather than the four-hinge observed in the 3-1 bridge and the Leeds bridge. This highlights the significant role of inter-ring bonding strength in the overall load-carrying capacity of masonry arch bridges.

5.5 Conclusions

A large-scale brickwork masonry arch bridge has been constructed and load tested to failure in the laboratory. The aim of the work presented is to provide a better understanding on the three-dimensional (3D) response and interactions between different components of the masonry arch bridge under patch loads, as well as to

examine crack propagation and failure mechanism of the bridge. Also, a comprehensive dataset is provided for engineers and researchers to develop both low and high-fidelity numerical models.

The masonry arch bridge constructed in the laboratory incorporated a header-bonded brickwork arch barrel, brickwork abutments and spandrel walls, and employed compacted crushed limestone backfill material. Type A engineering brick and type O mortar was used to reproduce the low bonding strength found in many in-service masonry arch bridges. The bridge was instrumented with various sensors to comprehensively monitor its 3D response under a series of patch loads (line loads of the sort applied in previous studies were not used as these may artificially induce a two-dimensional response). Also, GPR surveys were carried out to assess the internal structure of both the virgin bridge and the bridge after load testing to failure. The bridge was subjected to progressively increasing levels of loads to investigate damage accumulation and crack propagation. Detailed 3D responses and failure mechanisms of the bridge subjected to a high-level load and two failure-level loads are presented and discussed in the chapter. Key issues, such as crack evolution, load-carrying capacity and the associated failure mechanism, and in-plane and out-of-plane deformations of the spandrel walls are discussed. Based on the results obtained, the following conclusions can be drawn:

1. Both a localized 3D response and a global four-hinge mechanism were captured during the load tests. The high-level load test, involving an applied load of 566 kN, induced three hinges. The first hinge appeared in the vicinity of the applied load and was characterised by formation of tensile cracks in the arch intrados under the loading point; the second hinge formed near the springing closest to the applied load and led to formation of cracks in the arch extrados; the third hinge was located in the midspan region, with fragments of crushed mortar falling from joints in the arch intrados. Upon further increasing the load, to 639 kN, a fourth hinge was observed at the springing furthest from the applied load, evident due to the presence of a tensile crack on the arch intrados. Additionally, the arch barrel was observed to behave in a 3D manner directly under the patch loading. Here the highest deformations were observed on the bridge centreline, directly under the load, with these gradually diminishing in magnitude at monitoring locations further from the load in a transverse direction. Also, cracks in the arch intrados were observed to radiate outwards from the loaded location, with cracks orientated both transversely

and diagonally, forming web-like patterns in the region lying between the two compression zones.

2. Although the bridge was nominally symmetric, and later tests on the structure were all applied on the bridge centreline, the response of the bridge was found to be asymmetric. This was observed in post-test inspections and analysis of in-plane and out-of-plane deformations of the spandrel walls. Specifically, it was observed that the widths of cracks forming in the north-side spandrel wall were greater than those in the south-side wall, and that out-of-plane deformations of the north-side wall were also greater. This might be attributable to variability in the masonry material properties and/or the effects of the low- and mid-level testing that was undertaken prior to the high- and failure-level load tests.

3. As testing moved from the high-level load test to the failure-level load tests, the bridge experienced a significant increase in damage, with extensive cracking observed in both the arch barrel and the spandrel walls, leading to a marked decrease in the stiffness of the bridge. Nevertheless, the load-carrying capacities achieved in the two failure-level load tests, conducted at the quarter and three-quarter span points, were quite similar, with the residual strength of the bridge decreasing by only approximately 10% after the first of these tests. This indicates that the damaged bridge still had significant residual load-carrying capacity.

4. No noticeable in-plane deformations of the spandrel walls were observed until the high-level test. The latter test started to mobilise the global bridge failure mechanism, with major cracks forming in the spandrel walls. Upward movement of the arch barrel remote from the applied load then led to in-plane deformations of the spandrel walls.

5. Out-of-plane deformations of the spandrel walls were observed in the high-level and failure-level load tests, with maximum deformations occurring close to the location of the load. In terms of accumulated deformations, the 150kN low-level tests did not induce any noticeable residual out-of-plane deformations. As the load was increased to 250 kN, off-centreline loads positioned close to a given wall resulted in residual deformations and a gradual increase in accumulated deformations. Loading on the bridge centreline, or on the side of the bridge remote from a given spandrel wall, did not induce significant out-of-plane spandrel wall deformations. Moreover, the high-level and failure-level load tests led to substantial increases in spandrel wall

deformation. After all tests had been conducted, the maximum recorded out-of-plane deformation of a spandrel wall was 23.2 mm.

This study has furnished a comprehensive dataset, capturing the 3D response characteristics, failure mechanism, load-carrying capacity, and damage accumulation in a masonry arch bridge subjected to patch loading. The results provide valuable insights into the behaviour of masonry arch bridges, including the interaction between its constituent components. Specifically, the results can be used to calibrate both high-and low fidelity numerical models.

Acknowledgements

6 Digital image correlation based crack monitoring on masonry arch bridges

This chapter represents the slightly modified post-print version of the article: **B. Liu**, J. Collier, and V. Sarhosis "Digital image correlation based crack monitoring on masonry arch bridge", Engineering Failure Analysis, 169 (2025) p.109185. The formatting and numbering of equations, tables and figures have been adapted to this document.

6.1 Abstract

Masonry arch bridges remain a vital part of the UK's transportation network. The combination of increased traffic loads and more frequent climatic and anthropogenic disasters has heightened the risk of structural failures in these aging infrastructures, making effective monitoring essential for maintaining their safety and operational performance. In this study, a large-scale masonry arch bridge was constructed and tested under controlled laboratory conditions. Static patch loads were applied both centrically and eccentrically to the backfill surface of the bridge to induce the damage accumulation. Digital image correlation (DIC) was utilized to monitor the initiation and propagation of full-field strain/cracking in the spandrel wall of the bridge during different magnitudes of loading and unloading states. Comparing DIC data with readings from displacement gauges, the results confirmed that DIC could measure the deformations of the untreated surface with satisfied accuracy, using the inherent brick bond patterns and natural characteristics of the masonry surface as tracking points. DIC results provided valuable insights into the cracking behaviour of the masonry arch bridge throughout the entire loading-unloading states, offering important information on the load levels that induced the onset and the activation of hinges. Additionally, the interaction between the arch barrel and spandrel wall, as well as the crack mechanism in the spandrel wall, were analysed. The findings reported in the study demonstrate the significant potential of DIC for real-time non-contact monitoring of real masonry arch bridges, offering a better understanding of their structural behaviour under various loading scenarios.

6.2 Introduction

The three-dimensional nonlinear responses of masonry arch bridges are complex, as the interactions of different components, such as the arch barrel, spandrel walls, backfill,

and piers/abutments needs to be considered. While prior research has predominantly concentrated on understanding the structural behaviour of arch barrels subjected to external loads, it is crucial to consider the role of other bridge components in overall structural behaviour of the masonry arch bridges, as they can contribute towards their load-carrying capacity and failure mechanism [64,138]. For example, the presence of spandrel walls can effectively enhance the stiffness and load-carrying capacity of the masonry arch bridges. However, they are susceptible to out-of-plane deformations due to eccentric loads from vehicles or trains, which can induce horizontal soil pressures, leading to potential tilting or bulging failures of the walls [81]. Additionally, hydraulic effects such as floods can destabilize piers, triggering further risks of structural failure [115,171,179]. Despite their significance, the impact of spandrel walls on the overall stability and performance of masonry arch bridges has received comparatively limited attention in existing literature. Also, the interaction between arch barrel and spandrel walls, as well as the cracking behaviour of the spandrel walls, have not been well understood.

Long-term non-destructive (NDT) assessment of masonry arch bridges is necessary to ensure their safety and longevity, and it requires minimal intervention to the structures during their operation. One representative NDT method is vibration-based structural health monitoring, which evaluates structural damage by detecting variations in modal parameters, such as frequencies and damping ratios [168,180–182]. Despite its effectiveness in reflecting overall structural behaviour, this method offers limited information on localised failure and damage accumulation, which are critical in assessing masonry arch bridges. Existing masonry arch bridges are also characterised by their relatively strong units with weak bonding materials. Thus, cracking is mainly occurring at the mortar, brick to mortar interface or their combination [183].

Digital Image Correlation (DIC) is a non-contact monitoring approach which offers a refined solution by measuring surface strain and deformation with high precision. This method involves analysing changes in the pixel positions of sequentially captured images to identify surface displacements. It has been particularly useful in laboratory conditions for analysing strain and deformation of masonry structures under loads [184,185], enabling the visualization of evolving crack patterns and concentrated strain areas [186–189]. Furthermore, the capability of DIC for full-field measurement not only enables the identification of movement at any individual point or changes in distance between two points within the field of view [190], but also facilitates the use of virtual extensometers

to calibrate material properties, such as Young's modulus and Poisson's ratio [191].

Recently, DIC is increasingly recognized for its application in the field monitoring of real structures, such as masonry buildings and arch bridges [192]. It enables the continuous assessment of structural performance under real loading conditions, thereby providing crucial data that supports timely maintenance decisions [193]. Notably, Acikgoz et al. [194,195] utilized DIC to observe the deflection of a masonry rail viaduct subjected to train loads. The multi-position measurements allows the three-dimensional response of the bridge to be analysed, such as pier rotation and transverse and longitudinal response of arches. Rajaram et al. [196] applied DIC to measure the deformation and damage accumulation of a large-scale masonry building subjected to seismic loads. Moreover, Stockdale et al [197], although they did not utilise traditional DIC, but employed a similar non-destructive vision-based technique to investigate the failure mechanism of masonry arches and identify hinge locations.

From the analysis of the literature, it was demonstrated that one of the most significant advantages of using this optical metrology is its capability to detect strain localization patterns associated with the onset of wall cracking before it could be captured by the displacement sensor or visual inspection. Moreover, integrating field monitoring data from DIC with numerical simulations could facilitate the development of digital twin models for masonry arch bridge and could support a more accurate structural assessment [198]. Also, previous studies have highlighted that using DIC to monitor real masonry arch bridges holds significant promise. The traditional application of DIC requires extensive preparation of the surface of the testing specimens to provide high-contrast, randomly distributed speckle patterns for tracking pixel-level movement and deformation. However, when employing DIC to monitor the crack and strain response of real structures, extensive surface treatment is difficult to be achieved, especially for ageing masonry arch bridges with significant landscape and historical values.

This chapter aims to make use of DIC and provide a better understanding of the crack propagation and accumulation of damage in masonry arch bridges. A large-scale masonry arch bridge was constructed and tested under controlled laboratory conditions. Static patch loads were applied both centrically and eccentrically to the backfill surface of the bridge to induce the damage accumulation. DIC was utilized to monitor the initiation and propagation of full-field strain/cracking in the spandrel wall of the bridge during different loading and unloading states. Moreover, the critical loading values that induced cracks, crack propagation, as well as the interaction between the spandrel wall

and the arch barrel were analysed. Finally, the potential of using DIC for monitoring masonry arch bridges in the field was also discussed.

6.3 Experimental programme

6.3.1 Masonry arch bridge
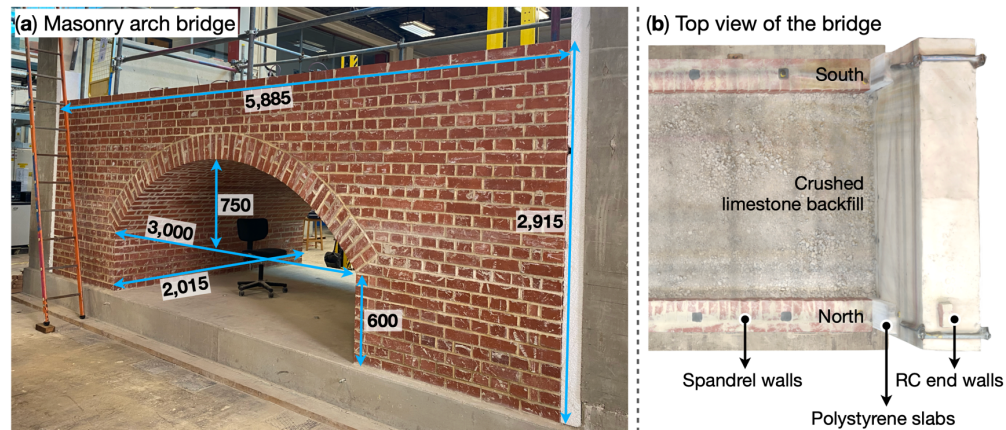
Figure 6.1 Masonry arch bridge specimen (all units in mm).

A large-scale masonry arch bridge was constructed, and load tested until failure. For the construction, type A engineering solid bricks were used, bonded together with lime mortar in a mix proportion of 1:2:9 (cement:lime:sand by volume). The bridge had a length of 5,885 mm, a height of 2,915 mm, and a width of 2,015 mm (see Figure 6.1 (a)). It contained a single-ring square arch barrel with a header bond pattern, 600 mm height stack-bonded abutments, one and half brick thick English bonded spandrel walls, and MOT type 1 graded crushed limestone for backfill material. In the longitudinal direction, the bridge was confined by two stiff reinforced concrete (RC) walls. The backfill was directly contacted with the RC walls, while four polystyrene sheets were placed between the spandrel walls and RC walls to avoid hard contact, allowing both in-plane and out-of-plane deflection of the spandrel wall (see Figure 6.1 (b)). The material characterisation, detailed design and construction of the masonry arch bridge can be found in chapter 4.

6.3.2 Loading protocol

Patch loads with increasing levels of magnitudes were applied to nine locations on the backfill surface, as illustrated in Figure 6.2. These loading locations were over the quarter-span, crown, and three-quarter span of the arch barrel, near the two sides of spandrel walls or at the longitudinal centre line of the bridge. Table 6.1 list the loading sequence. Specifically, the first two tests (T1 & T2) performed at point A and B were

served as trials. Start from T3 to T11, a low-level load with a magnitude of 150 kN was applied to nine locations sequentially. At each loading location, a static load was first applied (light blue in Table 6.1), followed by three loading cycles (cyclic) with the same loading rate and magnitude (highlighted in dark blue in Table 6.1). After the low-level loading tests, the loading magnitude was increased to 250 kN, less than 50 % of the load carrying-capacity of the bridge according to the preliminary numerical analysis, and the mid-level load was again applied to all the nine locations (T12 to T20). Similar with the low-level tests, at each loading locations, a static load was applied first (light orange in Table 6.1), and then three loading cycles were followed (dark orange in Table 6.1). For the low- and mid-level tests, a loading control with a rate of 10 kN/min was adopted for both the loading and unloading process, and the patch loading area was 300 x 300 mm.
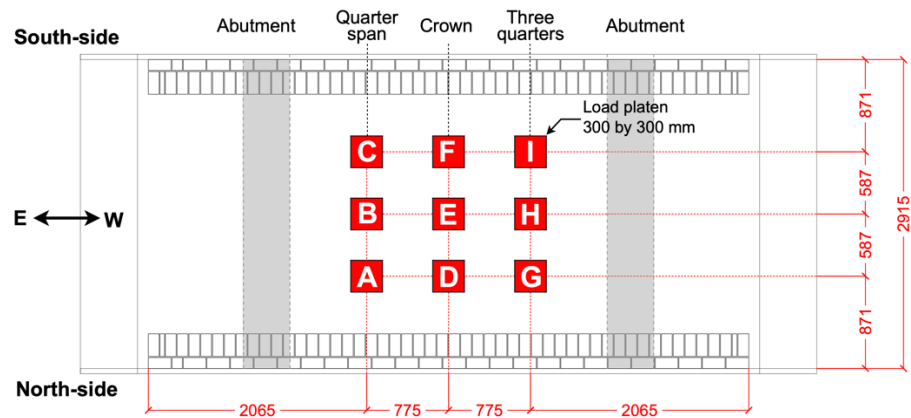
Figure 6.2 Nine loading locations on the backfill surface (all units in mm).

Table 6.1 Loading protocol adopted in the experimental campaign.

	T1	T2	T3	T4	T5	T6	T7	T8	T9	T10	T11	T12	T13	T14	T15	T16	T17	T18	T19	T20	T21	T22	T25
A	LS						LS/LC						MS/MC										
B		LS						LS/LC												MS/MC	HS	FS	
C			LS/LC														MS/MC						
D				LS/LC										MS/MC									
E					LS/LC													MS/MC					
F						LS/LC										MS/MC							
G									LS/LC			MS/MC											
H										LS/LC									MS/MC				FS
I											LS/LC				MS/MC								

Legend:

Low-level static (150 kN)	Low-level cyclic (150 kN)	Mid-level static (250 kN)	Mid-level cyclic (250 kN)
High-level static (560 kN)	Failure level static		

After the mid-level loading tests, a high-level load with a magnitude of 560 kN was applied at point B, over quarter-span of the arch barrel (T21, light green in Table 6.1). Then, two failure-level tests were conducted at point B and H, respectively, to assess the load-carrying capacity and residual performance of the bridge (T22 and T25, dark green in Table 6.1). A displacement control method with a rate of 0.05 mm/s was used for the loading application to better control the bridge's post failure behaviour, and the loading area was increased to 750 mm x 300 mm to induce the global failure mode of the bridge.

6.3.3   Instrumentation and digital image correlation (DIC)

The bridge was extensively instrumented using both contacting gauges and DIC to capture its response under loads. Deflections of the arch barrel, abutments, and spandrel walls were measured by 25 potentiometer gauges and 15 linear variable differential transformers (LVDTs). Also, 4 accelerometers were placed on the top of the spandrel walls to capture the vibration response of the bridge. The detailed instrumentation layouts, as well as the 3D response characteristics obtained from contact gauges have been reported in [145,177,181]. This chapter focused on the field deformation monitoring of the south-side spandrel wall obtained using DIC.

The 3D DIC setup is presented in Figure 6.3. Specifically, an independent stiff frame was sat in front of the south-side spandrel wall, with two pairs of low distortion lens monochrome cameras mounted on (see Figure 6.3 (a)). With three steel portals of the reaction frame, the south-side wall was separated into four parts. Two centre areas were inspected by two pairs of cameras, respectively. With the loads applied within the quarter-span and three-quarter span region, these two central areas of spandrel wall was expected to develop extensive cracks. Each field of view (FOV) had an approximate area of 1,400 mm x 1,400 mm, as shown in Figure 6.3 (b). The cameras used had 5,472 x 3,648 pixels resolution and 2.4 × 2.4 μm pixel size (HIKROBOT MV-CE200-11UM), and it was equipped with a lens having a F-number of F1.8 to F16 and a focal length of 6 mm (HIKROBOT MVL-KF0618M-12MPE). The F-stop was set to near F2.8 in accordance with the laboratory lighting conditions. Additionally, it should be noted that the MVS_DIC software that used for image capturing, developed by HIKROBOT, is equipped with automatic exposure and gain functions to ensure optimal image exposure. During the tests, cameras were positioned at around 1,356 mm in front of the spandrel wall, while the distance between the centre of the view on the spandrel wall to the lens, perpendicular to the lens, was 1397 mm according to the calibration information. The distance between two cameras was around 0.6 m (see Figure 6.3 (c)).
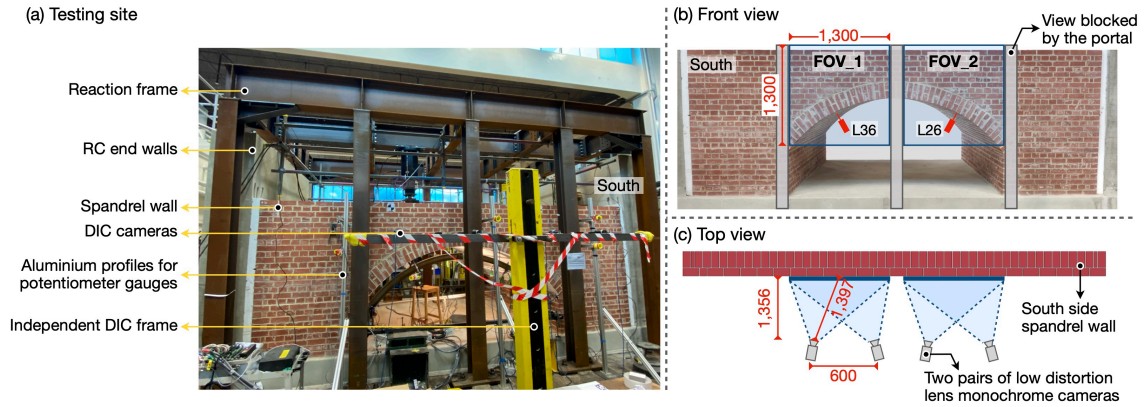
Figure 6.3 Experimental setup (all units in mm): (a) testing site; (b) Front view of the south-side spandrel wall showing the DIC inspection area; and (c) top view showing the locations of cameras.
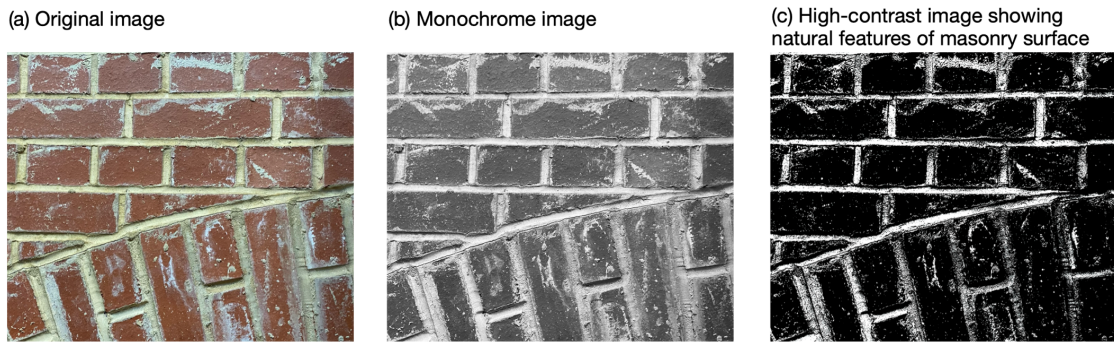
Figure 6.4 Natural features on the surface of masonry.

To enable tracking capabilities for DIC, the surface of object is usually prepared with a high-contrast, random speckle pattern. Performing such a surface treatment is unlikely for masonry arch bridges in the field, especially for those with special historical value. Thus, in this study, the south-side spandrel wall was left in its natural state without any surface preparation, and the brick bond pattern as well as the natural features of masonry, such as mortar debris and surface texture of bricks, were utilised as tracking points for DIC analysis (see Figure 6.4). Furthermore, to validate the accuracy of DIC results, data obtained from physical contact gauges was used to compare with the DIC measurements. For example, two LVDT gauges (L36 and L26 in Figure 6.3 (b)) placed at the quarter-span and three-quarter span points at the south edge of the arch intrados, respectively, were used to measure the radial deflection of the arch intrados under loads. Prior to testing, the DIC system was calibrated by taking 28 images of a standard calibration plate with different positions and orientations (see Figure 6.5 (a) and (b)). The plate had a dimension of 1,188 x 765 mm, with black marks on white backgrounds. Images collected were analysed by using the LaVision version 10 software equipped with both 2D and 3D strain analysis modules.

153
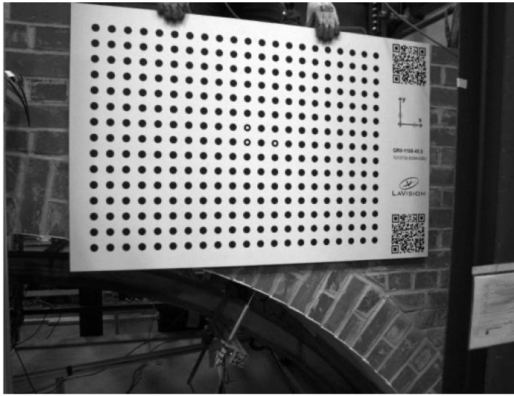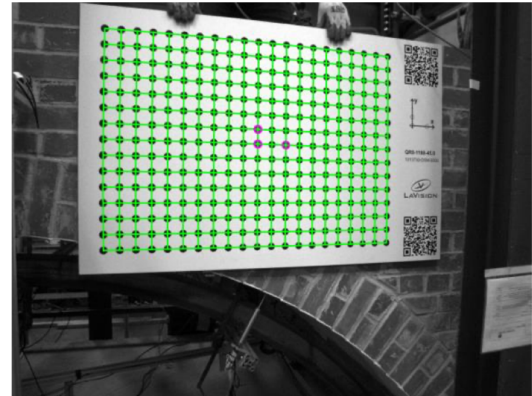
Figure 6.5 DIC calibration: (a) calibration image; and (b) calibrated image.

6.4 Results and discussion

6.4.1 Visual inspection on the crack propagation of the south-side wall

Visual inspection was performed after each test, and the crack pattern was carefully documented. Figure 6.6 shows the crack propagation of the south-side wall subject to increasing loading magnitudes. At the low-level loading tests, it is shown that the first crack was initiated at T6 with loading applied over the arch crown close to the south-side wall. After T6, a hairline crack was observed between arch ring and spandrel wall. Then, T11, where the load was applied over the three-quarter span of the arch close to the south-side wall resulted in the separation between arch ring and south wall extended (see Figure 6.6 (a)). As the loading magnitude increased to 250 kN, the medium level, loading over the quarter-span and three quarter-span locations close to the south-side wall led to the opening of tensile cracks at arch intrados under loads. Also, loading over crown of the arch near south-side wall led to the further propagation of the separation between the arch ring and the spandrel wall (see Figure 6.6 (b). It is worth noting that during the low- and mid-level loading tests, any loads applied at longitudinal central line and near the north-side wall did not cause any visible crack on the south-side of the bridge.

At the high-level and two failure-level tests, loads were applied at point B and H, along the longitudinal centre line of the bridge, over the quarter-span and three quarter-span locations, respectively. During these tests, significant crack evolution was observed (see Figure 6.6 (c) to (e)). The predominant crack mechanism of the south-side wall was influenced by the deflection of the arch ring. Specifically, at the non-loading side, cracks initiated from the top of the spandrel wall and propagated downwards, while at the loading side, cracks started from the spandrel wall-arch barrel interface and extended upwards diagonally. Moreover, the rotation of the wall at the non-loading side resulted

154

in several cracks initiated from the non-loading side springing and propagated diagonally downwards.
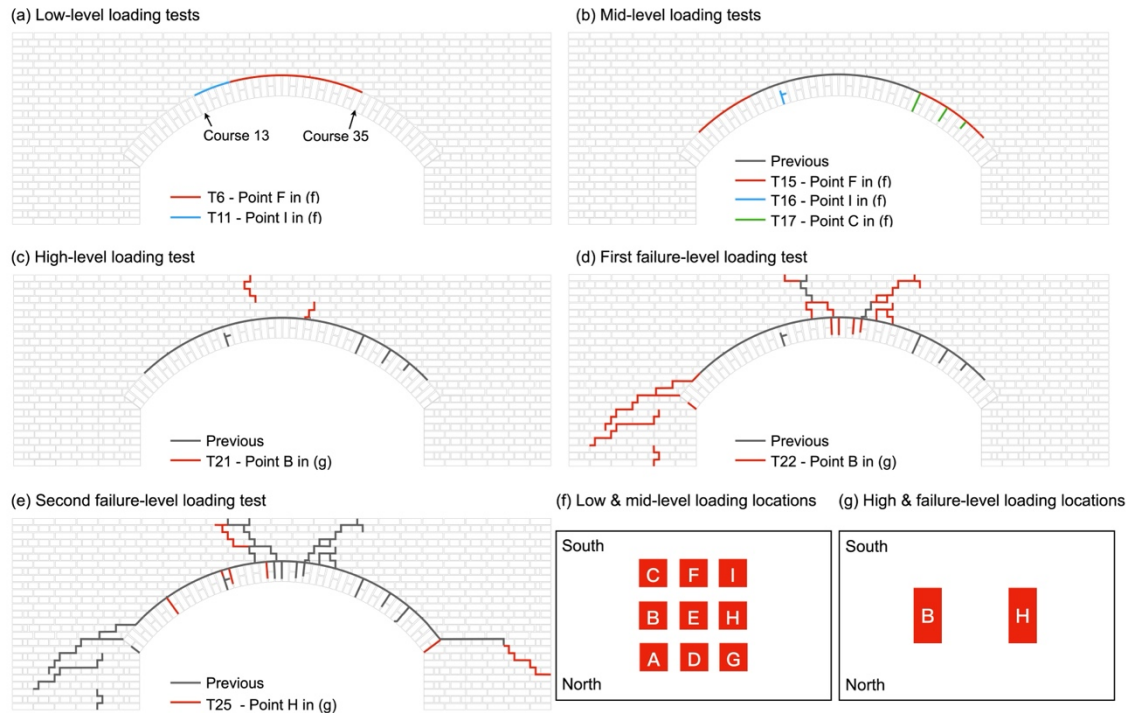
Figure 6.6 Crack propagation of the south-side spandrel wall at: (a) low loading level tests; (b) medium loading level tests; (c) high loading level test; (d) and (e) the first and second failure loading level tests; (f) and (g) show the loading locations at the low- and mid-level, as well as the high and failure level, respectively.

Visual inspections, though valuable for preliminary assessments of cracks, are substantially limited as the sole monitoring approach. First, these inspections are time consuming, especially for the detection of early-stage cracks in large-scale bridges. Second, safety protocols restricted to visually inspecting bridges until after all loads are removed. This delay prevents the capture of critical loading values that induce cracks, thus limiting a comprehensive understanding of the crack propagation and damage accumulation in the bridge. To overcome these challenges, DIC enabled us to obtain continuous, full-field strain monitoring throughout the loading and unloading processes. The results obtained from DIC are presented in the Section 6.4.2.

6.4.2 Validation: comparison of DIC and LVDT data

Figure 6.7 compares the radial deflection of the quarter-span and three-quarter span points at the arch barrel obtained from DIC and LVDT gauges. Specifically, during T21 and T22, a static load was applied to point B, over quarter-span of the arch barrel along the longitudinal centre line of the bridge (see Figure 6.2). L26 was placed at the loading side, south edge of the arch intrados (Figure 6.7 (a)), whereas L36 was placed at the non-

loading side, south edge of the arch intrados (Figure 6.7 (d)). With the 'strain gauge' function built in the software, the absolute value of the displacement at the radial direction of bricks where L26 and L36 attached to were extracted. It is worth noting that the DIC data and LVDT readings were not extracted from the same point of location, but from the same brick on the arch barrel.
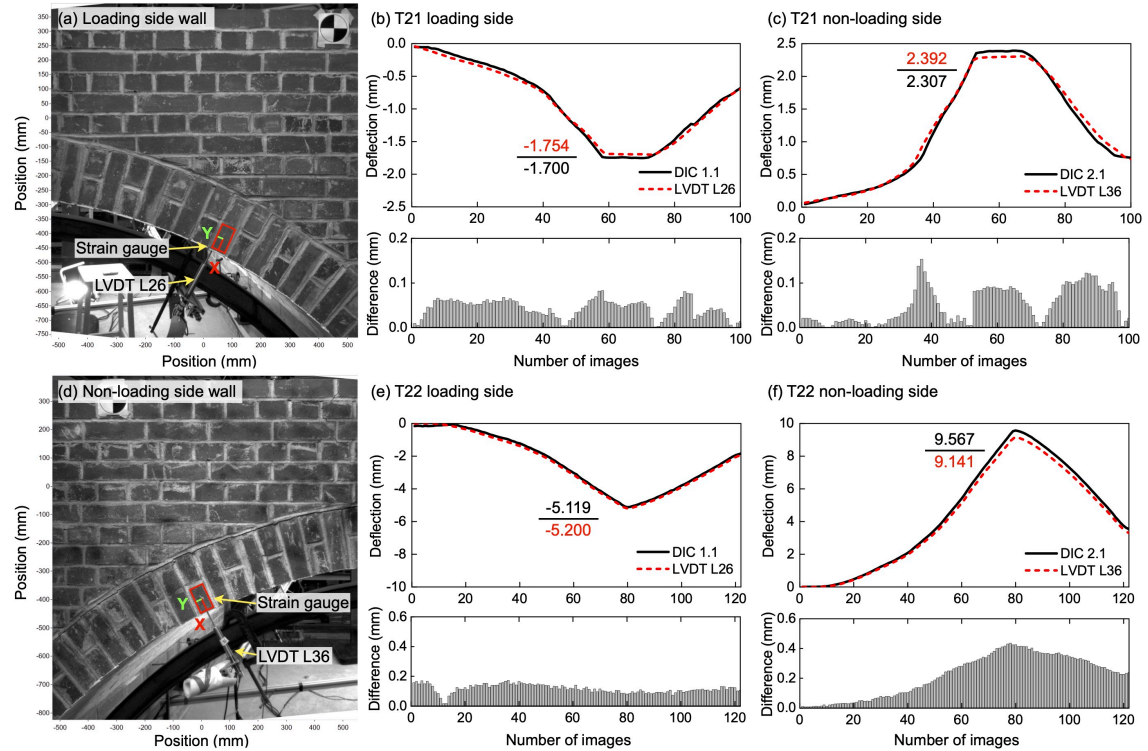
Figure 6.7 Comparison of radial deflection of the arch barrel at the loading and non-loading side between DIC and LVDTs: LVDTs and DIC inspection points at (a) loading side wall (quarter-span) and (d) non-loading side wall (three-quarter span); radial deflection comparison and differences between DIC and LVDT for (b) T21 loading side; (c) T21 non-loading side; (e) T22 loading side; and (f) T22 non-loading side.

By comparing the curves in Figure 6.7 (b), (c), (e), and (f), it is evident that deflections recorded by DIC and LVDT were nearly identical, in terms of both variation tendencies and peak values. When the load increased to its peak value, deviations between DIC and LVDT readings remained below 0.100 mm, with an exception at T22 on the non-loading side of the bridge (Figure 6.7 (f)), where the difference increased to 0.426 mm. Nonetheless, this difference, representing less than 5% of the bridge's response, and is considered minimal. Small errors in measurements obtained can be attributed to various reasons. Primarily, the use of masonry surface features and natural lighting conditions in DIC measurements likely impedes its ability to achieve the micrometre-level precision of 0.0001 mm, thus increasing the susceptibility of optical measurements to environmental interference. Additionally, the LVDT was attached to the header face of

the brick, whereas the DIC measured the stretcher face displacement of the same brick. Slight elastic deformations of the brick might cause observable differences in displacement readings at these distinct measurement points. Furthermore, LVDTs might not be perfectly perpendicular to the arch intrados, introducing further variances in the measurements. Despite these variations, the accuracy of DIC is confirmed to be acceptable for effectively monitoring crack behaviour in masonry arch bridges.

6.4.3   Damage monitoring

Following the validation, this chapter presents the analysis of the results obtained from DIC on the damage accumulation and crack propagation. Specifically, the critical load values that induce cracking are examined, such as the opening of the first crack, the occurrence of the first tensile crack at arch intrados, as well as the formation of hinges. This is then followed by the discussion of crack behaviour of the masonry arch bridge spandrel wall and the interaction mechanism between the arch ring and spandrel wall.

The first crack occurred at the south-side face of the bridge was observed at T6, when the static load with a magnitude of 150 kN was applied at point F, over the crown of the arch barrel close to the south-side spandrel wall (see Figure 6.8 (a)). Figure 6.8 (b) depicts the load-radial deflection curves obtained from LVDT placed underneath the loading location. The crack characterised the early-stage damage in the masonry arch bridge that the arch barrel and spandrel wall separated due to the downwards movement of the arch barrel under loading. From the DIC monitoring, the crack initialised when the load reached around 65 kN. At the peak load of 150 kN, the crack extended between quarter-span and three-quarter span of the arch, and the maximum width of the crack was approximately 0.40 mm, as shown in Figure 6.8 (c).

The load redistribution capability of an arch significantly affects the load-carrying capacity of a masonry arch bridge. However, the progressive formation of hinges and extensive deformation of the arch barrel can substantially alter the load distribution across the arch, resulting in increased stress concentration at the hinge locations, which may lead to bridge collapse [199]. Understanding the loads that induce hinges and the corresponding deformed shape of the arch is crucial for assessing the condition of masonry arch bridges and guiding maintenance strategies.

(a) Loading location

(b) Load deflection curve

(c) Max. normal strain distribution at the peak load
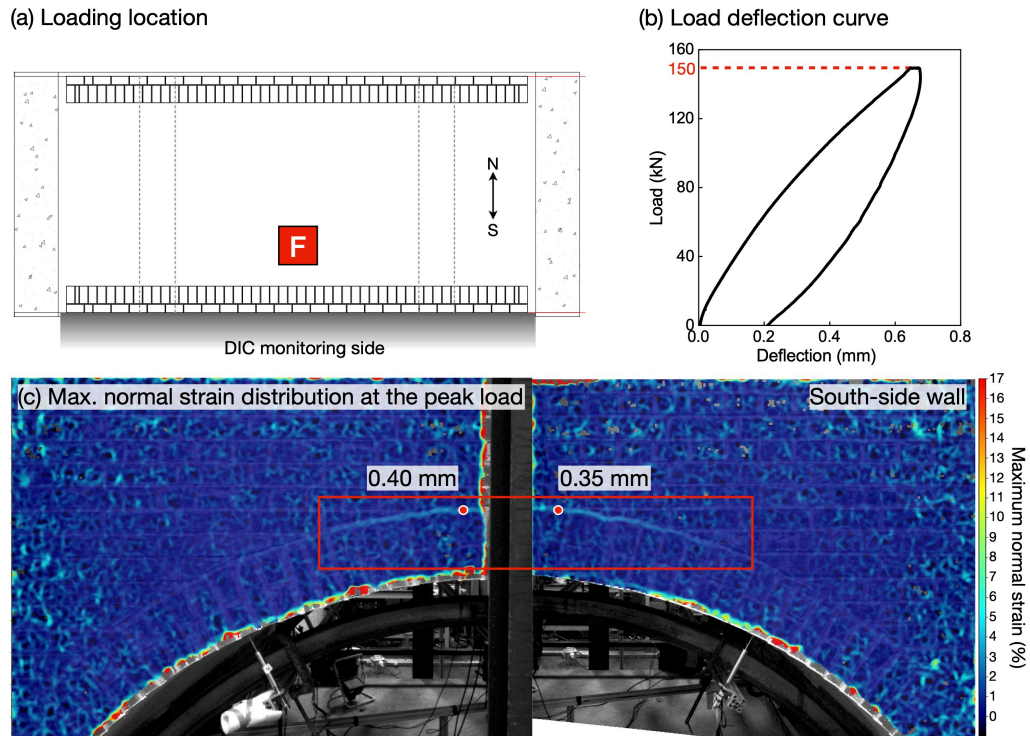
South-side wall

Figure 6.8 Results obtained from T6: (a) loading location; (b) load-radial deflection response of the arch intrados obtained from the LVDT placed underneath the loading location; and (c) maximum normal strain distribution of the south-side wall showing the opening of the first crack.

During T16 and T17, where medium-level loads were respectively applied over the three-quarter span and quarter-span of the arch near the south-side spandrel wall, tensile cracks were induced in arch intrados under loading locations. Figure 6.9 shows the results obtained from T16. Notably, Figure 6.9 (b) illustrates the maximum normal strain distribution on the south face of the bridge, highlighting a primary crack at the three-quarter span region between the arch barrel and the spandrel wall. Additionally, a tensile crack was observed at the arch intrados under the loading location. At these two locations, crack width versus load curves were derived from DIC by measuring the change in distance between two neighbouring bricks (see Figure 6.9 (c) and (d) respectively). The width of crack was captured by monitoring changes in the distance between two points, specifically, two points on a pair of neighbouring bricks located on either side of the cracked joint, with their connecting line perpendicular to the joint. The original data exported from DIC (grey lines in Figure 6.9 (c) and (d)) showed an approximately ± 0.1 mm level of fluctuation. This observed noise primarily resulted from factors such as insufficient and unstable lighting conditions and a lack of adequate high-contrast tracking points. However, for masonry structures, submillimeter-level accuracy is considered sufficient for examining cracks. To eliminate the influence of noise on data

trends, Savitzky-Golay filter algorithm was employed for data smoothing [200,201]. This filter functions by fitting successive subsets of adjacent data points with a low-degree polynomial through the method of linear least squares. It not only maintains the shape and features of the underlying data but also effectively reduces the data fluctuations caused by noise [202].
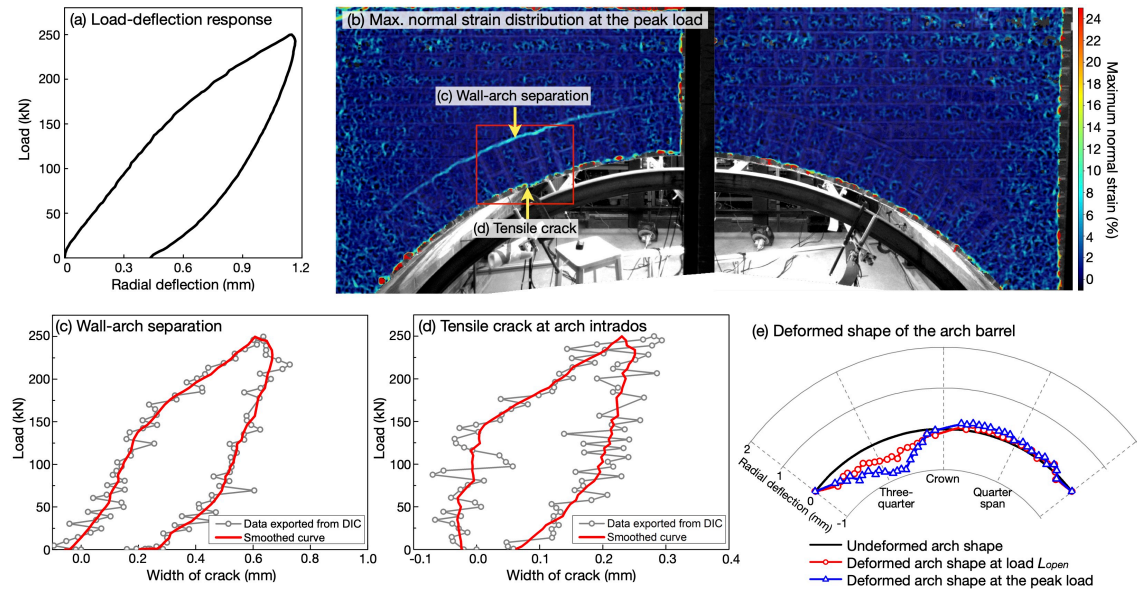
Figure 6.9 Results obtained from T16: (a) load-radial deflection response of the arch intrados obtained from the LVDT underneath the loading location; (b) maximum normal strain distribution on the south-side wall at the peak load; (c) and (d) development of the crack width of arch-wall separation and opening of the tensile crack at the arch intrados, respectively; (e) deformed profiles of the arch barrel.

The growth of crack width at the arch barrel-spandrel wall interface was almost linear, as this crack was formed previously at low loading level tests. Conversely, a noticeable change in the slope of the tensile crack width versus load curve (Figure 6.9 (d)) indicated an initiating load of approximately 170 kN for the first tensile crack. Moreover, Figure 6.9 (e) shows the deformed shapes (radial deflection) of the arch barrel at the load that induced the opening of tensile crack (L_{open}) and at the peak load of 250 kN. The primary deflection was between the loading side springing and the mid-span of the arch. Upon the initialisation of the tensile crack, the maximum radial deflection of the arch barrel was approximately -0.54 mm, which increased to -0.86 mm as the load raised from 170 kN to 250 kN, suggesting a more rapid deflection after the formation of the crack. Minimal radial deflection was noted in other sections of the arch barrel, with values on the non-loading half registering less than 0.2 mm.

Loading over the quarter-span of the arch near the south side spandrel wall (T17) resulted in similar behaviour of the bridge, in terms of both the arch deflection and

cracking development, as illustrated in Figure 6.10. At the quarter-span, the first tensile crack in the arch intrados initialised when the vertical load reached approximately 124 kN. This lower load from quarter-span, compared to that obtained from the three-quarter span, may be attributed to a combination of factors including the inherent variability in masonry properties and a loading sequence that resulted in reduced stiffness of the bridge at T17 than T16.
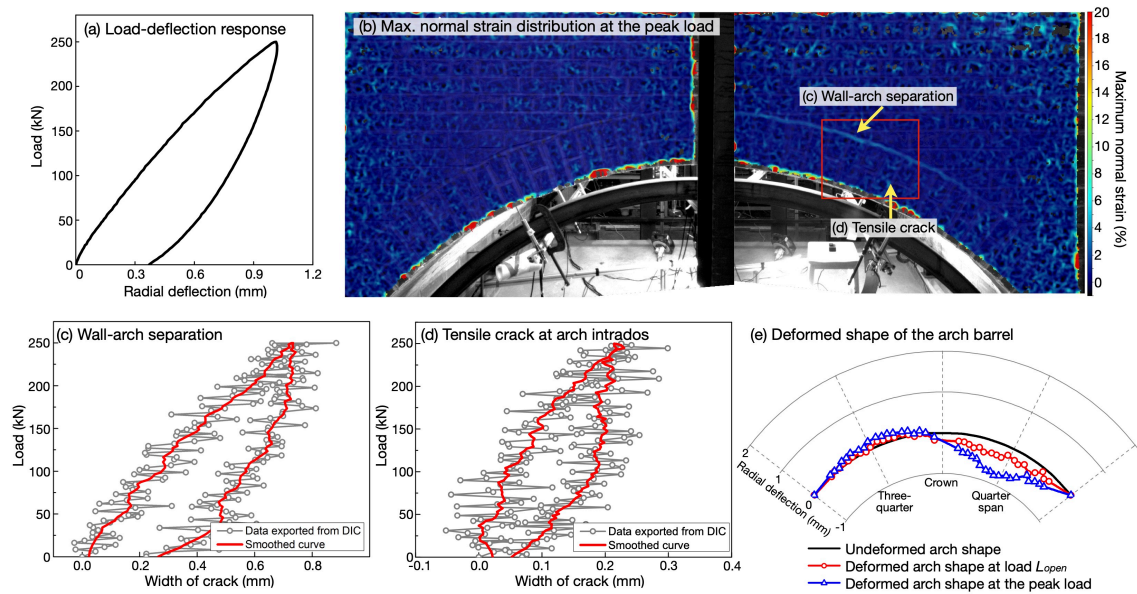
Figure 6.10 Results obtained from T17: (a) load-radial deflection response of the arch intrados obtained from the LVDT underneath the loading location; (b) maximum normal strain distribution on the south-side wall at the peak load; (c) and (d) development of the crack width of arch-wall separation and opening of the tensile crack, respectively; (e) deformed profiles of the arch barrel.

Following the mid-level tests, a high loading level test with a magnitude of 560 kN was performed at point B, located over the quarter-span of the arch along the longitudinal centreline of the bridge (see Figure 6.11 (a)). This test aimed to induce the global damage of the bridge. The formation of two hinges was captured by DIC at the loading side (see Figure 6.11 (b)). Figure 6.11 (c) and (d) show the relationship between load and crack width for the 1st and 2nd hinges, respectively. The critical loads that initiated these hinges were identified at the inflection points on the smoothed curves. From Figure 6.11 (c) it was shown that the first hinge was induced when the load increased to 378 kN (59% of the ultimate limit state, ULS, of the bridge), which was slightly higher than that observed at T17. This discrepancy can be attributed to the eccentric load that applied at T17, which caused more significant deformation on the south side of the arch, resulting in the localised crack in the arch intrados. Such eccentric loading likely caused greater deformation on the arch at the south-side. In contrast, during T21, the load was applied

along the longitudinal centreline of the bridge. This means that the first hinge's activation, representing the global damage mechanism, required the mobilization of the arch's three-dimensional effects, where deformation under the load point was maximized and diminished transversely as it moves away from the point of load application [145]. The 2nd hinge was observed near the loading side springing, represented by an opening of crack at the arch extrados. Its width development plotted in Figure 6.11 (d) suggested an inducing load of 429 kN (67% of the ULS of the bridge). Additionally, the third hinge was induced as well, which was located in the mid-span region and characterised by the crushing of the mortar joints. However, this hinge was not able to be captured by DIC as the presence of column of the steel reaction portal blocked the view of the cameras.

Figure 6.11 Crack opening obtained from T21: (a) loading location; (b) locations of hinges; (c) and (d) development of crack width at the first and second hinge locations, respectively.

Figure 6.12 shows the arch deformed profiles, normal strain and displacement maps of the bridge's south face at two stages, including the activation of two hinges and the peak load (Figure 6.12 (a)). It is worth noting that the deformed profile showing in Figure 6.12 (b) was the radial deflections of the arch, achieving by extracting the absolute displacement at the radial direction of every single brick on the arch that were visible in DIC monitoring areas. At stage 1, a separation between the arch barrel and the spandrel wall was observed near the loading location. Also, the arch at the hinge location had the maximum deflection, with other locations of the arch didn't deform significantly (Figure

6.12 (b) red line and Figure 6.12 (c)). After the formation of the hinges, a rapid damage accumulated with significant deformation of the arch occurred along with an increase in the load from approximately 450 kN to 560 kN (Figure 6.12 (b) blue line). The arch at the loading location moved further down from -0.7 mm to -1.8 mm, and more notably, the non-loading side of the arch moved upwards substantially from 0.3 mm to over 1.9 mm.
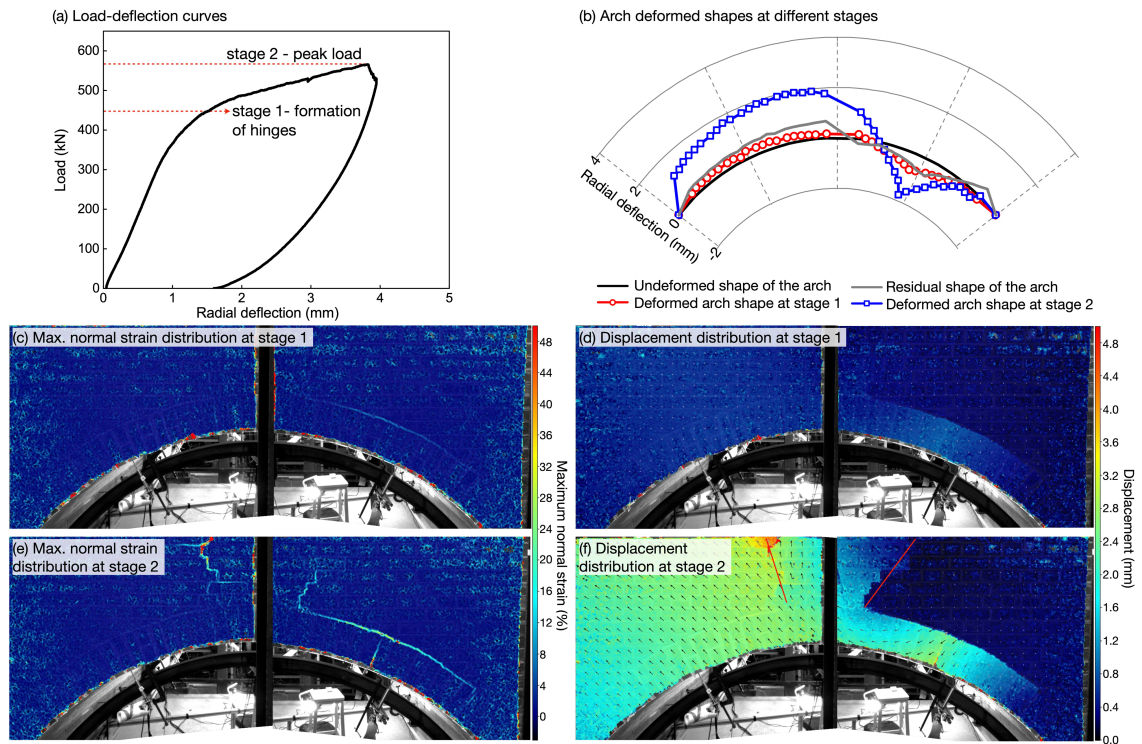
Figure 6.12 Response of the bridge at T21: (a) load-radial deflection curve obtained from the LVDT underneath the loading location; (b) arch deformed profiles at different stages; (c) and (d) maximum normal strain and displacement maps of the bridge south face at stage 1 (formation of the 1st and 2nd hinges); (e) and (f) maximum normal strain and displacement maps of the bridge south face at stage 2 (at the peak load).

The interaction between the arch barrel and spandrel wall in this case is primarily characterised by their deformation compatibility. The deformation of the arch barrel resulted in the formation of two distinct cracks in the spandrel wall. Specifically, at the loading side, the arch barrel moved downwards under loading. The downward movement of the arch activated the formation of the first hinge under the loading location, causing the lower right part of the arch (the blue segment in Figure 6.13 (a)) to rotate around the second hinge point and the upper left part (the red segment in Figure 6.13 (a)) to rotate around the third hinge, which in this case was located at the mid-span region. On the non-loading side, the arch barrel rotated around the fourth hinge at the springing (the green segment in Figure 6.13 (a)), pushing the spandrel wall to move in

two directions. The section of the spandrel wall over the mid-span of the arch barrel was pushed upwards, while the part adjacent to the three-quarter span of the arch moved upwards diagonally. Discrepancies in the movement of different part of the spandrel wall led to the formation of two diagonal cracks in the spandrel wall: one originated from the arch-wall interface between the loading side and the mid region, extending diagonally upwards, and another starting from the top of the wall between the mid region and the non-loading side, propagating diagonally downwards to the arch-wall interface at the mid-span of the arch, where the third hinge was located.
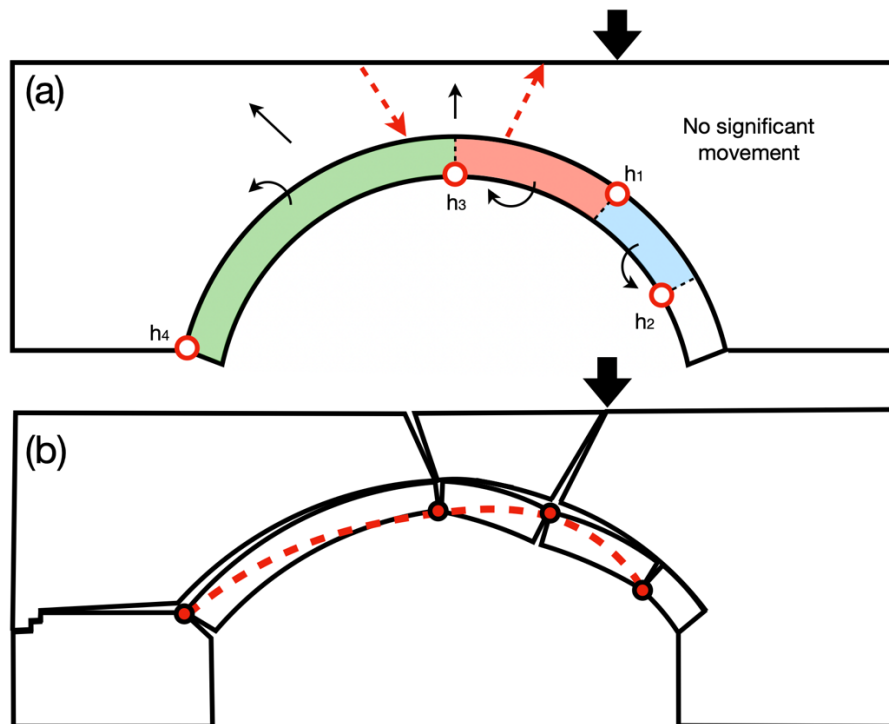
Figure 6.13 (a) Interaction between spandrel wall and the arch barrel in terms of their deformation compatibility; (b) failure mechanism.

At the same loading location B, the first failure level test was performed. Figure 6.14 shows the crack width responses at three identified hinge locations, illustrating significant reductions in the loads required to induce the first and second hinges after the activation of the global four-hinge mechanism in the previous high-level test T20. Specifically, the load resulting in the formation of the first hinge decreased by 52%, from 378 kN to 180 kN (Figure 6.14 (c)), and the load for the second hinge reduced by 40%, from 429 kN to 258 kN (Figure 6.14 (d)). Additionally, Figure 6.14 (e) highlights noticeable cracking between two bricks on the arch extrados in the mid-span region at an approximate load of 625 kN. It is important to note that Figure 6.14 (e) does not indicate the formation of the third hinge at this load, as the mortar joints between the

two courses at the mid-span of the arch barrel already been crushed under compression during the high-level test. However, the detection of this area was obscured by a steel portal, making it invisible to DIC. Thus, Figure 6.14 (e) implies that by the time the load reached 625 kN, the compression zone at the mid-span had extended to a wider area, indicating that bridge failure mechanism was fully activated.
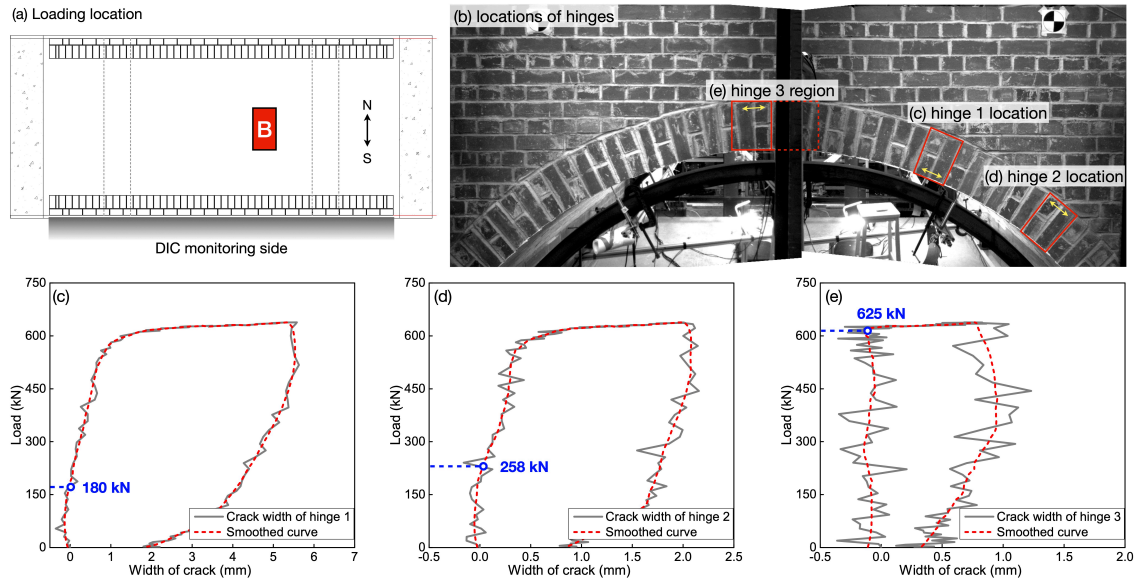
Figure 6.14 Crack opening obtained from T22: (a) loading location; (b) locations of hinges; (c) to (e) development of crack width at the first, the second, and the third hinge locations, respectively.

The arch deformed profiles, strain and displacement maps at different stages at T22 are shown in Figure 6.15. The load-carrying capacity of the bridge was identified as 639 kN in this test. Before the fully activation of the four-hinge mechanism, the load-deflection response of the bridge was almost linear, as the hinge 1 to 3 had been mobilised previously (see Figure 6.15 (a)). The behaviour of the bridge at this failure level could be primarily characterised by the accelerated deflection of the arch barrel, along with the propagation of the cracks initiated at T21 and significantly increase in the width of cracks and deformation of the spandrel wall. For instance, the maximum deflection of the arch barrel was equal to approximately 4.7 mm when the load reached 600 kN. However, as the load increased from 600 kN to 639 kN, the maximum deflection of the arch barrel raised significantly to 9.1 mm, indicating the loss of stability in the arch barrel. Moreover, After the fully activation of the four-hinge failure mechanism, the non-loading side spandrel wall rotated, evidenced by the opening of the joint and the noticeable displacement discontinuity between the arch barrel and the spandrel wall near the non-loading side springing (see Figure 6.15 (g) and (h)).
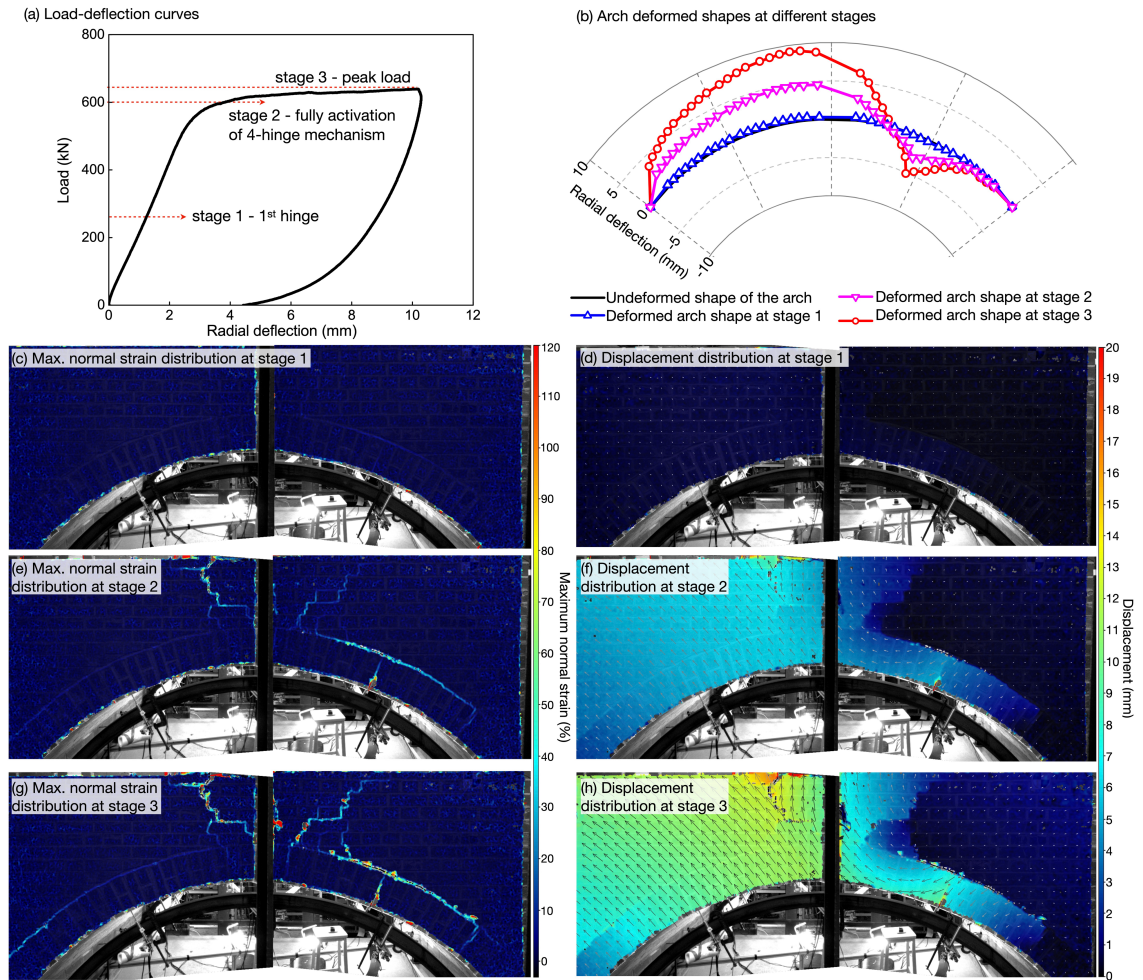
Figure 6.15 Response of the bridge at T22: (a) load-radial deflection curve of the arch intrados obtained from the LVDT positioned underneath the loading location; (b) arch deformation shapes at various loading stages; (c) and (d) maximum normal strain and displacement maps of the bridge south face at stage 1 (opening of the 1st hinge); (e) and (f) maximum normal strain and displacement maps of the bridge south face at stage 2 (fully activation of the four-hinge mechanism); (g) and (h) maximum normal strain and displacement maps of the bridge south face at stage 3 (at the peak load).

After the bridge failed under a patch load that applied at point B, the load was relocated to point H, positioned over the three-quarter span of the arch barrel along the longitudinal centreline of the bridge (see Figure 6.16 (a)), and the bridge was loaded to failure again to assess its residual behaviour. The development of crack width at three hinge locations is plotted in Figure 6.16 (c), (d), and (e), respectively. Notable, the activation of hinges occurred at reduced loading levels: the first hinge formed at 62 kN, the second at 312 kN, and the third at 261 kN. Loads inducing the first and third hinges are significantly lower than the loads observed during the first failure level test, indicating a substantial decrease in the bridge's stiffness. Furthermore, the load inducing the second hinge was slightly higher than that for the third hinge in this case. This discrepancy can be attributed to the mortar joints at the mid-span having been smashed

and softened by the previous tests, while the location around the second hinge had remained uncracked prior to this test. This led to variations in the hinge mobilisation, reflecting the altered structural behaviour of the bridge.
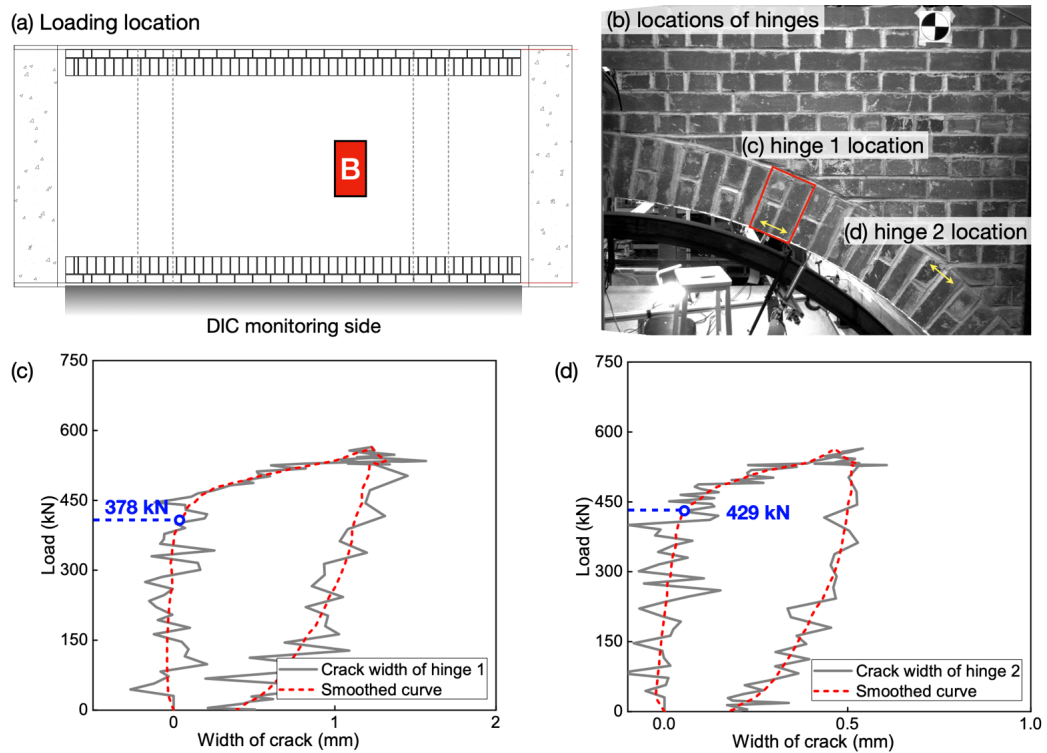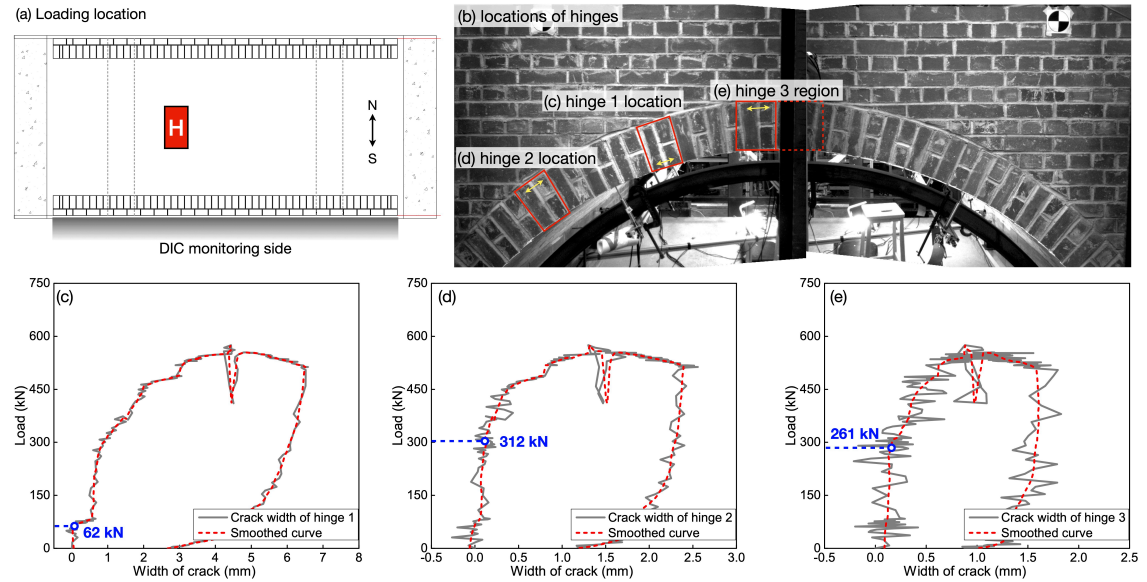

Figure 6.16 Crack opening obtained from T25: (a) loading location; (b) locations of hinges; (c) to (e) development of crack width at the first, the second, and the third hinge locations, respectively.

The load-deflection curve, arch deformed profiles, and strain and displacement maps for various stages at T25 are shown in Figure 6.17. The analysing area of DIC did not fully cover the camera view at the left side due to the presence of a cable. The residual capacity of the bridge was determined to be 575 kN (see Figure 6.17 (a)). The crack patterns and deflection responses of the bridge at T25 were similar to those observed from T22. Nevertheless, since multiple cracks in the spandrel wall fully opened during T22, forming weak planes, the crack patterns obtained in T25 followed those formed at T22. Also, the previously formed cracks led to the stiffness of the bridge became lower, resulting in the deflection of the bridge, including both the arch barrel and the spandrel wall, became more significant. When the load reached to its peak value, the maximum deflection of the arch barrel was similar to that observed from T22, the first failure level test. At the post failure stage, the deflection of the arch barrel became more rapid, and the maximum deflection of the arch was 14.78 mm. Furthermore, after the removal of the load, a significant residual deflection was observed in the arch intrados, with the maximum deflection equal to 6.1 mm (see Figure 6.17 (b)).
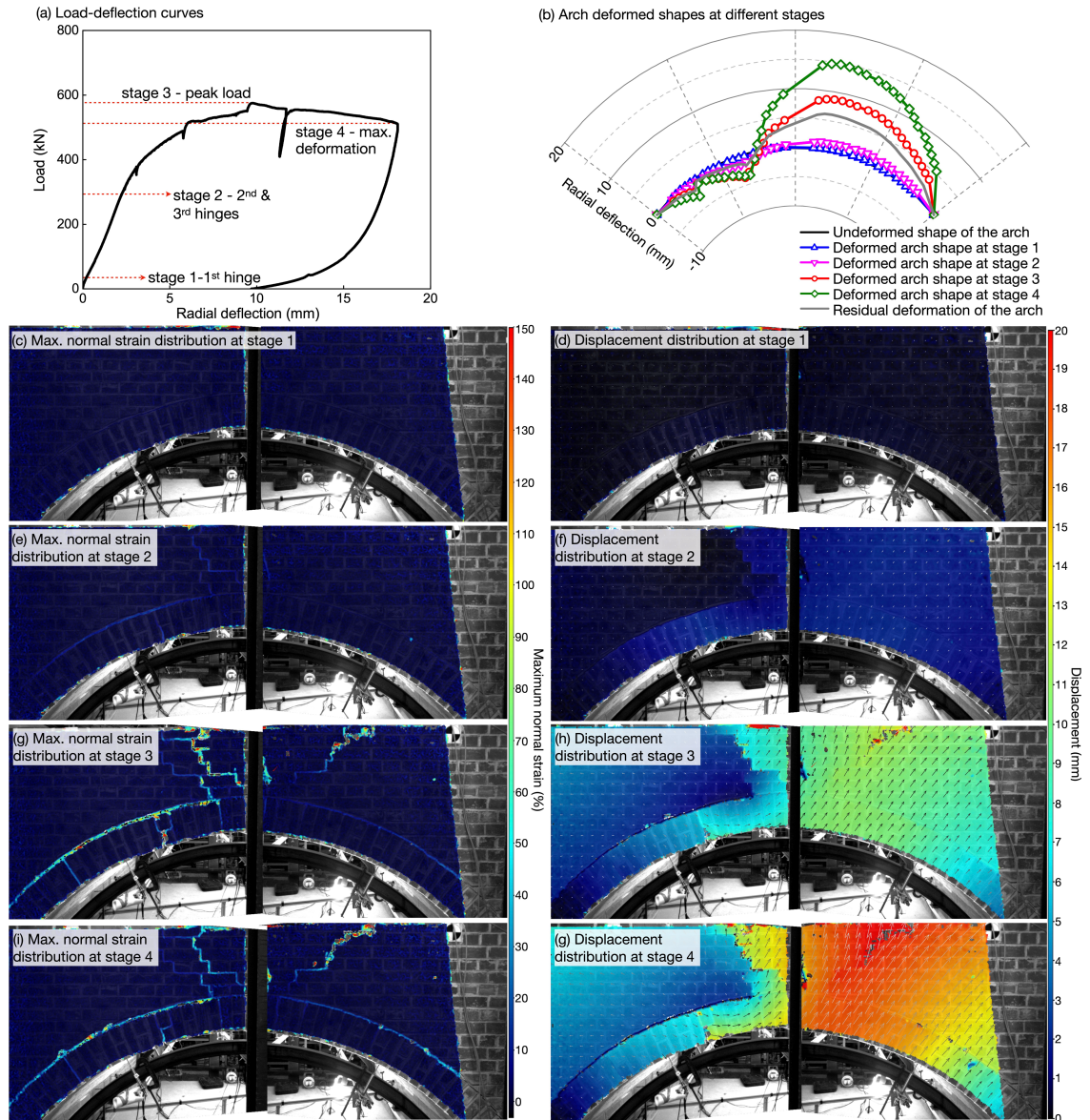
Figure 6.17 Response of the bridge at T25: (a) load-radial deflection curve of the arch intrados obtained from the LVDT positioned underneath the loading location; (b) arch deformation shapes at various loading stages; (c) and (d) maximum normal strain and displacement maps of the bridge south face at stage 1 (opening of the 1st hinge); (e) and (f) maximum normal strain and displacement maps of the bridge south face at stage 2 (activation of the 2nd and 3rd hinges); (g) and (h) maximum normal strain and displacement maps of the bridge south face at stage 3 (at the peak load); (i) and (g) maximum normal strain and displacement maps of the bridge south face at stage 4 (with the maximum deformation).

6.5 Conclusions

This chapter presents the results on the use of Digital Image Correlation (DIC) for full-field strain monitoring on a full-scale masonry arch bridge containing both the spandrel wall and arch barrel. The bridge was subjected to both centric and eccentric patch loads with increasing loading magnitudes to induce the damage accumulation from a virgin

state to failure. Two pairs of cameras were positioned on the south side of the bridge to monitor the crack initiation and propagation throughout the loading and unloading process. The surface of the masonry was left untreated, utilizing its inherent natural feature for pixel level movement tracking. Based on the results obtained, the following conclusions can be drawn:

1. Comparisons between DIC measurements and readings from LVDT confirmed that DIC can achieve a submillimetre level accuracy (i.e., 0.1 mm) for monitoring the movement and cracking in masonry. This level of precision is sufficient for detecting crack behaviour in masonry structures.

2. The application of the low-level load over the arch crown near the spandrel wall led to the separation between the arch barrel and spandrel wall, which occurred when the load was increased to 65 kN, representing the early-stage damage in the bridge. The mid-level tests that applied over the quarter-span and three-quarter span locations near the south-side spandrel wall resulted in the opening of the tensile cracks in arch intrados under the loading locations when the load was from 124 to 170 kN. However, these cracks are characterised by the localised damage rather the sign of the global failure.

3. The global four-hinge failure mechanism was activated during the high-level and failure-level tests that applied over the quarter-span and three-quarter span locations of the arch barrel along the longitudinal centreline of the bridge. The initial activation of the 1st and the 2nd hinges occurred at loads of 378 kN and 429 kN, respectively, corresponding to approximately 59% and 67% of the bridge's ultimate limit state. Once these hinges were formed, subsequent load applications led to their earlier activation.

4. The interaction between the arch barrel and spandrel wall under loads was primarily manifested by their deformation compatibility. As the load was applied, it induced the deformation in the arch barrel and resulted in crack opening, forming the hinges. This deflection prompted the rotational movement of the arch barrel, which pushed the non-loading side spandrel wall to move upward or diagonally upward. The displacement discontinuity in the spandrel wall led to diagonal cracks initiated and propagated in the spandrel wall.

This study highlights the efficacy of DIC in monitoring cracking behaviour of masonry arch bridges, providing a better understanding on the behaviour of the masonry arch

bridge and the interaction between the arch barrel and spandrel wall. However, it is noteworthy that maintaining camera stability for continuous long-term monitoring in real-world settings presents significant challenges. As a practical alternative, an intermittent, short-term monitoring approach can be employed, allowing for periodic assessments under similar loading conditions (i.e., when a similar type of train passes the bridge). By monitoring changes in crack width and length under train loads, the damage accumulation of the bridge can be evaluated. This approach not only ensures accurate measurements but also maintains operational feasibility by necessitating recalibrations to address potential disturbances.

Acknowledgement

7 Full lifecycle vibration-based monitoring of a masonry arch bridge

This chapter represents the slightly modified post-print version of the article: **B. Liu**, D. Kawabe, C. Kim, and V. Sarhosis, "Full life-cycle vibration-based monitoring of a full-scale masonry arch bridge with increasing levels of damage", Engineering Structures, 315 (2024) p. 118466. The formatting and numbering of equations, tables and figures have been adapted to this document.

7.1 Abstract

Structural health monitoring (SHM) is of great significance to maintain the safe operation of infrastructure, particularly for historic structures such as masonry arch bridges, as their material properties are deteriorating under effects such as climate change, but the demands of modern transport systems increase significantly. Vibration-based SHM has become a prevalent method for assessing the vulnerability of masonry arch bridges. However, one of the most critical limitations lies in the inability of correlate bridge's damage accumulation with the variation trends in its modal parameters. To address this issue, in the present study, full life-cycle vibration-based monitoring was conducted on a full-scale masonry arch bridge, progressing from an undamaged state to failure under laboratory conditions. Accumulated damage was induced by applying point loads with increasing magnitudes until the bridge failed. Vibration data, collected after each loading test, were analysed utilizing the stochastic subspace identification (SSI) method, and frequency and damping ratio for the first five modes were identified. The results demonstrated that the first-order frequency had the most pronounced correlation with the stiffness degradation and the damage accumulation in the masonry arch bridge. The evolution of early-stage damage, the formation of the first hinge, and the activation of a four-hinge mechanism were successfully captured through the frequency degradation. The findings of the study may provide valuable insights into the damage assessment of historic masonry arch bridge infrastructures.

7.2 Introduction

Masonry arch bridges remain a substantial portion of the infrastructure stock in the UK and Europe. Currently estimates indicate that there are approximately 200,000 masonry arch bridges and culverts in Europe and 40,000 masonry arch bridges in the UK. On the

railways, half the bridge spans in the UK network are of masonry arch construction, amounting to >25,000 spans[40]. After serving for decades, these historical masonry arch bridges are suffering sustained material degradation due to environmental effects, natural disasters, and climate change. On the other hand, the escalating demands imposed by the modern transport system, in terms of increased vehicle/train weights and speeds, pose a huge threat to the safety of masonry arch bridges [10]. Therefore, assessing and monitoring the health conditions of these aging bridges is of significant importance to prevent catastrophic failures and ensure the continued functionality of this transportation infrastructure.

Destructive testing methods, such as testing core samples drilled from a bridge, can accurately estimate the strength characteristics of the bridge [18]. However, these methods are usually prohibited in historic structures due to their irreversible and invasive nature. As an alternative, non-destructive testing (NDT) methods are used to assess the mechanical performance and detect damage for in-service masonry arch bridges. The predominant form of damage observed in masonry structures is cracking between masonry units due to their low-bond strength characteristics [203]. Therefore, visual inspection is usually adopted as the initial step for quickly evaluating the condition of masonry arch bridges, focusing on identifying their crack patterns [204]. For better distinguishing cracks, automated detection and annotation approaches enhanced by machine learning and deep learning have been developed [205–207]. Long-term monitoring of cracks enables the establishment of a digital twin model, serving both for documentation and structural assessment purposes [208–210]. However, a significant limitation of these approaches is their concentration on the surface-level features, offering restricted penetration into the inside of the masonry arch bridge, potentially leading to inaccuracies in assessing its structural integrity.

Vibration-based structural health monitoring (SHM), a representation NDT method, has gained increasing prominence in assessing conditions of infrastructures. Theoretically, damage in a structure can alter its stiffness, which consequently leads to variations in modal parameters, such as frequency, damping ratio, and mode shape [211]. By utilizing system identification methods to formulate dynamic responses as mathematical models, the modal parameters can be identified. In particular, output-only operational modal analysis has great potential for practical application since it does not affect the operation of the structure. Widely adopted operational modal analyses include stochastic subspace identification (SSI) in the time domain, frequency domain decomposition (FDD) in the

frequency domain, and advanced algorithms enhanced by artificial intelligence [182,212–216]. Although significant progress has been made in refining existing data processing strategies and developing novel ones for parameter identification, the application of these methods for real-bridge assessments remains a challenge.

The primary challenges in implementing vibration-based SHM system for assessing real masonry arch bridges are twofold: a) unlike testing scaled models under controlled laboratory conditions, for the real bridge assessment, the large size of the bridge, complexity in its geometry, environmental interferences, and nonlinearity of material properties make it difficult to precisely exam modal parameters [217,218]. Such limitations particularly hinder accurate early-stage damage detection, as the modal parameter changes induced by early-stage damage are usually indistinguishable from those caused by environmental factors [219,220]; b) Even though extensive data have been collected from field tests on actual masonry arch bridges [161,168,180,221–223], the parameters identified are representative only of the bridge's condition at the time of testing. The absence of long-term data makes it impossible to correlate the changes in modal parameters with variations in bridge's states, which hinders damage detection based on alternations in modal parameters, thereby making full life-cycle assessments of masonry arch bridges unfeasible. These challenges have been gradually acknowledged by researchers and engineers. For example, a recent study involving testing on a 2:1 scaled two-span masonry arch bridge subjected to the controlled pier settlement and rotation was performed. Despite observable progressive cracking on masonry, the variations in modal parameters showed weak correlation with the damage levels [224,225].

In this study, full life-cycle vibration-based monitoring was carried out on a full-scale masonry arch bridge under laboratory conditions. The masonry arch bridge comprised a single-span arch barrel, spandrel walls, abutments, and crushed limestone as the backfill material. Twenty-five loading tests were carried out on the masonry arch bridge, from an undamaged state to failure. By applying eccentric/centric patch loads with increasing loading magnitudes, the accumulated damage was triggered. Following each loading test, vibration response of the bridge was collected covering its entire lifecycle. This data was then analysed using the stochastic subspace identification (SSI) method [226,227], one of the output-only operational modal analysis and robust against the effect of environmental and operational variations, and frequency and damping ratio of the first five modes were identified. In addition, finite element (FE) analysis was performed to

identify mode shapes of the undamaged bridge, as well as to verify the experimental results. Moreover, correlation analysis between damage levels and variations in modal parameters was conducted.

7.3 Experimental campaign on a full-scale masonry arch bridge

7.3.1 Full-scale masonry arch bridge

A full-scale masonry arch bridge was constructed and tested under laboratory conditions. A photogrammetry model and an image of testing site is shown in Figure 7.1 (a) and (b), respectively. U-shape reinforced concrete (RC) walls and base slab were firstly constructed on the strong floor to accommodate the masonry arch bridge and provide longitudinal confinement. A dense reinforcement arrangement was adopted for the RC end walls so that they had sufficient stiffness to minimize their out-of-plane deformation under loading (more detailed description regarding the design, construction of masonry arch bridge, as well as materials used can be found in [145,177], chapter 4 and 5 of this thesis).
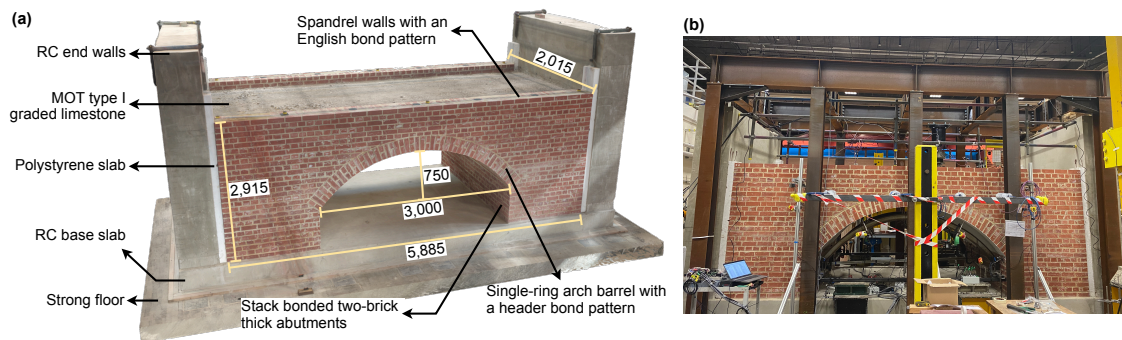
Figure 7.1 (a) A photogrammetry model for the full-scale masonry arch bridge constructed in the laboratory (all units in mm); (b) testing site.

7.3.2 Load testing scheme

Static/cyclic patch loads with increasing magnitudes were applied to induce the accumulated damage in the bridge. Nine loading locations were selected (point A to point I in Figure 7.2), covering both centric and eccentric locations, to trigger the three-dimensional (3D) behaviour of the bridge. Table 7.1 lists the loading protocol. Specifically, the low-level of load with a magnitude of 150 kN, less than 25% of the ultimate limit state (ULS) of the bridge, was applied as the first stage to investigate the elastic behaviour and early-stage cracking characteristics of the bridge. The first two low-level static tests performed at point A and B were served as trials. Then, loads were

173

applied to the nine loading locations sequentially via a load spreader beam with a cross section area equal to 300 x 300 mm. At each location, a static load was first applied, followed by three loading cycles with a same loading magnitude.

The loading magnitude was then increased to 250 kN (mid-level) with an aim to induce the plastic damage and crack propagation in the bridge. Similar to the low-level stage, point loads were applied to nine locations, commencing with a static load, succeeded by three loading cycles. The loading area was also 300 x 300 mm. A load control was adopted for the low- and mid-level static & cyclic tests, with the loading and unloading rate maintained at 10 kN/min.
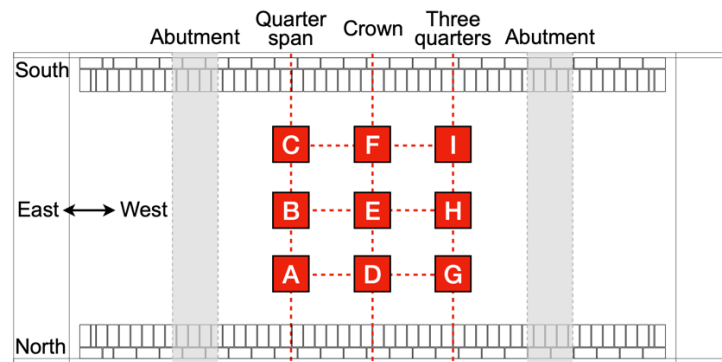
Figure 7.2 Nine loading points.

Table 7.1 Loading protocol.

No. of test	Loading level	Loading type	Area (mm)	Loading sequence (locations)
T1 & T2	Low-level (150 kN)	Static (trials)	300 x 300	A→B
T3 to T11	Low-level (150 kN)	Static & three cycles	300 x 300	C→D→E→F→A→B→G→H→I
T12 to T20	Mid-level (250 kN)	Static & three cycles	300 x 300	G→A→D→F→I→C→E→H→B
T21	High-level (560 kN)	Static	750 x 300	B
T22	Failure-level	Static	750 x 300	B
T23	Failure-level	Static	300 x 300	B
T24	Failure-level	Static	300 x 300	H
T25	Failure-level	Static	750 x 300	H

As the localised damage was observed during the mid-level tests, a larger spreader beam with a cross section area of 750 x 300 mm was adopted for the high-level and failure-level tests in order to induce the global failure to the bridge. At the high-level stage, a 560

kN static load was applied at Point B (T21). Subsequentially, the first failure-level test was carried out at Point B to assess the load-carrying capacity of the bridge (T22). Afterward, with an intension to investigate the influence of the loading area on the bridge's behaviour, a small platen was used (T23). However, the small platen was observed to be bending under loading, with one side of the platen embedded into the backfill, leading to the termination of the test. The same behaviour was also encountered during T24, conducted at Point H. Finally, the larger platen was utilized again, and the second failure-level test (T25) was conducted at Point H to examine the residual capacity and residual stiffness of the bridge. It is noteworthy that a displacement control was adopted for the high-level and failure-level tests to better control the bridge's post failure behaviour, and the loading and unloading rate was 0.05 mm/s.

7.3.3   Vibration testing programme

Vibration data from the bridge was collected following each loading test, except for T23 and T24, which were terminated due to safety issues. Four triaxial accelerometers were used for the vibration data collection. Each sensor was featured with an ultra-low noise characteristic (0.5 μg/√Hz), the maximum output range of ±15 g, and a resolution of 0.06 μg. They were mounted on the top of the spandrel walls for practical application, the locations of which are shown in Figure 7.3. Specifically, an accelerometer (A1 in Figure 7.3 (a)) was positioned on the north-side spandrel wall over the crown of the arch. Other three (A2, A3, and A4 in Figure 7.3 (a)) were installed on the south-side spandrel wall, located respectively over the quarter-span, crown, and three-quarter span of the arch barrel. The purpose for the un-symmetrical instrumentation was to capture the torsional motion of the bridge. In order to install the accelerometers, four square steel plates were firmly mounted to the target locations using chemical adhesive. Accelerometers were then attached to the steel plates by four strong magnets (Figure 7.3 (b)). These accelerometers were connected to a controller area network (CAN) system for data acquisition and a PC for data storage and real-time data display. The sampling rate was set to be equal to 200 Hz.

Vibration of the bridge was manually induced using a small hammer with a rubber head and a wood handle. Figure 7.3 (c) illustrates the locations of excitations. Specifically, L1 and L5 situated at the midpoints of the south and north-side spandrel walls, respectively, were subjected to horizontal excitations. L2, L3, and L4, positioned at the south edge, centre, and north edge of the arch intrados at the transversal central profile, were subjected to vertical excitations. At each of these points, ten impacts were done within a

time span of 1 minute, and an approximately 5 second interval was in between two impacts.
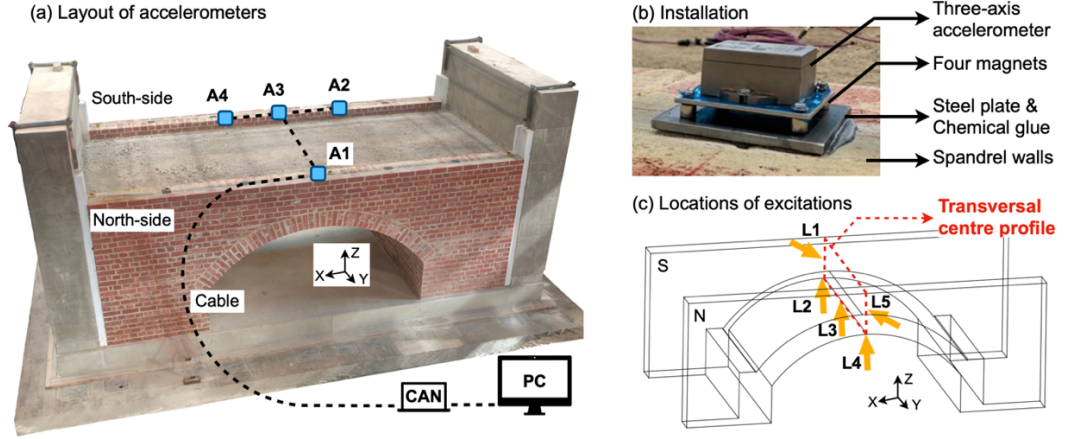
Figure 7.3 Vibration test setup: (a) Instrumentation; (b) accelerometer installation, and (c) locations of excitation for the vibration testing.

7.4 Modal parameters identification by stochastic subspace identification

Data-driven stochastic subspace identification (SSI) is one of the time-series system identification methods for operational modal analysis. Operational modal analysis whose external forces are implicitly modelled as white noise vectors has been adopted to practical vibration-based health monitoring because the structure can remain in its operational condition. The detailed mathematical derivations can be found in [227]. The dynamic behaviour of a vibration structure can be formulated by the proper equation of motions. The equation of motion in (6.1) generates the following first order differential equation called a state equation.

$$
\begin{aligned}
\dot{x}(t) &= Ax(t) + Bf(t) \\
y(t) &= Cx(t)
\end{aligned}
\tag{6.1}
$$

where

$$
x(t) = \begin{pmatrix} y(t) \\ \dot{y}(t) \end{pmatrix}, A = \begin{bmatrix} 0 & I \\ -M^{-1}K & -M^{-1}D \end{bmatrix}, B = \begin{bmatrix} 0 \\ M^{-1} \end{bmatrix}
\tag{6.2}
$$

where $x(t) \in \mathbb{R}^{2n}$, $y(t) \in \mathbb{R}^{n}$ and $f(t) \in \mathbb{R}^{n}$, which are the state, displacement, and external force vectors at continuous time t, respectively. $M, D, K \in \mathbb{R}^{n \times n}$ are the mass, damping and stiffness matrices. C denotes the output matrix, and I is a unit matrix with a proper size.

The continuous-time equations are discretised by choosing a certain fixed sampling

period δt with the discrete time instants $k \in \mathbb{N}$, where $t = k\delta t$. Under the zero-order hold assumption, the state space model shown in equation (6.1) is discretized. Furthermore, in a stochastic model, the external force is modelled as white noise vectors. Therefore, the deterministic state space model in (6.1) is given as follows.

$$\begin{aligned} x_{k+1} &= Ax_k + w_k \\ y_k &= Cx_k + v_k \end{aligned} \tag{6.3}$$

where $w_k \in \mathbb{R}^n$ and $v_k \in \mathbb{R}^m$ are zero-mean white noise vector. Here, m is the number of measurement points on the structure.

Since w_k and v_k are zero mean white noise vector sequences, and independent of x_k, $E[x_k w_k] = E[x_k v_k] = 0$. Then, the covariance matrix Λ_i is generated as follows.

$$\Lambda_i = E[y_{k+i} y_k^T] = CA^{i-1}(E[x_k x_k^T]C^T + E[w_k v_k^T]) \tag{6.4}$$

The block Hankel matrix is generated as follows for mathematical expressions.

$$H(k-1) = \begin{bmatrix} y_k & y_{k+1} & \cdots & y_{k+s} \\ y_{k+1} & y_{k+2} & \cdots & y_{k+s+1} \\ \vdots & \vdots & \ddots & \vdots \\ y_{k+r-1} & y_{k+r} & \cdots & y_{k+r+s-2} \end{bmatrix} \in \mathbb{R}^{r \times s} \tag{6.5}$$

Using the covariance matrices, the two multiplied block Hankel matrices are represented as follows.

$$H(r+k-1)H(0)^T = \begin{pmatrix} \Lambda_{r+k-1} & \Lambda_{r+k-2} & \cdots & \Lambda_k \\ \Lambda_{r+k} & \Lambda_{r+k+1} & \cdots & \Lambda_{k+1} \\ \vdots & \vdots & \ddots & \vdots \\ \Lambda_{2r+k-2} & \Lambda_{2r+k-3} & \cdots & \Lambda_{r+k-1} \end{pmatrix} = O_r A^{k-1} C_s \tag{6.6}$$

where $O_r = \left(C\ CA\ ...\ CA^{r-1}\right)^T, C_s = (A^{r-1}G\ A^{r-2}G\ ...\ G)$.

Considering $k = 1$ and $k = 2$, system matrix A is then obtained using singular value decomposition. In $k = 1$, equation (6.6) is decomposed as follows.

$$H(r)H(0)^T = O_r C_s = USV^T = [U_1\ U_2] \begin{bmatrix} S_1 & 0 \\ 0 & S_2 \end{bmatrix} \begin{bmatrix} V_1^T \\ V_2^T \end{bmatrix} \cong U_1 S_1 V_1^T \tag{6.7}$$

where U and V are unitary matrices with an appropriate size. And S is a diagonal matrix with non-negative real elements which are referred as singular values of $H(r)H(0)^T$.

Since components in $U_2 S_2 V_2^T$ are regarded as trivial components as ignored in the estimation. O_r and C_s are then generated as follows.

$$O_r \cong U_1 S_1^{\frac{1}{2}}, C_s \cong S_1^{\frac{1}{2}} V_1^T \tag{6.8}$$

In $k = 2$, using $H(r + 1)H(0)^T = O_r A C_s$ and substituting equation (6.8), the system matrix A is obtained as follows.

$$A = O_r^{-1} H(r + 1) H(0)^T C_s^{-1} = S_1^{-\frac{1}{2}} U_1^T H(r + 1) H(0)^T V_1 S_1^{-\frac{1}{2}} \tag{6.9}$$

Finally, by finding the corresponding natural frequencies and vectors of the system matrix A, the modal characteristics of the measured structure can be identified.

Figure 7.4 illustrates the data analysing scheme implemented in the study. In each vibration test campaign, sixty time-acceleration histories were recorded from four accelerometers. The pre-processing activity involved the filtering of acceleration records. Undesirable waveforms, characterised by the drift in acceleration signal, were removed, which could be attributed to the proximity of the excitation point to the accelerometer. Following this, the continuous time-acceleration histories were segmented into 3-second intervals. The time window was positioned to include 0.2s before and 2.8s after the peak acceleration response induced by each excitation. Subsequently, a low pass filter with an 80 Hz threshold was applied to remove the noise in the data. The final step of analysis involved SSI analysis and modal parameters output.
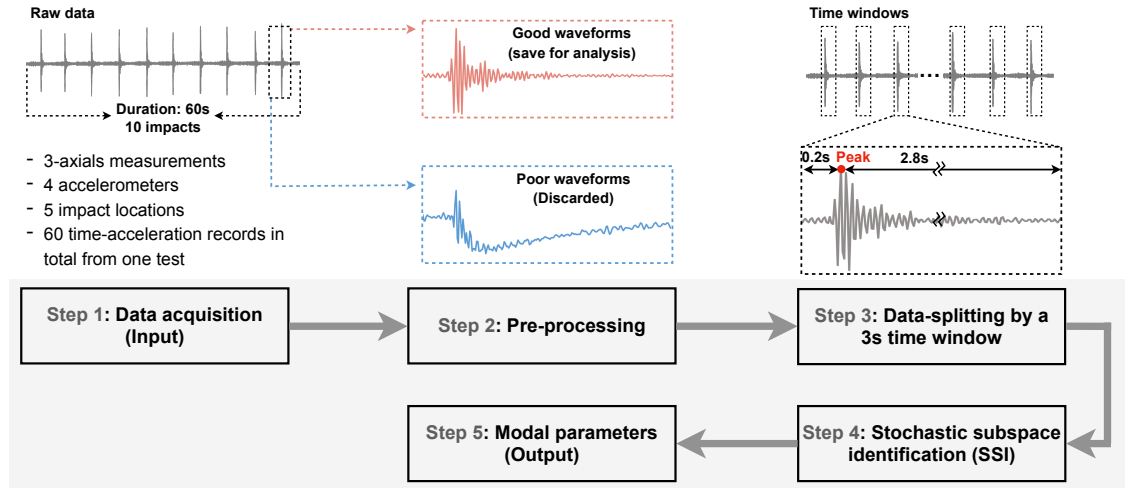
Figure 7.4 Data analysing scheme.

7.5 Results and discussion

7.5.1 Modal parameters identification of the undamaged bridge

Following the construction of the masonry arch bridge, the first vibration test was conducted to determine its modal parameters in an undamaged state. Also, a 3D macro

finite element (FE) analysis was conducted to verify the experimental results and to provide a better understanding of the modal parameters of the undamaged masonry arch bridge. The FE model had the identical dimensions as the experimental model constructed in the laboratory (see Figure 7.1). In the FE model, the masonry arch bridge was segmented into two components according to material characteristics: the brickwork part and the backfill part, as shown in Figure 7.5. Both components were simulated with homogeneous continuous materials, and the properties of which were adopted from small-scale material level tests. For example, the elastic modulus of the masonry and backfill was set to be equal to 4.7 GPa and 0.3 GPa, respectively [149]. The Poisson's ratio for the two parts was the same and equal to 0.3. Regarding the boundary conditions, the base of the bridge was fixed with zero degree of freedom. The horizontal (x-axis) movement and rotations along the x and y axes were constrained for the two lateral sides of the backfill, simulating the limitations imposed by the RC end walls. Moreover, the lateral sides of brickwork masonry were free, as the presence of four polystyrene slabs between masonry and RC walls providing negligible constraint on the movement of the spandrel walls (see Figure 7.1).
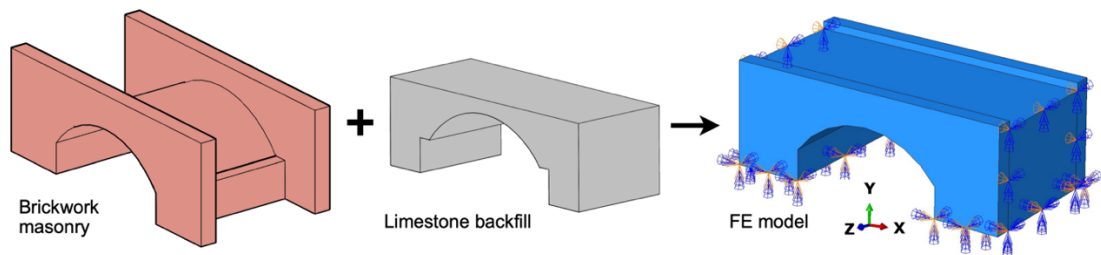
Figure 7.5 Macro FE model for the masonry arch bridge.

Table 7.2 Modal parameters of the undamaged bridge.

Order of mode	Experimental results				Numerical results	
	Model frequencies, f		Damping ratio, ξ		Model frequencies, f	
	Mean (Hz)	SEM (Hz)	Mean (10^{-3})	SEM (10^{-3})	Value (Hz)	Discrepancy, Δ (%)
1st mode	39.70	0.63	6.2	1.2	40.41	1.79
2nd mode	45.51	1.00	6.5	0.6	46.44	2.04
3rd mode	51.32	1.32	8.2	1.0	57.21	11.48
4th mode	61.14	1.40	13.8	1.8	60.67	0.77
5th mode	67.68	0.37	14.4	1.1	62.54	7.59

The vibration response obtained from the undamaged bridge was processed as per the scheme outlined in Figure 7.4. Table 7.2 presents the mean values and standard errors of the mean (SEM) for both frequencies (f) and damping ratios (ξ) for the first five modes. The SEM values were calculated by dividing the standard deviation by the square root of the sample size. Also, values of frequencies and the discrepancy (Δ) between the numerical and experimental results are listed in Table 7.2.

The frequency range for the first five modes of the undamaged bridge spanned from 39.70 Hz to 67.68 Hz, indicating a relatively high stiffness of the constructed masonry arch bridge model compared to those in the field [161,223]. Such a high stiffness characteristic of the experimental bridge was resulted from: (a) the limited length of the bridge at longitudinal direction (e.g., containing single-span); and (b) the presence of stiff RC end walls. Overall, the frequency values derived from vibration data showed high reliability, with a maximum coefficient of variation less than 10%. However, the identified damping ratios exhibited a relatively large variation. This high levels of variability in the damping ratio estimation is widely encountered in the field assessment of masonry arch bridge, as reported in [161,214,228–230]. The primary reasons might include that: a) masonry is nonlinear material with inherent variabilities in its material properties. Such nonlinearity can lead to inaccuracies in damping estimation; and b) compared to the natural frequencies which are primarily determined by the mass and stiffness of a structure, damping ratio measures the energy dissipation in the system, which is more vulnerable to be affected by the environmental noise, especially when the peak amplitude in the vibration data is small and close to the peak of noise.

The results of the FE analysis revealed that the computed frequencies were closely aligned with those from experimental tests, except for the third mode which had a discrepancy of 11.48%. Figure 7.6 illustrates the first five-order mode shapes determined by FE analysis, with the undeformed geometry highlighted in dot lines. Due to the limited number of accelerometers used in the experiments, mode shapes were unfortunately not able to be identified from the vibration data. It can be seen from FEM results that most of the deformation in the masonry arch bridge occurred within the region between two abutments. Specifically, the first and second mode shapes were identified as the 1st and 2nd transverse bending modes, respectively. In the first mode, deformation was mainly concentrated at the mid-span region, and the spandrel walls deformed in the out-of-plane direction, most notably at the midpoints of their upper sections. On the other hand, the third and fourth mode shapes were characterised by in-plane bending, with greater

deformation appeared in the backfill compared to the masonry. Notably, the third mode shape showed significant in-plane deformation at the wall ends, whereas the backfill ends experienced minimal deformation. This was resulted from the idealised boundary conditions adopted in the FE model, where the longitudinal movement at the backfill ends was restricted. Consequently, the third mode frequency obtained from FEM was higher than that obtained from experiments. Moreover, the fifth mode shape was characterised to be an asymmetrical torsion mode.
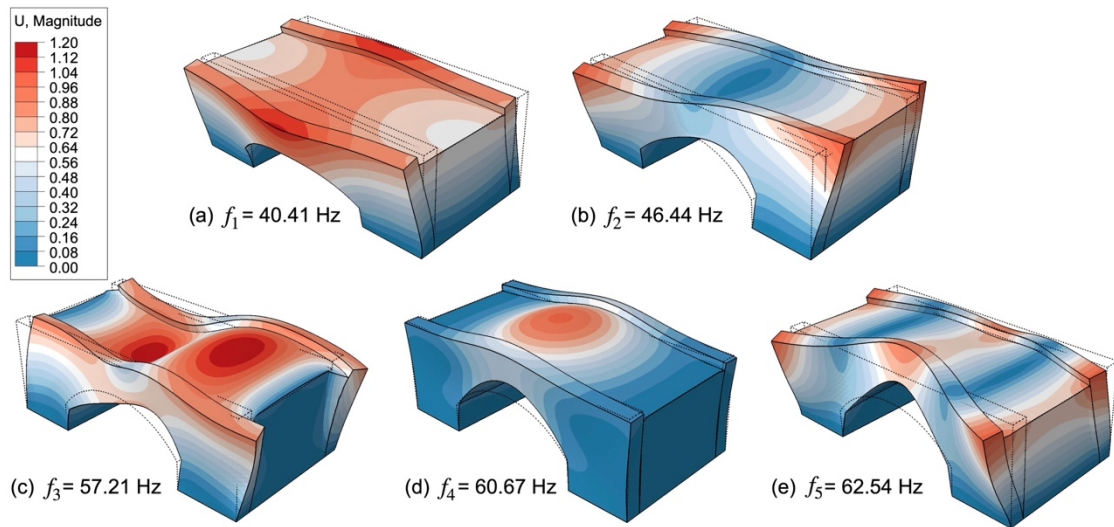
Figure 7.6 Frequencies and mode shapes of the undamaged masonry arch bridge identified from FEM: (a) to (e) show the 1st to the 5th mode, respectively.

7.5.2 Stiffness degradation and crack propagation of the masonry arch bridge

Results obtained from loading tests are discussed in this section. Damage level of the bridge was illustrated by stiffness derived from load-deflection curves and crack propagation through visual inspection.

For the stiffness (S_a) of the bridge, it was determined by calculating the slope of load-radial deflection curves (see Figure B1 in Appendix) within the 10% to 40% peak load interval. Although the stiffness derived from the load-deflection curve represents localized stiffness rather than a true global modal stiffness of the bridge, the analysis focuses on relative stiffness variation, measured consistently from same locations but under different damage conditions. Therefore, while not truly global, the results remain internally comparable. It is worth noting that two different loading platens were used during tests. The smaller one having a cross-section area of 300 mm x 300 mm was used for the low- and mid-level tests, whereas the larger one, which had a loading area of 750 mm x 300 mm, was used for the high-level and failure-level tests. The reason is because

the global failure mechanism of the masonry arch bridge was expected to be triggered during the failure-level tests. However, the small platen could potentially trigger the localised failure (i.e., punching shear/knife edge failure mode out of the backfill and bricks at the arch ring) according to the observation during the mid-level tests. In order to eliminate effects of different loading area on the stiffness characteristic, the stiffness values (S) were normalised by dividing S_a by the loading area (A):

$$S = \frac{S_a}{A} \qquad (6.10)$$
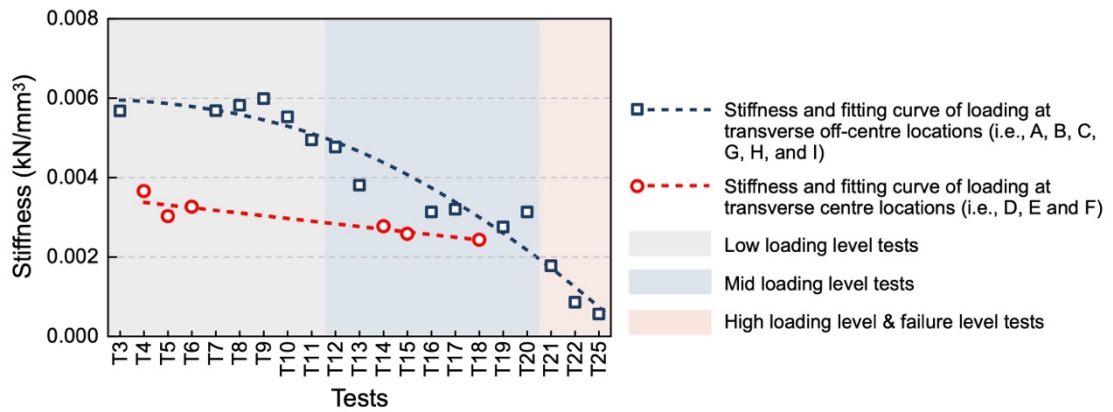
Figure 7.7 Variation in stiffness of the masonry arch bridge along the loading tests (see Figure 7.2 for loading points).

Figure 7.7 shows the variation in S along with the loading process. The data was divided into two groups, including the data points in red derived from the tests loading over the crown of the arch barrel (i.e., D, E, and F in Figure 7.2), and those in dark blue representing the results obtained from the tests loading over quarter and three-quarter span points (e.g., A, B, C, G, H, and I in Figure 7.2). These two groups of data were not directly comparable as the depth of backfill over quarter-span / three-quarter span and crown of the arch barrel was different. When loading at mid-span, the stiffness was observed to be lower than when the loads were located at the quarter- and three-quarter-span points. Because the shallower backfill depth over the crown of the arch led to a more concentrated load being applied to the arch barrel, which in turn resulted in greater elastic deformation of the arch barrel. Another reason could potentially attribute to the lower stiffness obtained from mid-loading locations was that these locations were farer from the supports (springings) compared to other quarter- and three-quarter span locations.
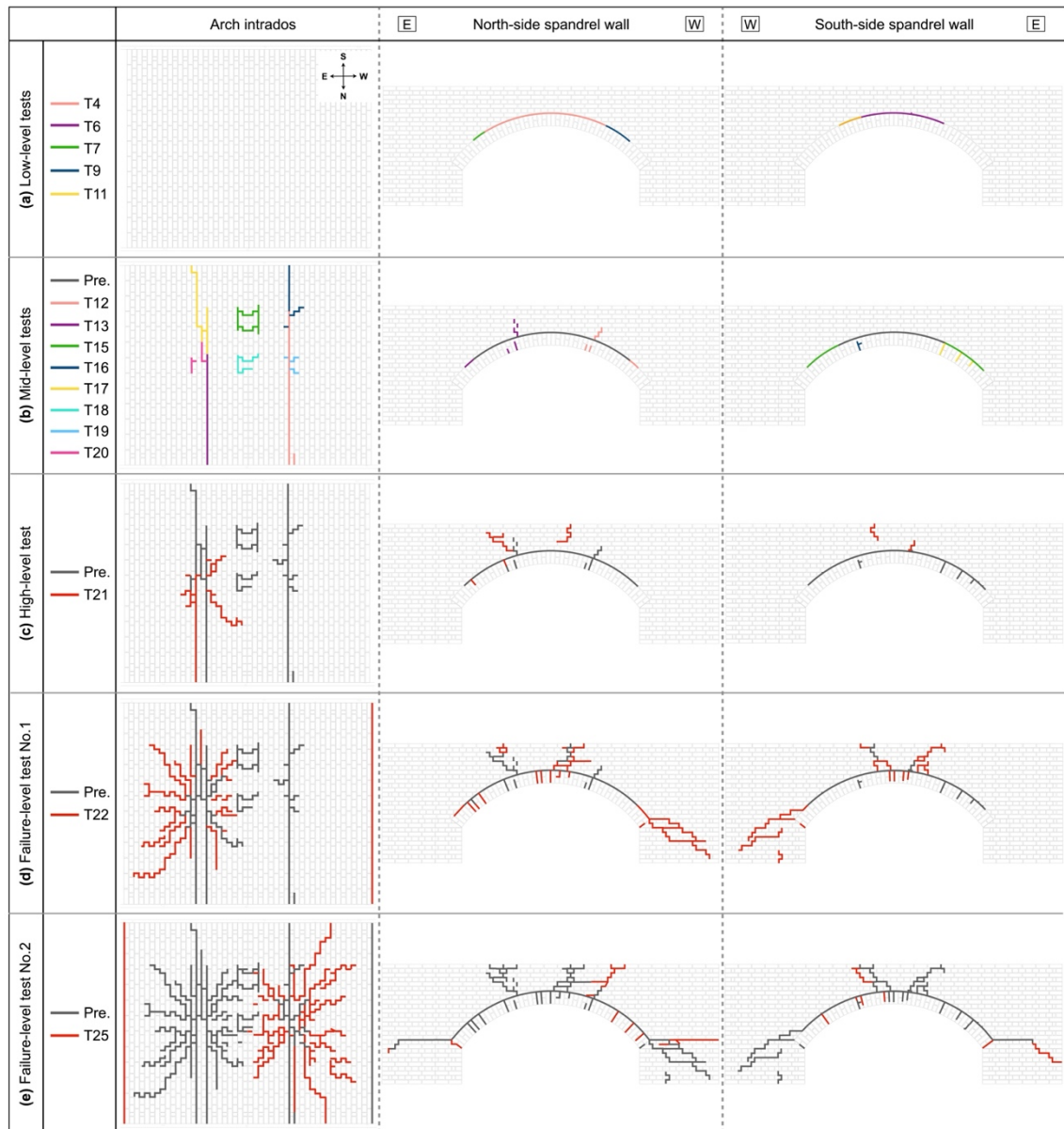
Figure 7.8 Crack evolution in the masonry arch bridge in (a) low-level loading tests; (b) mid-level loading tests; (c) high-level loading test; (d) the first and (e) the second failure-level loading test.

Stiffness degradation was resulted from the crack initiation and propagation in masonry under loads. Figure 7.8 shows the crack evolution in the arch intrados, north-side and south-side spandrel walls at different stages of load testing. Detailed damage accumulation mechanism and images showing cracks can be found in [145,177]. Specifically, during the low-level loading tests, point loads applied close to the spandrel walls (i.e., at the locations of A, C, D, F, G, and I) resulted in cracks initiated and propagated along the arch barrel-spandrel wall interfaces (Figure 7.8 (a)). However, these cracks were characterised by hairline cracks with a very thin width and almost completely closed after the removal of the loads. Regarding stiffness, it can be seen from

grey interval in Figure 7.7 that the degradation in stiffness of the bridge was marginal. For example, the value of S obtained from T11 was decreased by approximately 13% compared to that obtained from T3 (the last and first test with loading over the quarter-span / three-quarter span of the arch, respectively), and S obtained T6 was decreased by approximately 11% compared to that obtained from T4 (the last and first test with loading over the crown of the arch, respectively).

Figure 7.8 (b) illustrates the crack propagation observed from the masonry arch bridge during the mid-level tests. Damage mechanisms at this stage of testing include: a) loading over quarter-span and three-quarter span points close to the spandrel walls (i.e., points A, C, G, and H) resulted in tensile cracks initiated and extended at the arch intrados underneath the loading points. Also, in some cases such as T12 and T13, diagonal cracks were observed in the north-side spandrel walls. In addition, the separation between the spandrel wall and the arch barrel propagated further approaching to springings; b) Loading at the longitudinal central line (such as T18, T19, and T20 conducted at points B, E, and H, respectively) triggered localised crack patterns at the arch intrados. These cracks were resulted from the shear failure of the mortar joints; c) Loading at point D (T14), which was located over the crown of the arch barrel close to the north-side spandrel wall, did not lead to any visible damage. However, loading at its symmetrical points along the longitudinal centre line (T15 at the point F) resulted in the localised shear cracks occurred at the arch intrados. This square-shape crack pattern had similar dimensions to the loading platen. At the mid-level testing stage, a significant stiffness degradation was observed with the value of S dropped approximately by 34% (Figure 7.7 highlighted in the blue interval). Combined with cracking characteristics, this noticeable decrease in stiffness was mainly resulted from the formation of the first hinge and partially from the initiation of the localised shear cracks.

Figure 7.8 (c) shows the crack propagation observed after the high-level test (T21). A static load up to 560 kN (approximately 87% of the ULS of the bridge) was applied at point B over the arch quarter-span. During T21, three hinges were initially formed. The first hinge located underneath the load platen was fully activated, which was represented by the opening of tensile cracks at the arch intrados. The second and third hinges initially formed, as suggested by the cracks developed at east side of the loading location in the arch extrados and the smashed mortar joints at the mid-span of the arch intrados. In addition to this global damage, 3D cracking behaviour was triggered by the patch load,

and several cracks were observed at the arch intrados which initialized from the point underneath the loading location and propagated diagonally. Moreover, due to the upward movement of the arch barrel at the non-loading side, diagonal cracks were developed at both the north-side and south-side of spandrel walls. The formation of three hinges resulted in a substantial decrease in the stiffness of the bridge, which dropped by 43% with respect to the stiffness obtained from the last mid-level test.

Following the high-level loading test, two failure-level tests were conducted at point B and H respectively to assess the load-carrying capacity and residual capacity of the masonry arch bridge. Crack pattens developed from T22 and T25 were almost mirrored, i.e., with the fully activated four-hinge mechanism, the significant crack propagation on the spandrel walls due to the large deformation of the arch barrel, the extended diagonal tensile cracks at the arch intrados suggesting the 3D behaviour of the arch, and the rotation failure of the spandrel walls at the non-loading side with cracks commenced from the unloading side springing and propagated downwards. The failure of the bridge resulted in its stiffness dropped by over half from 1.78×10^{-3} kN·mm^{-3} (T21) to 8.6×10^{-4} kN·mm^{-3} (T22). Moreover, following the first failure-level test, the second failure-level test resulted in a further 35% degradation in S, from 8.6×10^{-4} kN·mm^{-3} (T22) to 5.6×10^{-4} kN·mm^{-3} (T25).

7.5.3 Variation in modal parameters

The vibration data obtained after each loading test were processed as per the scheme depicted in Figure 7.4. Table 7.3 lists the mean values and SEM of the identified modal parameters, including f and ξ. The SEM values indicated that ξ exhibited comparatively greater variability than f. However, the variability of results obtained under controlled laboratory conditions further emphasizes the potential for significant variability in outcomes when measuring real masonry arch bridges in the field, due to environmental factors.

Figure 7.9 shows the correlation between the normalised frequency ($f_{1,n}$ to $f_{5,n}$) and normalised stiffness (S_n). In this context, normalization of frequency involved dividing each frequency value by the frequency identified from the undamaged bridge (denoted as N). The normalization of stiffness values for tests loading at the quarter-span and three-quarter span locations was based on the stiffness derived from T3, whereas for tests performed over the arch's crown, normalization was referenced to the stiffness obtained from T4.

Table 7.3 Mean values and SEM of modal parameters identified from the masonry arch bridge with increasing levels of damage.

Tests	1st mode		2nd mode		3rd mode		4th mode		5th mode	
	f_1 (Hz)	ξ_1 ($\times 10^{-3}$)	f_2 (Hz)	ξ_2 ($\times 10^{-3}$)	f_3 (Hz)	ξ_3 ($\times 10^{-3}$)	f_4 (Hz)	ξ_4 ($\times 10^{-3}$)	f_5 (Hz)	ξ_5 ($\times 10^{-3}$)
New	39.70 (0.71)	6.18 (1.50)	45.51 (0.83)	6.55 (0.83)	51.33 (1.01)	8.25 (0.82)	61.14 (1.27)	13.84 (1.27)	67.68 (0.29)	14.41 (0.78)
T3	39.25 (1.27)	6.66 (1.79)	45.36 (1.55)	9.01 (1.99)	52.83 (2.01)	10.74 (2.13)	59.87 (1.91)	10.49 (1.35)	66.44 (0.76)	15.31 (1.79)
T4	37.46 (1.17)	15.30 (2.86)	44.85 (0.86)	10.09 (1.53)	52.92 (1.28)	14.38 (2.84)	60.96 (1.27)	11.58 (0.76)	67.05 (1.14)	15.85 (1.57)
T5	38.13 (1.08)	8.42 (1.32)	43.65 (0.73)	6.95 (1.49)	49.05 (1.03)	6.19 (0.98)	57.11 (1.38)	11.66 (1.30)	64.40 (0.94)	17.04 (1.33)
T6	37.76 (1.52)	10.28 (2.42)	45.42 (0.90)	7.00 (1.79)	51.12 (1.23)	10.39 (2.60)	57.98 (1.36)	15.96 (1.68)	64.87 (0.92)	14.91 (1.80)
T7	37.96 (0.98)	12.22 (2.59)	46.91 (1.02)	10.33 (1.99)	54.98 (1.17)	9.42 (0.96)	62.82 (0.54)	13.31 (1.36)	67.52 (0.58)	15.15 (1.21)
T8	36.97 (1.00)	9.79 (1.72)	43.75 (0.59)	6.92 (2.01)	48.27 (0.51)	6.14 (0.67)	55.39 (1.06)	7.91 (0.94)	64.43 (0.58)	13.88 (0.81)
T9	36.24 (1.10)	13.15 (2.33)	42.85 (0.81)	8.98 (1.59)	47.81 (0.84)	7.99 (2.43)	57.81 (1.13)	17.90 (3.04)	65.11 (0.83)	15.92 (1.95)
T10	36.13 (1.19)	13.97 (2.42)	44.86 (0.96)	6.69 (0.97)	51.12 (1.36)	9.48 (0.95)	59.40 (1.33)	11.66 (1.01)	65.77 (0.81)	15.74 (1.34)
T11	37.05 (1.14)	13.30 (2.49)	43.58 (1.07)	10.50 (1.98)	50.25 (1.21)	10.28 (1.61)	56.61 (1.29)	11.04 (1.87)	62.82 (0.92)	14.69 (1.38)
T12	34.89 (1.22)	18.45 (2.69)	42.81 (0.68)	7.85 (1.60)	48.74 (0.95)	5.74 (0.55)	54.40 (1.14)	9.25 (1.20)	63.60 (0.79)	16.82 (1.59)
T13	33.92 (1.12)	12.56 (1.60)	42.40 (0.74)	6.57 (0.65)	48.71 (0.99)	8.14 (0.72)	57.79 (1.24)	12.41 (1.53)	66.68 (0.64)	14.73 (1.34)
T14	35.86 (1.06)	12.76 (1.78)	42.93 (0.56)	5.02 (0.92)	47.74 (0.71)	4.53 (0.89)	53.98 (1.07)	6.74 (1.21)	65.07 (0.74)	12.30 (1.15)
T15	32.24 (1.27)	15.94 (1.50)	43.33 (1.17)	9.58 (1.13)	50.75 (1.10)	8.56 (0.95)	58.88 (1.23)	11.81 (1.51)	66.73 (1.23)	16.78 (1.99)
T16	33.66 (1.55)	13.21 (1.79)	42.36 (0.97)	6.74 (1.14)	49.25 (1.15)	5.38 (1.03)	58.29 (1.54)	9.10 (1.33)	67.06 (0.64)	12.45 (1.06)
T17	34.03 (1.19)	12.66 (1.45)	42.38 (1.17)	8.75 (1.43)	49.59 (0.95)	6.22 (0.95)	56.56 (1.07)	8.14 (1.02)	65.81 (0.60)	15.14 (1.78)
T18	35.78 (1.24)	13.47 (2.36)	43.95 (0.77)	7.03 (1.68)	50.19 (0.98)	8.79 (1.71)	59.55 (1.17)	10.60 (1.43)	66.84 (0.44)	12.21 (1.29)
T19	34.04 (1.28)	13.42 (1.83)	44.49 (0.89)	6.02 (1.00)	51.77 (1.16)	6.33 (1.14)	61.55 (1.15)	10.54 (1.26)	68.61 (0.56)	14.72 (2.14)
T20	32.32 (1.36)	19.28 (2.93)	42.81 (0.76)	7.62 (0.78)	49.54 (0.90)	7.09 (1.60)	57.61 (1.12)	11.95 (1.85)	68.45 (0.88)	17.25 (1.91)
T21	32.62 (1.69)	14.47 (2.67)	42.61 (0.70)	6.09 (1.68)	49.38 (1.11)	3.85 (0.52)	55.87 (1.48)	9.23 (2.27)	66.45 (0.51)	14.29 (1.98)
T22	29.59 (0.36)	15.75 (0.50)	40.33 (0.28)	8.30 (0.59)	47.87 (0.35)	4.65 (0.29)	57.39 (0.37)	11.19 (0.40)	68.41 (0.37)	12.80 (0.45)
T25	27.47 (0.27)	12.38 (0.35)	38.73 (0.37)	7.10 (0.26)	46.80 (0.31)	7.26 (0.33)	54.02 (0.32)	6.70 (0.23)	62.13 (0.29)	8.73 (0.26)

Figure 7.9 indicates a decreasing trend in frequencies across all five modes. However, as the mode order increased, the range of variation in normalised frequency became narrow. Specifically, the variation in $f_{1,n}$ spanned from 1.0 to 0.69 (Figure 7.9 (a)), while for $f_{5,n}$, it ranged from 1.01 to 0.92 (Figure 7.9 (e)). This characteristic indicates differing sensitivities of the modes to damage developed in the masonry arch bridge. The first order of mode, representing the global failure of the bridge, was characterised by the out-of-plane bending of the entire structure, with deformation mainly concentrated at the spandrel walls in the mid-span region (Figure 7.6 (a)). Following the bridge failure, extensive cracks developed in the arch intrados. Additionally, spandrel walls were separated into several parts by cracks, with two main cracks forming between the abutments. Such a damage pattern substantially reduced the stiffness of the bridge in the out-of-plane direction, resulting in a notable decrease in $f_{1,n}$.

In contrast, higher modes exhibited more complex deformation characteristics than the first mode. Specifically, the 2nd mode was also characterised by bending of the spandrel walls, with the largest deformation occurred at the conners of the walls, where no crack was observed. The 3rd and 4th modes displayed a vertical bending behaviour. In these two modes, deformation of the backfill was more pronounced than that of the masonry (Figure 7.6 (c) and (d)) because the backfill has a lower elastic modulus than masonry. Therefore, even though cracks developed in masonry parts (e.g., arch intrados and spandrel walls) reduced the stiffness of the structure, the progressive loading process caused the backfill to became slightly denser. These two effects together resulted in less pronounced variations in $f_{3,n}$ and $f_{4,n}$. Furthermore, the 5th mode showed asymmetrical deformations localised at specific locations such as corners and mid-points of spandrel walls, where no crack was triggered during the tests, leading to a comparatively stable development in $f_{5,n}$.

Focusing on the first order mode $f_{1,n}$, a strong correlation was observed between its variation and the stiffness degradation of the masonry arch bridge. Notably, the most pronounced decrease in $f_{1,n}$ during the low-level tests was occurred at T4, in which the first crack initialised between the spandrel wall and the arch extrados. Subsequently, $f_{1,n}$ experienced minor fluctuations until the completion of the low-level testing phase. The mean value of $f_{1,n}$ in this stage was 0.94, indicative of a 6% decrement in the bridge's first order frequency.

Mid-level tests with a higher loading magnitude led to the damage accumulated further,

including the formation of the first hinge at the arch barrel (observed at T12, T13, T16 and T17), the progression of separation between the arch barrel and spandrel walls (observed at T15), as well as several localised cracks (T18, T19, and T20). These damages triggered a marked reduction in $f_{1,n}$, falling from 0.94 in average before the mid-level testing to 0.85 in average for the mid-level tests. However, within the mid-level testing phase, the variation in $f_{1,n}$ did not exhibit a clear correlation to specific damage patterns. Fluctuations in $f_{1,n}$ was within 10% between 0.81 to 0.90, potentially influenced by environmental factors. Moreover, the crack development of the bridge during mid-level tests were not effectively captured by variations in $f_{2,n}$ to $f_{5,n}$.
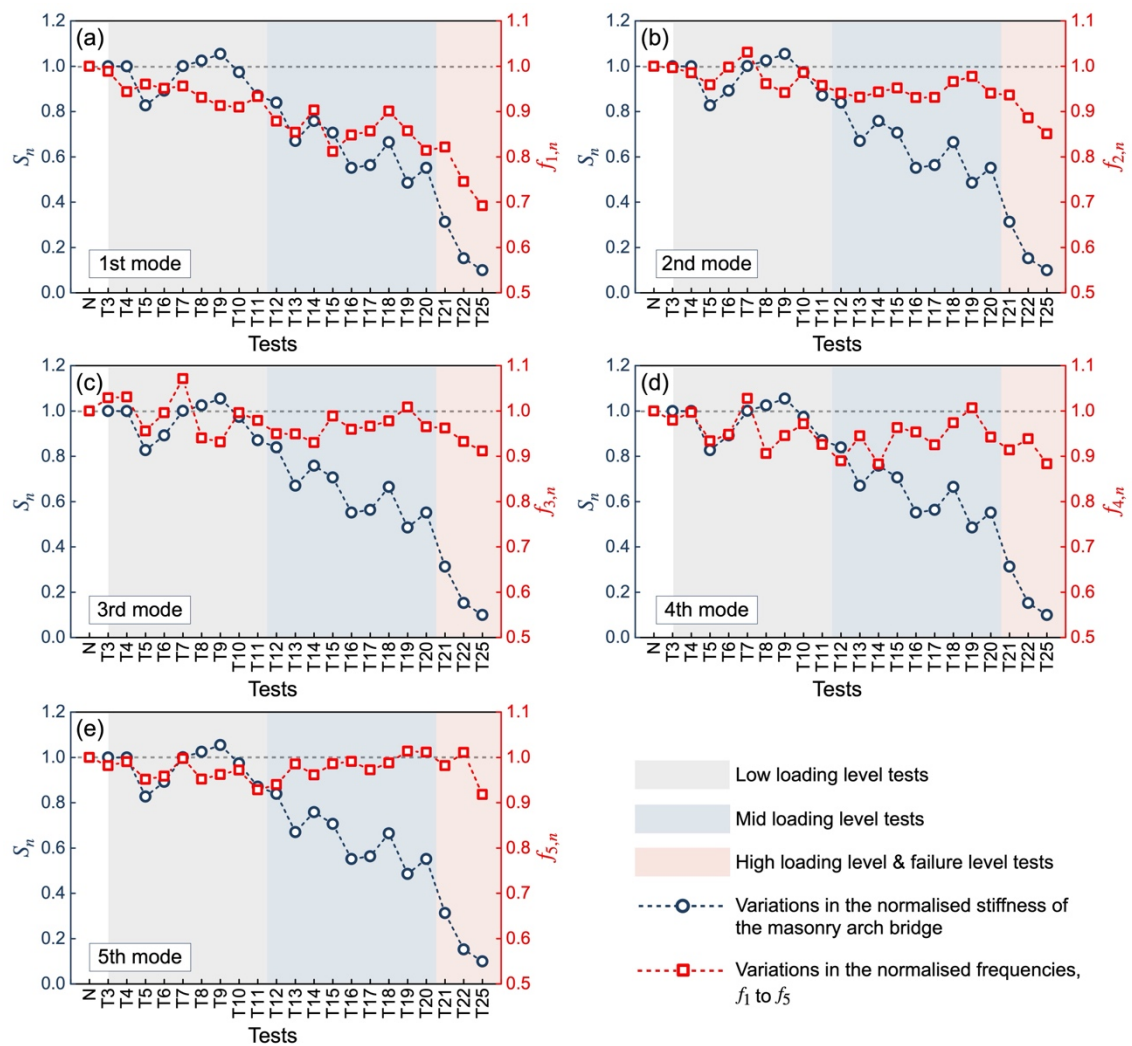
Figure 7.9 Correlation between normalised stiffness (S_n) and normalised frequency (f_n) of the masonry arch bridge along with the load testing process from undamaged state to failure: (a) to (e) shows the results for the 1st mode to the 5th mode.

Following the mid-level testing, a high-level load of 560 kN was applied at the quarter-span of the bridge (T21). This load on the one hand resulted in the initiation of the second hinge and the third hinge. On the other hand, some diagonal cracks were developed at

the arch intrados near the loading point. From the frequency perspective, the value of $f_{1,n}$ exhibited a minor reduction, declining from an average of 0.85 during mid-level testing to 0.82 after the high-level test. Also, variations in $f_{2,n}$ to $f_{5,n}$ were not significant. In contrast, there was a substantial decrease in structural stiffness according to the load-deflection curve, with S_n diminishing from 0.55 at T20 to 0.31 at T21. The marginal decrease in all the five order frequencies indicated their limited sensitivity to cracks developed in T21. However, it is noteworthy that the marked decrease in S_n was not fully attributable to structural damage. A shift in loading approach, from load control to displacement control for safety considerations, resulted in the load to be applied faster. This alternation potentially resulted in an underestimated stiffness value.
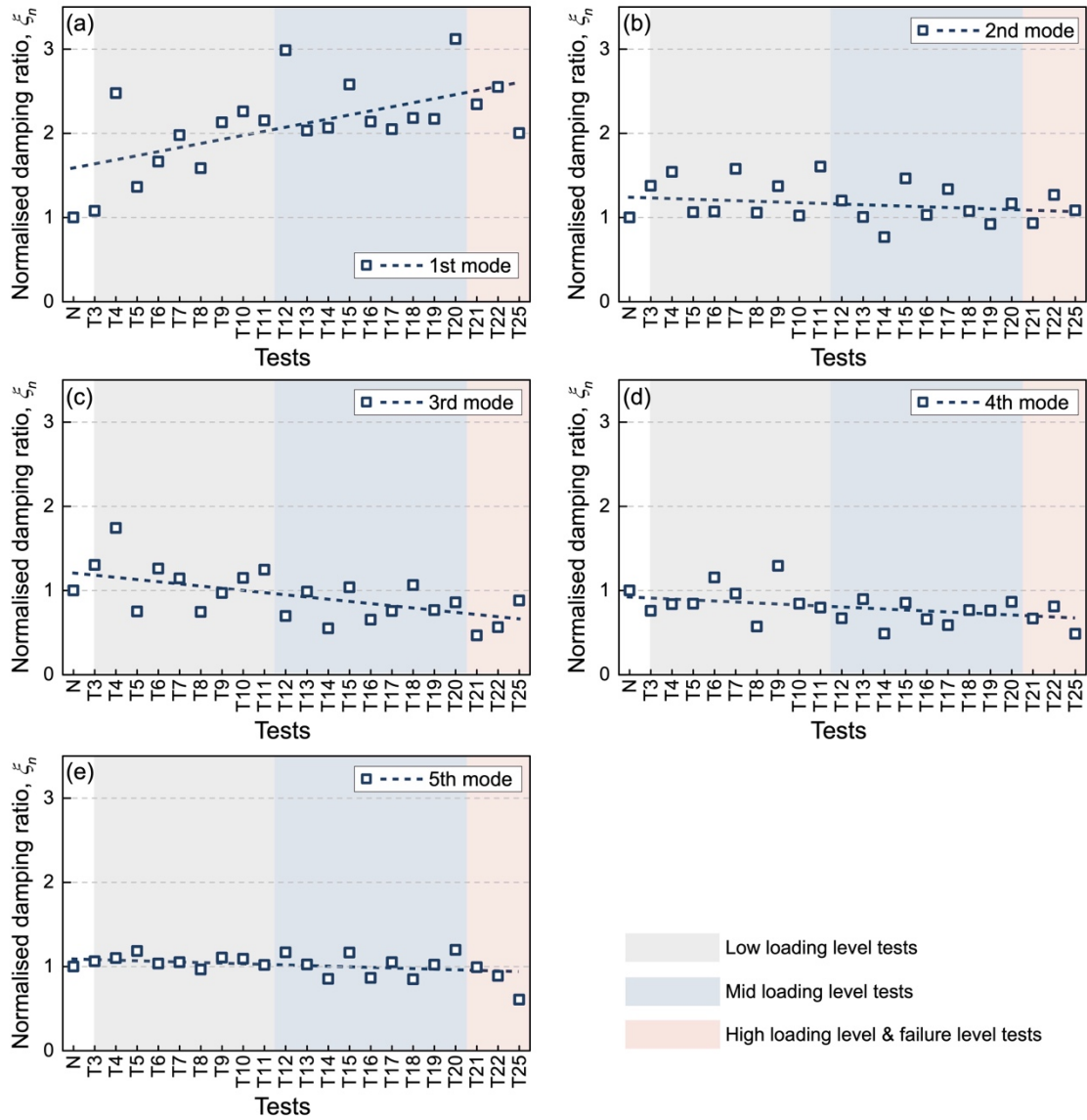
Figure 7.10 Variations in the normalised damping ratios of the masonry arch bridge: (a) to (e) shows the results for the 1st mode to the 5th mode.

During the first failure level test conducted at point B (T22), the global failure mechanism of the masonry arch bridge was fully activated. This resulted in that S_n decreased further by more than a half from 0.31 to 0.15. Accordingly, notable reductions were observed in the first three order frequencies $f_{1,n}$, $f_{2,n}$, and $f_{3,n}$. The most pronounced decline was found in $f_{1,n}$, which fell by approximately 9%. In comparison to the undamaged bridge, the values of $f_{1,n}$ to $f_{3,n}$ in the post-failure conditions showed decreases of 26%, 12%, and 7%, respectively.

After the first failure level test, the residual capacity of the masonry arch bridge was assessed by applying a static load at point H, located at the three-quarter span of the arch barrel (T25). A comparison of results from T22 and T25 revealed that the residual capacity of the masonry arch bridge reduced by merely 10% from 639 kN to 575 kN, suggesting the failed bridge still had a significant capacity. However, it was noted that S_n dropped around 35%, indicating a substantial decrease in the stiffness of the bridge. Compared to the values of frequencies obtained from the first failure-level test, all five order frequencies dropped after the second failure-level test. For example, $f_{1,n}$ to $f_{5,n}$ reduced by 7%, 4%, 2%, 6%, and 9%, respectively. Compared to the undamaged bridge, S_n and $f_{1,n}$ obtained from the last test reduced by 90% and 31%, respectively.

Figure 7.10 shows alternations in normalised damping ratios (ξ_n) throughout the loading process. ξ_n was normalised by dividing the values of damping ratio obtained from each test by that obtained from the undamaged bridge (N). It is noteworthy that the variation in ξ_n is more pronounced than f_n. For example, values of $\xi_{1,n}$ varied over 200%, which was around 7 times larger than the variation range of $f_{1,n}$. Similar to f_n, the range of variation in ξ_n became progressively narrowed as the mode order increased from the 1st to the 5th. Moreover, regarding the development trend, $\xi_{1,n}$ exhibited a notable increased trend along with the progression of damage and crack propagation, while $\xi_{2,n}$ to $\xi_{5,n}$ had a declining trend. Nevertheless, the specific correlation between ξ_n and damage accumulation of the bridge was less clear than that between S_n and f_n. Therefore, ξ_n may not be able to serve as an independent indicator for assessing damage levels in the masonry arch bridge.

7.5.4   Equivalent elastic modulus degradation

In the FE model, frequency of the bridge is determined by the mass, elastic modulus, and Poisson's ratio of the materials employed. Inspection on the bridge during tests revealed that the predominant damage to the masonry arch bridge was characterised by the

initiation and propagation of cracks in the masonry, resulting in a marked reduction in the bridge's stiffness. To evaluate the impact of crack extension on the global degradation in material properties of masonry, an equivalent elastic modulus (E') was adopted. Specifically, in the FE model (see Figure 7.5), the bridge's frequency was calculated with a progressively decreasing elastic modulus of masonry from 4.7 GPa to 1.2 GPa, while other calibrated parameters were maintained constant.
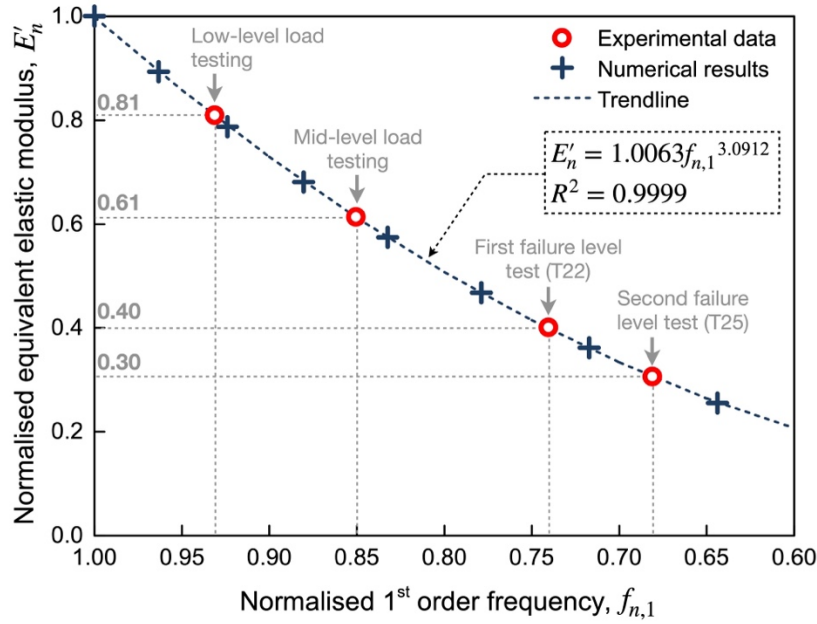
Figure 7.11 Correlation between the normalised equivalent elastic modulus of masonry (E'_n) and the normalised 1st mode frequency ($f_{n,1}$).

Figure 7.11 illustrates the correlation between the normalised equivalent elastic modulus of masonry (E'_n) and the normalised 1st mode frequency ($f_{n,1}$), which exhibits the highest sensitivity to damage observed in the bridge. According to the numerical results, a reduction in the masonry's elastic modulus from 4.7 GPa to 1.2 GPa, by approximately 75%, corresponded to a decrease in f_1 of the bridge from 40.41 Hz to 26.02 Hz, by about 36%. The trendline in Figure 7.11, derived from numerical results, suggests an around 70% degradation in E' for the failed bridge after T25 due to extensive cracking (Figure 7.8 (e)). Furthermore, analysis of average frequency values from low- and mid-level tests indicates early-stage cracks led to a degradation in the equivalent elastic modulus of masonry by 19% and 39%, respectively. Notably, the most pronounced decrease in the E' occurred during mid-level loading tests and the first failure-level test, coinciding with the formation of the first hinge and the complete activation of a four-hinge mechanism, respectively. It may be noteworthy that the magnitude of the mid-level loading was 250 kN, less than 50% of the bridge's load-

carrying capacity (639 kN), which is usually considered as a safe load that can be applied to the arch bridge according to [16,231]. However, the noticeable reduction in E' observed during the mid-level tests highlighted the necessity of performing continued inspection and monitoring of masonry arch bridges.

7.6 Discussion

This chapter found a significant correlation between the progressive accumulation of damage in a full-scale masonry arch bridge – from virgin to failure – and variations in its modal parameters, particularly the first mode frequency. The correlation improves the current understanding on the impact of structural damage on the dynamic characteristics of such bridges and highlights the significant potential of vibration-based structural health monitoring (SHM) in assessing the conditions of masonry arch bridges. However, transiting these experimental findings to practical applications requires careful adaptation due to several limitations and variables that could influence the outcomes.

First, the bridge tested under laboratory conditions features specific geometric configurations, material properties, boundary conditions, and cracking characteristics under specific loading scenarios that do not strictly representative of real masonry arch bridges in the field. Consequently, the experimental findings are specific to this prototype and may not be directly appliable to other real masonry arch bridges with different geometries, materials, loading and boundary conditions. This is due to the high sensitivity of modal parameters to such variations. This specificity highlights the necessity of a broader testing regime that includes a larger range of bridges to enhance the generalizability of the findings.

Additionally, most masonry arch bridges in the field are constructed over a hundred years ago. These infrastructures have significant degradation resulted from, for example, weathering, increasing traffic loads, and climate change. Thus, in the context of real-world applications, obtaining modal parameters of undamaged masonry arch bridges are generally impossible, posing a substantial challenge in establishing a baseline for evaluating the condition of these bridges based on their current modal parameters. However, SHM should be viewed as a long-term strategy. By continuously monitoring the modal parameters, it is possible to detect and quantify the progression of damage, such as crack extensions and further accumulation of structural damages, based on the

current state of the bridge.

7.7 Conclusion

In this study, full life-cycle vibration-based monitoring was carried out on a large-scale masonry arch bridge to investigate the correlation between the damage accumulation in the bridge and variation in its modal parameters. During experiments, static/cyclic patch loads were applied at nine locations with increasing magnitudes to trigger the accumulated damage and crack propagation. Post each loading test, hummer-induced vibration data was collected, and the modal parameters were evaluated by the stochastic subspace identification (SSI) method. Additionally, finite element (FE) modelling was conducted to identify mode shapes of the undamaged bridge and to verify the experimental results. Crack propagation, stiffness degradation, and changes in modal parameters including the frequency and damping ratio were discussed in the chapter.

From the investigation, a significant correlation was found between crack propagation, stiffness degradation in the masonry arch bridge, and variations in modal parameters. Among the five orders of mode identified, the first order of parameters showed the greatest sensitivity to the damage of the bridge. Specifically:

1. Early-stage damage in the bridge involved the cracks initialised and propagated at interfaces between the arch barrel and spandrel walls. While these cracks are not typically considered critical in affecting the capacity of the bridge, they led to an approximately 5% reduction in stiffness and a 6% decrease in the first order of frequency.

2. Mid-level loading tests resulted in more noticeable plastic damage, including the formation of the first hinge in the arch barrel; diagonal cracks appeared at spandrel walls; and localised shear cracks in the arch intrados. This global damage sign resulted in a significant stiffness degradation of approximately 45%, with a maximum of 19% decrease in the first order of frequency with respect to the undamaged bridge.

3. Application of a static load up to 560 kN initiated the second and third hinges in the arch barrel. However, this damage accumulation was not effectively detected by the frequency analysis, showing only a 4% decrease in the first order frequency.

4. Failure-level tests indicated a 639 kN of the capacity of the masonry arc bridge. After

the global failure mechanism was fully activated, both the stiffness and first order frequency reduced significantly by 51% and 9%, respectively, compared to the previous high-level loading test. Relative to the undamaged bridge, these values showed a decline of 85% and 26%, respectively.

5. Residual capacity was assessed by loading at the three-quarter span of the arch barrel. The crack patterns mirrored those in the first failure level test. Results showed that the bridge's residual capacity decreased slightly by 10%. However, the stiffness reduced substantially by 35%, which was captured by a further 7% decline in frequency.

6. Compared to frequency characteristics, variations in the damping ratio, specifically in the first mode, were more pronounced, indicating its higher sensitivity to structural damage. Nevertheless, the trend of variation in the damping ratio with increasing damage was less clear than that observed with frequency changes. Additionally, the damping ratio values exhibited greater variability than those of frequency. Therefore, using the damping ratio alone as an indicator for assessing the masonry arch bridges appears currently inadvisable, warranting further research.

Furthermore, a second bridge will be constructed and tested under high-cycle fatigue loads, and the vibration-based assessment of the bridge will be performed under a more realistic loading condition.

Acknowledgements

8 Conclusions and Future Research

8.1 Conclusions

Masonry arch bridges form a pivotal part of the transport networks of the UK and many other countries worldwide. In the UK alone, there are ~40,000 highway bridges and >25,000 railway spans of masonry arch construction. Weathering, demands of increasing traffic loads, plus factors such as increased frequency of flood events due to climate change have introduced extreme uncertainty in the long-term performance of such infrastructure assets. Therefore, gaining a better understanding of the behaviour of masonry arch bridges is necessary for informing their repair, maintenance, and rehabilitation strategies and thus improving their resilience and extending their service life. This dissertation focused on the comprehensive characterisation of mechanical and material properties of masonry, as well as the assessment of three-dimensional (3D) response of masonry arch bridges subjected to different types of loads. The conclusions of each part of the work include:

8.1.1 Characterisation on material and mechanical parameters of masonry arch bridges

Chapters 2 and 3 presented a series of small-scale material-level and component-level experimental tests to characterise material properties of masonry arch bridges, as well as masonry-backfill interaction mechanisms. The main conclusions are:

- The properties of masonry units, mortar, and their interfaces showed a certain degree of variability even under laboratory manufacture and testing conditions. Among other parameters, the tensile bond strength at the unit-mortar interface demonstrated the greatest variation.

- Masonry flat arches subjected to static loads had a three-hinge behaviour and failed due to either shear failure of centre joint or crushing of middle bricks under high compressive stress. Under fatigue loads, damage concentrated on one central joint, and cracks propagated with the increase in loading cycles and peak loads, leading to significant stiffness degradation of the specimens.

- The properties of backfill had a significant effect on the frictional properties between masonry and backfill, whereas the influence of investigated masonry bond types

195

could be considered negligible. The adoption of compacted crushed limestone as backfill material resulted in the ratio between the masonry-limestone interface friction angle and the internal friction angle of limestone ranging from 0.70 to 0.75. However, utilizing clay as the backfill material significantly reduced this ratio to approximately 0.35 to 0.39, particularly if interface cohesion was considered.

8.1.2 The 3D behaviour of a masonry arch bridge under static and quasi-static patch loads with increasing magnitudes

Chapters 4 and 5 reported results from experiments conducted on a large-scale masonry arch bridge subjected to static and quasi-static loads. Patch loads were applied at nine locations, including the central point and off-central points (close to the spandrel walls) over the quarter-span, crown, and three-quarter span of the arch barrel. Damage accumulation and crack propagation were observed as loading magnitudes increased. The bridge was ultimately loaded to failure sequentially at the longitudinal central line over the quarter-span and three-quarter span locations, allowing for assessment of the load-carrying and residual capacities of the bridge. The main conclusions are:

Crack formation and propagation:

- The first crack occurred between the arch barrel and a spandrel wall when a low-level eccentric load of 60 kN was applied at mid-span near the spandrel wall. Subsequent low-level loads near the spandrel wall led to further propagation of this hairline crack.

- The mid-level loads with a magnitude of 250 kN (around 50% of the predicted load-carrying capacity of the bridge, ULS) resulted in: (a) the opening of tensile cracks at the arch intrados transversely when loads were applied to the quarter- and three-quarter span points near the spandrel wall; (b) localised square-shaped shear cracks in the arch intrados directly under the loading locations when the loads were applied over the arch crown; and (c) short diagonal cracks initiating on spandrel walls.

- Loading up to 566 kN over the quarter-span of the arch barrel at the longitudinal central line led to significant crack propagation on the masonry arch bridge: (a) three hinges formed, with the first hinge appeared in the vicinity of the applied load, characterised by the formation of tensile cracks in the arch intrados under the loading point; the second hinge formed near the springing closest to the applied load, leading to cracks in the arch extrados; the third hinge located in the midspan region,

with fragments of crushed mortar falling from joints in the arch intrados; and (b) increasing deformation of the arch barrel trigged extended diagonal cracks on the spandrel walls.

- An increase in load from 566 kN to 639 kN at point B fully activated the global failure mechanism of the bridge, with the last (the fourth) hinge observed at the springing furthest from the applied load. In addition, cracks in the arch intrados were observed to radiate outwards from the loaded location, with cracks orientated both transversely and diagonally, forming web-like patterns in the region between the two compression zones, suggesting a 3D response of the arch barrel. The second failure level test with a load applied at the three-quarter point resulted in similar crack patterns observed from the first failure level loading test.

Load-carrying capacity, stiffness degradation, and failure mechanism

- Load-carrying capacity of the masonry arch bridge was identified to be 639 kN. The second failure-level test suggested that the residual capacity of the bridge had reduced by only 10% to 575 kN, while the stiffness of the bridge had decreased by around 35%. This indicates that the damaged bridge still had a significant residual load-carrying capacity.

- The global four-hinge failure was activated during the failure-level tests. Also, deflection of the arch barrel was captured through the ground penetrating radar (GPR) surveys. Additionally, the behaviour of arch barrel was characterised by a localised 3D response, with the highest deformations of the arch barrel observed directly under the load, and these deformations gradually diminishing in magnitude at monitoring locations further from the load in a transverse direction.

- The response of the bridge was found to be asymmetric. On the one hand, the widths of cracks forming in the north-side spandrel wall were greater than those in the south-side wall. On the other hand, out-of-plane deformations of the north-side wall were greater.

In-plane and out-of-plane deformation of spandrel walls

- No noticeable in-plane deformations of the spandrel walls were observed until the high-level test was conducted. This test initiated the global bridge failure mechanism, characterized by significant crack formation in the spandrel walls and upward movement of the arch barrel, which led to rotational failure of the spandrel

walls.

- Noticeable out-of-plane deformations of the spandrel walls were observed during the high-level and failure-level loading tests, with maximum deformations occurring near the load's location. Low- and medium-level loads induced slight out-of-plane deformations in the spandrel walls, but only when these loads were applied close to the spandrel walls. The out-of-plane deformations accumulated, reaching a maximum recorded deformation of 23.2 mm.

8.1.3 DIC monitoring on the spandrel wall

Digital Image Correlation (DIC) was utilised to monitor the full-field strain/displacement of the masonry arch bridge. Two pairs of cameras were positioned on the south side of the bridge to monitor the crack initiation and propagation throughout the loading and unloading process. The surface of the masonry was untreated, utilizing its inherent natural feature for pixel level movement tracking. Based on the results obtained, the following conclusions can be drawn:

- Comparisons between DIC measurements and readings from LVDT confirmed that DIC can achieve a submillimetre level accuracy (i.e., 0.1 mm) in monitoring movement of untreated masonry surfaces. This precision level is considered to be sufficient for detecting crack behaviour in masonry structures.

- Application of low-level loads over the arch crown near the south-side spandrel wall led to separation between the arch barrel and spandrel wall when the load reached approximately 65 kN, indicating early-stage damage in the bridge. Mid-level tests, applied over the quarter-span and three-quarter span locations near the south-side spandrel wall, resulted in the opening of tensile cracks in the arch intrados under the loading points when loads ranged from 124 to 170 kN. However, these cracks were indicative of localized damage rather than signs of global failure.

- The global four-hinge failure mechanism was triggered during high-level and failure-level tests, applied over the quarter-span and three-quarter span locations of the arch barrel along the longitudinal centreline of the bridge. The first and second hinges were initially activated at loads of 378 kN and 429 kN, respectively, corresponding to approximately 59% and 67% of the bridge's ultimate limit state. Once these hinges were formed, subsequent load applications resulted in their earlier activation.

- The interaction between the arch barrel and spandrel wall under loads was primarily manifested by their deformation compatibility. As loads were applied, they induced deformations in the arch barrel, leading to crack openings and hinge formation. This deflection prompted rotational movement of the arch barrel, pushing the non-loading side spandrel wall to move upward or diagonally upward. The displacement discontinuity in the spandrel wall led to diagonal cracks initiated and propagated in the spandrel wall.

8.1.4 Vibration-based monitoring of the bridge with increasing levels of damage

Along with the loading tests on the bridge, the hammer-induced vibration response was captured and analysed using the stochastic subspace identification (SSI) method. This analysis aimed to identify modal parameters of the bridge spanning its entire life cycle. The results obtained are detailed in Chapter 7, and the main conclusions are:

- Among the five orders of modal parameters identified, the first-order frequency had the most pronounced correlation with stiffness degradation and damage accumulation in the masonry arch bridge.

- Early-stage damage resulting from low-level loads (i.e., separation between the arch barrel and spandrel walls) led to an approximate 5% reduction in stiffness and a 6% decrease in the first-order frequency. Mid-level loads caused more noticeable plastic deformation of the backfill and damage to the masonry, resulting in a significant stiffness degradation of about 45%, with a maximum 19% reduction in the first-order frequency. The formation of three hinges in the bridge subjected to high-level loads was not effectively captured by the frequency analysis, showing only a 4% decrease in the first-order frequency. However, following the bridge's failure, there was a dramatic reduction in both stiffness and first-order frequency by 85% and 26%, respectively, relative to the undamaged bridge. These parameters declined further by 35% and 7% after the second failure-level test.

- Compared to frequency characteristics, variations in the damping ratio were more pronounced, indicating its higher sensitivity to structural damage. Nevertheless, the trend of variation in the damping ratio with increasing levels of damage was less clear than that observed with frequency changes.

8.2 Limitations and future research

Main limitations and suggestions for future investigation may include:

- This study utilised high strength type A engineering bricks and low-strength lime mortar. The purpose of using these specific materials include: (a) to reproduce the joint failure that commonly observed in real masonry arch bridges; and (b) to use the same materials that employed in in previous experimental tests on masonry arches/arch bridges carried out at Bolton Institute and University of Salford, thereby providing a degree of comparability between tests. However, the variability in material properties across real-world masonry arch bridges can significantly influence their behaviour and capacity. Future work is recommended to explore a broader range of materials (i.e., low strength bricks, natural stones, sand and clay as backfill materials, or the materials taken directly from the real bridges).

- The behaviour of masonry flat arches under static/fatigue bending loads reported in Chapter 2 was found to be significantly affected by the independent steel frame used for applying pre-compression. Further investigations are suggested to consider alternative specimen types and loading scenarios to minimize the influence of testing rig on the response of masonry specimens.

- In Chapter 3, masonry specimens manufactured for shear box tests were limited to two bond patterns (i.e., English bond and soldier course bond). For these two specific masonry pond patterns, it is found that their influence on the interface frictional behaviour was minimal. However, considering different bond patterns, masonry units, and mortar joint profiles may affect surface roughness and subsequently alter frictional behaviour and soil-structure interactions, it is recommended that future studies include a variety of brickwork or stone masonry bond patterns to assess their impact on the masonry-backfill interface behaviour.

- In Chapter 6, the bridge's stiffness was derived from the load-deflection response under different point loads. However, this represents localized stiffness rather than a true global modal stiffness. This is a key limitation of this experimental study, as the available data was restricted to load-deflection measurements. It is acknowledged that applying loads at different locations, even in an undamaged state, could result in varying stiffness values. However, the analysis focused on relative stiffness variation, consistently measured at the same location but under different damage conditions. While not fully representative of global stiffness, the results

remain internally comparable. For future studies, it is recommended to estimate global modal stiffness, which could be more effectively achieved using validated high-fidelity numerical simulations.

- While this study considered specific material combinations and controlled conditions, real-world masonry arch bridges exhibit significant variability in masonry strength, mortar properties, and backfill composition. Moreover, structural defects such as cracks, voids, and irregularities can greatly influence bridge performance. Future research is recommended to investigate these factors experimentally and numerically to enhance the predictive accuracy of models and improve bridge assessment and conservation strategies.

- In future work, high-fidelity numerical models are suggested to be developed and validated against the experimental data reported in this dissertation. With the calibrated parameters, numerical models of real masonry arch bridges can be developed, and the response and failure mechanisms of these real bridges can be investigated with a higher level of confidence.

- The detailed documentation of crack propagation, stiffness degradation, and load-deflection curves provides a foundation for developing a dynamic digital twin model. This model would feature damage updating capabilities to reflect the impact of existing cracks and damage on bridge behaviour. Once validated against experimental findings, this digital twin could be applied to real masonry arch bridges for ongoing assessment and management.

- With the increasing frequency of extreme weather events, the resilience of masonry arch bridges under flood-induced forces remains a critical area for further research. Future investigations should explore the effects of hydrodynamic forces, including scouring and subsidence, through experimental studies and advanced numerical modelling. Understanding these impacts will help inform better preservation and reinforcement strategies for masonry bridges and improve their resilience.

References

[1]   Karimian S. A Computational Modelling Strategy for Historic Masonry Structures. The University of Leeds, 2015.

[2]   Tripadvisor. Things to Do in Zwickau n.d. https://www.tripadvisor.co.uk/Attractions-g187402-Activities-Zwickau_Saxony.html (accessed March 4, 2025).

[3]   Kaushik Patowary. The World's Largest Brick Bridge. Amusing Planet 2020. https://www.amusingplanet.com/2020/06/the-worlds-largest-brick-bridge.html (accessed March 4, 2025).

[4]   Miri M. Modelling of Repair Techniques for Masonry Arch Bridges. Cardiff University, 2005.

[5]   Orbán Z, Gutermann M. Assessment of masonry arch railway bridges using non-destructive in-situ testing methods. Eng Struct 2009;31:2287–98. https://doi.org/10.1016/j.engstruct.2009.04.008.

[6]   Walker PJ. Strength and Erosion Characteristics of Earth Blocks and Earth Block Masonry. Journal of Materials in Civil Engineering 2004;16:497–506. https://doi.org/10.1061/(asce)0899-1561(2004)16:5(497).

[7]   Shrive NG, Sayed-Ahmed EY, Tilleman D. Creep analysis of clay masonry assemblages. Canadian Journal of Civil Engineering 1997;24:367–79. https://doi.org/10.1139/l96-126.

[8]   Kallioras S, Guerrini G, Tomassetti U, Marchesi B, Penna A, Graziotti F, et al. Experimental seismic performance of a full-scale unreinforced clay-masonry building with flexible timber diaphragms. Eng Struct 2018;161:231–49. https://doi.org/10.1016/j.engstruct.2018.02.016.

[9]   Scozzese F, Ragni L, Tubaldi E, Gara F. Modal properties variation and collapse assessment of masonry arch bridges under scour action. Eng Struct 2019;199. https://doi.org/10.1016/J.ENGSTRUCT.2019.109665.

[10]   Wang J, Tomor AK, Melbourne C, Yousif S. Critical review of research on high-cycle fatigue behaviour of brick masonry. Constr Build Mater 2013;38:602–9. https://doi.org/10.1016/j.conbuildmat.2012.09.010.

[11]   McKibbins LD, Melbourne C, Sawar N, Gaillard CS. Masonry arch bridges: condition appraisal and remedial treatment. London: CIRIA; 2006.

[12]   Tomor A, Verstrynge E. A joint fatigue-creep deterioration model for masonry with acoustic emission based damage assessment. Constr Build Mater 2013;43:575–88. https://doi.org/10.1016/j.conbuildmat.2013.02.045.

[13]   Casas JR. A probabilistic fatigue strength model for brick masonry under compression. Constr Build Mater 2009;23:2964–72. https://doi.org/10.1016/j.conbuildmat.2009.02.043.

[14]   Roberts TM, Hughes TG, Dandamudi VR, Bell B. Quasi-static and high cycle fatigue strength of brick masonry. Constr Build Mater 2006;20:603–14. https://doi.org/10.1016/j.conbuildmat.2005.02.013.

[15]   Koltsida IS, Tomor AK, Booth CA. Experimental evaluation of changes in strain under compressive fatigue loading of brick masonry. Constr Build Mater 2018;162:104–12. https://doi.org/10.1016/j.conbuildmat.2017.12.016.

[16]   Augusthus-Nelson L, Swift G. Experimental investigation of the residual behaviour of damaged masonry arch structures. Structures 2020;27:2500–12. https://doi.org/10.1016/j.istruc.2020.08.008.

[17]   Sarhosis V, Oliveira D V., Lourenco PB. On the mechanical behavior of masonry. Computational Modeling of Masonry Structures Using the Discrete Element Method, 2016, p. 1–27. https://doi.org/10.4018/978-1-5225-0231-9.ch001.

[18]   Mazzotti C, Sassoni E, Pagliai G. Determination of shear strength of historic masonries by moderately destructive testing of masonry cores. Constr Build Mater 2014;54:421–31. https://doi.org/10.1016/j.conbuildmat.2013.12.039.

[19]   Dorji J, Zahra T, Thambiratnam D, Lee D. Strength assessment of old masonry arch bridges through moderate destructive testing methods. Constr Build Mater 2021;278:122391. https://doi.org/10.1016/j.conbuildmat.2021.122391.

[20]   Loverdos D, Sarhosis V. Automatic image-based brick segmentation and crack detection of masonry walls using machine learning. Autom Constr 2022;140:104389. https://doi.org/10.1016/j.autcon.2022.104389.

[21]   Loverdos D, Sarhosis V, Adamopoulos E, Drougkas A. An innovative image processing-based framework for the numerical modelling of cracked masonry structures. Autom Constr 2021;125:103633. https://doi.org/10.1016/j.autcon.2021.103633.

[22]   Dhanasekar M, Prasad P, Dorji J, Zahra T. Serviceability assessment of masonry arch bridges using digital image correlation. Journal of Bridge Engineering 2019;24. https://doi.org/10.1061/(ASCE)BE.1943-5592.0001341.

[23]   Borlenghi P, Saisi A, Gentile C. ND testing and establishing models of a multi-span masonry arch bridge. J Civ Struct Health Monit 2023. https://doi.org/10.1007/s13349-022-00666-1.

[24]   Acikgoz S, DeJong MJ, Soga K. Sensing dynamic displacements in masonry rail bridges using 2D digital image correlation. Struct Control Health Monit 2018;25:e2187. https://doi.org/10.1002/stc.2187.

[25]   Roselli I, Malena M, Mongelli M, Cavalagli N, Gioffrè M, De Canio G, et al. Health

assessment and ambient vibration testing of the "Ponte delle Torri" of Spoleto during the 2016–2017 Central Italy seismic sequence. J Civ Struct Health Monit 2018;8:199–216. https://doi.org/10.1007/s13349-018-0268-5.

[26] La Mendola L, Lo Giudice E, Minafò G. Experimental calibration of flat jacks for in-situ testing of masonry. International Journal of Architectural Heritage 2019;13:619–29. https://doi.org/10.1080/15583058.2018.1453886.

[27] Srinivas V, Sasmal S, Ramanjaneyulu K, Ravisankar K. Performance evaluation of a stone masonry arch railway bridge under increased axle loads. Journal of Performance of Constructed Facilities 2014;28:363–75. https://doi.org/10.1061/(ASCE)CF.1943-5509.0000407.

[28] Ramos LF, Manning E, Fernandes F, Fangueiro R, Azenha M, Cruz J, et al. Tube-jack testing for irregular masonry walls: Prototype development and testing. NDT & E International 2013;58:24–35. https://doi.org/10.1016/j.ndteint.2013.04.004.

[29] Orbán Z, Gutermann M. Assessment of masonry arch railway bridges using non-destructive in-situ testing methods. Eng Struct 2009;31:2287–98. https://doi.org/10.1016/j.engstruct.2009.04.008.

[30] De Santis S, Tomor AK. Laboratory and field studies on the use of acoustic emission for masonry bridges. NDT & E International 2013;55:64–74. https://doi.org/10.1016/j.ndteint.2013.01.006.

[31] Verstrynge E, Lacidogna G, Accornero F, Tomor A. A review on acoustic emission monitoring for damage detection in masonry structures. Constr Build Mater 2021;268:121089. https://doi.org/10.1016/j.conbuildmat.2020.121089.

[32] Ahmad SHS. Static Analysis of Masonry Arches. PhD thesis. University of Salford, 2017.

[33] Zampieri P, Faleschini F, Zanini MA, Simoncello N. Collapse mechanisms of masonry arches with settled springing. Eng Struct 2018;156:363–74. https://doi.org/10.1016/j.engstruct.2017.11.048.

[34] Callaway PA. Soil-structure interaction in masonry arch bridges. University of Sheffield, 2007.

[35] Royles R, Hendry AW. Model tests on masonry arches. Proceedings of the Institution of Civil Engineers 1991;91:299–321. https://doi.org/10.1680/iicep.1991.14997.

[36] Melbourne C, Gilbert M. The behaviour of multiring brickwork arch bridges. Struct Eng 1995;73:39–47.

[37] Melbourne C, Gilbert M. Analysis of multi-ring brickwork arch bridges. Arch bridges: Proceedings of the First International Conference on Arch Bridges, vol. 73, Bolton, UK: Thomas Telford Publishing; 1995, p. 225–38.

[38] Ronca P, Franchi A, Crespi P. Structural failure of historic buildings: masonry fatigue tests for an interpretation model. In: Modena, Lourenço PB, Roca P, editors. Structural Analysis of Historical Constructions, London: Taylor & Francis Group; 2004, p. 273–80.

[39] Alexakis H, Liu H, DeJong MJ. Damage identification of brick masonry under cyclic loading based on acoustic emissions. Eng Struct 2020;221:110945. https://doi.org/10.1016/j.engstruct.2020.110945.

[40] Sarhosis V, De Santis S, De Felice G. A review of experimental investigations and assessment methods for masonry arch bridges. Struct Infrastruct Eng 2016;12:1439–64. https://doi.org/10.1080/15732479.2015.1136655.

[41] Lemos J v. Discrete Element Modeling of Masonry Structures. International Journal of Architectural Heritage 2007;1:190–213. https://doi.org/10.1080/15583050601176868.

[42] D'Altri AM, Sarhosis V, Milani G, Rots J, Cattari S, Lagomarsino S, et al. A review of numerical models for masonry structures. Numerical Modeling of Masonry and Historical Structures, Elsevier; 2019, p. 3–53. https://doi.org/10.1016/B978-0-08-102439-3.00001-4.

[43] Occhipinti G, Caliò I, D'Altri AM, Grillanda N, De Miranda S, Milani G, et al. Nonlinear finite and discrete element simulations of multi-storey masonry walls. Bulletin of Earthquake Engineering 2022;20:2219–44. https://doi.org/10.1007/s10518-021-01233-7.

[44] Sarhosis V, Sheng Y. Identification of material parameters for low bond strength masonry. Eng Struct 2014;60:100–10. https://doi.org/10.1016/j.engstruct.2013.12.013.

[45] Lourenço PB, Rots JG, Blaauwendraad J. Continuum Model for Masonry: Parameter Estimation and Validation. Journal of Structural Engineering 1998;124:642–52. https://doi.org/10.1061/(ASCE)0733-9445(1998)124:6(642).

[46] Maheri MR, Motielahi • F, Najafgholipour MA. The effects of pre and post construction moisture condition on the in-plane and out-of-plane strengths of brick walls. Mater Struct 2011;44:541–59. https://doi.org/10.1617/s11527-010-9648-y.

[47] Khalaf FM. New test for determination of masonry tensile bond strength. Journal of Materials in Civil Engineering 2005;17:725–32. https://doi.org/10.1021/cen-v078n033.p016.

[48] H. Varum. Seismic assessment, strengthening and repair of existing buildings . Universidade de Aveiro, 2003.

[49] Phaiju S, Man Pradhan P. Experimental work for mechanical properties of brick

and masonry panel. Journal of Science and Engineering 2018;5.

[50] Sarangapani G, Venkatarama Reddy B v., Jagadish KS. Brick-Mortar Bond and Masonry Compressive Strength. Journal of Materials in Civil Engineering 2005;17:229–37. https://doi.org/10.1061/(ASCE)0899-1561(2005)17:2(229).

[51] Riddington JR, Naom NF. Finite element prediction of masonry compressive strength. Comput Struct 1994;52:113–9. https://doi.org/10.1016/0045-7949(94)90261-5.

[52] Jafari S, Rots JG, Esposito R, Messali F. Characterizing the Material Properties of Dutch Unreinforced Masonry. Procedia Eng, vol. 193, Elsevier Ltd; 2017, p. 250–7. https://doi.org/10.1016/j.proeng.2017.06.211.

[53] Singh SB, Munjal P. Bond strength and compressive stress-strain characteristics of brick masonry. Journal of Building Engineering 2017;9:10–6. https://doi.org/10.1016/J.JOBE.2016.11.006.

[54] British Standard. BS EN 772 Methods of test for masonry units. 2001.

[55] Borri A, Corradi M, Castori G, De Maria A. A method for the analysis and classification of historic masonry. Bulletin of Earthquake Engineering 2015;13:2647–65. https://doi.org/10.1007/s10518-015-9731-4.

[56] Ismail N, Ingham JM. In-plane and out-of-plane testing of unreinforced masonry walls strengthened using polymer textile reinforced mortar. Eng Struct 2016;118:167–77. https://doi.org/10.1016/j.engstruct.2016.03.041.

[57] Melbourne C, Walker PJ. Load tests to collapse on a full-scale model six metre span brick arch bridge. TRRL Contractor Report CR 189. London: 1990.

[58] ASTM C270. Standard specification for mortar for unit masonry. West Conshohocken, PA, USA: 2007.

[59] British Standard. BS EN 772-1 Methods of test for masonry units - Part 1: Determination of compressive strength. 2000.

[60] British Standard. BS EN 1052-2 Methods of test for masonry- Part 2: determination of flexural strength. 1999.

[61] British Standard. BS EN 12390-6 Testing hardened concrete - Part 6: Tensile splitting strength of test specimens. 2000.

[62] Drougkas A, Roca P, Molins C. Material Characterization and Micro-Modeling of a Historic Brick Masonry Pillar. International Journal of Architectural Heritage 2016;10:887–902. https://doi.org/10.1080/15583058.2016.1157711.

[63] British Standard. BS EN 1015-11 Methods of test for mortar for masonry - Part 11: Determination of flexural and compressive strength of hardened mortar. 2020.

[64] Callaway P, Gilbert M, Smith CC. Influence of backfill on the capacity of masonry

arch bridges. Proceedings of the Institution of Civil Engineers: Bridge Engineering 2012;165:147–58. https://doi.org/10.1680/bren.11.00038.

[65] Manual of Contract Documents for Highway Works. Volume 1 Specification for Highway Works. Department for Transport, United Kingdom; 2016.

[66] ASTM-2011. Standard test method for direct shear test of soils under consolidated drained conditions. 2011.

[67] Bareither CA, Benson CH, Edil TB. Comparison of shear strength of sand backfills measured in small-scale and large-scale direct shear tests. Canadian Geotechnical Journal 2008;45:1224–36. https://doi.org/10.1139/T08-058.

[68] D'Altri AM, Sarhosis V, Milani G, Rots J, Cattari S, Lagomarsino S, et al. Modeling strategies for the computational analysis of unreinforced masonry structures: review and classification. Archives of Computational Methods in Engineering 2020;27:1153–85. https://doi.org/10.1007/s11831-019-09351-x.

[69] Drougkas A. Macro-modelling of orthotropic damage in masonry: combining micro-mechanics and continuum FE analysis. Eng Fail Anal 2022;141:106704. https://doi.org/10.1016/j.engfailanal.2022.106704.

[70] British Standard. BS EN 1052-1 Methods of test for masonry - Part 1: Determination of compressive strength. 1999.

[71] Sahu S, Sarkar P, Davis R. Quantification of uncertainty in compressive strength of fly ash brick masonry. Journal of Building Engineering 2019;26:100843. https://doi.org/10.1016/j.jobe.2019.100843.

[72] Sinha BP. Model studies relating to load bearing brickwork. PhD thesis. Univ. of Edinburgh, 1967.

[73] Seaton AM. Bond strength performance characteristics of brick-mortar interfaces. PhD thesis. Sheffield Hallam University, 2004.

[74] ASTM C952-12. Standard test method for bond strength of mortar to masonry units. 2012.

[75] British Standard. BS EN 1052-3 Methods of test for masonry-Part 3: Determination of initial shear strength. British Standard 2002.

[76] Milani G, Lourenço PB. Simple Homogenized Model for the Nonlinear Analysis of FRP-Strengthened Masonry Structures. I: Theory. J Eng Mech 2013;139:59–76. https://doi.org/10.1061/(ASCE)EM.1943-7889.0000457.

[77] Kamiński T, Kużawa M, Rabiega J. Investigation of the historical Osobowicki Bridge in Wroclaw. 2 ARCH'10 – 6th International Conference on Arch Bridges, Serbia: 2010, p. 8. https://doi.org/10.13140/2.1.3988.0487.

[78] Yoshioka O. Basic characteristics of Shinkansen-induced ground vibration and its reduction measures. Proceedings of the International Workshop Wave, 2000, p.

219–37.

[79] Hendry AW. Masonry properties for assessing arch bridges. 1990.

[80] Bareither CA, Benson CH, Edil TB. Comparison of shear strength of sand backfills measured in small-scale and large-scale direct shear tests. Canadian Geotechnical Journal 2008;45:1224–36. https://doi.org/10.1139/T08-058.

[81] Pulatsu B, Erdogmus E, Lourenço PB. Comparison of in-plane and out-of-plane failure modes of masonry arch bridges using discontinuum analysis. Eng Struct 2019;178:24–36. https://doi.org/10.1016/j.engstruct.2018.10.016.

[82] Gilbert M, Smith CC, Pritchard TJ. Masonry arch analysis using discontinuity layout optimisation. Proceedings of the Institution of Civil Engineers - Engineering and Computational Mechanics 2010;163:155–66. https://doi.org/10.1680/eacm.2010.163.3.155.

[83] Grosman S, Bilbao AB, Macorini L, Izzuddin BA. Numerical modelling of three-dimensional masonry arch bridge structures. Proceedings of the Institution of Civil Engineers - Engineering and Computational Mechanics 2021;174:96–113. https://doi.org/10.1680/jencm.20.00028.

[84] Chen X, Zhang J, Xiao Y, Li J. Effect of roughness on shear behavior of red clay-concrete interface in large-scale direct shear tests. Canadian Geotechnical Journal 2015;52:1122–35. https://doi.org/10.1139/cgj-2014-0399.

[85] Taha A, Fall M. Shear Behavior of Sensitive Marine Clay-Concrete Interfaces. Journal of Geotechnical and Geoenvironmental Engineering 2013;139:644–50. https://doi.org/10.1061/(asce)gt.1943-5606.0000795.

[86] Yavari N, Tang AM, Pereira JM, Hassen G. Effect of temperature on the shear strength of soils and the soil–structure interface. Canadian Geotechnical Journal 2016;53:1186–94. https://doi.org/10.1139/cgj-2015-0355.

[87] Silva IN, Indraratna B, Nguyen TT, Rujikiatkamjorn C. Shear behaviour of subgrade soil with reference to varying initial shear stress and plasticity index. Acta Geotech 2022. https://doi.org/10.1007/s11440-022-01477-w.

[88] Han F, Ganju E, Salgado R, Prezzi M. Effects of interface roughness, particle geometry, and gradation on the sand-steel interface friction angle. Journal of Geotechnical and Geoenvironmental Engineering-ASCE 2018;144:1–12. https://doi.org/10.1061/(ASCE)GT.1943.

[89] Ho TYK, Jardine RJ, Anh-Minh N. Large-displacement interface shear between steel and granular media. Geotechnique 2011;61:221–34. https://doi.org/10.1680/geot.8.P.086.

[90] Rouaiguia A. Residual shear strength of clay-structure interfaces. International Journal of Civil & Environmental Engineering IJCEE-IJENS 2010;10:5–14.

[91]   Yin K, Fauchille A-L, Di Filippo E, Kotronis P, Sciarra G. A review of sand–clay mixture and soil–structure interface direct shear test. Geotechnics 2021;1:260–306. https://doi.org/10.3390/geotechnics1020014.

[92]   Lemos LJ, Vaughan PR. Clay-interface shear resistance. Geotechnique 2000;50:55–64.

[93]   Ravera E, Laloui L. Failure mechanism of fine-grained soil-structure interface for energy piles. Soils and Foundations 2022;62:101152. https://doi.org/10.1016/j.sandf.2022.101152.

[94]   Uesugi M, Kishida H, Tsubakihara Y. Behavior of sand particles in sand-steel friction. Soils and Foundations 1988;28:107–18. https://doi.org/10.3208/SANDF1972.28.107.

[95]   Littleton I. An experimental study of the adhesion between clay and steel. J Terramech 1976;13:141–52.

[96]   Sarhosis V, Forgács T, Lemos J v. A discrete approach for modelling backfill material in masonry arch bridges. Comput Struct 2019;224:106108. https://doi.org/10.1016/j.compstruc.2019.106108.

[97]   Forgács T, Sarhosis V, Ádány S. Shakedown and dynamic behaviour of masonry arch railway bridges. Eng Struct 2021;228. https://doi.org/10.1016/J.ENGSTRUCT.2020.111474.

[98]   Oliveira D v., Lourenço PB, Lemos C. Geometric issues and ultimate load capacity of masonry arch bridges from the northwest Iberian Peninsula. Eng Struct 2010;32:3955–65. https://doi.org/10.1016/J.ENGSTRUCT.2010.09.006.

[99]   Bayraktar A, Hökelekli E. Seismic Performances of Different Spandrel Wall Strengthening Techniques in Masonry Arch Bridges. International Journal of Architectural Heritage 2021;15:1722–40. https://doi.org/10.1080/15583058.2020.1719234.

[100] Bayraktar A, Hökelekli E. Nonlinear soil deformability effects on the seismic damage mechanisms of brick and stone masonry arch bridges. International Journal of Damage Mechanics 2021;20:431–52. https://doi.org/10.1177/1056789520974423.

[101] Pantò B, Chisari C, Macorini L, Izzuddin BA. A hybrid macro-modelling strategy with multi-objective calibration for accurate simulation of multi-ring masonry arches and bridges. Comput Struct 2022;265. https://doi.org/10.1016/J.COMPSTRUC.2022.106769.

[102] ASTM C 496-85. Standard test method for splitting tensile strength of cylindrical concrete specimens. 2004.

[103] Potyondy JG. Skin friction between various soils and construction materials. Géotechnique 1961;11:339–53. https://doi.org/10.1680/geot.1961.11.4.339.

[104] O'Rourke TD, Druschel SJ, Netravali AN. Shear strength characteristics of sand-polymer interfaces. Journal of Geotechnical Engineering 1990;116:451–69. https://doi.org/10.1061/(ASCE)0733-9410(1990)116:3(451).

[105] Lee S. Influence of surface topography on interface strength and counterface soil structure. PhD Thesis. Georgia Institute of Technology, 1998.

[106] Frost JD, DeJong JT, Recalde M. Shear failure behavior of granular–continuum interfaces. Eng Fract Mech 2002;69:2029–48. https://doi.org/10.1016/S0013-7944(02)00075-9.

[107] Dove JE, Frost JD. Peak friction behavior of smooth geomembrane-particle interfaces. Journal of Geotechnical and Geoenvironmental Engineering 1999;125:544–55. https://doi.org/10.1061/(ASCE)1090-0241(1999)125:7(544).

[108] Tovar-Valencia RD, Galvis-Castro A, Salgado R, Prezzi M. Effect of surface roughness on the shaft resistance of displacement model piles in sand. Journal of Geotechnical and Geoenvironmental Engineering 2018;144. https://doi.org/10.1061/(ASCE)GT.1943-5606.0001828.

[109] Kestell Floyer J. English brick buildings of the fifteenth century. Archaeological Journal 1913;70:121–32. https://doi.org/10.1080/00665983.1913.10853220.

[110] Cecchi A, Milani G. A kinematic FE limit analysis model for thick English bond masonry walls. Int J Solids Struct 2008;45:1302–31. https://doi.org/10.1016/j.ijsolstr.2007.09.019.

[111] Taguchi T, Cuadra C. Influence of bond types on brick masonry strength. The 2015 World Congress on Advances in Structural Engineering and Mechanics (ASEM15), Incheon, Korea: 2015.

[112] Milani G, Lourenço PB. 3D non-linear behavior of masonry arch bridges. Comput Struct 2012;110:133–50. https://doi.org/10.1016/j.compstruc.2012.07.008.

[113] Abdou L, Saada RA, Meftah F, Mebarki A. Experimental investigations of the joint-mortar behaviour. Mech Res Commun 2006;33:370–84. https://doi.org/10.1016/j.mechrescom.2005.02.026.

[114] Gambarotta L, Lagomarsino S. Damage models for the seismic response of brick masonry shear walls. Part I: the mortar joint model and its applications. Earthq Eng Struct Dyn 1997;26:423–39.

[115] Tubaldi E, Macorini L, Izzuddin BA. Three-dimensional mesoscale modelling of multi-span masonry arch bridges subjected to scour. Eng Struct 2018;165:486–500. https://doi.org/10.1016/J.ENGSTRUCT.2018.03.031.

[116] Cox D, Halsall R. Brickwork arch bridge. Berkshire, UK: The brick development association; 1996.

[117] ASTM D4318-10. Standard test methods for liquid limit, plastic limit, and plasticity index of soils. 2010.

[118] ASTM D698-12. Standard test methods for laboratory compaction characteristics of soil Using standard effort. 2012.

[119] ASTM D2487-11. Standard practice for classification of soils for engineering purposes (unified soil classification system). West Conshohocken, PA: 2017. https://doi.org/10.1520/D2487-11.

[120] AASHTO. T 236-08. Standard method of test for direct shear test of soils under consolidated drained conditions. American Association of State Highway and Transportation Officials 2018;3.

[121] Rankine W. On the stability of loose earth. Philos Trans R Soc Lond 1857;147:9–27. https://doi.org/10.1098/rstl.1857.0003.

[122] Pulatsu B, Erdogmus E, Lourenço PB. Influence of soil-backfill depth on the strength and behavior of masonry arch bridges in the transverse direction. 13th North American Masonry Conference, Salt Lake, UT, USA: 2019, p. 16–9.

[123] Wang C-D. Lateral stress caused by horizontal and vertical surcharge strip loads on a cross-anisotropic backfill. Int J Numer Anal Methods Geomech 2005;29:1341–61. https://doi.org/10.1002/nag.462.

[124] Mandl G, De Jong LNJ, Maltha A. Shear zones in granular material. Rock Mechanics 1977;9:95–144.

[125] Rowe PW. The stress-dilatancy relation for static equilibrium of an assembly of particles in contact. Proc R Soc Lond A Math Phys Sci 1962;269:500–27.

[126] Abu-Farsakh M, Coronel J, Tao M. Effect of soil moisture content and dry density on cohesive soil–geosynthetic interactions using large direct shear tests. Journal of Materials in Civil Engineering 2007;19:540–9. https://doi.org/10.1061/(ASCE)0899-1561(2007)19:7(540).

[127] Ferreira FB, Vieira CS, Lopes ML. Direct shear behaviour of residual soil–geosynthetic interfaces – influence of soil moisture content, soil density and geosynthetic type. Geosynth Int 2015;22:257–72. https://doi.org/10.1680/gein.15.00011.

[128] Tsubakihara Y., Kishida H. Frictional behaviour between normally consolidated clay and steel by two direct shear type apparatuses. Soils and Foundations 1993;33:1–13. https://doi.org/10.3208/sandf1972.33.2_1.

[129] Hu L, Pu J. Testing and Modeling of Soil-Structure Interface. Journal of Geotechnical and Geoenvironmental Engineering 2004;130:851–60. https://doi.org/10.1061/(ASCE)1090-0241(2004)130:8(851).

[130] Han F, Ganju E, Salgado R, Prezzi M. Effects of Interface Roughness, Particle

Geometry, and Gradation on the Sand-Steel Interface Friction Angle. Journal of Geotechnical and Geoenvironmental Engineering 2018;144. https://doi.org/10.1061/(ASCE)GT.1943.

[131] Kim UG, Hyodo M, Koga C, Orense RP. Effect of fines content on the monotonic shear behavior of sand-clay mixtures. In: Hyodo M, Murata H, Nakata Y, editors. Geomechanics and Geotechnics of Particulate Media: Proceedings of the International Symposium on Geomechanics and Geotechnics of Particulate Media, vol. 12–14, Ube, Japan: CRC Press; 2006.

[132] Dafalla MA. Effects of clay and moisture content on direct shear tests for clay-sand mixtures. Advances in Materials Science and Engineering 2013;2013. https://doi.org/10.1155/2013/562726.

[133] Tsubakihara Y, Kishida H, Nishiyama T. Friction between cohesive soils and steel. Soils and Foundations 1993;33:145–56. https://doi.org/10.3208/SANDF1972.33.2_145.

[134] Heyman J. The safety of masonry arches. Int J Mech Sci 1969;11:363–85. https://doi.org/10.1016/0020-7403(69)90070-8.

[135] Pippard AJS, Chitty L. A study of voussoir arch. London, HMSO: National Building Studies; 1951.

[136] Melbourne C, Tomor AK. Test report-effect of weak/deteriorated masonry on the performance of arch bridges. Salford, UK: 2005.

[137] Melbourne C, Gilbert M, Wagstaff M. The behaviour of multi-span masonry arch bridges. Arch bridges: Proceedings of the First International Conference on Arch Bridges, Bolton, UK: Thomas Telford Publishing; 1995, p. 489–97.

[138] Gilbert M, Smith C, Melbourne C, Wang J. An experimental study of soil-arch interaction in masonry arch bridges. Advances in Bridge Maintenance, Safety Management, and Life-Cycle Performance, Porto, Portugal: CRC Press; 2006, p. 819–20.

[139] Fanning PJ, Boothby TE, Roberts BJ. Longitudinal and transverse effects in masonry arch assessment. Constr Build Mater 2001;15:51–60. https://doi.org/10.1016/S0950-0618(00)00069-6.

[140] Fanning PJ, Boothby TE. Three-dimensional modelling and full-scale testing of stone arch bridges. Comput Struct 2001;79:2645–62. https://doi.org/10.1016/S0045-7949(01)00109-2.

[141] Zani G, Martinelli P, Galli A, di Prisco M. Three-dimensional modelling of a multi-span masonry arch bridge: Influence of soil compressibility on the structural response under vertical static loads. Eng Struct 2020;221:110998. https://doi.org/10.1016/j.engstruct.2020.110998.

[142] Forgács T, Rendes S, Ádány S, Sarhosis V. Mechanical Role of Spandrel Walls on

the Capacity of Masonry Arch Bridges. Proceedings of ARCH 2019. ARCH 2019. Structural Integrity, vol 11. Springer, Cham., 2020, p. 221–9. https://doi.org/10.1007/978-3-030-29227-0_21.

[143] Papa T, Grillanda N, Milani G. Three-dimensional adaptive limit analysis of masonry arch bridges interacting with the backfill. Eng Struct 2021;248:113189. https://doi.org/10.1016/j.engstruct.2021.113189.

[144] Fanning PJ, Boothby TE. Three-dimensional modelling and full-scale testing of stone arch bridges. Comput Struct 2001;79:2645–62. https://doi.org/10.1016/S0045-7949(01)00109-2.

[145] Liu B, Sarhosis V, Booth A, Gilbert M. The 3D response of a large-scale masonry arch bridge – Part II: Performance at failure. Eng Struct 2024;313:118308. https://doi.org/https://doi.org/10.1016/j.engstruct.2024.118308.

[146] Augusthus-Nelson L, Swift G, Melbourne C, Smith C, Gilbert M. Large-scale physical modelling of soil-filled masonry arch bridges. International Journal of Physical Modelling in Geotechnics 2018;18:81–94. https://doi.org/10.1680/jphmg.16.00037.

[147] Gilbert M, Smith C, Wang J, Callaway PhA, Melbourne C. Small and large-scale experimental studies of soil-arch interaction in masonry bridges. Proceedings of 5th International Conference on Arch Bridges 2007:381–8.

[148] National Highways, Design Manual for Roads and Bridges (DMRB): Highway Structures and Bridges CD 376. Unreinforced masonry arch bridges. 2020.

[149] Liu B, Drougkas A, Sarhosis V. A material characterisation framework for assessing brickwork masonry arch bridges: from material level to component level testing. Constr Build Mater 2023;392:132347. https://doi.org/10.1016/j.conbuildmat.2023.132347.

[150] Sarhosis V, Sheng Y. Identification of material parameters for low bond strength masonry. Eng Struct 2014;60:100–10. https://doi.org/10.1016/j.engstruct.2013.12.013.

[151] Liu B, Drougkas A, Sarhosis V, Smith CC, Gilbert M. Experimental investigation on the shear behaviour of the brickwork-backfill interface in masonry arch bridges. Eng Struct 2023;292:116531. https://doi.org/10.1016/j.engstruct.2023.116531.

[152] Hillerborg A. The theoretical basis of a method to determine the fracture energy GF of concrete. Mater Struct 1985;18:291–6. https://doi.org/10.1007/BF02472919.

[153] Conde B, Díaz-Vilariño L, Lagüela S, Arias P. Structural analysis of Monforte de Lemos masonry arch bridge considering the influence of the geometry of the arches and fill material on the collapse load estimation. Constr Build Mater 2016;120:630–42. https://doi.org/10.1016/j.conbuildmat.2016.05.107.

[154] Liu B, Muhit I, Sarhosis V. Stochastic load-carrying capacity assessment of brick masonry arch bridges. In: Biondini & Frangopol, editor. Life-Cycle of Structures and Infrastructure Systems, Milano, Italy: CRC Press; 2023, p. 1392–9.

[155] Simoncello N, Zampieri P, Gonzalez-Libreros J, Pellegrino C. Experimental behaviour of damaged masonry arches strengthened with steel fiber reinforced mortar (SFRM). Compos B Eng 2019;177:107386. https://doi.org/10.1016/j.compositesb.2019.107386.

[156] Wang J. The three dimensional behaviour of masonry arches. PhD Thesis. University of Salford, 2004.

[157] Melbourne C, Wang J. The 3-dimensional behaviour of masonry arches. Proceedings of the 5th International Conference on Bridge Management, University of Surrey: Thomas Telford Publishing; 2005, p. 121–8.

[158] Zhang Y, Macorini L, Izzuddin BA. Mesoscale partitioned analysis of brick-masonry arches. Eng Struct 2016;124:142–66. https://doi.org/10.1016/j.engstruct.2016.05.046.

[159] Wang J. The three dimensional behaviour of masonry arches. PhD Thesis. University of Salford, 2004.

[160] Sarhosis V, Oliveira DV, Lemos JV, Lourenco PB. The effect of skew angle on the mechanical behaviour of masonry arches. Mech Res Commun 2014;61:53–9. https://doi.org/10.1016/j.mechrescom.2014.07.008.

[161] Bautista-De Castro Á, Sánchez-Aparicio LJ, Carrasco-García P, Ramos LF, González-Aguilera D. A multidisciplinary approach to calibrating advanced numerical simulations of masonry arch bridges. Mech Syst Signal Process 2019;129:337–65. https://doi.org/10.1016/j.ymssp.2019.04.043.

[162] Solla M, Caamaño JC, Riveiro B, Arias P. A novel methodology for the structural assessment of stone arches based on geometric data by integration of photogrammetry and ground-penetrating radar. Eng Struct 2012;35:296–306. https://doi.org/10.1016/j.engstruct.2011.11.004.

[163] Stavroulaki ME, Riveiro B, Drosopoulos GA, Solla M, Koutsianitis P, Stavroulakis GE. Modelling and strength evaluation of masonry bridges using terrestrial photogrammetry and finite elements. Adv Eng Softw 2016;101:136–48. https://doi.org/10.1016/j.advengsoft.2015.12.007.

[164] Solla M, Riveiro B, Lorenzo H, Armesto J. Ancient Stone Bridge Surveying by Ground-Penetrating Radar and Numerical Modeling Methods. J Bridge Eng 2014;19:110–9. https://doi.org/10.1061/(ASCE)BE.1943-5592.0000497.

[165] Orbán Z, Gutermann M. Assessment of masonry arch railway bridges using non-destructive in-situ testing methods. Eng Struct 2009;31:2287–98. https://doi.org/10.1016/j.engstruct.2009.04.008.

[166] Helmerich R, Niederleithinger E, Trela C, Bień J, Kamiński T, Bernardini G. Multi-tool inspection and numerical analysis of an old masonry arch bridge. Struct Infrastruct Eng 2012;8:27–39. https://doi.org/10.1080/15732471003645666.

[167] Kishen JMC, Ramaswamy A, Manohar CS. Safety Assessment of a Masonry Arch Bridge: Field Testing and Simulations. J Bridge Eng 2013;18:162–71. https://doi.org/10.1061/(ASCE)BE.1943-5592.0000338.

[168] Erduran E, Gonen S, Pulatsu B, Soyoz S. Damping in masonry arch railway bridges under service loads: An experimental and numerical investigation. Eng Struct 2023;294:116801. https://doi.org/10.1016/j.engstruct.2023.116801.

[169] Sarhosis V, Forgács T, Lemos J V. A discrete approach for modelling backfill material in masonry arch bridges. Comput Struct 2019;224. https://doi.org/10.1016/J.COMPSTRUC.2019.106108.

[170] Scozzese F, Ragni L, Tubaldi E, Gara F. Modal properties variation and collapse assessment of masonry arch bridges under scour action. Eng Struct 2019;199:109665. https://doi.org/10.1016/j.engstruct.2019.109665.

[171] Han Y, Chun Q, Gao X. Flood-induced forces and collapse mechanism of historical multi-span masonry arch bridges: The Putang bridge case. Eng Fail Anal 2023;153:107564. https://doi.org/10.1016/j.engfailanal.2023.107564.

[172] Dimitrios N, Souzana T, Stavroula P. Arch stone bridges: procedures for evaluation of structural integrity. International Journal of Architectural Heritage 2023;17:1484–504. https://doi.org/10.1080/15583058.2022.2042624.

[173] Learnt L. Spandrel walls - managing the risks. 2012.

[174] Reccia E, Milani G, Cecchi A, Tralli A. Full 3D homogenization approach to investigate the behavior of masonry arch bridges: The Venice trans-lagoon railway bridge. Constr Build Mater 2014;66:567–86. https://doi.org/10.1016/j.conbuildmat.2014.05.096.

[175] Conde B, Ramos LF, Oliveira D V., Riveiro B, Solla M. Structural assessment of masonry arch bridges by combination of non-destructive testing techniques and three-dimensional numerical modelling: Application to Vilanova bridge. Eng Struct 2017;148:621–38. https://doi.org/10.1016/j.engstruct.2017.07.011.

[176] Bertolesi E, Milani G, Lopane FD, Acito M. Augustus Bridge in Narni (Italy): Seismic Vulnerability Assessment of the Still Standing Part, Possible Causes of Collapse, and Importance of the Roman Concrete Infill in the Seismic-Resistant Behavior. IJAH 2017:1–30. https://doi.org/10.1080/15583058.2017.1300712.

[177] Sarhosis V, Liu B, Gilbert M. The 3D response of a large-scale masonry arch bridge – Part I: Performance under low and medium loading levels. Eng Struct 2023;316:118496. https://doi.org/https://doi.org/10.1016/j.engstruct.2024.118496.

[178] Mertol HC, Baran E, Bello HJ. Flexural behavior of lightly and heavily reinforced steel fiber concrete beams. Constr Build Mater 2015;98:185–93. https://doi.org/10.1016/j.conbuildmat.2015.08.032.

[179] Zampieri P, Zanini MA, Faleschini F, Hofer L, Pellegrino C. Failure analysis of masonry arch bridges subject to local pier scour. Eng Fail Anal 2017;79:371–84. https://doi.org/10.1016/j.engfailanal.2017.05.028.

[180] Conde B, Ramos LF, Oliveira D V., Riveiro B, Solla M. Structural assessment of masonry arch bridges by combination of non-destructive testing techniques and three-dimensional numerical modelling: Application to Vilanova bridge. Eng Struct 2017;148:621–38. https://doi.org/10.1016/j.engstruct.2017.07.011.

[181] Liu B, Kawabe D, Kim C, Sarhosis V. Full life-cycle vibration-based monitoring of a full-scale masonry arch bridge with increasing levels of damage. Eng Struct 2024;315:118466. https://doi.org/https://doi.org/10.1016/j.engstruct.2024.118466.

[182] Kim C-W, Kawatani M. Pseudo-static approach for damage identification of bridges based on coupling vibration with a moving vehicle. Structure and Infrastructure Engineering 2008;4:371–9. https://doi.org/10.1080/15732470701270082.

[183] Liu B, Sarhosis V, Lemos JV. Quantification of the crack propagation and global failure mechanism of single- and multi-ring masonry arch bridges. Eng Struct 2024;306:117805. https://doi.org/10.1016/j.engstruct.2024.117805.

[184] Basha SH, Guo Z-X, Xie X. Effect of Structural Bonding Patterns on Mechanical Characteristics of Clay Brick Masonry under Different Loadings Using Digital Image Correlation Technique. Journal of Materials in Civil Engineering 2022;34. https://doi.org/10.1061/(ASCE)MT.1943-5533.0004457.

[185] Bolhassani M, Hamid AA, Rajaram S, Vanniamparambil PA, Bartoli I, Kontsos A. Failure analysis and damage detection of partially grouted masonry walls by enhancing deformation measurement using DIC. Eng Struct 2017;134:262–75. https://doi.org/10.1016/j.engstruct.2016.12.019.

[186] Bello I, Martínez-Abella F, Wardeh G, González-Fonteboa B. Complete stress-strain analysis of masonry prisms under compressive loading-unloading cycles through digital image correlation. Eng Struct 2024;298:117088. https://doi.org/10.1016/j.engstruct.2023.117088.

[187] Bhat ZM, Singh Y, Agarwal P. Characterization of mechanical behavior of different types of masonry with a detailed investigation of full-field strain using digital image correlation. Constr Build Mater 2023;407:133502. https://doi.org/10.1016/j.conbuildmat.2023.133502.

[188] Hemmat M, Zarrin O, Totoev YZ, Masia MJ. An experimental study on the in-plane seismic performance of the confined semi-interlocking masonry system

using DIC method. Structures 2024;63:106400. https://doi.org/10.1016/j.istruc.2024.106400.

[189] Ghorbani R, Matta F, Sutton MA. Full-Field Deformation Measurement and Crack Mapping on Confined Masonry Walls Using Digital Image Correlation. Exp Mech 2015;55:227–43. https://doi.org/10.1007/s11340-014-9906-y.

[190] Roselli F, Alforno M, Manuello Bertetto A, Venuti F. Experimental investigation of the effect of brick pattern on the structural response of masonry arches and barrel vaults. Constr Build Mater 2023;368:130434. https://doi.org/10.1016/j.conbuildmat.2023.130434.

[191] Cuadros-Rojas E, Garcia-Ramonda L, Roca P, Pelà L. Experimental analysis of the compressive behaviour of perforated brick masonry using digital image correlation. Constr Build Mater 2024;431:136471. https://doi.org/10.1016/j.conbuildmat.2024.136471.

[192] Dhanasekar M, Prasad P, Dorji J, Zahra T. Serviceability assessment of masonry arch bridges using digital image correlation. Journal of Bridge Engineering 2019;24. https://doi.org/10.1061/(ASCE)BE.1943-5592.0001341.

[193] Koltsida I, Tomor A, Booth C. The use of digital image correlation technique for monitoring masonry arch bridges. 7th International Conference on Arch Bridges, 2013, p. 681–90.

[194] Acikgoz S, DeJong MJ, Soga K. Sensing dynamic displacements in masonry rail bridges using 2D digital image correlation. Struct Control Health Monit 2018;25:e2187. https://doi.org/10.1002/stc.2187.

[195] Acikgoz S, DeJong MJ, Kechavarzi C, Soga K. Dynamic response of a damaged masonry rail viaduct: Measurement and interpretation. Eng Struct 2018;168:544–58. https://doi.org/10.1016/j.engstruct.2018.04.054.

[196] Rajaram S, Vanniamparambil PA, Khan F, Bolhassani M, Koutras A, Bartoli I, et al. Full-field deformation measurements during seismic loading of masonry buildings. Struct Control Health Monit 2017;24. https://doi.org/10.1002/stc.1903.

[197] Stockdale G, Yuan Y, Milani G. The behavior mapping of masonry arches subjected to lumped deformations. Constr Build Mater 2022;319:126069. https://doi.org/10.1016/j.conbuildmat.2021.126069.

[198] Grosman S, Fang Q, Macorini L, Izzuddin BA. Computational strategy for the design of monitoring for masonry arch bridges using DIC procedures. Life-Cycle of Structures and Infrastructure Systems, London: CRC Press; 2023, p. 1530–7. https://doi.org/10.1201/9781003323020-188.

[199] Carr AJ, Jáuregui DV, Riveiro B, Arias P, Armesto J. Structural evaluation of historic masonry arch bridges based on first hinge formation. Constr Build Mater

2013;47:569–78. https://doi.org/10.1016/j.conbuildmat.2013.05.084.

[200] Liu B, Yue F, Chen B, Man X, Chen L, Jaisee S. Study on bond performance , flexural and crack extension behavior of base concrete prisms strengthen with strain-hardening cementitious composites (SHCC) using DIC technology. Constr Build Mater 2020;251:119035. https://doi.org/10.1016/j.conbuildmat.2020.119035.

[201] Press WH, Teukolsky SA. Savitzky-Golay smoothing filters. Computers in Physics 1990. https://doi.org/10.1063/1.4822961.

[202] Schafer R. What Is a Savitzky-Golay Filter? [Lecture Notes]. IEEE Signal Process Mag 2011;28:111–7. https://doi.org/10.1109/MSP.2011.941097.

[203] Sarhosis V, Garrity SW, Sheng Y. Influence of brick-mortar interface on the mechanical behaviour of low bond strength masonry brickwork lintels. Eng Struct 2015;88:1–11. https://doi.org/10.1016/J.ENGSTRUCT.2014.12.014.

[204] Brackenbury D, Brilakis I, DeJong M. Automated defect detection for masonry arch bridges. International Conference on Smart Infrastructure and Construction 2019 (ICSIC), ICE Publishing; 2019, p. 3–9. https://doi.org/10.1680/icsic.64669.003.

[205] Loverdos D, Sarhosis V. Automatic image-based brick segmentation and crack detection of masonry walls using machine learning. Autom Constr 2022;140:104389. https://doi.org/10.1016/j.autcon.2022.104389.

[206] Rezaie A, Godio M, Achanta R, Beyer K. Machine-learning for damage assessment of rubble stone masonry piers based on crack patterns. Autom Constr 2022;140:104313. https://doi.org/10.1016/j.autcon.2022.104313.

[207] Dong C-Z, Catbas FN. A review of computer vision–based structural health monitoring at local and global levels. Struct Health Monit 2021;20:692–743. https://doi.org/10.1177/1475921720935585.

[208] Loverdos D, Sarhosis V. Geometrical digital twins of masonry structures for documentation and structural assessment using machine learning. Eng Struct 2023;275:115256. https://doi.org/10.1016/j.engstruct.2022.115256.

[209] Muhit IB, Kawabe D, Loverdos D, Liu B, Yukihiro Y, Kim C-W, et al. A framework for digital twinning of masonry arch bridges. Life-Cycle of Structures and Infrastructure Systems, London: CRC Press; 2023, p. 817–24. https://doi.org/10.1201/9781003323020-99.

[210] Pantoja-Rosero BG, Achanta R, Beyer K. Digital twins of stone masonry buildings for damage assessment. Structural Analysis of Historical Constructions 2023, 2024, p. 1437–45. https://doi.org/10.1007/978-3-031-39603-8_115.

[211] Carden EP, Fanning P. Vibration Based Condition Monitoring: A Review. Struct Health Monit 2004;3:355–77. https://doi.org/10.1177/1475921704047500.

[212] Srinivas V, Sasmal S, Ramanjaneyulu K. Damage-sensitive features from non-linear vibration response of reinforced concrete structures. Struct Health Monit 2014;13:233–50. https://doi.org/10.1177/1475921713520028.

[213] Zhang E, Wu D, Shan D. Novel tensor subspace system identification algorithm to identify time-varying modal parameters of bridge structures. Struct Health Monit 2022;21:1541–54. https://doi.org/10.1177/14759217211036024.

[214] Chang K-C, Kim C-W. Modal-parameter identification and vibration-based damage detection of a damaged steel truss bridge. Eng Struct 2016;122:156–73. https://doi.org/10.1016/j.engstruct.2016.04.057.

[215] Entezami A, Shariatmadar H, De Michele C. Non-parametric empirical machine learning for short-term and long-term structural health monitoring. Struct Health Monit 2022;21:2700–18. https://doi.org/10.1177/14759217211069842.

[216] Kaewnuratchadasorn C, Wang J, Kim C. Neural operator for structural simulation and bridge health monitoring. Computer-Aided Civil and Infrastructure Engineering 2023. https://doi.org/10.1111/mice.13105.

[217] Kamariotis A, Chatzi E, Straub D. A framework for quantifying the value of vibration-based structural health monitoring. Mech Syst Signal Process 2023;184:109708. https://doi.org/10.1016/j.ymssp.2022.109708.

[218] Kostić B, Gül M. Vibration-Based Damage Detection of Bridges under Varying Temperature Effects Using Time-Series Analysis and Artificial Neural Networks. Journal of Bridge Engineering 2017;22. https://doi.org/10.1061/(ASCE)BE.1943-5592.0001085.

[219] Zhou HF, Ni YQ, Ko JM. Constructing input to neural networks for modeling temperature-caused modal variability: Mean temperatures, effective temperatures, and principal components of temperatures. Eng Struct 2010;32:1747–59. https://doi.org/10.1016/j.engstruct.2010.02.026.

[220] Liu C, DeWolf JT. Effect of Temperature on Modal Variability of a Curved Concrete Bridge under Ambient Loads. Journal of Structural Engineering 2007;133:1742–51. https://doi.org/10.1061/(ASCE)0733-9445(2007)133:12(1742).

[221] Bencardino F, Curto R, Scavelli V. Inspection and Structural Rehabilitation of an Existing Masonry Arch Railway Bridge. Applied Sciences 2023;13:2973. https://doi.org/10.3390/app13052973.

[222] Borlenghi P, Saisi A, Gentile C. ND testing and establishing models of a multi-span masonry arch bridge. J Civ Struct Health Monit 2023;13:1595–611. https://doi.org/10.1007/s13349-022-00666-1.

[223] Bayraktar A, Türker T, Altunişik AC. Experimental frequencies and damping ratios for historical masonry arch bridges. Constr Build Mater 2015;75:234–41. https://doi.org/10.1016/j.conbuildmat.2014.10.044.

[224] Civera M, Calamai G, Zanotti Fragonara L. System identification via Fast Relaxed Vector Fitting for the Structural Health Monitoring of masonry bridges. Structures 2021;30:277–93. https://doi.org/10.1016/j.istruc.2020.12.073.

[225] Civera M, Mugnaini V, Zanotti Fragonara L. Machine learning-based automatic operational modal analysis: A structural health monitoring application to masonry arch bridges. Struct Control Health Monit 2022;29. https://doi.org/10.1002/stc.3028.

[226] Peeters B, De Roeck G. Reference-based stochastic subspace identification for output-only modal analysis. Mech Syst Signal Process 1999;13:855–78. https://doi.org/10.1006/mssp.1999.1249.

[227] Van Overschee P, De Moor B. Chapter 3: Stochastic Identification. Subspace Identification for Linear Systems, New York: Springer; 1993, p. 53–69. https://doi.org/10.1007/978-1-4613-0465-4.

[228] Gönen S, Soyöz S. Seismic analysis of a masonry arch bridge using multiple methodologies. Eng Struct 2021;226:111354. https://doi.org/10.1016/j.engstruct.2020.111354.

[229] Pelà L, Aprile A, Benedetti A. Seismic assessment of masonry arch bridges. Eng Struct 2009;31:1777–88. https://doi.org/10.1016/j.engstruct.2009.02.012.

[230] Borlenghi P, Saisi A, Gentile C. ND testing and establishing models of a multi-span masonry arch bridge. J Civ Struct Health Monit 2023;13:1595–611. https://doi.org/10.1007/s13349-022-00666-1.

[231] CS 454 Assessment of highway bridges and structures. Design Manual for Roads and Bridges. vol. May. 2022.

Appendix A: Publication list

Journal Publications

1. **Liu, B.**, Collier, J. and Sarhosis, V. Digital image correlation based crack monitoring on masonry arch bridges. Engineering Failure Analysis, 2025; 169: 109185.

2. **Liu, B.**, Kawabe, D., Kim, CW. and Sarhosis, V. Full life-cycle vibration-based monitoring of a full-scale masonry arch bridge with increasing levels of damage. Engineering Structures, 2024; 315: 118466.

3. Sarhosis, V., **Liu, B.**, and Gilbert, M. The 3D response of a large-scale masonry arch bridge - Part I: Performance under low and medium loading levels. Engineering Structures, 2024; 316: 118496.

4. **Liu, B.**, Sarhosis, V., Booth, A. and Gilbert, M. The 3D response of a large-scale masonry arch bridge - Part II: Performance at failure. Engineering Structures, 2024; 313: 118308.

5. **Liu, B.**, Sarhosis, V., and Jose, L. Quantification of the crack propagation and global failure mechanism of single- and multi-ring masonry arch bridges. Engineering Structures, 2024; 306: 117805.

6. Del Giudice, L., Katsamakas, A., **Liu, B.**, Sarhosis, V., Vassiliou M. Physical modelling of unreinforced masonry walls using a sand-based 3D printer. Engineering Structures, 2024; 305:117665.

7. **Liu, B.**, Drougkas, A. and Sarhosis, V. A material characterisation framework for assessing brickwork masonry arch bridges: From material level to component level testing. Construction and Building Materials, 2023; 397:132347.

8. **Liu, B.**, Drougkas, A., Sarhosis, V., Smith, C.C. and Gilbert, M. Experimental investigation on the shear behaviour of the brickwork-backfill interface in masonry arch bridges. Engineering Structures, 2023; 292:116531.

Conference proceedings

1. **Liu, B.** and Sarhosis, V. Three-dimensional response of masonry arch bridges: an experimental study. In 18th International Brick and Block Masonry Conference (IB2MaC), Birmingham, UK, 2024.

2. **Liu, B.** and Sarhosis, V. Material characterization for masonry arch bridge: an experimental investigation. In 18th International Brick and Block Masonry Conference (IB2MaC), Birmingham, UK, 2024.

3. Loverdos, D., **Liu, B.**, and Sarhosis, V. Automated post-earthquake damage-assessment of masonry buildings using computer-vision. In 18th International Brick and Block Masonry Conference (IB2MaC), Birmingham, UK, 2024.

4. Firoozmand, F., **Liu, B.**, Loverdos, D., and Sarhosis, V. AI-aided detection of the response of free-standing ancient columns subjected to earthquake. In 18th World Conference on Earthquake Engineering (WCEE2024). Milan, Italy, 2024.

5. **Liu, B.**, Muhit, I.B. and Sarhosis, V. Stochastic load-carrying capacity assessment of brick masonry arch bridges. In Eighth International Symposium on Life-Cycle of Structures and Infrastructure Systems (IALCCE2023). CRC Press. Milano, 2023.

6. Muhit, I.B., Kawabe, D., Loverdos, D., **Liu, B.**, Yukihiro, Y., Kim, C.W., and Sarhosis, V. A framework for digital twinning of masonry arch bridges. In Eighth International Symposium on Life-Cycle of Structures and Infrastructure Systems (IALCCE2023). CRC Press. Milano, 2023.

7. **Liu, B.**, Sarhosis, V. and Yan, Z. Mechanical behaviour of brickwork multi-ring masonry arch bridges constructed with different bond types. In International Conference on Structural Analysis of Historical Constructions (SAHC2023). Cham: Springer Nature Switzerland. Kyoto, 2023.

Appendix B: Load-deflection curves of the bridge

(a) Load-deflection curves under low-level loads
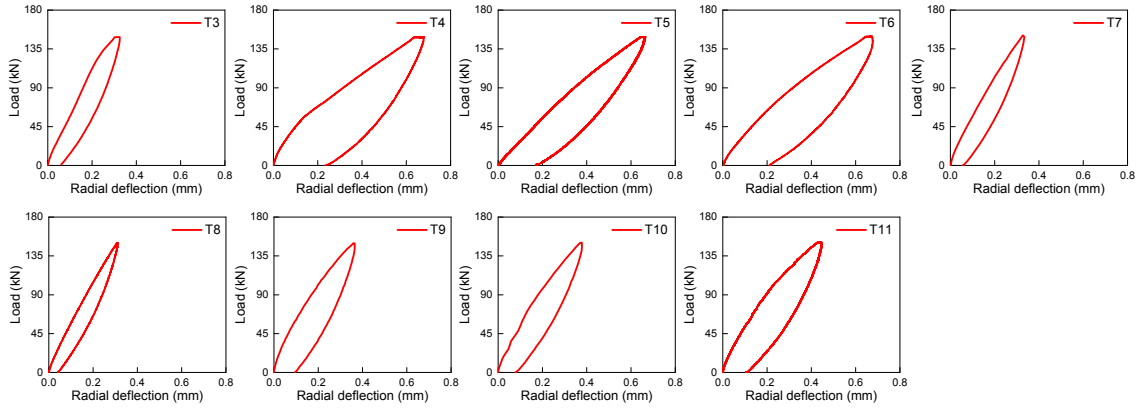
(b) Load-deflection curves under mid-level loads
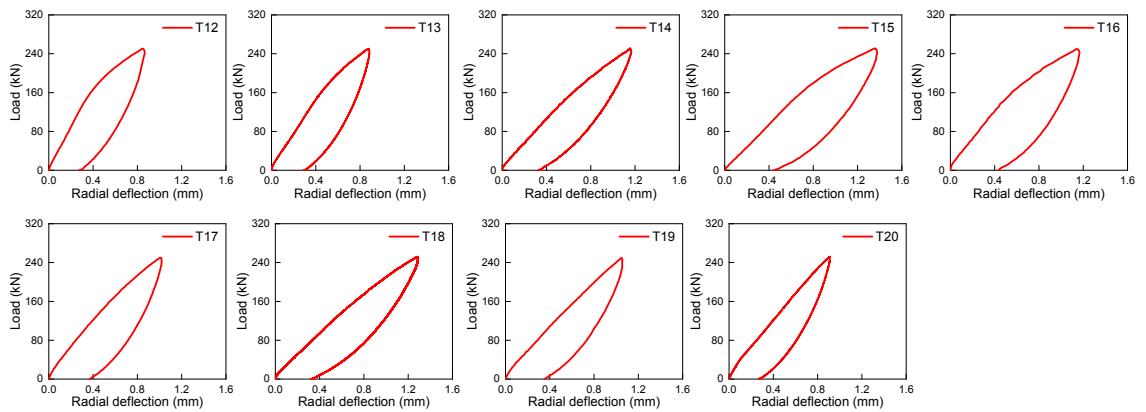
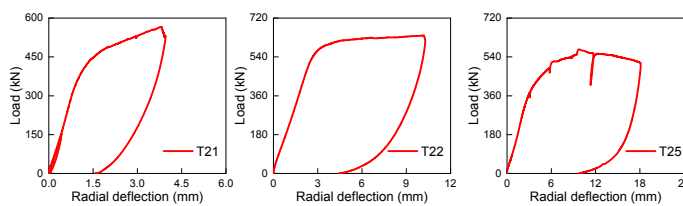(c) Load-deflection curves under high-level and failure-level loads

Figure B1. Load-radial deflection curve of the masonry arch bridge obtained from loading tests; (a) T3 to T11 were under the low-loading level with a loading magnitude of 150 kN; (b) T12 to T20 were under the mid-loading level with a loading magnitude of 250 kN; (c) T21 was under the high loading level with a loading magnitude of 560 kN; T22 and T25 were the failure level test.

223